GENERAL ATOMIC

GA-A13737
UC-77

HTGR FUELS AND CORE DEVELOPMENT PROGRAM

QUARTERLY PROGRESS REPORT FOR THE PERIOD ENDING NOVEMBER 30, 1975

Prepared under
Contract E(04-3)-167
Project Agreement No. 17
for the San Francisco Operations Office
U.S. Energy Research and Development Administration

DATE PUBLISHED: DECEMBER 31, 1975

Printed in the United States of America
Available from
National Technical Information Service
U.S. Department of Commerce
5285 Port Royal Road
Springfield, Virginia 22161
Price: Printed Copy $7.60; Microfiche $2.25

DISCLAIMER

GA-A13737
UC-77

HTGR FUELS AND CORE DEVELOPMENT PROGRAM

QUARTERLY PROGRESS REPORT FOR THE PERIOD ENDING NOVEMBER 30, 1975

Prepared under
Contract E(04-3)-167
Project Agreement No. 17
for the San Francisco Operations Office
U.S. Energy Research and Development Administration

GENERAL ATOMIC PROJECT 3224 DATE PUBLISHED: DECEMBER 31, 1975

QUARTERLY REPORT SERIES

GA-4072-December, 1962, through February, 1963
GA-4350-March, 1963, through May, 1963
GA-4569-June, 1963, through August, 1963
GA-4937-September, 1963, through November, 1963
GA-5104-December, 1963, through February, 1964
GA-5366-March, 1964, through May, 1964
GA-5618-June, 1964, through August, 1964
GA-5866-September, 1964, through November, 1964
GA-6113-December, 1964, through February, 1965
GA-6418-March, 1965, through May, 1965
GA-6671-June, 1965, through August, 1965
GA-6869-September, 1965, through November, 1965
GA-7010-December, 1965, through February, 1966
GA-7181-March, 1966, through May, 1966
GA-7396-June, 1966, through August, 1966
GA-7553-September, 1966, through November, 1966
GA-7801-December, 1966, through February, 1967
GA-7981-March, 1967, through May, 1967
GA-8200-June, 1967, through August, 1967
GA-8356-September, 1967, through November, 1967
GA-8530-December, 1967, through February, 1968
GA-8662-March, 1968, through May, 1968
GA-8860-June, 1968, through August, 1968
GA-9090-September, 1968, through November, 1968
GA-9227-December, 1968, through February, 1969
GA-9372-March, 1969, through May, 1969
GA-9660-June, 1969, through August, 1969
GA-9815-September, 1969, through November, 1969
GA-9944-December, 1969, through February, 1970
GA-10088-March, 1970, through May, 1970
GA-10288-June, 1970, through August, 1970
GA-10399-September, 1970, through November, 1970
GA-10501-December, 1970, through February, 1971
GA-10661-March, 1971, through May, 1971
Gulf-GA-A10784-June, 1971, through August, 1971
Gulf-GA-A10930-September, 1971, through November, 1971
Gulf-GA-A10999-December, 1971, through February, 1972
Gulf-GA-A12150-March, 1972, through May, 1972
Gulf-GA-A12222-June, 1972, through August, 1972
Gulf-GA-A12422-September, 1972, through November, 1972
Gulf-GA-A12515-December, 1972, through February, 1973
Gulf-GA-12599-March, 1973, through May, 1973
Gulf-GA-A12725-June, 1973, through August, 1973
Gulf-GA-A12818-September, 1973, through November, 1973
GA-A12916-December, 1973, through February, 1974
GA-A13030-March, 1974, through May, 1974
GA-A13126-June, 1974, through August, 1974
GA-A13253-September, 1974, through November, 1974
GA-A13353-December, 1974, through February, 1975
GA-A13444-March, 1975, through May, 1975
GA-A13592-June, 1975, through August, 1975

ABSTRACT

This publication continues the quarterly report series on the HTGR Fuels and Core Development Program. The Program covers items of the base technology of the High-Temperature Gas-Cooled Reactor (HTGR) system. The development of the HTGR system will, in part, meet the greater national objective of more effective and efficient utilization of our national resources. The work reported here includes studies of reactions between core materials and coolant impurities, basic fission product transport mechanisms, core graphite development and testing, the development and testing of recyclable fuel systems, and physics and fuel management studies. Materials studies include irradiation capsule tests of both fuel and graphite. Experimental procedures and results are discussed and, where appropriate, the data are presented in tables, graphs, and photographs. More detailed descriptions of experimental work are presented in topical reports; these are listed at the end of the report.

INTRODUCTION

This report covers the work performed by the General Atomic Company under U.S. Atomic Energy Commission Contract AT(04-3)-167, Project Agreement No. 17. This Project Agreement calls for support of basic technology associated with the fuels and core of the gas-cooled, nuclear power reactor systems. The program is based on the concept of the High-Temperature Gas-Cooled Reactor (HTGR) developed by the General Atomic Company.

Large HTGR systems will be placed in operation starting in the early 1980's following the operation of the 330-MW(e) prototype in 1975. Characteristics of these advanced systems include:

1. A single-phase gas coolant allowing generation of high-temperature, high-pressure steam with consequent high-efficiency energy conversion and low thermal discharge.

2. A prestressed concrete reactor vessel (PCRV) offering advantages in field construction, primary system integrity, and stressed member inspectability.

3. Graphite core material assuring high-temperature structural strength, large temperature safety margins, and good neutron economy.

4. Thorium fuel cycle leading to U-233 fuel which allows good utilization of nuclear resources and minimum demands on separative work.

CONTENTS

FIGURES

TABLES

4. HTGR FISSION PRODUCT MECHANISMS
189A No. SU001

TASK 100: FISSION PRODUCT TRANSPORT

Subtask 120: Fission Metal Release

Interim Report on Strontium Diffusion in Bare ThO_2 Kernels

Introduction and Summary. This is an interim report of the results of annealing tests being performed in the temperature range 980° to 1390°C to measure the release of strontium from previously irradiated bare kernels of ThO_2. Diffusion coefficient data derived from these tests are consistent with data for $(Th,U)O_2$ kernels reported previously (Ref. 4-1).

The previous data were derived from annealing tests on five samples of coated particles at temperatures in the range 1400° to 1650°C. Two of the five samples of coated particles were BISO coated and the others were triplex coated. The present tests represent the first direct measurement of strontium release from bare fuel kernels and the first measurement on ThO_2 kernels.

Experimental. The experimental technique by which the present annealing tests are conducted has been previously described (Ref. 4-2). In the present application, this technique was modified in the following manner. The cold finger, used previously to collect fission products that escape from the graphite crucible containing the particles, is not used. The graphite crucible serves to collect the strontium released from the bare ThO_2 kernels. Periodically, the crucible is removed and analyzed for Sr-89 and Sr-90 using radiochemical techniques. The bare kernels are placed in a new crucible and the anneal is continued.

This altered arrangement permits the temperature of the crucible to be monitored directly, and thus a more accurate measure of the temperature is obtainable. The disadvantage of this arrangement is that strontium begins to escape from the graphite crucible at temperatures above approximately 1300°C for the conditions of the experiments, and analysis of the graphite crucible for released strontium is then not adequate. Release from the graphite crucible depends on the wall thickness of the crucible and the time between successive strontium analyses. Since the present annealing experiments are conducted primarily to determine strontium migration in kernels at temperatures in the range between 800° and 1200°C, the loss of strontium from the graphite crucible is apparently not serious. However, analysis of the materials external to the crucible for deposited strontium is currently being made.

In addition to the alteration of removing the cold finger, a tantalum boat containing crushed mullite is placed in the tantalum containment tube to within a few centimeters of the graphite crucible. This arrangement permits the concurrent monitoring of cesium release since mullite has been found to efficiently collect cesium that escapes from the graphite crucible.

Results. The results to date for strontium are shown in Table 4-1. These results are to be regarded as preliminary since (1) the accumulated annealing time is only 400 hr, (2) complete retention of the strontium by the graphite crucible has yet to be confirmed, and (3) the data at 1390°C may be affected by a reaction between the carbon of the crucible and the ThO_2 (to produce ThC_2).

The listed values of D' were calculated according to the equation $D' = \pi(f_1 - f_2)^2/36(t_1 - t_2)$, where D' is the reduced diffusion coefficient (sec^{-1}) and f_i is the fractional release at time t_i (sec). The temperatures listed in Table 4-1 are estimated to be accurate to ±50°C. The data of Table 4-1 are plotted in Fig. 4-1 along with previous estimates (Ref. 4-1) of the reduced diffusion coefficient for migration of strontium in $(Th,U)O_2$ kernels.

TABLE 4-1
DATA FOR STRONTIUM DIFFUSION IN ThO_2 KERNELS

Capsule Irradiation	HB-1
Particle Batch No.	4222-02-101
Kernel Diameter	494 μm
Estimated Fast Fluence	$\sim 3.1 \times 10^{21}$ n/cm^2
Estimated Thermal Fluence	$\sim 2.4 \times 10^{21}$ n/cm^2
Kernel Density	9.86 g/cm^3
Irradiation Temperature	<700°C
Burnup	0.9% FIMA

Sample No.	Annealing Temp (°C)	Isotope[(a)]	D' (sec^{-1})	$\frac{10^4}{T(°K)}$
5787-26	1390	Sr-89	1.3×10^{-9}	6.01
		Sr-90	1.2×10^{-9}	6.01
5787-27	1280	Sr-89	1.3×10^{-12}	6.44
		Sr-90	2.0×10^{-12}	6.44
5787-29	1160	Sr-89	1.2×10^{-12}	6.98
		Sr-90	1.0×10^{-12}	6.98
5787-30	1080	Sr-89	1.9×10^{-14}	7.39
		Sr-90	4.9×10^{-13}	7.39
5787-31	980	Sr-89	1.2×10^{-16}	7.98
		Sr-90	--	7.98

[(a)] The isotope used to determine the value of D'.

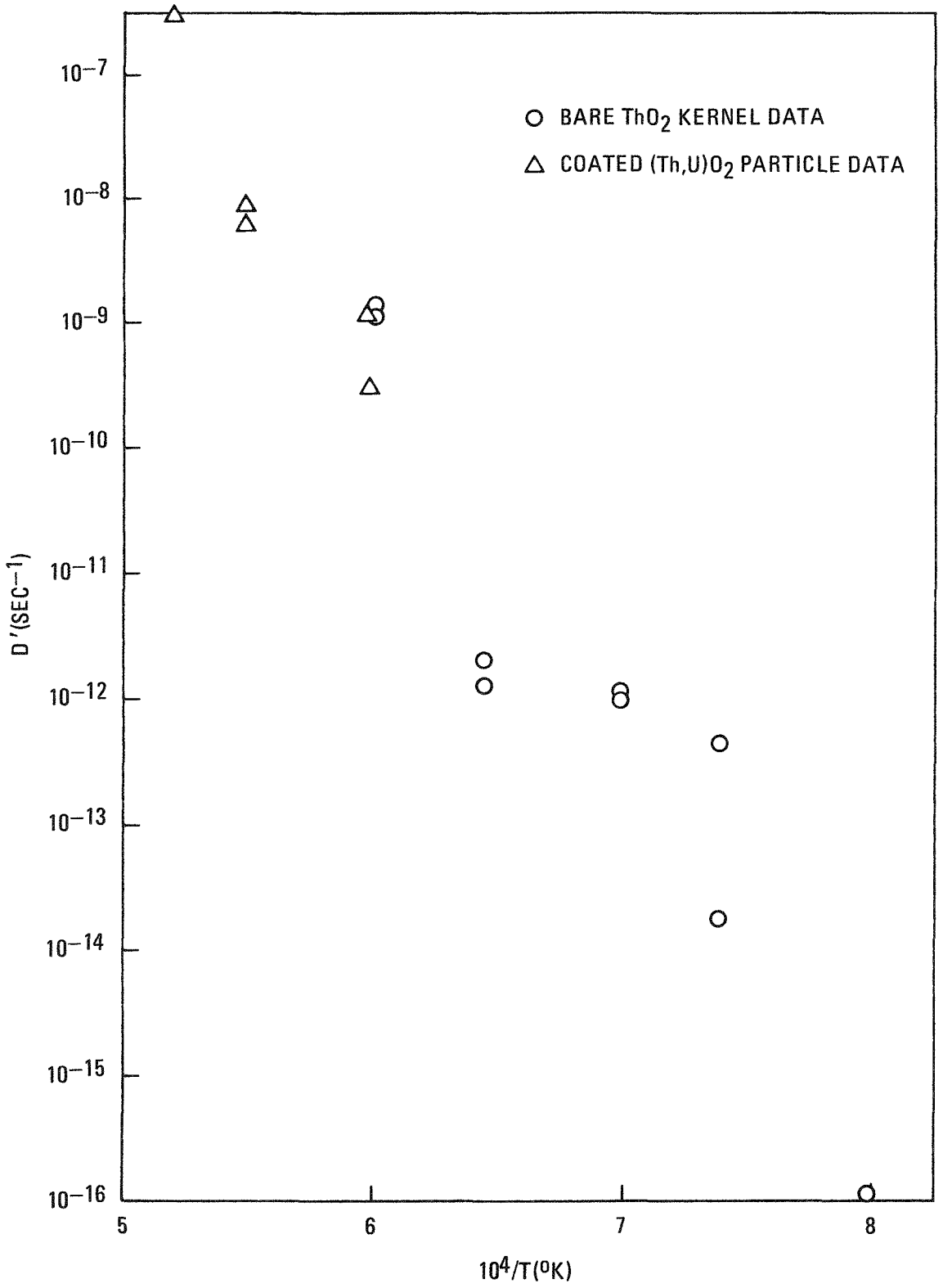

Fig. 4-1. Reduced diffusion coefficients for strontium in oxide kernels

If all the data of Table 4-1 are accepted without qualification and combined with the data for coated particles (Ref. 4-1), then a least-squares analysis yields an expression for the reduced diffusion coefficient given by $D' = 5.1 \times 10^{8} \exp(-137{,}800/RT)$. This expression is practically identical to the expression previously derived (Ref. 4-1) on the basis of the data for the coated particles only. (Note that the coated particles had experienced a 3% FIMA burnup whereas the bare kernels used in the present experiments had experienced a 0.9% burnup.)

Possibly the most reliable data of Table 4-1 are those for the intermediate temperatures, 1080° to 1280°C. The data at 1390°C, as mentioned, may be subject to increased release resulting from the reaction-induced degradation of the ThO_2 kernel; the data at 980°C may be subject to large error as a result of the small release that has occurred to date in the relatively short annealing time. Thus, as is evident from Fig. 4-1, the true slope on the plot of log D' versus $10^4/T(°K)$ for the bare kernel data may be smaller than found by use of all the data shown in Fig. 4-1.

In any event, the reduced diffusion coefficient for strontium release from ThO_2 kernels at low burnup will apparently be small enough to make recoil release of strontium from the kernel the dominant loss mechanism (Ref. 4-3) for temperatures encountered in HTGRs under normal operating conditions.

TASK 200: FISSION PRODUCT TRANSPORT CODES

Subtask 220: Validation of Codes and Input Data

Cesium Sorption on French (CEA) Graphite and Matrix Material

Introduction and Summary. Sorption isotherms for cesium sorbed on Pechiney P_3JHAN graphite and Le Carbone Lorraine (LCL) matrix material have been generated using the mass spectrometric Knudsen cell technique. These sorption isotherms will serve as input to FIPER code analysis of cesium

behavior in the CEA Cadarache Pegase loop (CPL-2) and the P_3JHAN graphite data as input to analysis of cesium behavior in the CEA Saclay Spitfire loop experiment (SSL-1). The LCL matrix is composed of 88 wt % LCL graphite powder (LCL-8102) and 12 wt % LCL resin No. 2 (a thermosetting phenyl formaldehyde resin). Comparison of isotherms for the CEA materials with reference GA isotherms reveals that P_3JHAN and H-451 graphites exhibit similar sorption characteristics, but LCL matrix material is significantly less sorptive of cesium than GA matrix material.

Experimental. The sample materials were supplied by CEA and experiments were performed at GA by using the mass spectrometric technique (Refs. 4-4 through 4-6). In this technique, a sample of the graphite (with particles in the size range of 44 to 74 μm) with sorbed cesium is placed in a molybdenum Knudsen cell. Initially the cesium is in the form of the nitrate, and a preliminary heating of the nitrate-impregnated graphite in the cell converts the sorbate to metal. The cell is then maintained at a series of temperatures and the diffusion of metal vapor from the cell is monitored by the mass spectrometer. The vapor and sorbed concentrations of the metal are determined from a knowledge of the initial and final quantities of sorbate and the time profile of the effusing metal. The data points and associated fits of the points are presented in Tables 4-2 and 4-3 and Figs. 4-2 and 4-3.

Data points in the Freundlich regime were fitted to the equations presented in Tables 4-2 and 4-3 by the use of the FUNFIT code (Ref. 4-7). Data in the Henrian regime were fit with lines of unit slope. The intersection of these lines determined the transition concentration, C_t, marking the change from Henrian to Freundlich behavior. The assigned value of C_t for the matrix material has a larger uncertainty than the like value for P_3JHAN due to the small number of data points for the former in the Henrian regime. The uncertainty is compounded by the apparent fall-off of pressure at low cesium concentrations.

Comparisons of reference GA cesium isotherms with the isotherms generated for the French material are shown in Figs. 4-4 and 4-5. The

TABLE 4-2
CESIUM SORPTION DATA FOR PECHINEY P_3JHAN

Conc. ($\frac{\mu mole\ Cs}{g\ C}$)	Log[(a)] Conc.	Log P (atm)[(a)(b)]				
		800°C	900°C	1000°C	1100°C	1200°C
6.76	0.83	-6.30	-5.38	-4.60	-3.94	-3.37
6.51	0.81	-6.39	-5.42	-4.60	-3.90	-3.29
6.28	0.79	-6.37	-5.42	-4.62	-3.93	-3.34
5.63	0.75	-6.57	-5.58	-4.74	-4.02	-3.40
4.89	0.69	-6.93	-5.92	-5.06	-4.34	-3.71
3.35	0.52	-7.77	-6.66	-5.72	-4.91	-4.22
2.67	0.42	-8.09	-7.01	-6.10	-5.33	-4.66
1.89	0.27	-8.53	-7.43	-6.50	-5.71	-5.02
1.37	0.13	-8.94	-7.78	-6.79	-5.95	-5.22
0.821	-0.08	-9.28	-8.11	-7.13	-6.29	-5.56
0.483	-0.31	-9.65	-8.44	-7.43	-6.56	-5.81
0.188	-0.72	-10.03	-8.89	-7.94	-7.12	-6.42
0.104	-0.98	-10.39	-9.24	-8.26	-7.43	-6.71
0.0495	-1.30	-11.16	-9.98	-8.99	-8.14	-7.41

(a) Log represents logarithm to the base 10; ln [as in footnote (b)] represents logarithm to the base e.

(b) $\ln P(F) = A + B/T + (D+E/T) \ln C$

$\ln P(H) = A + B/T + [(D-1) + E/T] \ln C_t + \ln C$

$P(F)$ = vapor pressure (atm) in the Freundlich (F) region

$P(H)$ = vapor pressure (atm) in the Henrian (H) region

C = concentration of sorbate (μmole Cs/g C)

C_t = transition concentration of sorbate (μmole Cs/g C)

T = temperature (°K)

$A = 12.1$

$B = -3.83 \times 10^4$

$D = -0.55$

$E = 5.69 \times 10^3$

$C_t = 1.9$ μmoles/g

TABLE 4-3
CESIUM SORPTION DATA FOR CEA MATRIX MATERIAL

Conc. ($\frac{\mu moles\ Cs}{g\ C}$)	Log[(a)] Conc.	Log P (atm)[(a)(b)]				
		800°C	900°C	1000°C	1100°C	1200°C
267	2.42	-2.25	-1.61	-1.08	-0.623	-0.228
177	2.24	-2.50	-1.86	-1.32	-0.860	-0.460
106	2.03	-3.31	-2.60	-2.01	-1.50	-1.07
67.9	1.83	-3.56	-2.83	-2.21	-1.68	-1.23
41.8	1.62	-4.27	-3.53	-2.90	-2.37	-1.91
32.3	1.50	-4.83	-4.04	-3.37	-2.80	-2.30
22.0	1.34	-5.30	-4.49	-3.80	-3.22	-2.71
19.2	1.28	-5.67	-4.79	-4.05	-3.42	-2.88
16.1	1.20	-6.03	-5.07	-4.27	-3.58	-2.99
13.9	1.14	-6.33	-5.28	-4.39	-3.64	-2.98
9.30	0.96	-6.93	-5.82	-4.87	-4.07	-3.38
6.30	0.80	-7.65	-6.46	-5.45	-4.59	-3.85
4.10	0.61	-8.26	-7.06	-6.04	-5.18	-4.43
1.50	0.17	-9.17	-7.95	-6.92	-6.05	-5.29
0.677	-0.16	-9.64	-8.44	-7.42	-6.55	-5.80
0.311	-0.50	-10.14	-8.97	-7.98	-7.13	-6.40
0.204	-0.69	-10.90	-9.78	-8.84	-8.03	-7.33

(a) Log represents logarithm to the base 10; ln [as in footnote (b)] represents logarithm to the base e.

(b) $\ln P(F) = A + B/T + (D+E/T) \ln C$

$\ln P(H) = A + B/T + [(D-1) + E/T] \ln C_t + \ln C$

P(F) = vapor pressure (atm) in the Freundlich (F) region

P(H) = vapor pressure (atm) in the Henrian (H) region

C = concentration of sorbate (μmole Cs/g C)

C_t = transaction concentration of sorbate (μmole Cs/g C)

T = temperature (°K)

A = 14.8

$B = -4.11 \times 10^4$

D = -0.82

$E = 4.57 \times 10^3$

C_t = 1.3 μmoles/g

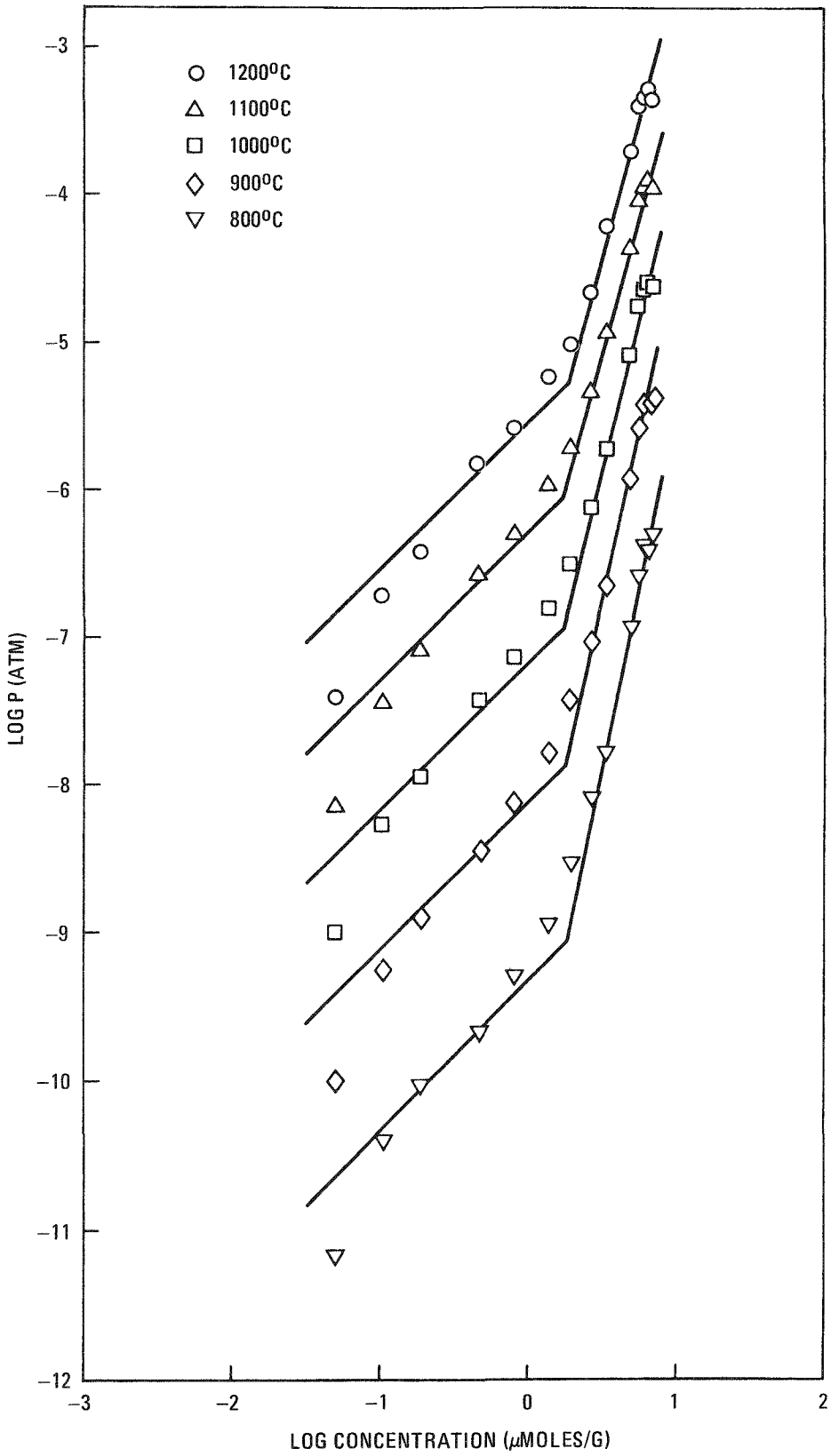

Fig. 4-2. Sorption isotherms for Cs on unirradiated P_3JHAN graphite

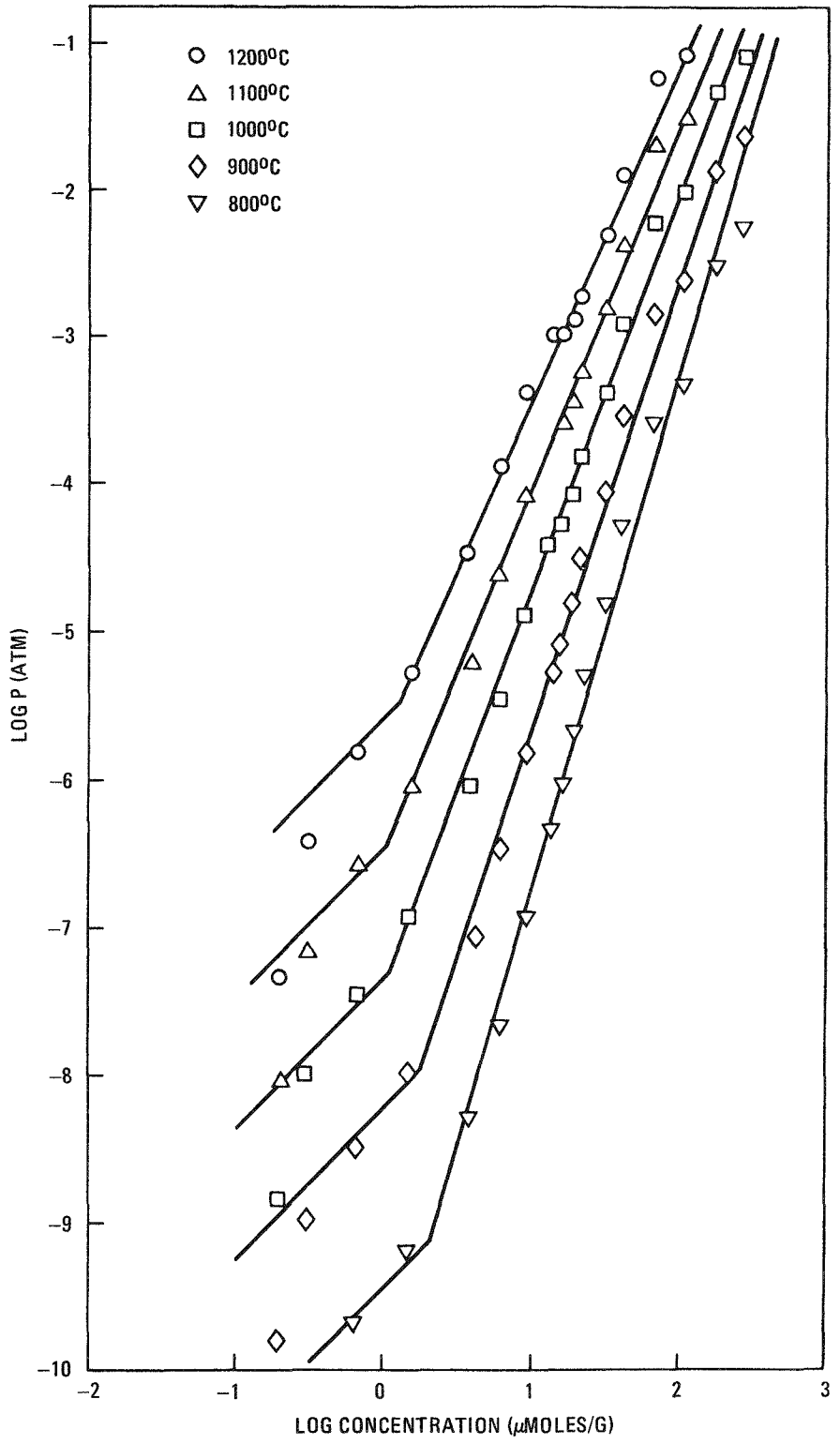

Fig. 4-3. Sorption isotherms for Cs on French resinated graphite matrix material

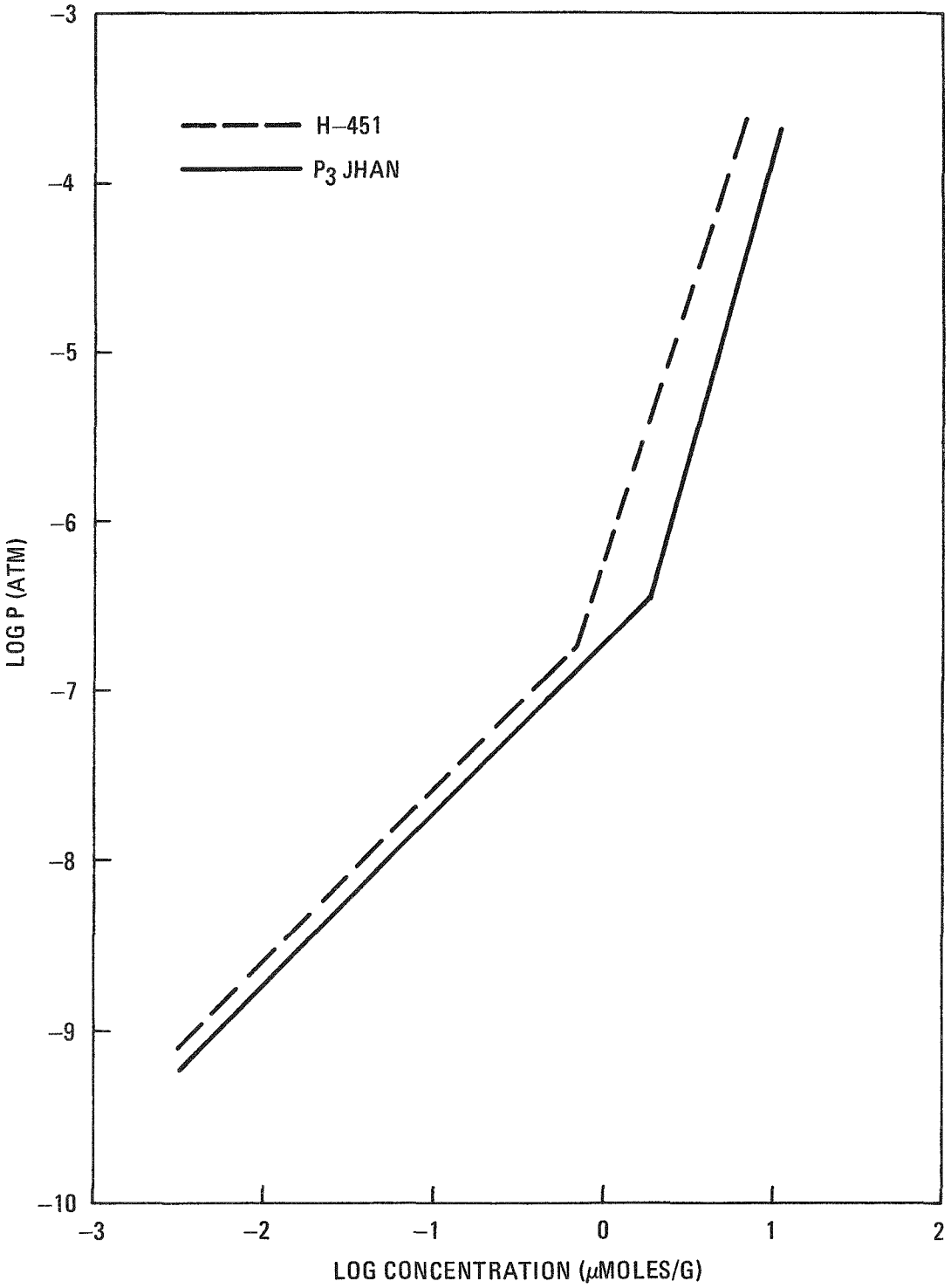

Fig. 4-4. Comparative sorption isotherms for Cs on unirradiated P_3JHAN and H-451 graphite at 1300°K

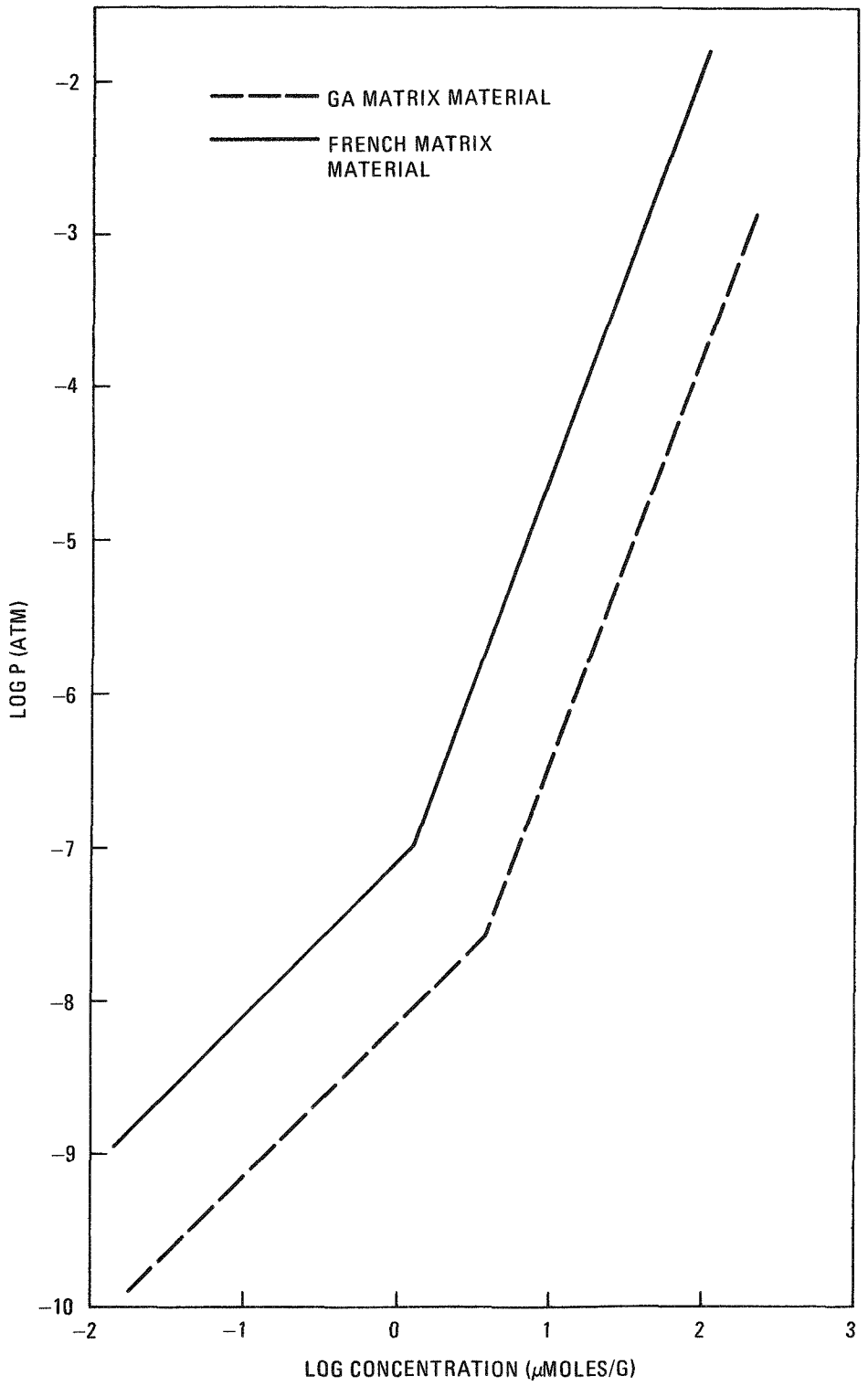

Fig. 4-5. Comparative sorption isotherms for Cs on unirradiated GA and French matrix materials at 1300°K

isotherms for P_3JHAN and H-451 graphites exhibit similar characteristics, the differences being revealed by a larger C_t for P_3JHAN (1.9 versus 0.8 μmoles/g) and a larger concentration dependence of pressure in the Freundlich regime ($C^{3.7}$ versus $C^{3.2}$). The French matrix material is significantly less sorptive of cesium than the GA matrix material; the two materials have comparable C_t values (1.3 versus 4.0) and an identical Freundlich regime concentration dependence ($C^{2.7}$). This lower sorptivity manifests itself in differing partition coefficients exhibited at constant temperature for the two types of reference materials. If a temperature of 1300°K and a pressure of 10^{-8} atm (Henrian regime) is assumed, the respective partition coefficients are:

$$\phi_{GA(1300°K)} = 38.0$$

$$\phi_{CEA(1300°K)} = 2.3$$

The effect of these partition coefficients on metallic release will be determined by the inclusion of GA and CEA partition coefficients and isotherm constants in FIPER code runs.

TASK 300: FISSION PRODUCT DATA REVIEW

Interim Report on Fission Gas Data

The report, "Behavior of Fission Product Gases in HTGR Fuel Material," (Ref. 4-8) covering fission product gas data has been written and is in review. This report presents (1) a review of experimental data on the behavior of fission product gases (including noble gases and halogens) in HTGR fuel materials, (2) current reference data for use as input to computer codes utilized to calculate the fission gas inventory in the primary coolant circuit of the HTGR, and (3) the basis for the selection of the reference data. A summary of the report is given below; details are given in the following section (Fission Product Data Status and Needs).

Experimental data in the report are used to deduce the effect of the following variables on fission gas release: fuel configuration, temperature, half-life, neutron flux level, neutron fluence, and fuel hydrolysis. Experimental results indicate:

1. Fission gas release from HTGR fuel elements is governed by the amount of uranium and thorium contamination [i.e., exposed uranium and thorium (including particles with leaky coatings) in as-manufactured fuel rods] and by the number of failed particles resulting from coating failure during irradiation.

2. The reference value of the fractional release, R/B, for Kr-85m at 1100°C is 5×10^{-3} for failed fuel particles in a constrained configuration (as occurs in fuel rods where cracked particle coatings are constrained from opening up by the matrix material).

3. The temperature dependence of the R/B for Kr-85m is described by a combination of an activation energy of 0.8 kcal/mole, dominant at temperatures below 600°C, and an activation energy of between 14 and 19 kcal/mole, dominant between 900° and 1500°C.

4. The R/B depends on a power of the nuclide half-life; the exponent of the half-life term varies from about 0.2 below 650°C to 0.5 above 850°C.

5. The R/B for a given fuel configuration is independent of neutron flux level (fission rate density), neutron fluence, and burnup.

6. The R/B for Kr-85m at 1100°C for failed particles containing hydrolyzed carbide fuel is $\sim$0.15.

7. Iodine and tellurium isotopes should be treated as if they were xenon isotopes; bromine and selenium isotopes should be treated as if they were krypton isotopes.

This report is an interim report on experimental data relating to the behavior of fission product gases in HTGR fuel material. The data are being confirmed and extended through continuing work at General Atomic and other laboratories.

Fission Product Data Status and Needs

Introduction and Summary

The status and needs of fission product transport data have been evaluated. These transport data are used in calculations of (1) the release of fission products to the primary circuit of the HTGR and (2) the distribution of fission products in the primary circuit. The evaluation is based on (1) a review of strontium transport data (Ref. 4-1), (2) a review of the behavior of fission product gases (Ref. 4-8), (3) core release calculations in which the contributions and associated uncertainties of many processes are evaluated (Ref. 4-3), and (4) a review of cesium transport data, which is in progress.

In summary, the greatest need for additional data exists in relation to the distribution of fission products in the primary coolant circuit. Less extensive work is required in the areas of metallic and gaseous fission product transport.

Adequate data on plateout distribution in the primary circuit are clearly lacking. The basic need is for sorption data for iodine and cesium on primary circuit metals. Iodine and cesium are the two elements of most concern from the standpoint of safety and plant maintenance, respectively. These data must include the effect of the surface condition of the metals on sorptivity and must be applicable to sorbate pressures in the range between 10^{-9} and 10^{-13} atm.

For the existing metallic fission product transport data, the largest uncertainties are found (Ref. 4-3) for cesium transport. These uncertainties can be reduced to acceptable levels by (1) continued development

of models and in-core tests for cesium transport in graphite and (2) measurement of cesium transport on reference pyrocarbons that have experienced the full range of neutron fluence for the HTGR. New data on metallic fission products are also needed for (1) the effect of graphite burnoff (i.e., extent of graphite oxidation) on transport and sorptivity, (2) the effect of hydrolysis of carbide kernels on release, and (3) the release from oxide fuel kernels.

Based on the present gaseous fission product transport data, uncertainties in fission gas release are found to be relatively small (Ref. 4-3). However, work is needed to (1) verify that constrained failed fuel particles are representative of failed particles in fuel rods, (2) determine the temperature dependence of fission gas release for temperatures above 1500°C, (3) determine the extent of the release of fission gases when particles fail, (4) confirm present data for reference-type fuel, and (5) establish the effect of fuel hydrolysis on fission gas release.

Details on the fission product data status and needs are presented below.

Fission Product Plateout Data

At present, only preliminary estimates can be made for the sorption isotherms needed to estimate plateout distribution in the primary circuit of the HTGR. The data of primary interest involve sorption of iodine on graphite and sorption of iodine and cesium on low- and high-alloy metals (the alloys are distinguished here by a low or relatively larger content of chromium and/or nickel). The available data for sorption of iodine on graphite (Refs. 4-9 through 4-11) and iodine on low-alloy metals (Refs. 4-11 through 4-15) are inadequate and data for the other sorption cases of interest are lacking.

Uncertainties in calculating the plateout distribution in the primary circuit arise from: (1) the necessity to extrapolate the available data to

low vapor pressures of interest, i.e., to pressures in the range 10^{-9} to 10^{-13} atm, (2) the lack of data for some materials of interest, (3) the lack of data on the effect of exposure of the surfaces of the primary circuit materials to the atmospheres encountered in HTGRs under normal operating conditions, and (4) the question of the significance of differences in time available for equilibration under laboratory conditions as compared with reactor conditions (thus, whether penetration of the reactor surfaces by sorbates is only significant under reactor conditions).

Also, related to the calculation of plateout distribution is the possible problem of carbon dust and the deposition of carbon on surfaces of the primary coolant circuit. The carbon may not only change the surface characteristics and thus alter plateout, but also fission products may chemisorb on the dust particles and thus affect the circulating activity.

In the evaluation of uncertainties in core release calculations (Ref. 4-3) the plateout distributions have the largest uncertainties; this is a reflection of the status of the data presented above. Clearly additional experimental data are needed.

Metallic Fission Product Release Data

Metallic fission product release into the primary circuit can be conveniently discussed in terms of migration in the kernel, particle coatings, fuel rod matrix, and graphite web; migration across the fuel rod matrix - graphite web gap; and desorption from the graphite web - coolant hole boundary.

Release From Kernels. Understanding of the release of metallic fission products from the particle kernels is limited. For oxide kernels some data are available on the release of strontium, cesium, and silver. For strontium in ThO_2 at low burnups, the diffusive release is small under reactor conditions (see Task 100) so that release by recoil is dominant (Ref. 4-3); no data are available for the higher burnups (i.e., up to 7.5%

FIMA). Also the diffusive release is very strongly dependent on temperature (see Task 100).

In the case of cesium, release from oxide kernels is also small (Refs. 4-16, 4-17, 4-18). The recognition of this is more important for cesium than for strontium, since in the current method of calculation for cesium release, migration of cesium through the particle coatings is regarded as rate-determining. By accounting for the actual release of cesium from the kernel, the calculated amount of cesium released could be significantly reduced. In spite of the general observation (Refs. 4-16, 4-17, 4-18) of small cesium release from oxide kernels, there is large scatter in the available data. Reduced diffusion coefficients applicable to UO_2-coated particles (Ref. 4-18) are about 10^4 larger than those found for kernels of ThO_2 and $(Th,U)O_2$ (Refs. 4-16, 4-17) (as well as for the corresponding thorium carbides). Within each of these data sets, the scatter is between factors of 10^1 and 10^2; the variation with burnup may contribute to this scatter. The release of cesium is further complicated by the occurrence of a trapped fraction (Ref. 4-19), i.e., a fraction of the cesium in the kernel that is not released or released only slowly; the trapped fraction is apparently strongly dependent on burnup and temperature. The small release parameters (reduced diffusion coefficients) considered above presumably apply to release of the trapped fraction. The understanding of the mechanism of cesium release from kernels will be needed for accurate calculation of cesium release into the primary circuit of the HTGR. Reduced diffusion coefficients for the release of silver from oxide (UO_2) kernels (Ref. 4-18) are approximately the same as for cesium and have about the same uncertainty.

For carbide kernels, there are documented data only for cesium (Ref. 4-17) and strontium (Ref. 4-1) release. The cesium data apply to ThC_2 or $(Th,U)C_2$ with relatively low burnups, have a large scatter, and are limited in temperature range, but otherwise are not distinguishable from data on oxide kernels. However, for the reference-type UC_2 kernels (high density, 200-μm diameter), cesium release appears to be relatively high (Ref. 4-20);

in one case the cesium was found mostly in the buffer layer of particle coatings after a 4-month irradiation at 700°C for particles with high burnup (around 60% FIMA). In this case, barium behaved like cesium, while lanthanides were retained in the kernel. The distribution of strontium is not known for this case. There are, however, some data (Ref. 4-1) on strontium release from carbide fuel kernels with FIMA values below 20%. The data are scattered by more than two orders of magnitude.

In general, there is very little information about the release of metallic fission products from carbide kernels, although the release can be expected to be extensive for elements such as cesium. Since the UC_2 kernels are placed only in TRISO coated particles, which retain fission products quantitatively (Ref. 4-21) when intact, the release of fission products from UC_2 kernels is of interest only for failed particles, at least in regard to the primary circuit activity.

There are two additional considerations associated with release from kernels of failed particles. In the case of failed oxide particles, conversion of the oxide to the carbide becomes possible above about 1100°C as the gaseous reaction products (mainly CO) escape and the equilibrium is shifted in favor of conversion. No documented quantitative data on this reaction exist. The other consideration involves the effect of hydrolysis on the release of fission metals from carbide kernels of failed particles; data on fission gas release exist (Ref. 4-8) but not on metallic fission product release.

Migration in Particle Coatings. The available data on migration of metallic fission products in particle coatings primarily apply to the pyrocarbon coatings with some data available (Ref. 4-22) on migration through the SiC coating. For the buffer regions of the coated particles, no data on migration of fission products exist. Also, to describe migration of fission products through the coatings, distributions between different coating layers, i.e., partition factors, are needed. The partition factors are known only in a rudimentary way (Refs. 4-23 through

4-27) and those values documented are not suitable for use in release calculations because partition factors depend strongly on material properties as well as on temperature, burnup, and fluence.

In core release calculations (Ref. 4-3), the current practice is to assume that transport through only one of the materials comprising the particles is rate-determining for release and thus to assume that transport through the remaining materials is so rapid as to introduce no resistance to release. In the case of cesium, migration through the pyrocarbon layer(s) is assumed to be rate-determining. Extensive measurements (Refs. 4-3, 4-19, 4-28) on migration of cesium in pyrocarbon have been made with agreement between the results from different laboratories. However, a large scatter exists in these data and this scatter has been found to be an important contributor to the uncertainty in the calculated release from the core of the HTGR (Ref. 4-3). The uncertainty is associated with the variation in materials properties and the neutron fluence experienced. A clear demonstration of the difference between high-temperature isotropic (HTI) and low-temperature isotropic (LTI) pyrocarbon has been presented (Ref. 4-19); however, for the LTI pyrocarbon, which is of primary interest for current designs of HTGRs, lack of understanding of the large variation with material properties persists. The effect of the material properties is not yet well enough understood (Ref. 4-19) to account for the variation introduced into the migration parameter but, apparently, some correction could be made for the effect of neutron fluence.

The importance of cesium diffusion in pyrocarbon (release from BISO fertile particles) for core release calculations may be reduced if account is taken of cesium release from oxide kernels; however, this possibility has yet to be established. Also, in this connection, the concentration of cesium in the buffer of carbide kernel particles, which have experienced moderate to high burnup, may indicate that the effect of the buffer (presumably significantly modified by recoil fragments and neutron fluence) on cesium release should be taken into account.

In the case of strontium, migration is apparently only important for failed TRISO particles with carbide kernels. The limited data (Refs. 4-1, 4-18) indicate that there is no difference in strontium migration in LTI and HTI pyrocarbon and that apparently there is little effect of neutron fluence [corresponding to FIMA values of 23% or less for $(Th,U)C_2$ particles].

There is some information about the migration of silver (Ref. 4-18), barium (Refs. 4-19, 4-29, 4-30), and europium (Ref. 4-29) in pyrocarbon. For the same pyrocarbon type, the logarithm of the diffusion coefficient has been shown (Ref. 4-30) to be linearly related to the reciprocal of the atomic radius for the elements cesium, barium, strontium, and europium.

The migration of fission products through SiC layers is small enough so that, at least for cesium and strontium, release is completely negligible during the life of the fuel in the HTGR (Ref. 4-22). The small release is apparently a result of the low solubility (Ref. 4-27) of the fission product metals in SiC. In the case of silver transport, there is uncertainty about the retention by SiC layers (Ref. 4-22).

Transport Across Fuel Rod - Graphite Gap and Desorption at the Graphite Web - Coolant Hole Boundary. Transport in the matrix material surrounding the fuel particles in fuel rods is taken to be rapid in core release calculations (Ref. 4-3). There are apparently no data for migration in the matrix material but this is not a serious deficiency. Transport across the gap is treated as a vapor phase transfer in core release calculations. At equilibrium, the results of this transport are calculated on the basis of the equilibrium isotherms for sorption of the fission product metals in the matrix material of the fuel rods and in the graphite web. Also, desorption of the metallic fission products at the graphite web - coolant hole boundary is calculated on the basis of the equilibrium sorption isotherms for graphite.

Extensive measurements have been conducted for sorption of strontium (Refs. 4-1, 4-16, 4-31, 4-32) and cesium (Refs. 4-2, 4-16, 4-33) on

reference matrix and graphite materials including irradiated graphites. In addition to the data on cesium and strontium sorptivity, data on nonreference materials have been obtained for barium and rubidium (Refs. 4-34, 4-35) sorptivity on graphites and barium, europium, and samarium relative sorptivities on graphite and matrix material (Ref. 4-36). The bulk of the measurements have involved the Knudsen cell mass spectrometer method (Ref. 4-1); other measurements have been made with the isopiestic method (Ref. 4-1). The agreement between experiments using the two methods is acceptable. A range of sorbate concentrations between 10^{-3} and 10^{2} μmole sorbate/gram sorbent has been covered; for low concentrations, the vapor pressure has been shown to be proportional to the sorbate concentration (Henrian regime) and for high concentrations, to depend on a power of the sorbate concentration (Freundlich regime).

In the Knudsen cell mass spectrometer measurements, the samples were generally in powder form and a correction to the data for grain size had to be made by comparing adsorptions on samples in various states of subdivision, including those representative of the HTGR core. These comparisons were conducted, for the most part, only at one temperature and a few pressures. The use of powdered samples in the Knudsen cell, mass-spectrometer method ensured rapid equilibration and thus reduced the duration of the experiment.

The irradiated reference graphite used in sorption measurements had experienced only a single neutron fluence, about 3.5×10^{21} n/cm^2. Most of the data on the dependence of sorptivity on neutron fluence have been obtained with the aid of nonreference graphites (Refs. 4-31, 4-37). The effect of irradiation has been to increase the sorptivity by as much as a factor of ten or larger.

Extension of these results to include the effect of mixed species and burnoff of the sorbing material would be desirable, but perhaps the best course at present for confirmation of these data resides in the validation program (Ref. 4-38) in which predicted releases are compared with observations in loops, capsules, and reactors. The expectation is that this

comparison will permit an assessment of (1) the importance of simultaneous irradiation and sorption, (2) the effect of neutron fluence on sorptivity, (3) the experimental methods used in laboratory sorption measurements, and (4) the effect of mixed species. Items (2), (3), and (4) are also amenable to laboratory experiments and such data, particularly on mixed species, would be useful to supplement existing data.

The effect of oxidation (burnoff) of the graphite and matrix materials of the core on sorption of metallic fission products needs to be assessed.

The evaluation of core release calculations (Ref. 4-3) shows that the release for normal operating conditions is insensitive to variation in the sorptivity of cesium and strontium with the exception of strontium sorptivity on graphite. These calculations, however, did not take into account the effect of irradiation on sorptivity.

Migration in Graphite. There are extensive data on the migration of strontium (Refs. 4-1, 4-32, 4-39) and cesium (Refs. 4-16, 4-36, 4-40 through 4-48) in various graphites. In addition, some data are available on the migration of barium (Refs. 4-32, 4-36, 4-49) and europium (Refs. 4-36, 4-39).

The migration of strontium in graphite is of the classical type (i.e., described by Fick's law) for moderate concentrations and is not strongly dependent on the type of graphite (Ref. 4-1) providing it is highly graphitized. Note that the fractional standard deviation of the average estimated value of the diffusion coefficient for strontium in graphite is relatively low ($\sim$0.3). Furthermore, there is no significant difference between in-pile and out-of-pile behavior (Refs. 4-1, 4-39). Above a concentration of about 1 μg strontium/g graphite, the diffusion coefficient is dependent on the concentration (Ref. 4-1); this dependence has not been well characterized. However, the concentrations of strontium to be encountered in HTGRs under normal operating conditions (Ref. 4-50) are expected to be mostly in the concentration-independent region.

A potential factor of influence on strontium migration is graphite oxidation (i.e., graphite burnoff); French investigations (unpublished results) found that homogeneous oxidation of type P_3JHAN graphite increased the diffusion coefficient of strontium by a factor of about three; these results need to be checked for the reference graphite. Note that for the mean burnoff to be expected in the HTGR ($\sim$0.1%), the increase in the strontium diffusion coefficient is less than 40% based on the French data. Also, the question of the effect of oxidation on the migration of other species in graphite is raised by these results (see below).

For barium and europium, the in-pile diffusion coefficient is about the same as that of strontium (Ref. 4-32).

For cesium, the migration in graphite is clearly different from that expected at moderate concentrations for simple Fickian diffusion. The transport of cesium in graphite appears to involve a relatively rapid surface diffusion and a relatively slow uptake by the bulk graphite. When viewed in terms of cesium profiles in graphite samples, as for example in the postirradiation examination of Peach Bottom fuel test elements (Ref. 4-36), these processes appear as fast and slow components, the former being regarded as associated with surface diffusion and the latter with bulk diffusion. Several models of these processes have been considered (Refs. 4-32, 4-51). One of these models, a two-component diffusion model, has been applied to the analysis of Peach Bottom data (Ref. 4-32).

The bulk of the experimental data (Refs. 4-36, 4-40 through 4-47) on cesium migration were derived from a variety of types of experiments, including in-pile as well as out-of-pile experiments. These data compare favorably with the steady-state diffusion coefficients derived from Peach Bottom data using the two-component diffusion model (Ref. 4-32). A reasonable approximation is to regard all of these data as representing permeation coefficients. In several cases (Refs. 4-36, 4-46, 4-47), the data are reported as permeation coefficients (coefficients derived from flux measurements) and in other cases (Refs. 4-41 through 4-44) the derived

diffusion coefficients are from long-time experiments. These data are mostly associated with concentrations <0.2 μmole/g graphite; a concentration dependence of cesium migration exists (Refs. 4-41, 4-45), the transport of cesium being greater at larger cesium concentrations.

A least-squares analysis of the bulk of the experimental data (Refs. 4-36, 4-40 through 4-47) on cesium migration yields a temperature dependence which is in agreement with recent laboratory experiments on cesium migration through unirradiated graphite (Refs. 4-16, 4-48). However, the laboratory experiments have transport coefficients roughly a factor of ten larger than the bulk of the cesium data, implying that out-of-pile experiments yield larger transport coefficients than in-pile experiments. Clearly questions remain about the validity of the comparison of the laboratory and in-pile data and the implications of the differences.

In one of the laboratory experiments on cesium migration (Ref. 4-16), an oxidizing atmosphere was found to be associated with increased transport of cesium. This is not unlike the effect of burnoff on strontium transport reported above.

Finally, note should be taken of the observations (and conditions) in which the migration of barium (Ref. 4-49) and strontium (Ref. 4-52) have been found to exhibit the complex behavior found for cesium.

In the evaluation of core release calculations (Ref. 4-3), the largest uncertainty for cesium release into the primary coolant circuit of the HTGR arises from the uncertainty in cesium transport in graphite. It is clear that to reduce this uncertainty, further understanding of the mechanisms of cesium transport is needed.

Fission Gas Release

The status of fission product gas data is covered in detail in a recent report (Ref. 4-8). This report contains (1) a review of experimental data on the behavior of fission product gases (including noble gases

and halogens) in HTGR fuel materials, (2) current reference data for use as input to computer code calculations of the fission gas inventory in the primary circuit of the HTGR under normal conditions, and (3) the basis for the selection of the reference data. A summary of the data in Ref. 4-8 is presented below.

Fuel Configuration. Studies of the fission gas release characteristics of various fuel configurations indicate the following:

	Kr-85m R/B at 1100°C
Intact coated fuel particles	Negligible*
Contamination	0.30
Bare fuel kernels (in fuel rod)	0.04
Unconstrained failed fuel particles	0.02
Constrained failed fuel particles	0.005

The constrained failed fuel particle is the particle configuration that appears to be representative of failed particles in fuel rods; thus, the Kr-85m R/B value of 5×10^{-3} is considered to be the reference value for failed fuel particles (unhydrolyzed) in fuel rods. (A constrained failed particle is a failed particle with a cracked coating in a fuel rod where the crack is constrained by the matrix material from opening up.) The reference value of 5×10^{-3} for failed particles may be higher if the constrained failed particle configuration is not representative of failed particles in fuel rods. Under temperature transients during HTGR operation, more severe types of failure, such as pressure vessel failure where the particle coating breaks into many pieces, are possible. Thus, the extent of such types of failure has to be established and corresponding fractional release (R/B) values determined if necessary.

Temperature Dependence of R/B. Examination of existing data on the temperature dependence of fission gas release shows that the activation

*Relative to the release from other sources.

energy for Kr-85m R/B is described by a combination of an activation energy of 0.8 kcal/mole, dominant at temperatures below 600°C and an activation energy of between 14 and 19 kcal/mole, dominant between 900° and 1500°C. The temperature dependence data are based mainly on nonreference-type fuel and fuel configurations.

A shortcoming of the temperature dependence data is the lack of data at temperatures above 1500°C. Data at high temperature (in the range 1500° to 1800°C) are needed to permit more accurate analysis of fission gas release in reactor systems during temperature transients where fuel temperatures in some portions of the core may rise as much as 500°C above normal.

Half-Life Dependence of R/B. Fission gas release (R/B) is found to depend on a power of the nuclide half-life; the exponent of the half-life term varies from about 0.2 below 650°C to 0.5 above 850°C. These values are based on observations in capsules, loops, and reactors.

Dependence of R/B on Neutron Flux and Fluence. Fission gas release appears to be independent of neutron flux level (fission rate density), but there is conflicting evidence in this area. Assuming no neutron flux level dependence is a conservative approach from the standpoint of predicting in-pile (capsule, loop, and reactor) fission gas release on the basis of laboratory (low flux level) test data.

Available information on the effect of neutron fluence on fission gas release (including the effect of fuel burnup on R/B) indicates that the effect is not important and can be neglected in reactor calculations, except for the possible increase in fission gas release due to coating degradation. This latter effect is accounted for by the use of particle failure models and R/B values for failed particles.

Hydrolysis. The hydrolysis of exposed fissile UC_2 particles will increase the fission gas release from the affected particles. The recommended value of R/B for hydrolyzed carbide kernels in failed particles is

around 0.15. This value is based on data for unirradiated fuel particles and is considered to be conservative. Results for irradiated particles indicate appreciably lower values; apparently fuel burnup induces a significant passivation. Additional data are needed.

Release of Halogens and Chalcogens. Results indicate that normal reactor operating temperatures are generally high enough that the release of iodine isotopes from fuel material is essentially identical to that of xenon isotopes. The release of tellurium isotopes is also found to be similar to that of xenon isotopes. Thus, iodine and tellurium isotopes should be treated as if they were xenon isotopes. Little information exists on the release of bromine and selenium isotopes. In reactor calculations, they are conservatively assumed to release like krypton isotopes.

TASK 400: TRITIUM TRANSPORT

A report, "A Review of Tritium Behavior in HTGR Systems," has been written and is in review.

TASK 500: PLATEOUT AND LIFTOFF

Work under this task is continuing; there are no current results to report.

TASK 600: COOLANT IMPURITY/CORE MATERIAL INTERACTION

Subtask 610: Reaction of Coolant Impurities With Fuel Materials

Reaction of CO with UC_2

Introduction and Summary. There is potential for reactions of exposed UC_2 fissile kernel material with impurities in the HTGR coolant. Since a major gaseous impurity is CO, the possibility of UC_2 oxidation exists via the reaction

$$UC_2 + 2CO = UO_2 + 4C \quad . \qquad (4\text{-}1)$$

Thermodynamic calculations for this reaction show that it may proceed at temperatures below about 1400°C when the partial pressure of CO is $\geq 4.7 \times 10^{-4}$ atm (i.e., 10 ppm at 47 atm, which corresponds to the present technical specification limit for total oxygen-containing impurities in the HTGR). Oxidation of UC_2 can bring about a possible decrease in kernel material density with a corresponding expansion of the affected fuel and potential increase in the fission gas release, R/B. However, slow oxidation of exposed fuel carbides by CO may be beneficial since hydrolysis of UC_2 would be precluded.

In order to predict the impact of CO oxidation of kernel material on core performance, it is necessary to know the rate of reaction of Eq. 4-1 at the expected low partial pressure of CO present in the reactor. In work reported previously (Ref. 4-2), experiments at 500 ppmv CO and 1150°C were described. The main conclusion drawn from those tests was that complete oxidation of UC_2 kernels could occur at the experimental conditions in about 200 hr. In recent work, attempts to verify the earlier results using the thermogravimetric technique described below have been unsuccessful in that present observed reaction rates are much lower than those reported in Ref. 4-2. It is conjectured that the apparent oxidation which occurred in the early work was due to the presence of other oxidizing impurities, including H_2O, CO_2, or O_2, which were either inadequately removed by the purification train or desorbed from the furnace tube walls or other components. In the new work described below, extensive precautions were taken to exclude the extraneous oxidants from the reaction zone; thus, the oxidation rates reported are due to the CO reaction (Eq. 4-1). Results of the new work indicate that the reaction rate is very low, leading to the conclusion that the reaction is relatively unimportant in the HTGR.

Method. A thermogravimetric method was used in which samples of UC_2 were suspended from a Cahn RG automatic recording microbalance and exposed to preselected partial pressures of CO at temperatures up to 1100°C. The

rate of reaction was calculated from the weight change of the specimen with time after subtracting the contribution of microbalance readout drift normally present at the conditions of the test. Chemical analysis of the reaction product was used to verify the integrated amount of reaction that had taken place at the end of each specimen oxidation.

Apparatus. Figure 4-6 is a schematic of the reaction apparatus used to conduct the oxidation studies. Since UC_2 readily reacts with O_2, CO_2, and H_2O, special precautions were necessary to remove these impurities from the reactant gas mixture. The gas mixture was purified by passing it through a charcoal trap maintained at -78°C to remove H_2O, through a hot copper bed maintained at 650°C to remove O_2, through an Ascarite* trap to remove CO_2, and finally through a $MgClO_4$-P_2O_5 trap to remove residual H_2O.

The concentration of CO in the He carrier gas was established by mixing pure CO and He streams by means of precise needle valves and calibrated flowmeters. The concentration of CO was calculated from the settings on the flowmeters, and then verified by mass spectrometric analysis of the gas mixture collected at the exit of the reaction furnace.

The change in the weight of the specimen was continuously monitored with the Cahn RG microbalance operated at an absolute sensitivity better than 2 μg. Sample temperatures were maintained to ±2°C with a Marshall single-zone, Kanthal A wound, tube furnace connected to a Barber-Coleman SCR and temperature controller. The temperature of the sample was measured with a calibrated chromel-alumel thermocouple located adjacent to the sample pan in the annulus between the interior of the tube furnace and the exterior of the quartz reaction tube. The temperature difference between the exterior and interior of the reaction tube was measured at the run temperatures and found to be less than 10°C at all temperatures.

The samples of UC_2 were contained in open platinum pans to allow maximum contact with the flowing gases. The pans were hung from the balance by means of a 0.010-in. platinum hangdown wire.

*Ascarite is NaOH in asbestos.

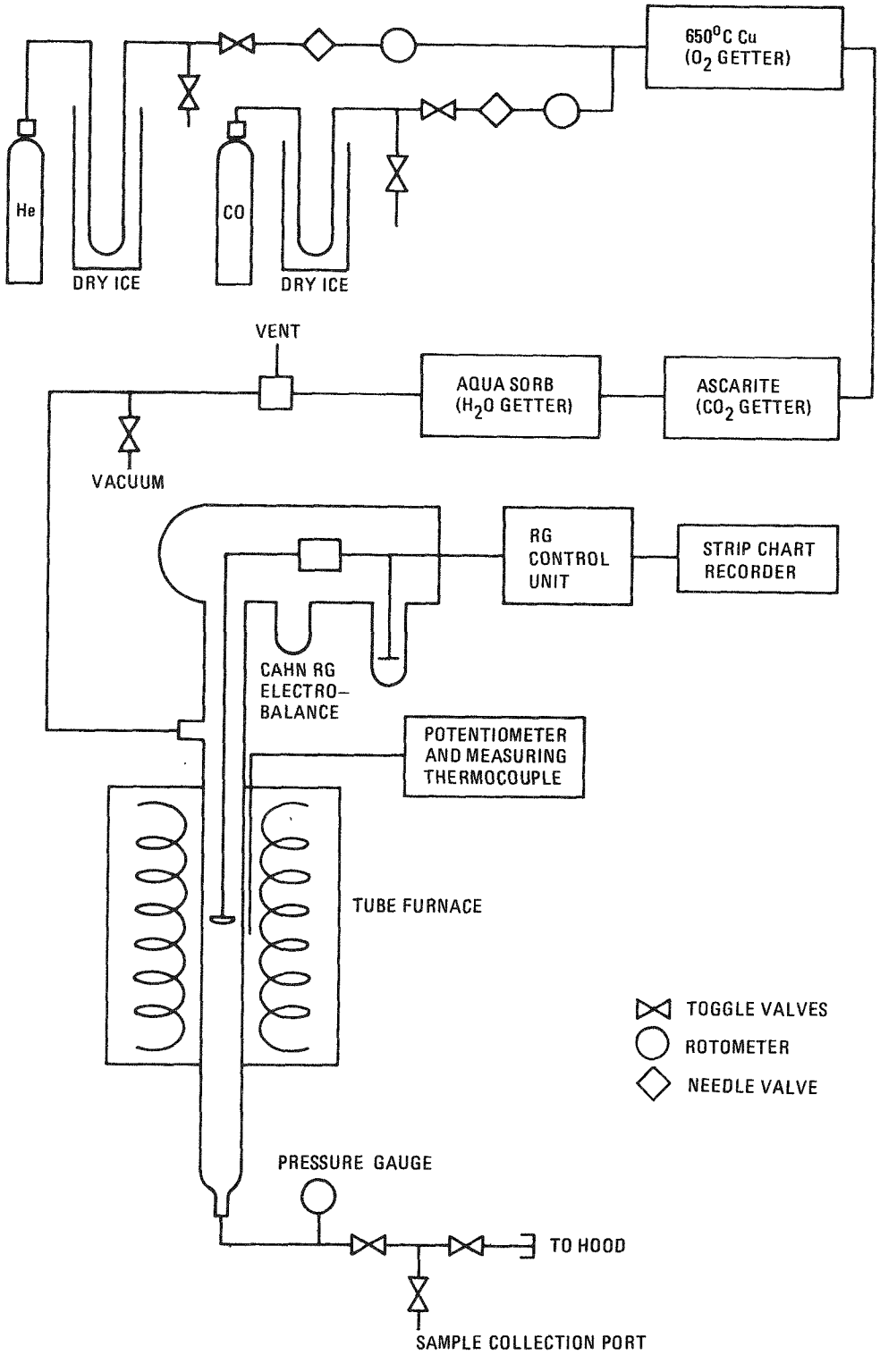

Fig. 4-6. Oxidation apparatus

Materials. The UC_2 was reference HTGR fissile kernel material and consisted of fully enriched (93%) thorium doped* kernels. The composition of the kernels is given in Table 4-4. The carbon monoxide was ultra high purity grade, guaranteed to be >99.8% pure. Reactor grade He (99.998% pure) was used for all experiments.

Procedure. Samples of UC_2 were weighed into small graphite crucibles and fired at 2100°C for 6 hr in vacuum (approximately 40-μm pressure). This treatment converted any preoxidized uranium back to the carbide. One of the pretreated samples was then ground to a powder with a mortar and pestle. The reaction tube was positioned within the furnace and the system was evacuated. The system was subsequently backfilled with the He/CO mixture and reevacuated three times. After the final backfill, the exit gas was vented to the hood and the flow rate was adjusted to 200 cm^3/min.

During this initial flushing procedure the furnace was heated to the temperature of interest but maintained in a lowered position. After the sample atmosphere was stablized, the furnace was raised until the sample was positioned within the uniform heat zone of the furnace. After allowing 5 min for temperature equilibration and microbalance trace stablization, the run time was initiated.

In order to change the run temperature, the furnace was lowered and the new temperature set. To initiate the next run the furnace was simply repositioned around the sample.

Gas samples were periodically obtained from the exit end of the flow system. The percent CO in the sample was determined by means of a Consolidated Electrodynamics mass spectrometer gas analyzer.

Results. Figure 4-7 shows a typical curve of the change in weight of the sample, Δw, as a function of the exposure time, t. The curves show a

*The small amount of Th is added to the kernel to aid in the spheroidization process.

TABLE 4-4
CHEMICAL COMPOSITION OF UC_2 MATERIAL

U	89.35 wt %
C	9.25 wt %
Th	1.53 wt %
O	155 ppm-wt
P	73 ppm-wt
Fe	98 ppm-wt
Ni	29 ppm-wt
Cr	<25 ppm-wt
Mn	<25 ppm-wt
Al	<50 ppm-wt

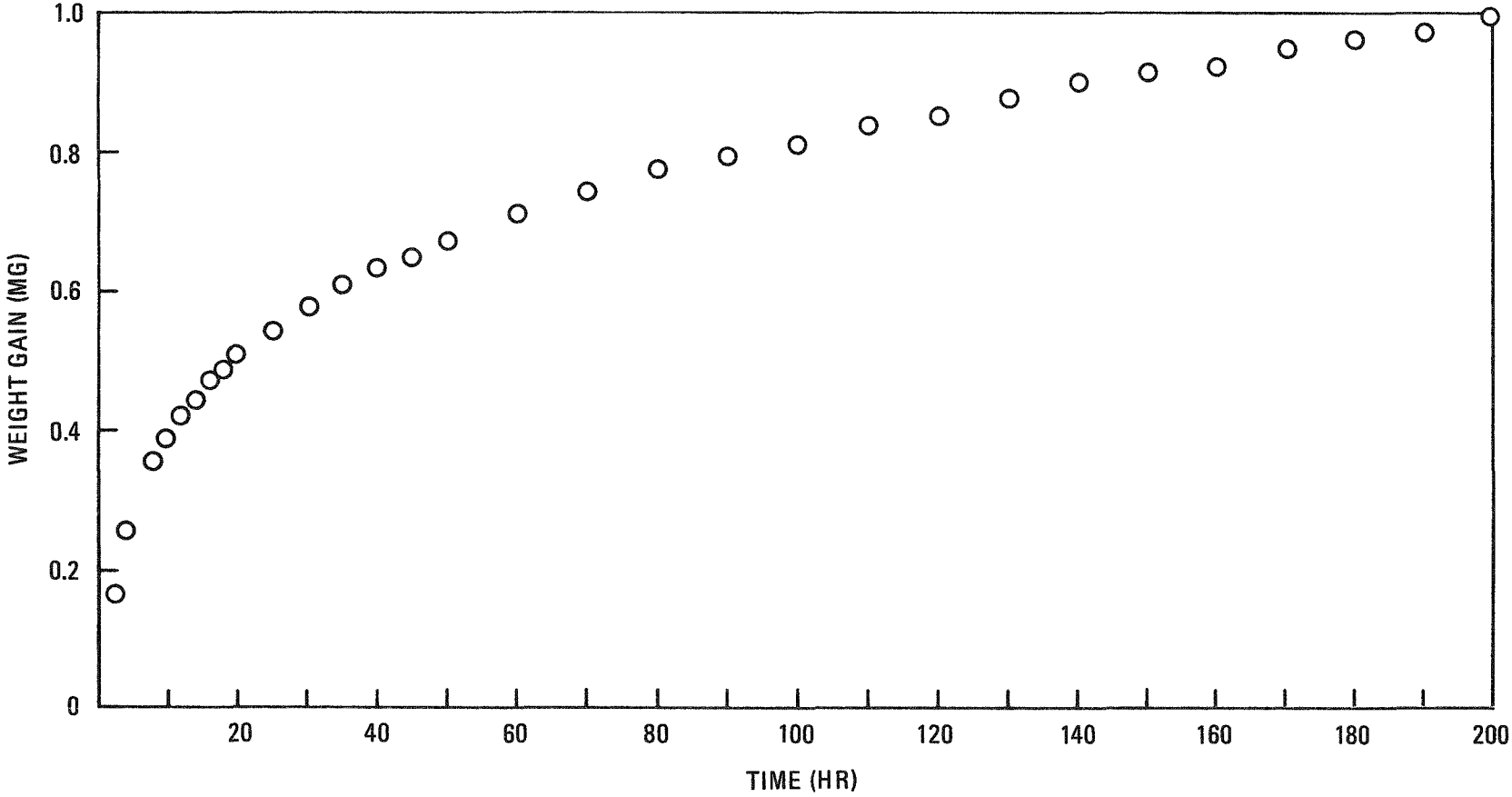

Fig. 4-7. Typical weight gain versus time curve for UC_2; 25.4% CO, 960°C, initial sample weight = 106.4 mg

characteristic rapid increase in weight followed by a region in which $d(\Delta w)/dt$ decreases with time. The initial portions of the curves are followed by an approximately linear portion, with $d(\Delta w)/dt$ being relatively constant. This linear portion of the curve was used to define the rate parameter R, which is expressed as

$$R(\%/hr) = \frac{d\Delta w}{dt} \frac{100}{0.216w} \quad ,$$

where w is the initial weight of the sample and 0.216 is the fractional weight change assuming that the reaction stoichiometry agrees with Eq. 4-1. Since the linear portion of the reaction occurs after an apparent 0.9% weight gain, only $\leq$4% of the carbide has reacted prior to obtaining the kinetic data.

To date, the reaction has been studied at temperatures ranging from 900°C, a typical HTGR operating temperature, to 1100°C using 25.4 ± 0.9% carbon monoxide. The observed rates of reaction, together with the calculated rate parameter R, are shown in Table 4-5. The rates of reaction were corrected for a steady microbalance drift of 0.0004 ±0.0001 mg/hr. This drift rate was determined by measuring the rate of weight gain of an inert UO_2 sample at the run temperatures. As is evident from Table 4-5 the rate of reaction at temperatures below 1000°C is experimentally limited by the balance drift. Even at 1049°C, the drift accounted for 35% of the rate. Thus, the low temperature rates are very inaccurate.

In Fig. 4-8 the rate parameter measured at a constant CO concentration of 25.4% (1 atm total pressure) is plotted as a function of temperature in an Arrhenius diagram. The scatter in the data is apparently caused by inaccuracies inherent in measuring very small weight changes. A least-squares treatment of the data yields an activation energy of 41 kcal/mole with a standard deviation at the 95% confidence level of 20 kcal/mole.

In one experiment, the final reaction product was analyzed and found to consist of 88.05% U, 0.66% O and 9.35% C. Making the assumption that

TABLE 4-5
RATE PARAMETERS VERSUS TEMPERATURE FOR THE CO + UC_2 REACTION

Temperature (°C)	Net Weight Gain[a] (10^3 mg/hr)	R[b] (10^3 %/hr)
899	0.24	1.0
927	0.22	0.96
960	0.54	2.3
1007	0.70	3.0
1036	1.9	8.3
1049	0.7	3.0
1066	1.40	6.1
1081	2.6	11.1
1090	1.1	4.8
1100	5.2	22.6

(a) Corrected for microbalance drift of 0.4×10^{-3} mg/hr.

(b) Based on a total weight gain of 21.6% of the initial weight.

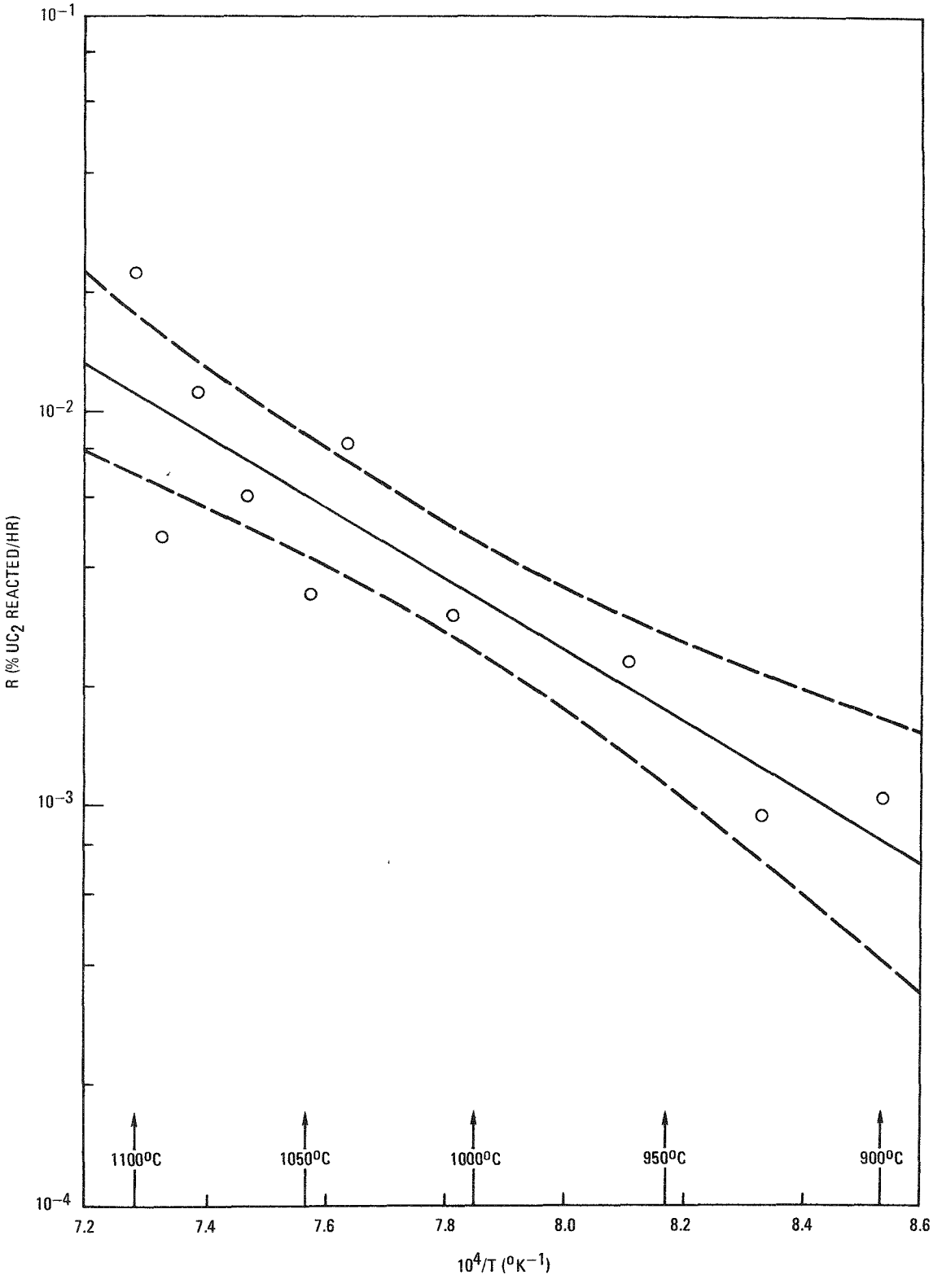

Fig. 4-8. Temperature dependence of rate parameters for the reaction of UC_2 with CO (P_{CO} = 0.25 atm)

all the oxygen resides as UO_2, this chemical composition is comprised of 91.7 wt % UC_2 and 5.5 wt % UO_2. The weight gain for this experiment was 1.83% of the initial weight. This corresponds to 8.5% reaction, in excellent agreement with the extent of reaction determined by chemical analyses (8.3%). The fact that the sample gained slightly more weight than the calculated amount can be explained by a small amount of carbon deposition occurring on the platinum pan (deposition was observed on the quartz furnace liner). The analysis of the reaction product did show a slight increase in carbon content of about 0.2 wt %.

Discussion. The above results indicate that the reaction rates of crushed UC_2 in 0.25 atm CO at temperatures up to 1100°C are almost immeasureably low, the measured reaction rate being substantially affected by the drift of the sensitive microbalance (approximately 0.4 μg/hr). Furthermore, the use of crushed UC_2 rather than bare kernel material is believed to yield conservatively high reaction rates. Because the reaction rates at relatively high CO pressure were so low, measurements at lower CO concentration have not yet been successful, and no precise extrapolation to the low CO partial pressure expected in the reactor is possible. If it is assumed, however, that the reaction rate is inversely proportional to CO pressure, the rate of reaction at postulated reactor conditions of approximately 500 μatm CO and at 1100°C would be only about 5×10^{-5} %/hr.

This extrapolation, if valid, would mean that only about 1% of the exposed UC_2 would be oxidized during a 4-year fuel lifetime. A low reaction rate at low CO concentration is consistent with the observation of virtually no fuel oxidation in Peach Bottom HTGR Core 1 fuel, even though the CO partial pressure was consistently between about 10 and 20 μatm during the lifetime (12,000 hr) of Core 1 operation and virtually all fuel particle coatings had failed early in life.

Although it may be reasonably concluded that this reaction is relatively unimportant in the HTGR, some additional tests are planned to verify this conclusion. These tests will be performed at higher temperatures, up

to approximately 1300°C where the reaction rates are more easily monitored, so that the pressure dependence of the rate parameter can be determined.

TASK 700: PLANNING AND COORDINATION

Current activity in this task is involved with evaluating the fission product chemistry program in view of the fission product data status and needs (see Task 300).

TASK 900: INTEGRAL TESTS

Current activity in this task is involved with preparation for the surveillance of fission products and coolant impurities in the primary circuit of the Fort St. Vrain HTGR during startup.

REFERENCES

4-1. Myers, B. F., and W. E. Bell, "Strontium Transport Data for HTGR Systems," USAEC Report GA-A13168, General Atomic, December 6, 1974.

4-2. "HTGR Base Program Quarterly Progress Report for the Period Ending February 28, 1974," USAEC Report GA-A12916, General Atomic, March 29, 1974.

4-3. Alberstein, D., ed., "HTGR Accident Initiation and Progression Analysis Status Report, Volume V, AIPA Fission Product Source Terms," ERDA Report GA-A13617, General Atomic, to be published.

4-4. "HTGR Base Program Quarterly Progress Report for the Period Ending August 31, 1970," USAEC Report GA-10288, Gulf General Atomic, September 30, 1970.

4-5. "HTGR Base Program Quarterly Progress Report for the Period Ending May 30, 1969," USAEC Report GA-9372, Gulf General Atomic, June 27, 1969.

4-6. "HTGR Base Program Quarterly Progress Report for the Period Ending February 28, 1967," USAEC Report GA-7801, General Atomic, Division of General Dynamics, April 20, 1967.

4-7. Doering, D. A., "FUNFIT, N-Space Function Fitting," Gulf General Atomic unpublished data, May 1, 1968.

4-8. Myers, B. F., et al., "The Behavior of Fission Product Gases in HTGR Fuel Material," ERDA Report GA-A13723, General Atomic, to be published.

4-9. Salzano, F. L., "The Behavior of Iodine in Graphite," Carbon 2, 73 (1964).

4-10. Salzano, F. J., "Summary of Fission Product Adsorption Work at BNL," paper presented at the Seventh AEC Air Cleaning Conference, October 10-12, 1961, Brookhaven National Laboratory (TID-7627).

4-11. "Public Service Company of Colorado 330-MW(e) High-Temperature Gas-Cooled Reactor Research and Development Program, Quarterly Progress Report for the Period Ending September 30, 1967," USAEC Report GA-8270, General Atomic, Division of General Dynamics, October 30, 1967.

4-12. Milstead, C. E., W. E. Bell, and J. H. Norman, "Deposition of Iodine on Low Chromium-Alloy Steel," Nucl. Appl. Tech. 7, 361 (1969).

4-13. "GCR Annual Report" (draft), Oak Ridge National Laboratory, to be published.

4-14. Gray, D. L., and F. H. Neill, "Design of a Loop for Fission Product Deposition Tests up to 1500°F," USAEC Report ORNL-TM-2532, Oak Ridge National Laboratory, June 1969.

4-15. Neill, F. H., "Adsorption and Desorption of Iodine on Mild Steel," USAEC Report ORNL-TM-2763, Oak Ridge National Laboratory, April 1970.

4-16. "HTGR Fuels and Core Development Program Quarterly Progress Report for the Period Ending May 31, 1975," ERDA Report GA-A13444, General Atomic, June 30, 1975.

4-17. "HTGR Base Program Quarterly Progress Report for the Period Ending May 31, 1974," USAEC Report GA-A13030, General Atomic, June 28, 1974.

4-18. Brown, P. E., and R. L. Faircloth, "Metal Fission Product Behavior in HTR UO_2-Coated Particle Fuel," Am. Ceram. Soc. Bull. 54, 440 (1975).

4-19. Morgan, M. T., H. J. deNorwall, and R. L. Towns, "Release of Fission Products from Pyrocarbon-Coated HTGR Fuel Particles During Post-Irradiation Anneals," USAEC Report ORNL-TM-4539, Oak Ridge National Laboratory, December 1974.

4-20. Smith, C. L., General Atomic, private communication.

4-21. Adams, C. C., et al., "Fission Product Release Measurements on TRISO Fuel Particles Irradiated in Capsule P-13F," USAEC Report GA-9383, Gulf General Atomic, October 22, 1969.

4-22. Nabielek, H., et al., "Performance Limits of Coated Particle Fuel, Part III, Fission Product Migration in HTR Fuel," Dragon Project unpublished data, June 1974.

4-23. Biedstein, H., P. Müllner, and P. Angelberger, "Postirradiation Examination of Coated Fuel Particles; Determination of Cs-137 Release," Dragon Project unpublished data, July 1970.

4-24. Betz, G., et al., "Determination of the Distribution of Metallic Fission Products in Fuel Particle Coatings by the Ion Sputtering Technique," Dragon Project unpublished data, July 1970.

4-25. Chenaglia, B., et al., "The Diffusion of Strontium and Cesium in Pyrolytic Silicon Carbide," Dragon Project unpublished data, July 1972.

4-26. Verce, E. H., H. Walther, and J. York, "The Behavior of Silicon Carbide Coatings in the HTR," paper presented at the International Conference on Nuclear Fuel Performance, British Nuclear Energy Society, London, October 15-19, 1973, paper No. 20.

4-27. "HTGR Base Program Quarterly Progress Report for the Period Ending February 29, 1968," USAEC Report GA-8530, Gulf General Atomic, March 29, 1968.

4-28. Hooper, E. W., "The Diffusion of Cesium in the Outer Pyrolytic Carbon Layer of Unirradiated Coated Fuel Particles," Atomic Energy Research Establishment unpublished data, February 1975.

4-29. Faircloth, R. L., F. C. W. Pummery, and B. A. Rolls, "Diffusion of Barium, Strontium, and Cesium in Various Grades of Reactor Graphite," in Proceedings of the Symposium: Thermodynamics with Emphasis on Nuclear Materials and Atomic Transport in Solids, Vol. II, International Atomic Energy Agency, Vienna, 1966, pp. 133-152.

4-30. "HTGR Base Program Quarterly Progress Report for the Period Ending May 31, 1967," USAEC Report GA-7981, General Atomic, Division of General Dynamics, September 29, 1967.

4-31. "HTGR Base Program Quarterly Progress Report for the Period Ending May 31, 1968," USAEC Report GA-8662, Gulf General Atomic, June 28, 1968.

4-32. "HTGR Fuels and Core Development Program Quarterly Progress Report for the Period Ending August 31, 1975," ERDA Report GA-A13592, General Atomic, September 30, 1975.

4-33. Staley, H. G., General Atomic unpublished data.

4-34. "Public Service Company of Colorado 330-MW(e) High-Temperature Gas-Cooled Reactor Research and Development Program, Quarterly Progress Report for the Period Ending September 30, 1965," USAEC Report GA-6830, General Atomic, Division of General Dynamics, December 31, 1965.

4-35. "Public Service Company of Colorado 330-MW(e) High-Temperature Gas-Cooled Reactor Research and Development Program, Quarterly Progress Report for the Period Ending March 31, 1966," USAEC Report GA-7086, General Atomic, Division of General Dynamics, May 11, 1966.

4-36. Wallroth, C. F., et al., "Postirradiation Examination of Peach Bottom Fuel Test Element FTE-3," USAEC Report GA-A13004, General Atomic, August 15, 1974.

4-37. Milstead, C. E., "Effects of Irradiation on the Cesium Sorption Characteristics of Graphite," Gulf General Atomic Report GA-8589, April 19, 1968.

4-38. Jensen, D. D., et al., "Planning Guide for Validation of Fission Product Transport Codes," ERDA Report GA-A13386, General Atomic, April 15, 1975.

4-39. Rowland, P. R., "Mechanics of Fission Product Migration in Nuclear Graphite," paper presented at the Fourth London International Carbon and Graphite Conference, September 23-27, 1974, Imperial College, London.

4-40. Bryant, E. A., et al., "Rates and Mechanisms of the Loss of Fission Products from Uranium-Graphite Fuel Material," Nucl. Sci. Eng. 15, 288 (1963).

4-41. Flowers, R. H., "The Relation of Fission Product Release Limitations to the Design and Operation of a Large HTR Station," Atomic Energy Research Establishment unpublished data, 1970.

4-42. deNordwall, H. J., and L. R. Zumwalt, General Atomic unpublished data, May 1968.

4-43. Vanslager, F. E., et al., "Fission Product Transport in HTGR System - A Summary," USAEC Report GA-10073, Gulf General Atomic, April 22, 1970.

4-44. Haire, M. J., and L. R. Zumwalt, "Cesium Diffusion Coefficients and Other Results for the Analysis of Peach Bottom D13-05 Fuel Element Activity Profiles," USAEC Report Gulf-GA-A12492, Gulf General Atomic, July 26, 1973.

4-45. Chandra, D., and J. H. Norman, "Investigations of Cesium Transport Through Graphite," Gulf General Atomic unpublished data, May 15, 1973.

4-46. Zumwalt, L. R., General Atomic unpublished data.

4-47. "Cooperative Research and Development Program CEA-GAI on HTGR-Fuel Section, Progress Report for the Period of July 1 to December 31, 1973," CEA Report DMECN-HTR 74-518, March 1, 1974.

4-48. McEnaney, B., and R. D. Mehew, "Sorption and Diffusion of Cesium in Some Nuclear Graphites," Dragon Project unpublished data, November 1974.

4-49. Skerker, A. L., and L. R. Zumwalt, "Fast and Slow Diffusion of Barium in Reactor Grade Graphite," Trans. Am. Nucl. Soc. 15, 760 (1972).

4-50. Alberstein, D., P. D. Smith, and M. J. Haire, "Metallic Fission Product Release From the HTGR Core," ERDA Report GA-A13258, General Atomic, May 15, 1975.

4-51. "HTGR Fuels and Core Development Program Quarterly Progress Report for the Period Ending November 30, 1974," ERDA Report GA-A13253, January 31, 1975.

4-52. Besenbruch, G. E., et al., "Diffusional Behavior of Strontium in Graphite," Trans. Am. Nucl. Soc. 12, 81 (1969).

6: HTGR ALTERNATE FUEL SYSTEM STUDIES
189A No. SU047

SUMMARY

The objectives of this task are:

1. To evaluate high conversion HTGRs with a standard fuel element.

2. To evaluate high conversion HTGRs with a modified fuel element design.

3. To evaluate plutonium-fueled HTGRs.

4. To evaluate fuel systems that minimize reprocessing and refabrication operations.

The milestones to be accomplished under this task in FY-76 are:

1.	Topical report, high conversion ratio potential	10/30/75
2.	Topical report, value of U-233 and U-236	10/30/75
3.	Topical report, plutonium in the HTGR	12/1/75
4.	Development plan, high conversion ratio standard element	3/1/76
5.	Development plan, fully optimized conversion ratio	3/1/76
6.	Development plan, Pu-fueled HTGR	3/1/76

7.	Development plan, alternate recycle fuel	3/1/76
8.	Topical report, high conversion ratio HTGR	6/30/76
9.	Topical report, alternate recycle fuel	6/30/76

The topical reports on high conversion ratio potential (Ref. 6-1) and on U-233 and U-236 neutronic values (Ref. 6-2) have been completed. The more important conclusions contained in these two topical reports are summarized here.

A preliminary survey study of many potential means for increasing the conversion ratio in the HTGR has begun. The results of this preliminary study will be used as the basis for discussions for the formulation of the fuel development Program Plans required later under Task 6. The final results of this evaluation will be included in the next quarterly report.

HIGH CONVERSION RATIO POTENTIAL

Summary

The fuel cycle design variables for HTGR reactors have in the past been selected primarily with the goal of minimizing the fuel cycle cost over a relatively short time period. Typically, the criterion for selection of the fuel cycle at the time a project is committed is to achieve the lowest possible fuel cycle cost averaged over a time period of 15 yr or more. On this basis, HTGR plants have been chosen to have very low fuel cycle costs but with some sacrifice in minimizing uranium ore requirements relative to what could be achieved under rules favoring resource optimization more strongly.

The conversion ratio* value typically chosen for commercial HTGRs has been about 0.66 in recent years. This value can be increased significantly

*Conversion ratio is defined as the ratio of fissile atoms produced to fissile atoms consumed in a reactor cycle.

to about 0.8 with the standard HTGR fuel element and could reach 0.9 with a modified fuel element design. The higher conversion ratio provides a significant reduction in uranium ore consumption; i.e. the ore required at a conversion ratio of 0.80 is about 59% of that required at 0.66.

There may be a misconception in the industry that the currently committed conversion ratio of 0.66 for the HTGR is limited by technical features. This is not the case at all, and changing economic conditions are expected to make cores with higher conversion ratios more attractive in the future. In contrast, light water reactors are limited in conversion ratio increases for changes other than more frequent refueling because of core materials and lattice spacing limitations, i.e., the U-238 loading is constrained.

A secondary benefit of higher conversion ratios is that the production of long-lived actinides decreases significantly, thereby reducing the quantities of high level wastes. This benefit will likely increase in importance because of the greater number of regulatory controls (and resultant costs) currently being imposed on waste storage systems.

Capability of HTGR for Resource Conservation

From the early days of the reactor development program in the U.S., the potential has been recognized for optimizing the utilization of uranium resources by means of high gain converter reactors. An early design study for the USAEC showed that conversion ratios well above 0.80 were feasible with the HTGR system (Ref. 6-3). The goal of high gain reactors has been sidetracked somewhat because of an intense pressure in the marketplace to achieve the lowest possible evaluated fuel cycle cost. The relatively low conversion ratio of light water reactors, which are most prevalent, has undoubtedly influenced the movement toward lower conversion ratios in thermal reactors in order to improve the economics of the fuel cycle.

The HTGR, with Th/U-233 in graphite elements, is especially efficient for utilization of uranium because of the absence of parasitic neutron

absorbers in the core structure and because of the favorable neutronics of the fissile U-233 generated (Refs. 6-4,6-5). The immediate design tradeoffs that yield higher conversion ratios are:

1. Higher fertile load.
2. More frequent refueling (semiannual).
3. Lower power density.
4. Shorter fuel lifetime.

These tradeoffs, except semiannual refueling, all push the economics of the fuel cycle toward lower fuel depletion (burning) costs, higher fuel working capital costs, and higher fuel fabrication and processing costs. Semiannual refueling yields an increased conversion ratio without the penalty for inventory and fuel handling costs.

The conversion ratio improvements that are available with the current fuel element design are shown in Table 6-1, where the changes are shown in progressive steps. An increase in thorium load is the most directly available change. The HTGR concept has a special flexibility because the fertile material (thorium) and the fissile material (fully enriched uranium) are contained in separate coated fuel particles. The relative quantities can be varied in either initial cores or in reload segments without complicating the enrichment or fabrication steps. The primary limitation on thorium loading is the space available for coated fuel particles within fuel rods. Current improvements in coated particles show strong promise for thinner coatings, which would effectively remove the volume limitation. The increase in conversion ratio to 0.71 shown in Table 6-1 is for an increase of 25% in thorium loading and is consistent with the thinner coatings on fuel particles.

A reduction in power density provides a further increase in conversion ratio partially because of an increase in neutron thermalization resulting from the added moderator material, but primarily because there is more volume available with which to increase the total reactor thorium loading.

TABLE 6-1
CONVERSION RATIO IMPROVEMENTS

Case	Fissile Conversion Ratio	Relative Ore Requirement
Reference HTGR	0.66	1.0
Increase Th load	0.71	0.85
Add semiannual fueling	0.76	0.71
Add reduced power density (lower to 6 W/cm^3)	0.82	0.53
Add U-233 feed to reload fuel	0.87	Zero during period of consuming U-233 stockpile
Modify fuel element and/or Th blanket	∿0.92 to 0.95	

A lower density requires a larger reactor vessel; therefore, this change must be incorporated during the initial design phase of a reactor. The reactor vessel cost increases as a result of the lower power density. However, for modest (10 to 15%) power density reductions, the total cost of generating power does not appear to increase appreciably because the core pressure drop decreases, and hence the plant efficiency increases.

Finally, Table 6-1 indicates the savings in uranium ore for increased conversion ratio. The amount of uranium required for feed is approximately proportional to one minus the conversion ratio; therefore, there is strong leverage from even small changes in conversion.

Longer term design improvements would require the development of a new fuel block capable of containing about twice the thorium loading now possible. The relationship between conversion ratio and thorium loading is shown in Fig. 6-1 for 3-, 4-, and 6-yr fuel lifetimes, and for both annual and semiannual fueling for the 4-yr case. This figure shows that modified designs can achieve a conversion ratio of 0.9 with annual refueling, U-235 feed, and no change in power density.

From the results shown in Fig. 6-1 and other study results, it has been concluded that:

1. Increasing the total core thorium loading is the most effective means of increasing the HTGR conversion ratio.

2. The three most effective means of increasing the total core thorium loading are:

    a. Increasing the reactor core volume, i.e., reducing the power density.

    b. Utilizing advanced fertile particle designs that allow higher thorium loadings per unit volume of fuel rod.

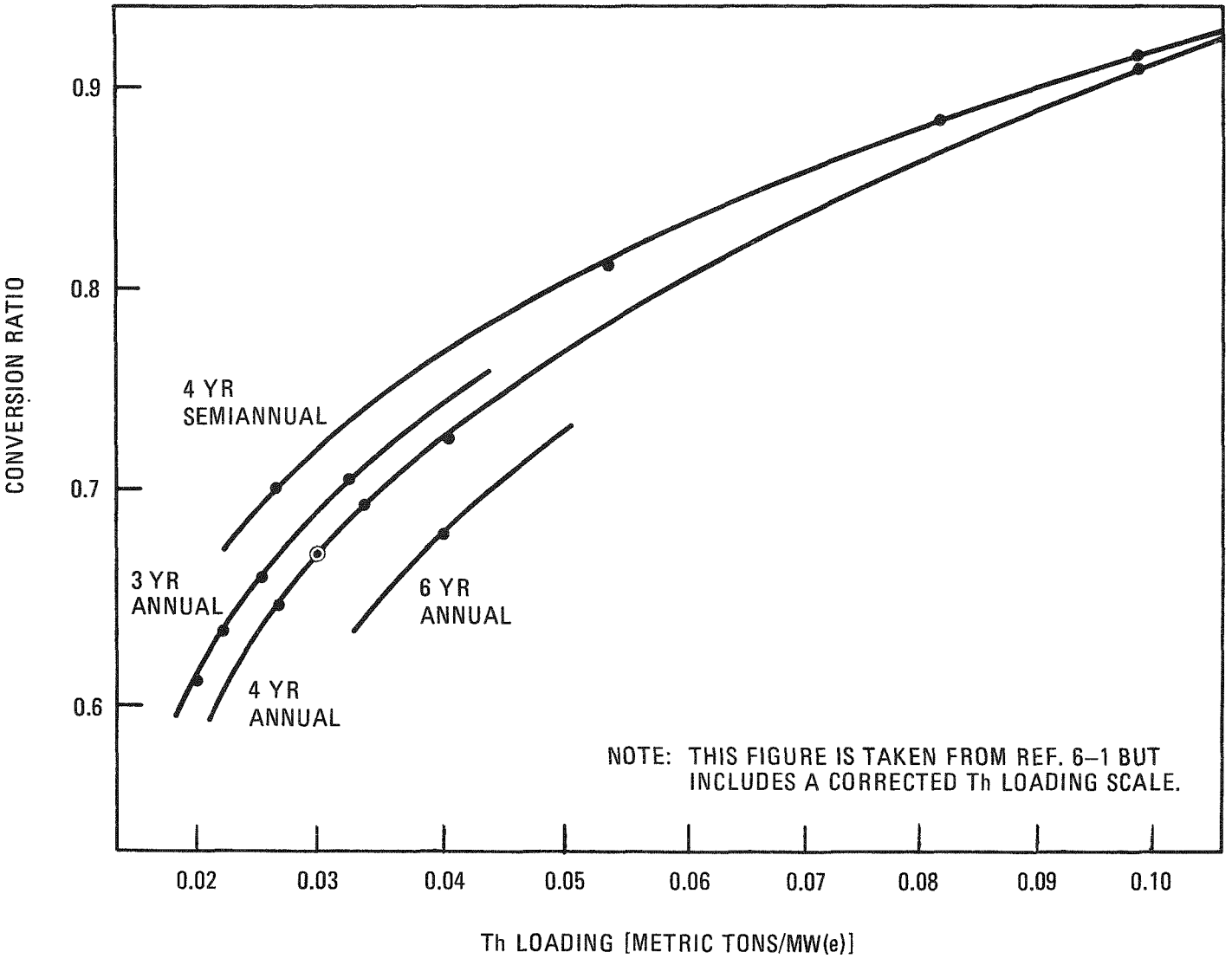

Fig. 6-1. Conversion ratio versus total thorium loading for various designs

c. Increasing the available fuel rod volume per fuel block by modifying the fuel block and/or the fuel rod design.

3. Increasing the refueling frequency and/or reducing the in-core residence time are effective in increasing the conversion ratio for relatively low thorium loading designs. For heavy thorium loadings with a conversion ratio >0.85, refueling frequency does not have a strong effect on the conversion ratio.

4. Under the constraints of the present fuel particle and block design, an appreciable increase in the conversion ratio (to 0.82) can be achieved by reducing the power density to 6 W/cm^3 and refueling semiannually.

Benefits in Resource Utilization

The increased fissile inventory for the higher conversion ratio will result in an increase in uranium resource requirements for the initial core, but the reduced annual consumption results in a significant savings over the 40-yr life of a plant.

The U_3O_8 feed material required for the HTGR and the LWR are shown in Table 6-2, based on a capacity factor of 0.8 and a tail enrichment of 0.3%. Recycle operation was assumed for the PWR as well as for the HTGR. For the HTGR, the 40-yr demand is decreased by about 43% for a conversion ratio of 0.82 and by 54% for a conversion ratio of 0.90. The percentage of reduction is even greater relative to a light water reactor (PWR).

Economic Tradeoffs

The conversion ratio influences the fuel cycle component of energy cost directly by affecting the depletion, processing, and working capital contributions of fuel costs. Indirectly, the conversion ratio also affects the reactor plant components of energy costs by causing a change in the

TABLE 6-2
U_3O_8 FEED REQUIREMENT
[tons/MW(e)]

	HTGR at 0.66 C.R.[a]	HTGR at 0.82 C.R.	HTGR at 0.90 C.R.	PWR at 0.60 C.R.
Initial core	0.44	0.64	0.94	0.50
Annual reload	0.105	0.058	0.035	0.16
40-yr total	4.53	2.90	2.30	6.66

[a] C.R. = conversion ratio.

plant efficiency. A high conversion ratio yields lower age peaking factors, and this effect results in reduced core pressure drop.

The tradeoffs that can be made between the C/Th ratio and power density in order to change the conversion ratio and total power cost are shown in Fig. 6-2. For example, a change in C/Th ratio from 240 to 180 would result in a slight reduction in power generation cost and an increase in the conversion ratio to about 0.72. The cost effect of a lower pressure drop is a more significant contribution than that from the increased inventory cost with a heavier thorium loading.

Figure 6-2 also shows the benefits of more frequent refueling in increasing the conversion ratio and lowering power cost. In this case, the fuel elements would have the same design life of 4 yr, but half the annual change in elements would be performed each 6 months.

Reduction in Radioactive Wastes

An additional benefit of higher conversion ratios in the HTGR which has been recognized recently is that the production of actinide wastes, such as neptunium and plutonium, is greatly reduced (Ref. 6-6). This effect is shown in Fig. 6-3 for recycle of all bred uranium. Further, the actinide production from U-233 fissions is significantly lower than from U-235. The actinide buildup with U-233 feed, as could be produced from a thorium-blanketed fast breeder reactor (FBR), would be significantly reduced. In an expanding HTGR reactor economy, including U-233 fueled cores, the average fuel exposure would be from 4 to 6 yr of irradiation, and the overall actnide production rate would be reduced by about a factor of 20 from the current HTGR reference value.

NEUTRONIC VALUES OF U-233 AND U-236 IN THE HTGR

Summary

An accurate determination of the neutronic values of bred U-233 and U-236 is a necessity for the proper evaluation of HTGR fuel values and

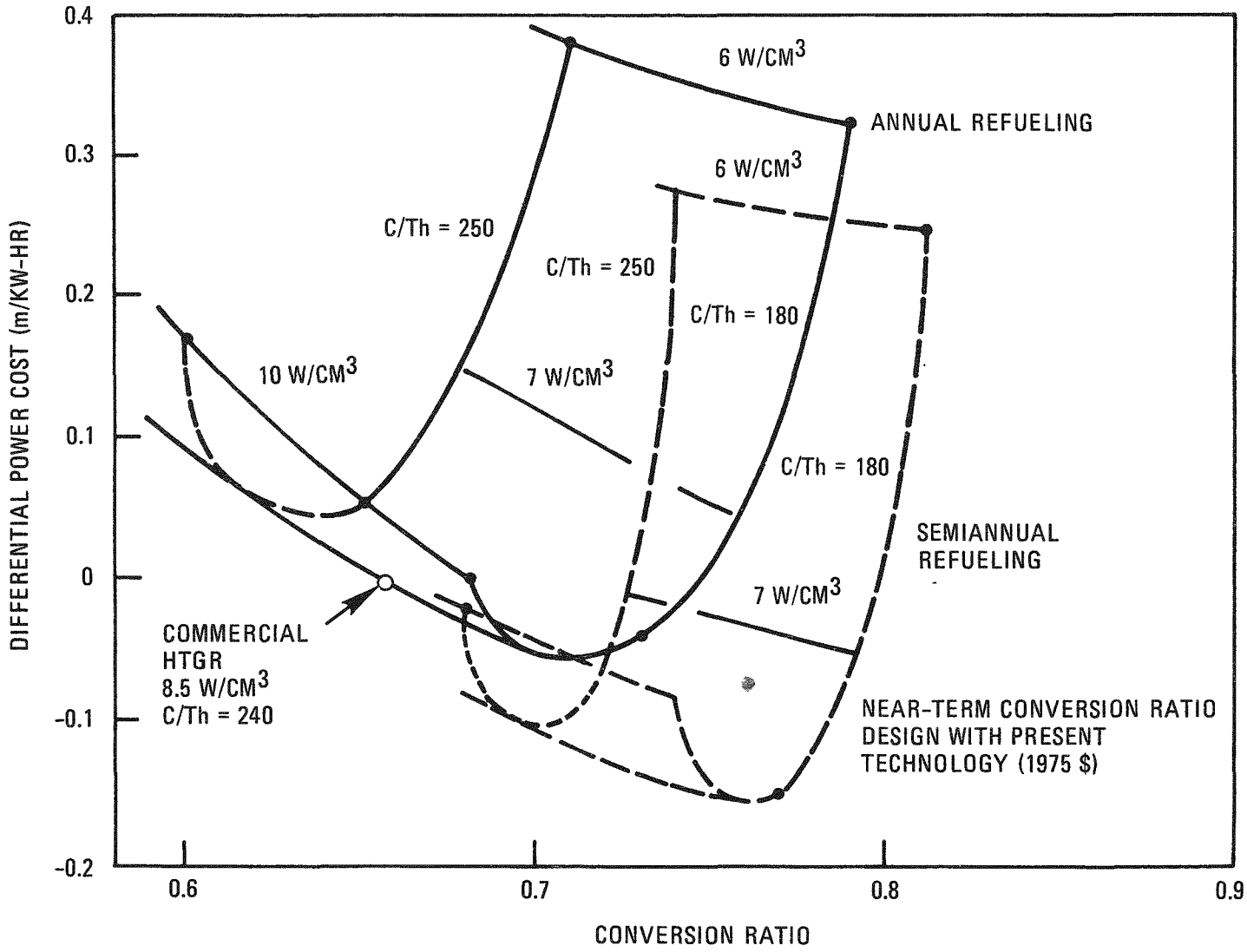

Fig. 6-2. Effects of conversion ratio on power cost

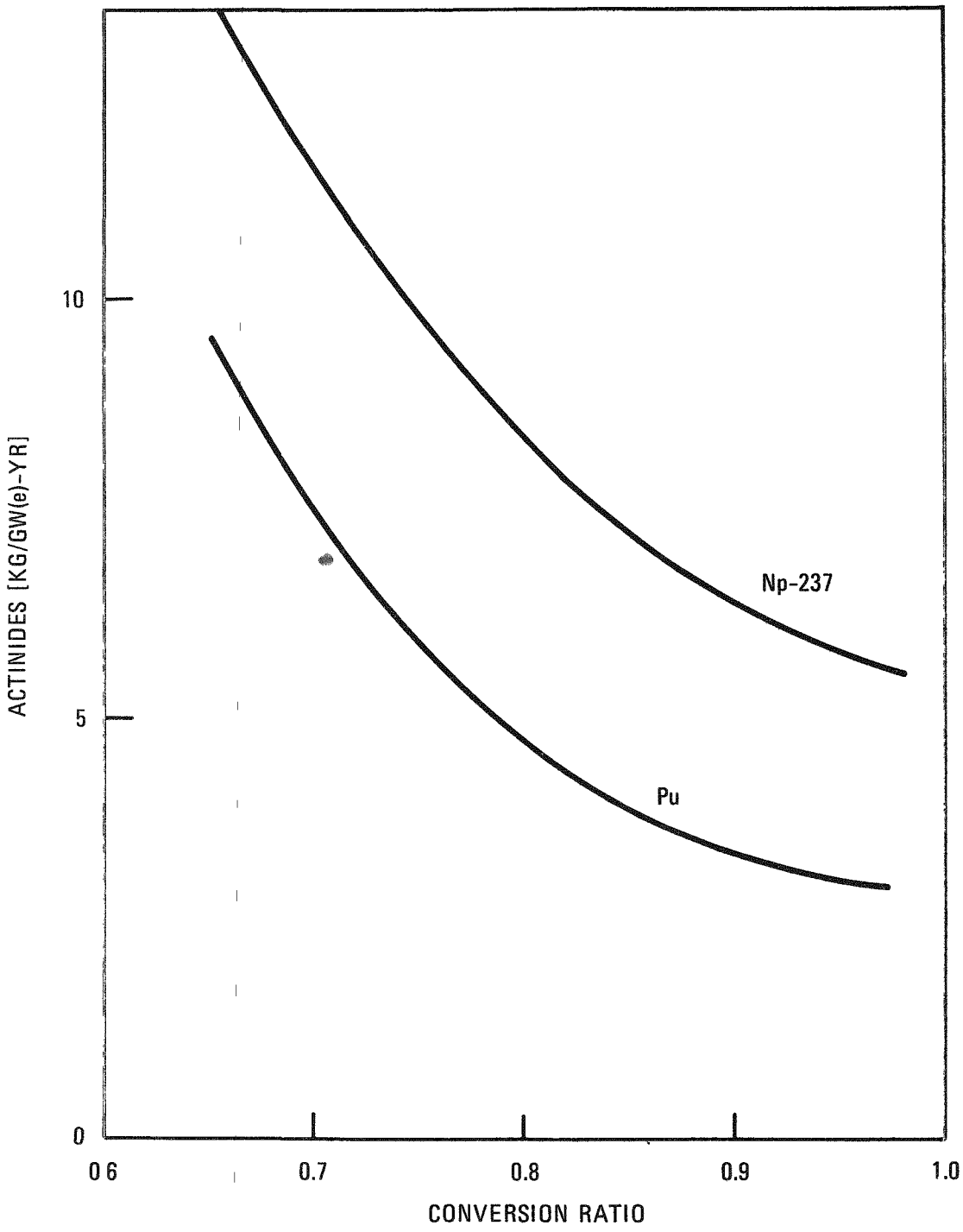

Fig. 6-3. Actinide production versus conversion ratio (24^{th} yr)

related fuel costs. The results of an extensive evaluation of the U-233 worth in the HTGR was published in 1972 (Ref. 6-7). Other reports (Refs. 6-8,6-9) have briefly summarized the results of U-236 value calculations performed at General Atomic. The results of more recent calculations of the value of these isotopes with particular emphasis on the U-236 value calculation are reported in Ref. 6-2 and are summarized here. A more detailed description of the cross-section determination of U-236 in the reference HTGR fuel management strategy is included in Ref. 6-2 and is not reported here. An understanding of the details of the cross-section determination is required to arrive at the proper value of the U-236 parity in the HTGR.

The results of this evaluation are in close agreement with previously reported values. The neutronic parity values, i.e., the value relative to the value of U-235 in fully enriched uranium, are:

1.	U-233	1.43
2.	U-236 in bred U	-0.58 to -0.65
3.	U-236 in discharged feed uranium	
	First discharge segment	-0.25
	Equilibrium discharge	-0.20

U-236 Buildup During Core Operation

U-236 In-Core Inventory

The U-236 fuel cycle cost penalty is proportional to the product of the in-core U-236 inventory and the effective cross section of U-236. The latter is a function of the loading per block and the recycle particle characteristics. The U-236 inventory depends on the particular mode of operation being followed, i.e., nonrecycle, selective recycle, full recycle, etc. The several possible strategies are described below and illustrated in Fig. 6-4.

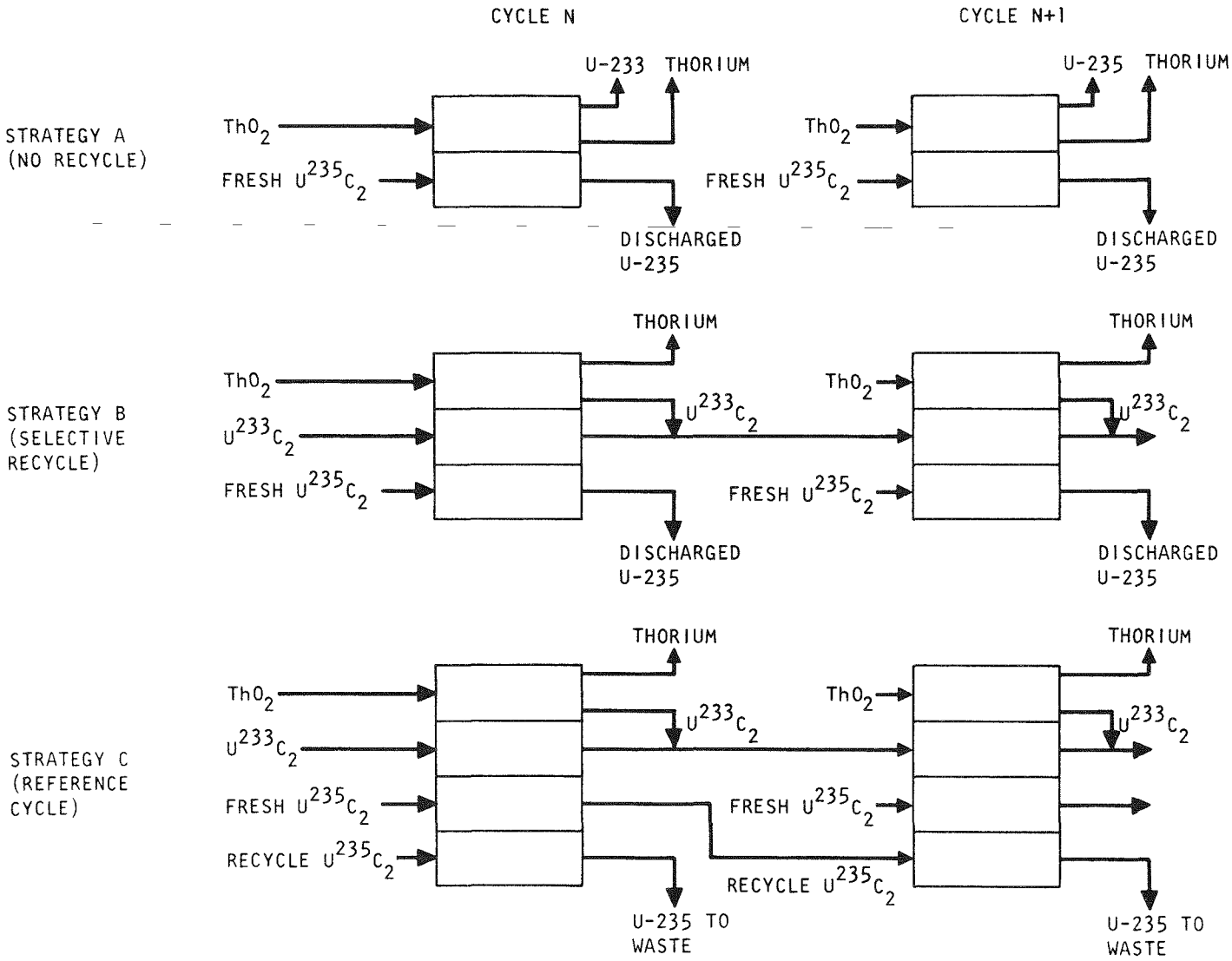

Fig. 6-4. Alternate fuel cycle strategies

Strategy A. No recycle of either the U-233 or U-235 is assumed in strategy A. However, it is assumed that the bred fuel can be separated from the residual feed (U-235) uranium in the reprocessing plant. The U-233 is assumed to have a value about 40% greater than that of U-235 in 90% enriched uranium, reduced as appropriate by the added cost of fabricating U-233 fuel elements over fresh fuel (U-235) elements. The discharged feed (U-235) value is reduced as appropriate by the negative value of the contained U-236. In about 5 yr a steady-state condition is achieved with respect to the U-236 inventory of about 350 kg in an 1160-MW(e) reactor, or 0.30 kg/MW(e), as shown in Fig. 6-5.

Strategy B. In this strategy, recycle of the bred uranium is assumed but the residual feed uranium is recovered and sold as in strategy A. The reduced U-236 inventory reflects the fact that less feed uranium (U-235) is required with bred U recycle than in the nonrecycle mode of operation, and hence less U-236 will be formed. The average inventory is about 270 kg U-236 in an 1160-MW(e) HTGR, or about 0.23 kg/MW(e).

Strategy C. This is the current reference strategy for the U.S. HTGR program. The bred uranium is recovered and continuously recycled as in stragety B. The recovered feed uranium is recycled once more through the reactor, after which it is recovered in the reprocessing plant and buried. It is assumed to have zero value. The average U-236 in-core inventory is about 500 kg for an 1160-MW(e) HTGR, or about 0.43 kg/MW(e).

Strategy D. In this strategy, all of the discharged uranium is continuously recycled. Hence the U-236 steadily builds up, as shown in Fig. 6-5. Strategy D can result whenever a mixed thorium-uranium oxide or carbide is used as the basic fuel, or when the discharged separate fissile and fertile particles are mixed in the reprocessing plant. The discharged feed uranium has a U-235 enrichment of about 30%. The U-236 enrichment is about 50%. After one more 4-yr cycle through the core (i.e., strategy C), its fissile enrichment is only about 4% and its value is negligible.

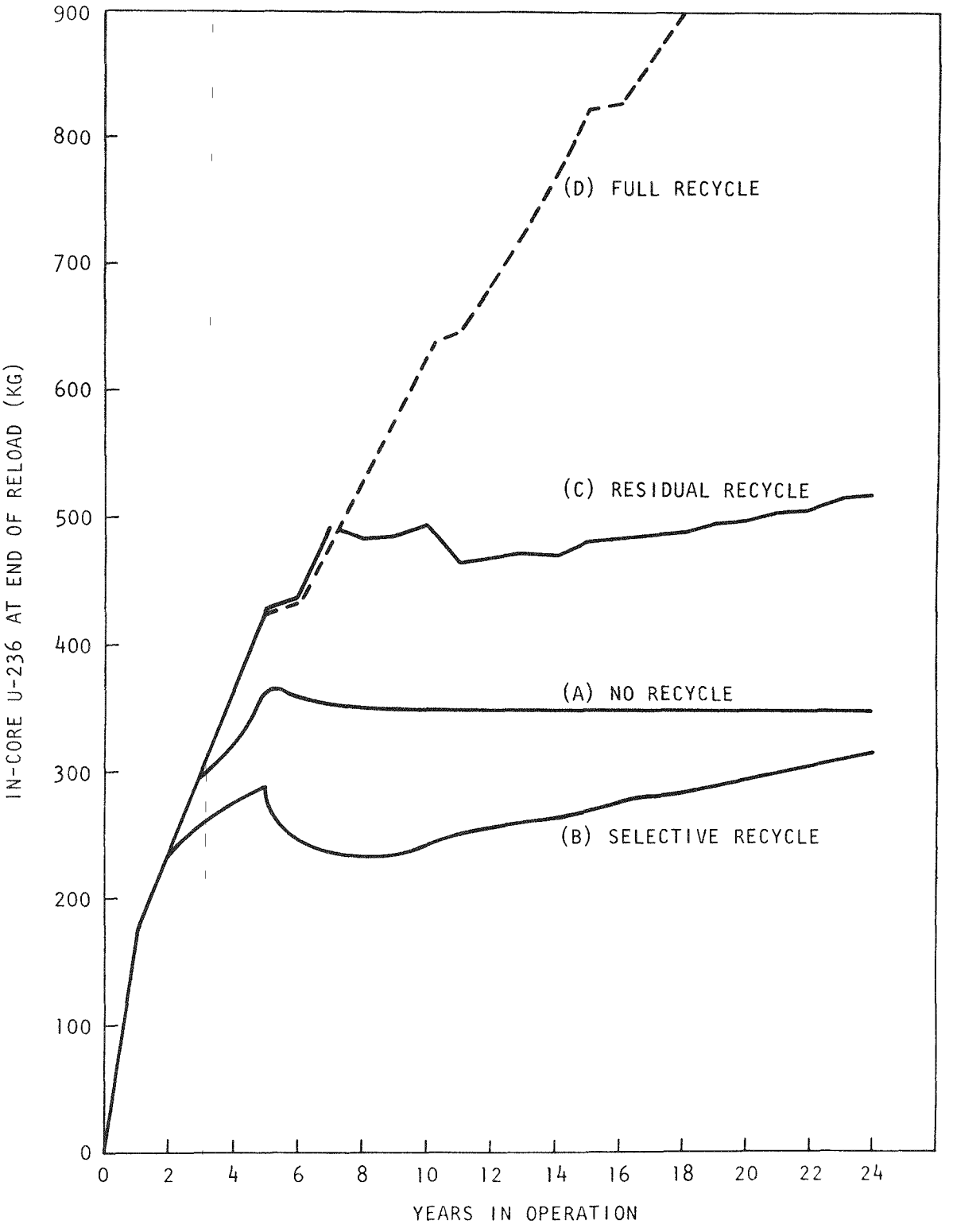

Fig. 6-5. In-core U-236 inventory [1160-MW(e) HTGR]

U-236 Cross Sections

As mentioned earlier, the poisoning effect of U-236 is proportional to its effective cross section. The majority of parasitic neutron absorptions that occur in U-236 result from neutron captures in the large resonance at about 6 eV. The relative average cross section for various recycle strategies is shown in Fig. 6-6. For a self-generated recycle mode, the concentration of U-236 increases with time. The composition of recycled fuel also changes with exposure and with the particular mode of recycle assumed. Both of these effects have been included in the U-236 cross-section calculations summarized in Fig. 6-6. The estimated number of recycle blocks per reload at equilibrium that contain the recycle U-235 with high U-236 content is also given.

The average cross section in the case of full recycle steadily decreases since the U-236 continues to build up as the uranium is recycled. For the reference cycle, the U-236 cross section decreases to a constant value since the in-core inventory is limited by the yearly disposal of the residual feed uranium that has been recycled once. The effective cross section is low since the U-236 is concentrated into a small number of blocks. A high uranium loading per element is required for these fuel blocks due to the fact that the residual uranium is only about 30% enriched. Such concentration leads to significant self-shielding of the U-236.

In addition to the grain and fuel rod self-shielding effects, the reference residual recycle strategy employs positioning the residual U-235 recycle blocks near the bottom reflector. In these locations near the reflector, the ratio of epithermal to thermal flux is lower than the core average ratio. This further reduces the effective U-236 cross sections in the residual U-235 recycle elements. The relative cross section shown in Fig. 6-6 takes into account both the rod shielding and the spatial dependence effect on the U-236 cross section.

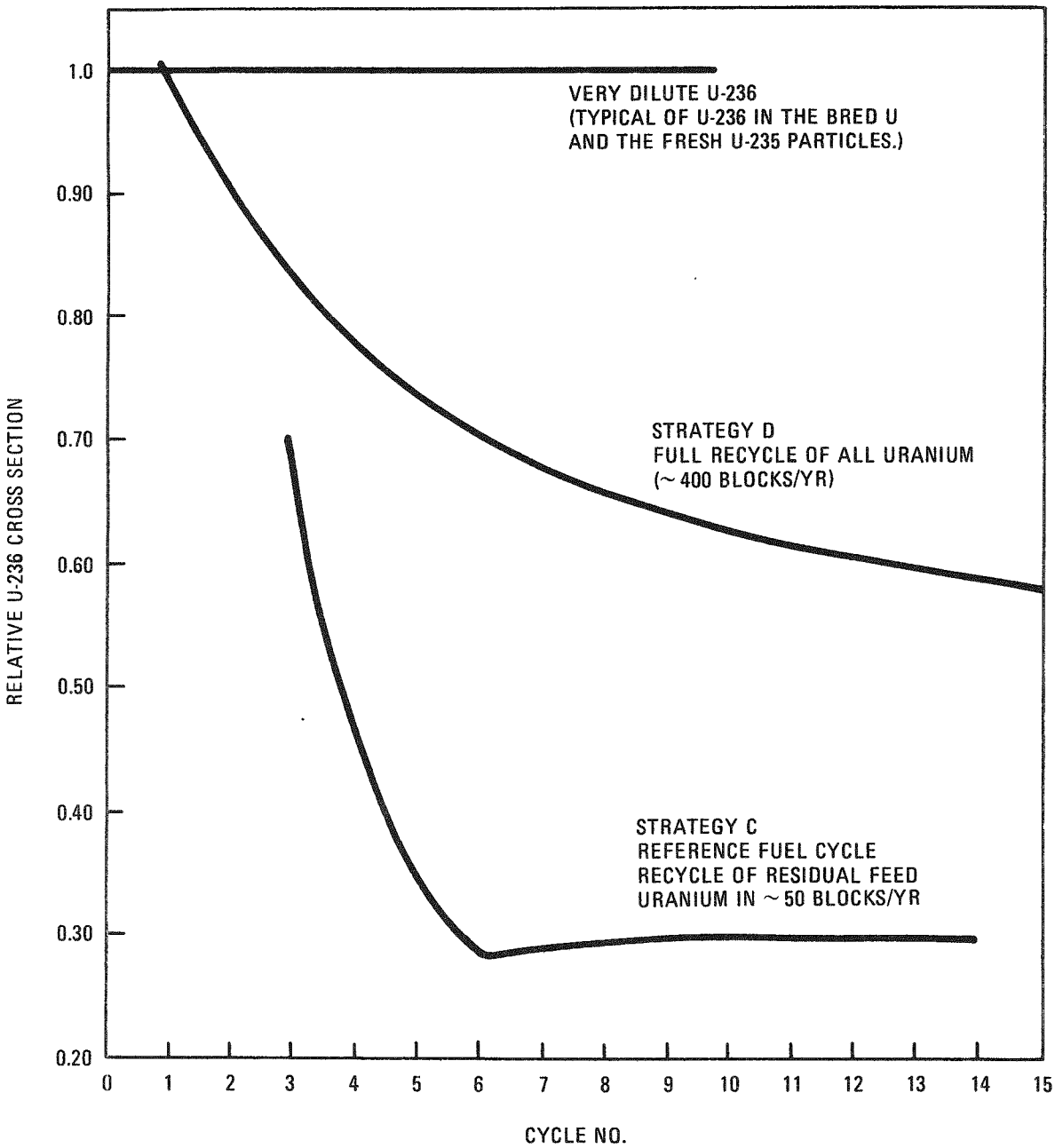

Fig. 6-6. U-236 cross section versus exposure

U-236 Penalty to Fuel Cycle Cost

Effect of U-236 on Discharged Feed Uranium Value

The majority of the U-236 in-core inventory in the HTGR results from parasitic neutron captures in the U-235 in the feed uranium. The feed uranium is recovered and recycled one more time in the reference cycle strategy. At equilibrium, the discharged feed uranium is typically 30% enriched in U-235 and contains about 50% U-236.

The recycled feed uranium fissile and fertile loadings per element are adjusted such that those elements have the same power matching characteristics as the fresh makeup elements they replace. The low enrichment requires that the uranium loading per block in these elements be ≥ 3 times the loading of fresh makeup blocks in the same core location. This lumping effect significantly reduces the U-236 epithermal resonance and thus reduces its negative parity.

In addition to the resonance shielding effect, there is a spatial shielding component due to the positioning of the recycled elements near the bottom reflector in a high thermal-to-epithermal flux region. The combination of both effects is to reduce the effective U-236 cross section, and parity, to $\sim$30% of the infinite dilute value characteristic of the U-236 value in the bred uranium fuel.

Detailed "indifference" calculations were performed in which mass flows for nonrecycle and recycle of feed uranium of varying compositions were compared. The ERDA "book value" of the discharged feed uranium was varied until equal fuel costs were obtained for the nonrecycle and the various recycle cases. These results are shown in Fig. 6-7, where the fractional book value and the equivalent negative U-236 parity are plotted as a function of the ratio of U-236 to U-235 in the irradiated feed uranium.

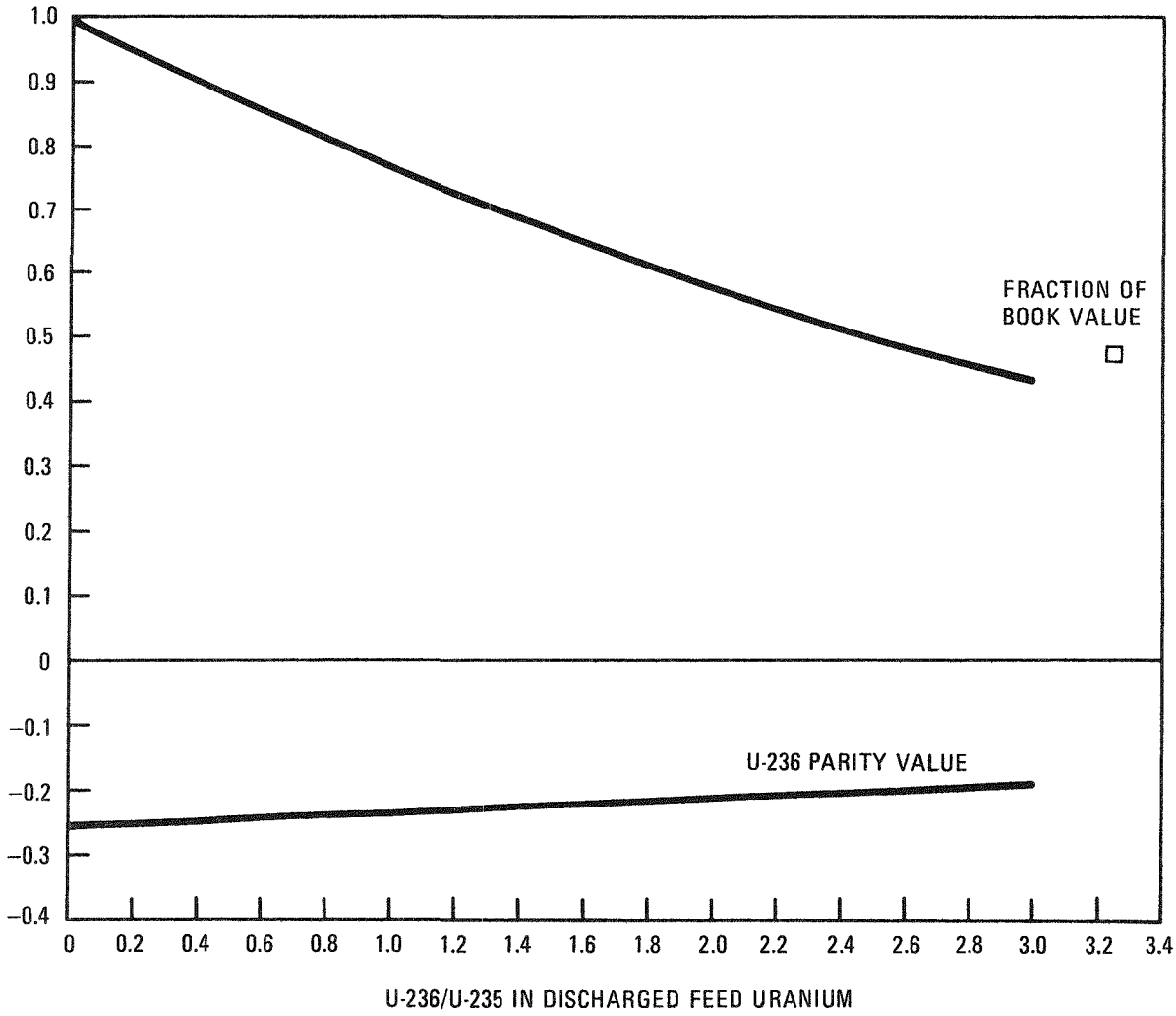

Fig. 6-7. Relative book value and U-236 parity in discharged feed uranium

From Fig. 6-7 it is seen that the negative U-236 parity value in discharged feed uranium varies from -0.25 to -0.20, depending on the composition of the discharged uranium. This is about one-third of the value of U-236 in the bred fuel stream.

Effect of U-236 on Bred U Value

The value of the bred uranium will change with the number of times the material has been recycled through the reactor since the higher isotopes U-234, U-235, and U-236 will build up. The rate at which this occurs is shown in Fig. 6-8. The U-233 enrichment drops from 92% for 1-yr-old fuel (which will be loaded again 2 yr after reactor startup) to 60% for 20-yr-old recycle fuel. Within that time period, U-234 and U-235 reach an equilibrium enrichment of 25% and 8.5%, respectively. The U-236 enrichment continues to increase.

The effect of this changing isotopic content on the relative inherent or neutronic value of the contained U-233, assuming the value of the U-235 is determined solely by ore and enrichment costs, is shown in Fig. 6-9. "Uncontaminated" U-233 has a value relative to U-235 in 90% enriched uranium of about 1.43. As U-234 and U-236 build up, the U-233 value as deduced from indifference calculations drops, so that after 25 yr of operation, the effective value of the U-233 in the bred uranium is about 1.35. The U-233 value averaged over 15 yr of plant operation is about 1.39, and this is the number frequently used in fuel cycle cost evaluations.

An equivalent method of determining the changing bred uranium value is to assign a value to all uranium isotopes: U-233, U-234, U-235, and U-236. The result is:

	Value Relative to U-235
U-233	1.43
U-234	0
U-235	1
U-236	-0.58 to -0.65

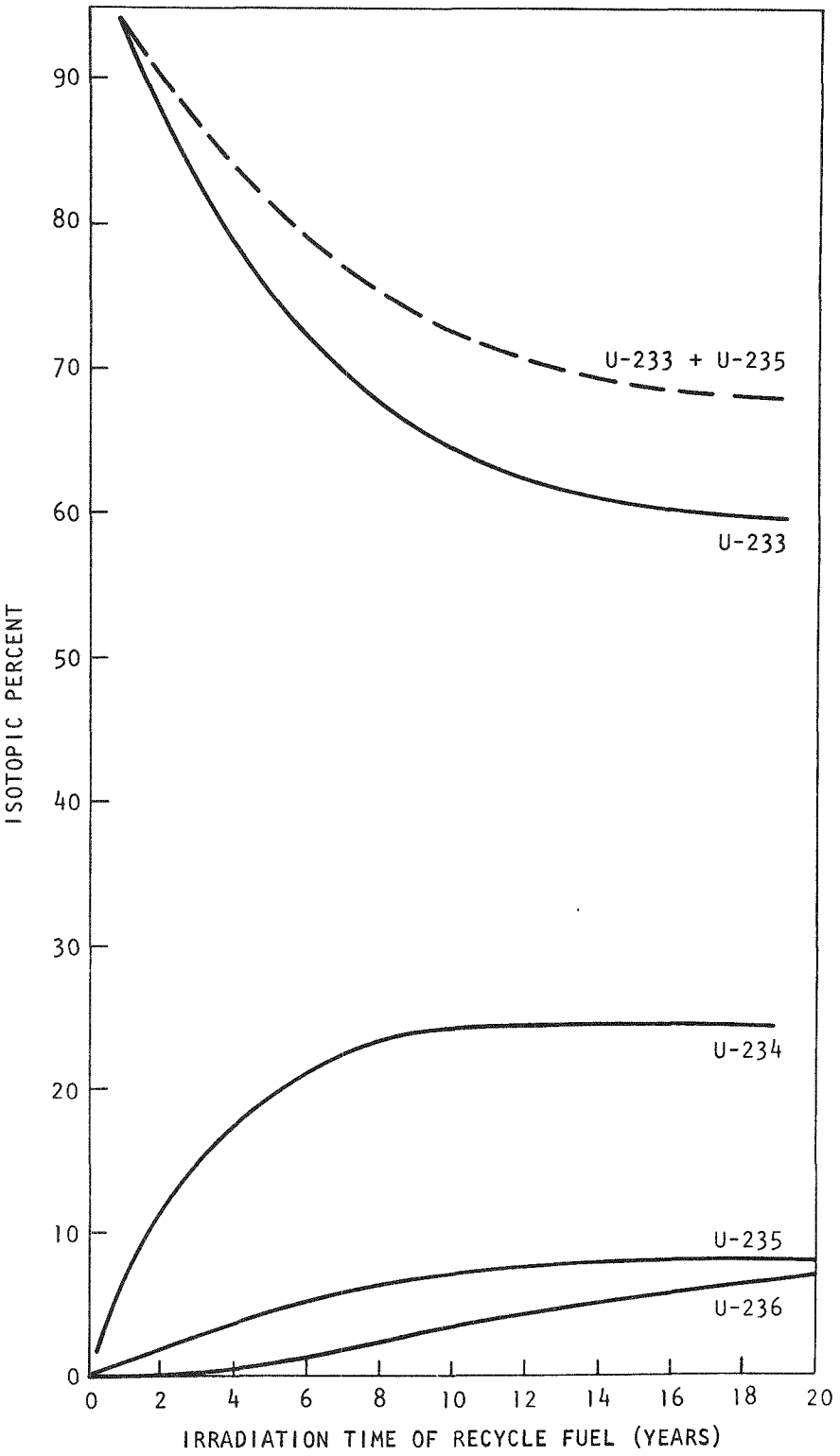

Fig. 6-8. Isotopic composition of recycle fuel as a function of irradiation time

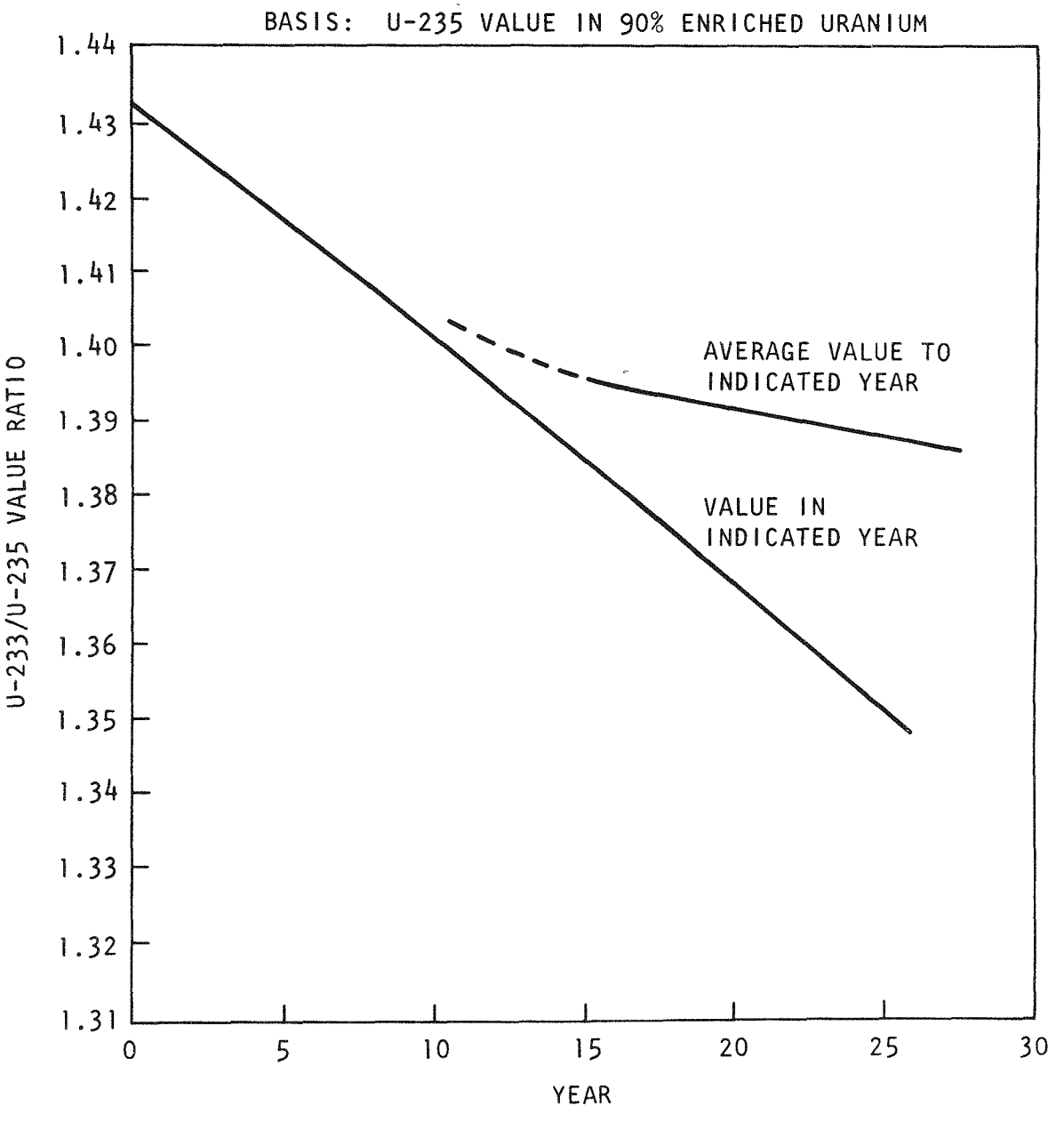

Fig. 6-9. Relative U-233 value

That is, U-236 in very dilute concentrations, such that its absorption cross section is unshielded, has a negative value which is 58% of the value of U-235 in 90% enriched uranium. For example, if U-235 is worth $20/g, U-236 would be worth -$11.6/g. The above values assume a working capital rate of 10%. At 15%, the dilute U-236 value is -0.65, or -$12.9/g if U-235 is $20/g.

The details of the regression analysis method that was used to obtain these parity values is described in Ref. 6-2.

REFERENCES

6-1. Brogli, R. H., et al., "The High Conversion HTGR for Resource Conservation," ERDA Report GA-A13606, General Atomic, October 1, 1975.

6-2. Rothstein, M. P., et al., "Neutronic Values of U-233 and U-236 in the HTGR," ERDA Report GA-A13728, General Atomic, to be published.

6-3. "Design Study Report for TARGET, a 1000-MW(e) High-Temperature Gas-Cooled Reactor," USAEC Report GA-4706, General Atomic, Division of General Dynamics, March 9, 1964.

6-4. Dahlberg, R. C., R. F. Turner, and W. V. Goeddel, "HTGR Fuel and Fuel Cycle Summary Description," General Atomic Report GA-A12801, January 21, 1974.

6-5. Brogli, R. H., and K. R. Schultz, "Thorium Utilization in an FBR/HTGR Power System," in Proc. American Power Conference 36, 247 (1974).

6-6. Raman, S., C. W. Nestor, Jr., and J. W. T. Dabbs, "The ^{233}U ^{232}Th Reactor as a Burner for Actinide Wastes," paper presented at the Conference on Nuclear Cross Sections and Technology, Washington, D.C., March 1975.

6-7. Asmussen, K. E., and R. K. Lane, "U-233 Indifference Value for Use in HTGRs," Gulf General Atomic Report Gulf-GA-A12204, August 1, 1972.

6-8. Lane, R. K., C. H. George, and R. C. Dahlberg, "Comparative Fuel Utilization in the HTGR and PWR," Gulf General Atomic Report Gulf-GA-A12592, April 15, 1973.

6-9. Dahlberg, R. C., "Effects of U-236 and Other Uranium Isotopes on HTGR Fuel Cycle," General Atomic Report GA-A13408, March 1, 1975.

8. HTGR PHYSICS
189a No. SU002

REANALYSIS OF THE HTGR CRITICAL CONTROL ROD EXPERIMENTS

Previous General Atomic analyses (Refs. 8-1, 8-2) of the control rod worth experiments performed during the HTGR critical experiment program (Ref. 8-3) have overestimated the worth of a single control rod by about 5% and the worth of a control rod pair by about 14%. A careful reanalysis of this experiment has been performed; the results show essentially perfect agreement for the single control rod experiment and an overestimation of about 10% for the worth of two control rods.

This analysis differs from the previous analyses primarily in the composition of the central region of the critical experiment (which was reconstructed from the original records) and in the use of a detailed two-dimensional triangular geometry transport theory code (Ref. 8-4) for the calculation of the two-control-rod critical experiment configuration.

During an examination of the results, it was found that the treatment of the stainless steel outer cladding of the control rods is important in the analysis of the two control rod experiments. Specifically, it was found that the homogenization procedure currently used in HTGR designs will cause the control rod worth to be overpredicted by $\sim$3% for a single rod calculation. If it is assumed that the overestimate of the single control rod worth due to homogenized cladding and poison applies to each of the rods in the two-control-rod experiment, the 10% overestimate of the worth of two control rods is reduced to about 7%.

Future two-dimensional transport theory calculations of the worth of HTGR control rod pairs should represent the outer cladding of the control rod explicitly. The control rod outer cladding could have been shown

rather easily in the triangular geometry transport theory calculation of the two control rod experiment. Unfortunately, the two-control-rod calculation was too expensive to repeat with the funding available under this task.

A topical report giving the details of this work has been prepared and will be distributed in the near future.

REFERENCES

8-1. Nirschel, R. J., E. M. Gillette, and J. R. Brown, "Experimental and Analytical Results for HTGR Type Control Rods of Hafnium and Boron in the HTGR Critical Facility," USAEC Report Gulf-GA-A9354, Gulf General Atomic, January 31, 1973.

8-2. Davison, W., "HTGR Critical Control Rod Experiment Re-Analysis," General Atomic unpublished data, October 5, 1973.

8-3. Bardes, R. G., et al., "Results of HTGR Critical Experiments Designed to Make Integral Checks on the Cross Sections in Use at Gulf General Atomic," USAEC Report GA-8468, Gulf General Atomic, February 12, 1968.

8-4. Reed, W. H., et al., "TRIPLET: A Two-Dimensional, Multigroup, Triangular Mesh, Planar Geometry Explicit Transport Code," Los Alamus Scientific Laboratory Report, LA-5428-MS, October 1973.

8-5. Hackney, R., "Neutron Cross Sections for Control Systems in Large HTGRs," General Atomic unpublished data.

9. HTGR FUEL DEVELOPMENT AND ENGINEERING
189a No. SU003

TASK 100: FUEL DEVELOPMENT PLANNING AND COORDINATION

During this report period the executive summary of the Fuel Development Program was issued and the complete text was prepared as GA-A13647. However, issue of the document has been deferred pending resolution of uncertainties resulting from recent changes in the HTGR business.

TASK 200: ACCELERATED IRRADIATION TESTS

Subtask 210: Fresh Fuel Qualification

Summary and Conclusions

Postirradiation examination of capsules P13Q, P13R, and P13S continues on schedule.

The fission gas release from the 1100°C cell (cell 2) of capsule P13T increased significantly during this reporting period. This cell contains many test variables, including a large number of WAR fissile particles. An analysis indicated that the gaseous release from cell 2 is within expected levels based upon measured preirradiation fuel contamination levels and fuel performance model predictions. However, because of the rapid change in fission gas release rate, the insertion of capsules P13U and P13V was delayed to permit time to further evaluate the performance of fuel in P13T.

Capsules P13R and P13S

Capsules P13R and P13S are the seventh and eighth in a series of irradiation tests to demonstrate the integrity of reference and alternate

LHTGR fuels over a wide range of irradiation conditions. The capsules were discharged from the GETR on October 31, 1974 and the disassembly and postirradiation examination commenced at the GA hot cell facility on December 5, 1974.

Capsule disassembly, dosimetry and burnup analyses, fuel rod dimensional changes, and the results of the fuel rod and unbonded particle visual examinations were summarized in a previous quarterly report (Ref. 9-1). Fission gas release (TRIGA activation), metallography, gamma-ray spectrometry, and radiography examinations have been completed. Fuel particle and coating density measurements and acid leaching studies are currently in progress. The results of all postirradiation examinations will be presented in a topical report, which is currently in preparation.

Capsule P13Q

Capsule P13Q, which was designed to evaluate the performance of LHTGR fresh fuel irradiated in integral bodies under nominal LHTGR operating conditions, completed its scheduled irradiation in the ORR on February 27, 1975. Disassembly and postirradiation examination of the capsule commenced in the GA hot cell facility on April 21, 1975.

The results on the capsule disassembly, fuel rod dimensional change measurements, and visual examination of the fuel rod and unbonded particle specimens were reported in the previous quarterly report (Ref. 9-2). Postirradiation fission gas release measurements, radiography, and gamma-ray spectrometry examinations have been completed. Metallographic examination of 8 to 10 fuel rods and particle and coating density measurements are planned, but have been delayed due to the heavy work load in the GA hot cell facility.

Capsule P13T

Capsule P13T is the ninth in a GA series of LHTGR fuel irradiation tests conducted under the HTGR Fuels and Core Development Program. P13T is

a large-diameter capsule containing two cells. Cell 1 is a qualification test of reference fresh fuel [TRISO UC_2 (VSM) and BISO ThO_2 particles] irradiated at 1300°C. Cell 2 is an evaluation test of reference fresh fuel and recycle fissile fuel [TRISO UC_xO_y (WAR) particles] irradiated at 1100°C. The capsule was inserted in the ORR reactor in May 1975 and will be irradiated to a peak test fluence of 8.5×10^{21} n/cm^2 (E > 0.18 MeV)$_{HTGR}$.

The capsule has presently reached an estimated peak fast fluence of 3.1×10^{21} n/cm^2 (E > 0.18 MeV)$_{HTGR}$. The fuel rod temperatures measured with tungsten-rhenium (W/Re) thermocouples are close to design except for the rods near the top of the core. These temperatures range from about 1000° to 1200°C because of the large change in the neutron flux from the beginning to the end of each cycle. This fluctuation will continue throughout the irradiation. Five pairs of W/Re and chromel/alumel (C/A) thermocouples placed in various locations in the capsule are indicating that the W/Re thermocouples are decalibrating. The decision has been made to change control of the temperature in cell 2 by switching from a W/Re to a C/A thermocouple, as has been done for cell 1.

The fission gas release of the two cells is low: 4×10^{-6} and 6×10^{-6} (R/B Kr-85m) for cells 1 and 2, respectively. The fission gas release of cell 2 increased significantly at a fluence of 1.5×10^{21} n/cm^2. This increase in release is within expected predicted limits using current fuel performance models (Ref. 9-3) and accounting for the measured preirradiation fuel contamination levels. The fission gas release profiles measured for capsule P13T are plotted in Fig. 9-1.* These values are seen to fluctuate considerably during the irradiation, which is partly caused by the continuously changing neutron flux profiles during each reactor cycle.

Capsules P13U and P13V

Capsules P13U and P13V will test TRISO WAR UC_xO_y and BISO ThO_2 coated particles under normal and thermal cycling conditions to peak LHTGR

*Figures appear at the end of Section 9.

temperatures and fluences. Each capsule will be 31.75 mm in diameter and similar in design to capsules P13R and P13S. Five fuel rod cells and one unbonded particle cell will be tested in each irradiation test vehicle.

The two capsules were scheduled to be inserted in the GETR in November 1975. All fuel rod bodies and unbonded particle crucibles were completed and construction of the test vehicles was on schedule. However, as a result of the increase in fission gas release in cell 2 of P13T, a decision was made to delay insertion of capsules P13U and P13V to allow additional time to evaluate the in-pile performance of the fuel. Based upon recent calculations, it appears these particles are performing within expected limits. Capsules P13U and P13V have now been rescheduled for insertion in the GETR during February 1976. The irradiation of the capsules will be completed on schedule because of an increased flux in GETR which was not accounted for in prior estimates of irradiation times.

TASK 300: INTEGRAL FUEL SYSTEM TESTING

Subtask 310: Peach Bottom Fuel Test Elements

Summary

Fuel test element FTE-6 was irradiated for 645 EFPD in Peach Bottom Unit 1, Core 2. The results of the postirradiation examination (PIE) can be summarized as follows:

1. Significant bowing had been observed over the fuel body, suggesting up to 50% ultimate stress level for restraint bow: ≤45-mil bow over a graphite body of 31-in. length and 2.74-in. diameter in a sleeve of nominal 12-mil clearance.

2. Fuel rod bowing had been observed in fuel rods from bodies 2 and 3: ≤22 mils over 1.94 in.

3. Fuel rod shrinkage irregularities support local power and temperature peaking as observed in Peach Bottom end-of-life (EOL) gamma scans.

4. From the dimensional characterization of fuel rods, rods containing $(Th,U)C_2$ TRISO/ThC_2 TRISO fuel showed the lowest irradiation strain: ≤2.2% shrinkage.

5. Fuel rods of the UO_2 TRISO/ThO_2 BISO variety experienced the greatest shrinkage of the four varieties of fuel contained in FTE-6: ≤3.2% shrinkage.

6. All fuel rod types revealed a certain amount of anisotropy in dimensional change.

Introduction

Irradiation of FTE-6 began in core position CO2-01 on July 11, 1971 at 252.4 EFPD of Core 2 operation. FTE-6 was irradiated in this position for 645.0 EFPD, with EOL occurring at 897.4 EFPD of Core 2 operation on October 31, 1974. The average radial power factor over the residence time of FTE-6 in Core 2 was 0.93 and energy production was 9.04×10^{-4} kW-days. FTE-6 was removed from the core, gamma scanned, and stored on November 25, 1974.

The Hallam cask supposedly containing RTE-6 left Peach Bottom on May 23, 1975. However, after arrival at ORNL and during the canister removal operation, it was discovered that FTE-6 was shipped instead of RTE-6. This necessitated the writing of an incident report by ORNL and an unusual occurrence report by GA. The element left ORNL on June 19, 1975 and arrived at GA on June 23, 1975. Delayed neutron studies on the cask were done, and the cask was unloaded into the high-level cell on June 25, 1975. Delayed neutron studies were repeated on the element without shielding. PIE operations began on June 30, 1975 and were completed on August 19, 1975.

The fuel contained in FTE-6 is described in Table 9-1.*

Irradiation Performance

The calculated burnup and fluence for FTE-6 are given in Table 9-2.

The axial temperature distributions for FTE-6 at various times during Core 2 operation were generated using the TREVER code (Ref. 9-4). The temperature distributions are shown in Fig. 9-2. The temperature point locations calculated by TREVER as shown in Fig. 9-3. The time average bulk temperature and the maximum and minimum temperatures during life for the fuel rods and spine samples are given in Tables 9-3 and 9-4. FTE-6 was in core location C02-01 from 252.4 to 897.4 EFPD. The test element power history is shown in Fig. 9-4. Figures 9-5 and 9-6 show the core operating parameters and power history, respectively.

The test element temperatures were based on a one-dimensional heat transfer analysis (TREVER code) with the results modified to allow for axial heat conduction in the unfueled gap between each of the three fuel bodies in the element. This correction results in a drop in the temperatures at the ends of the fuel bodies and was derived by nondimensionalizing the results of the TAC2D code axial temperature distribution calculation from Ref. 9-5. The GAUGE code radial core power for FTE-6 was given the axial distribution shown by curve A in Fig. 9-7 (Ref. 9-6), since FTE-6 was two or more locations away from a control rod. The fast flux axial distribution used was calculated by the FEVER code for middle of life (see Fig. 9-8).

The graphite material properties (thermal conductivity, emissivity, and thermal and irradiation strain) used in this analysis were taken from Ref. 9-7. The test element cross section (Fig. 9-3) shows the element sleeve (3.49 in. O.D., 2.75 in. I.D.) of H-381 graphite, the fuel body of H-327 graphite (2.74-in. O.D.), and the relative position of the fuel holes. FTE-6 had eight 0.50-in.-I.D. fuel holes. A constant fuel thermal conductivity of 5 Btu/hr-ft-°F was used. The thermal and irradiation

*Tables follow the text of Section 9.

strain characteristics for TRISO/BISO type fuel were used (taken from the SHRINK code results of Ref. 9-8). Figure 9-9 shows the calculated end-of-life fuel rod radial irradiation strain distribution for a TRISO/BISO type fuel rod. Comparison with measured strains will be done after analysis of measurements.

The test element was instrumented with two thermocouples, a W/Re type at the spine hole I.D. and a C/A type near the fuel body outer surface positioned about halfway into the active core (Fig. 9-3). From the radial temperature distribution given in Fig. 9-3 (TAC2D results from Ref. 9-5), it is seen that the W/Re thermocouple should indicate a temperature between the maximum and minimum fuel temperatures (TREVER points A and B) at a point about 60% from temperature B to A. The temperature indicated by the C/A thermocouple should be close to the fuel body surface temperature (TREVER point D).

Irradiation of the W/Re thermocouple causes the resistance of the wires to increase, resulting in a decrease in the indicated thermocouple temperature. Thus, an irradiation correction is required for the W/Re thermocouple. It is recognized that this correction is dependent upon the irradiation temperature and the path of the wires through the core; therefore, a correction for the particular thermocouple installation is required. Since such a correction is not available, the following correction for capsule P13M was used:

$$\frac{T_{corrected}}{T_{indicated}} = \frac{T_i - 0.183 - 3.02\phi + 0.215\phi^2}{T_i(0.993 - 0.121\phi + 0.009\phi^2)} \quad ,$$

where $\phi(10^{21}$ n/cm$^2)$ is the thermal flux (E < 2.38 eV). The thermocouple data for each time point calculated by TREVER are plotted in Fig. 9-2; the complete thermocouple data history is shown in Fig. 9-10 (Ref. 9-8). The beginning-of-life W/Re thermocouple data (Fig. 9-2 at 252 EFPD) agree well with the TREVER calculations. In Fig. 9-10 the W/Re indicated reading falls with time as expected (due to irradiation), while the corrected

reading rises sharply. In Ref. 9-9 it was concluded that the P13M decalibration formula overcorrects the data and that the actual temperature lies somewhere in between. Taking this into consideration, the W/Re data plotted in Fig. 9-2 generally agree with the TREVER calculations in that the corrected and uncorrected thermocouple readings usually bracket the calculated result. From Figs. 9-2 and 9-10, it appears that the C/A thermocouple was shorted out near the bottom of the element.

Disassembly Operations

All disassembly operations were performed according to Ref. 9-10 "Postirradiation Examination Procedure for Peach Bottom Test Element FTE-6." The helium-filled aluminum canister containing FTE-6 was removed from the Hallam cask and injected into the high-level cell without incident. The canister was girdle-cut approximately 3/16 in. deep and 4 ft from the top end, and the piece removed. The element was pulled out until clear of the canister, thereby exposing the thermocouple contacts. The remaining portion of the canister was discarded. At this point, the identity of the element was checked and the test element was photographed (Fig. 9-11). A composite of the total element is shown in Fig. 9-12. Thermocouple measurements were then taken and recorded (Table 9-5). No preirradiation thermocouple measurements were available; however, the postirradiation measurements seemed to be in line with preirradiation and postirradiation measurements from other Peach Bottom instrumented test elements.

In order to section the fuel element, it was supported horizontally by a series of V-rollers, which facilitated horizontal and rotational movement. A special extension drill was inserted through the purge gas inlet hole in the upper reflector and a hole was drilled through the porous graphite plug. While the bodies were held down, the upper reflector was removed by plunge cutting through the sleeve at a point about 2 in. below the sleeve-reflector joint. This section was stored for later gamma scanning. A plunge cut was then made 2 in. from the bottom of the element and the small section was discarded. The sleeve was then girdle-cut $\sim$0.37 in. deep without hitting the lower reflector. This was done to remove the

thermocouples; however, there was difficulty in the removal and the wire thermocouple had to be forcibly removed. Six inches of the outer sheathing was stripped from the end of the thermocouple and was lodged in the center body.

The intact element had appeared normal, but extreme difficulty was encountered when the body removal process began. The fuel bodies could not be moved with the push rod per the normal procedure. Two 3-in. sections of the sleeve were removed from either end of the sleeve containing the bodies. After an unsuccessful attempt to free the bodies by twisting, it was decided to cut the sleeve longitudinally. Due to the extreme difficulty encountered in removing the fuel bodies, extensive fuel body outer diameter and bow measurements were made. Unfortunately, because the sleeve was cut longitudinally, only two sleeve I.D. measurements could be made. However, sleeve thicknesses were measured on sections of the longitudinally cut sleeve for end-of-life fuel body sleeve gap determination.

Fuel Element Examination

Photographs of the entire length of the element were taken prior to examination of the element exterior with short-focus binoculars and the in-cell Kollmorgan (Fig. 9-12). No cracks or abnormalities were found. The overall length of the element and sleeve diameters at various intervals were measured (Table 9-6). The overall length was determined with a steel rule and confirmed by transversing the length of the element with a saw head. The horizontal movement of the saw head can be determined within ±1/32 in. The length change was -0.628.

Sleeve outside diameters were determined with calibrated snap-on dial indicator gauges; the two inside diameters and the longitudinal sleeve sections were measured in the hot cell hood after removal of fuel bodies. The accuracy of the postirradiation diameter measurements was ±0.001 in. The only preirradiation dimensions available were the manufactured tolerances, which are two and five times larger. The average dimensional changes (Table 9-6) are -0.13 for the sleeve O.D. and -0.09 for the sleeve

I.D. Thus, it can be concluded that the sleeve experienced very little shrinkage.

Fuel Body Examination

Visual Examination. Each fuel body was photographed and visually inspected at high magnification, as shown in Figs. 9-13 through 9-15. No cracks or abnormalities were found. Data for the three fuel bodies are given in Tables 9-7 through 9-9.

Structural Integrity and Dimensional Changes. After the fuel bodies were removed from the graphite sleeve, each body was placed on a granite surface plate and measured with a special device (Fig. 9-16). Extensive bow was observed in all three bodies. The bow was measured across each of the eight fuel holes in the body to determine the uniformity of the bow. The worst cases were observed in bodies 1 and 2, holes 3 and 7, and body 3, holes 1 and 5. The bow was up to 45 mils over the 31-in.-long bodies, as compared to a 12-mil total nominal clearance between the fuel body and sleeve.

Figures 17a through 171 illustrate the bow across opposite holes of each body. The bow was nearly identical on each side of the bodies, indicating uniform bow around the axis of the bodies. It is anticipated that residual stress work will give more insight into the bow observed in the bodies. The results of the bow measurements are summarized in Table 9-10. From Table 9-10 it can be seen that the maximum bow was located toward the center of the element, as would be expected due to higher expected temperature and fluence in this area. Radial gamma-scanning results indicate power variations between fuel rod stacks of ±30% (Fig. 9-18), which could be responsible for this extensive bow.

Dimensional changes in the longitudinal and transverse directions of the fuel bodies are included in Tables 9-7 through 9-9. The average values determined are given in Table 9-11.

The fuel body length change follows the expected trend of greater shrinkage at the center of the element, where higher temperatures and fluences are experienced. The outside diameter change for body 3, however, was greater than expected in relation to the overall element change. This difference is eventually due to the power variations caused by Th-filled spine samples located in body 3.

The radial gaps can be determined from Tables 9-6 through 9-9 by comparing the as-measured dimensions of the sleeve and graphite body and from thickness measurements of the sleeve sections. The calculated radial gaps are given in Table 9-12. The gap changes can be attributed to the extreme bow observed in the fuel bodies. The gap changes that occurred at locations 2 and 3 of Table 9-12 represent approximate locations of large bow observed along fuel bodies 1 and 2 (see Table 9-10). Unfortunately, the gap measurements at positions 2, 3, and 4 in Table 9-12 were determined from sleeve thicknesses and no other means for measurements was available.

Fuel Rod and Spine Examination

Removal. Following visual inspection, bow measurements, and dimensional measurements, the fuel bodies were placed in a special holding fixture to facilitate the removal of the center samples. A hole was drilled through the bottom sample hole plug and a push rod was inserted. The upper sample hole plug was unscrewed, and the distances from the top of the spine samples to the edge of the holes were measured. These measurements are compared with preirradiation measurements in Table 9-13. The spine samples were pushed out one at a time, identified, and placed in a pan. These operations were carried out over a special pan that would catch any loose fuel particles from the drilled holes; none were found. No problems were encountered during the removal of spine samples. The spine samples are described in Table 9-14.

Following removal of the spine samples, holes were drilled in the bottom of the fuel bodies to enable the fuel to be pushed out using the

special discharge fixture. The graphite plugs capping the fuel holes were easily removed. The distances from the top of the fuel rods to the edge of the fuel holes were measured. These measurements, as well as fuel stack lengths, are compared to preirradiation measurements in Table 9-15. Data may be used to make fine adjustments to spine sample locations, if required. However, the associated error appears large because strain data vary considerably from the values deduced from the composite spine sample stack measurements in Table 9-14.

The fuel bodies were then placed in the mechanical push device with Dillon load gauges ranging from 0 to 250 lb; the force required to start movement did not exceed 50 lb and that required to sustain movement did not exceed 30 lb (Table 9-16). The fuel rods were pushed onto the trough and visually examined. The stack length was measured (Table 9-15).

Structural Integrity and Dimensional Changes. After each fuel rod stack was removed it was examined visually (Table 9-16) and photographed. In all three bodies, there was a high degree of matrix end cap and surface cracking, as well as surface "pock" marks (see Figs. 9-19 through 9-30).

Fuel rod bowing was visually apparent in bodies 2 and 3 (Figs. 9-31 through 9-34), and a special fixture was made to measure the observed bowing. Up to 0.022 in. bow was measured over the fuel rod length of 2 in. Table 9-17 summarizes the results. This bowing may be attributed to power variations or inhomogeneities. Orientation information was lost, and there is presently no good explanation for this effect. Dimensional changes for the longitudinal and transverse directions of the fuel rods are shown in Fig. 9-35. The average values are shown in Table 9-18.

A comparison of TREVER calculated fuel rod (TRISO/BISO) radial strains (Fig. 9-9 and Table 9-18) is shown in Table 9-19. From the data presented, it can be concluded that the turnaround for body 2 predicted by TREVER does not occur. TREVER tends to overestimate the strain for body 1 and underestimates the strain for two fuel rod varieties in body 2 (UO_2 TRISO/ThO_2

BISO and UO_2 TRISO/ThC_2 BISO). However, TREVER calculations for UO_2 TRISO/ThO_2 BISO in body 3 match somewhat. The differences in the calculated and measured strains may be related to power perturbations and bowing effects, which eliminate the heat transfer gap on one side and increase it on the opposite side. A detailed error analysis on fuel rod dimensional data is necessary prior to further judgments.

Peach Bottom EOL gamma scan data (Fig. 9-36) indicate step power and temperature distribution with peaking at the lower end of body 3. This peaking may explain some of the irregularities in measured strains between bodies 2 and 3, as indicated in Fig. 9-35. The peaking can be attributed to thorium-fueled spine samples, which cause local temperature and power variations from U-233 fission. Gamma scanning of the spine samples is required, as well as recomputation of TREVER predictions of radial strain using new temperature data.

The data also indicate that fuel rods containing $(Th,U)C_2$ TRISO/ThC_2 TRISO experienced the least shrinkage, and fuel rods containing UO_2 TRISO/ThO_2 BISO experienced the greatest amount of shrinkage. The latter fuel rod type shrank the greatest throughout the total element and significantly in body 3 in the area of the thorium-fueled spine samples.

The high incidence of matrix end cap cracking in the fuel rods can be attributed to the manufacturing process.

Hot Cell Gamma Scanning

During the disassembly of FTE-6 a gamma scan facility was being installed in the GA low-activity-level hot cell. Although the facility and experimental techniques had not been perfected, some practice scans were obtained on FTE-6 fuel bodies and on individual fuel rods after removal from the fuel bodies. These preliminary results are included here, together with a brief description of the gamma scan facility.

System Description. The experimental arrangement for gamma scanning (Fig. 9-37) consists of the GA low-level cell, the scanner, the collimator system, the detector, electronics, the pulse height analyser, recording devices, and the computer. Scanning is performed in the GA low-level cell where background activity is negligible. A scanner device driven by a variable speed motor carries the fuel body past the collimator opening. A locator, which is attached to the scanner driver mechanism, sends a pulse signal to a recorder once during every revolution of the drive shaft. For each shaft revolution, the scanner carriage moves the fuel body 0.040 in. (1.02 mm) past the collimator opening. The collimator opening was 0.023 by 0.875 in. (0.052 by 22.23 mm).

A high-resolution Ge(Li) detector is positioned 2-1/4 in. (5.7 mm) in front of the collimator. The detector signal is input to a 4096 channel pulse height analyzer - tape deck - computer based data acquisition system and to the single channel analyzers (SCA) - rate meter - recorder system. The gamma ray spectra are stored either in the computer memory or on magnetic tape for computer processing at a later date. The SCA system is used to provide an instantaneous graphical display of the peak activities of selected isotopes. Also, the locator pulse signal from the scanner drive mechanism is superimposed on the signal, which provides a record of distance traveled as a function of time.

A typical setup procedure for scanning is briefly as follows:

1. Count a calibration standard to determine the system gain-intercept values.

2. Align fuel body and crystal with collimator system.

3. Set scanning speed.

4. Select count time for accumulating spectra.

5. Set rate meters, locator pulser, and recorders.

Preliminary Results. With the center fuel body placed in front of the collimator and the collimator-detector system aligned on a single fuel hole (as shown in Fig. 9-37), the fuel body was rotated. The gamma activities of Zr-95 and Cs-137 were continuously monitored using the SCA - rate meter - recorder system. A typical rotating scan from body 2 is shown in Fig. 9-18. There appears to be a significant variation in gamma activities between fuel holes. Although at that time there was concern about the reproducibility of scanning measurements, it is believed that relative differences observed during a continuous scan are valid and the differences between holes are real. These differences are believed to be caused by differences in fuel loading and inhomogeneous fuel loading within a rod, both of which can affect the local temperature profile and local fuel performance. Using a linear relationship between count rate and power rating, a ±30% power variation at 95% confidence (two standard deviations) can be derived from Fig. 9-18.

Attempts were made to perform axial scans along the fuel body; however, these attempts were abandoned because at that time absolute activities could not be reproducibly measured.

Following removal of fuel from the bodies, a few fuel rods from body 2, hole 2 were scanned. Some rods reveal significant variation in gamma activity over the length of the rod (Fig. 9-38), indicating fuel rod loading inhomogeneity. With the completion and calibration of the gamma scan facility, further scanning of FTE-6 fuel rods is being scheduled for early 1976.

TASK 400: OUT-OF-PILE PARTICLE TESTING AND EVALUATION

Work on this task is continuing; there are no current results to report.

TASK 500: FUEL ROD TEST AND EVALUATION

Summary

All the required fuel rods for thermal and mechanical property measurements during FY-76 were manufactured during this report period.

Discussion

The objectives of the fuel rod testing and evaluation program are to select and evaluate candidate fuel rod materials and processes for large HTGR fresh and recycle fuel systems and to provide reliable data for HTGR core design by measuring the thermal and mechanical properties of fuel rods under HTGR conditions.

Work in this quarter has been concentrated on the initial phase of the program, fabrication of prototype large HTGR fuel rods for unirradiated property measurement. Nineteen types of prototype large HTGR fuel rods have been fabricated for thermal conductivity, thermal expansion, and strength measurements. The fuel rod types include compacts with different fuel particle types [TRISO UC_2 (WAR) and TRISO UC_2 (VSM) with BISO ThO_2], different fuel loadings (Th/U ratios of 10, 20, and 40), different shim types (Great Lakes Carbon Company H-451, Union Carbide Corporation TS-1240, and PoCo X-4029), and different shim loadings (0, 11, 23, and 36 vol %). The rods were fabricated by intrusion bonding (injection) with two different matrix types and cured in two different types of graphite (H-451 and TS-1240) at several conditions of firing temperature and firing rate (1600° and 1800°C; 10°C/min and 22°C/min). The complete test matrix for this study is shown in Table 9-20.

TASK 600: FUEL DESIGN AND PERFORMANCE MODELS

Subtask 620: Fuel Performance Models

Summary

The large body of experimental data presented this quarter shows that LHTGR fuel performance models (Ref. 9-3) provide a conservative description of fuel behavior over the range of expected LHTGR fast neutron exposures and kernel burnups in the temperature range 1040° to 2000°C. The favorable comparison between the performance model predictions and observed behavior justifies use of the models to predict LHTGR fuel behavior under all conceivable HTGR core operating conditions including those postulated for the maximum hypothetical fission product release (MHFPR) event.

In order to provide a concise summary, LHTGR performance model predictions and experimental fissile and fertile fuel performance data are plotted in Figs. 9-39 and 9-40 showing fuel failure as a function of equivalent LHTGR irradiation time and temperature. Equivalent LHTGR irradiation time is defined as the time required in a LHTGR to achieve burnups experienced by fuel during LHTGR capsule irradiation tests. Out-of-pile heating data are also included in Figs. 9-39 and 9-40. These data are included to show the effects of temperature on fuel failure after the fuel has experienced a given burnup.

The conclusions to be drawn for fissile and fertile fuel are the same. The first is that good performance has been demonstrated for both fuel types. The second is that the LHTGR fuel performance models presented in Ref. 9-12 provide a generally conservative description of LHTGR fuel performance at temperatures as high as 2000°C. The positive correlation between the fuel test results and LHTGR performance models justifies use of the models when predicting fuel behavior under any HTGR core operating environment, including the conditions postulated for the MHFPR event.

Introduction

Models that describe the performance of LHTGR fissile and fertile fuel have been developed from the results of test programs which demonstrate the effects of fast neutron exposure, kernel burnup, and temperature on the integrity of reference LHTGR fuel particle coatings (Ref. 9-3). A continuing test program is being carried out to verify the model predictions and to extend the data base that supports the models. An important application of the fuel performance models is in the analysis of the MHFPR event that is used for reactor siting evaluation. The MHFPR is a hypothetical, nonmechanistic event leading to fission product release from a reactor core that would result in potential hazards not exceeded by those from any accident considered to be credible (Ref. 9-13). The MHFPR analysis is used to evaluate potential reactor sites in order to limit maximum possible radiation doses experienced by individuals positioned at the exclusion area boundary or within the low population zone boundary and is intended to be analogous to the TID-14844 interpretation of the loss of coolant accident (LOCA) used to evaluate the engineered safety features and the sites for light water reactors. The MHFPR event postulated for the LHTGR is described in detail in Appendix 2A of the General Atomic Standard Safety Analysis Report (Ref. 9-14). The reactor would shut down during a MHFPR event; however, fuel temperatures would increase slowly with time due to decay heat, as shown in Fig. 9-41 (Ref. 9-14). Fuel performance at any time during a MHFPR event would be directly related to the temperatures within the core.

A comparison is presented of LHTGR fuel performance predictions made using the models described in Ref. 9-3 with experimental observations made since publication of Ref. 9-3. The experimental results described are from tests that were conducted over the range of operating conditions treated in Ref. 9-3. These test results show that the models provide a conservative description of fuel performance for reactor operating conditions expected for normal operation or postulated for a MHFPR event. These observations justify application of the LHTGR fuel performance models to studies of the MHFPR event.

Description of LHTGR Fuel

Development of the LHTGR has been directed toward the thorium cycle. This has led to a complete separation of the fissile (U-235) and fertile (Th-232) material in different coated particles (Ref. 9-15). The fissile fuel consists of TRISO coated, spherical UC_2 fuel kernels (Ref. 9-16). The TRISO coating is a four-layer composite that includes a buffer layer and three structural coatings consisting of a SiC layer sandwiched between two layers of pyrolytic carbon (PyC). The buffer layer is a low-density ($\sim$1.10 g/cm^3 PyC layer, which provides void volume that contains the gaseous fission product inventory built up during irradiation. The structural layers provide the primary barriers to fission product release. The coatings are designed for zero failure and manufactured to high quality standards, which results in less than 0.5% failure of coatings in fuel that is irradiated to peak LHTGR fissile fuel burnup (78% FIMA*) and fast neutron exposure [8×10^{21} n/cm^2 (E > 0.18 MeV)$_{HTGR}$] at 1250°C. In order to release gaseous fission products (including iodine), all three structural coating layers (inner PyC, SiC, and outer PyC) must fail. The nominal properties of reference LHTGR TRISO fissile fuel particles are given in Table 9-21.

Reference LHTGR fertile fuel consists of BISO coated, spherical ThO_2 kernels (Ref. 9-16). The BISO coating contains two layers; a low-density PyC inner layer (buffer) and a medium-to-high-density outer PyC layer. The buffer layer provides void volume for the accumulation of gaseous fission products while the outer PyC layer is the primary barrier to fission product release. The outer PyC layer on BISO fertile fuel must fail before gaseous fission product release (including iodine) will occur. The BISO coatings are designed and manufactured to limit fuel failure to less than 0.5% in fertile fuel that experiences peak LHTGR fertile burnup (7.5% FIMA) and fast neutron exposure [8×10^{21} n/cm^2 (E > 0.18 MeV)$_{HTGR}$] at temperatures less than 1250°C. The nominal properties of reference LHTGR fertile fuel particles are given in Table 9-21.

*FIMA = fissions per initial heavy metal atom.

The fissile and fertile particles are intimately blended into fuel rods in a random close-packed array. Graphite shim particles (about the size of BISO fertile particles) are blended with the fuel particle mixture in order to obtain close particle packing. The rods are right circular cylinders that are bonded together with a matrix consisting of carbonized pitch and graphite flour.

LHTGR Fuel Test Program

Out-of-Pile Testing. The performance of LHTGR fuel is being demonstrated by both irradiation testing and out-of-pile heating of unirradiated and irradiated fuel particles. The overall test program proposed to study the performance of LHTGR fuel is described in Ref. 9-17. The out-of-pile program is designed to study performance limiting phenomena that are controlled by temperature, time, and the chemistry of individual fuel particles. Examples of the phenomena studied are kernel migration (movement of kernels toward the hot side of a particle under the influence of a thermal gradient) and reactions between metallic fission products and the SiC coating on TRISO fissile fuel. Two test configurations are used. In the first, a thermal gradient is imposed across the particles to study fissile and fertile kernel migration and the kinetics of SiC - fission product reactions in TRISO fissile fuel. In the other configuration, particles are heated in the absence of a thermal gradient to study the kinetics of SiC - fission product reactions. Tests are conducted on both unirradiated and irradiated fuel particles to evaluate the effects of kernel burnup and the presence of fission products on the kinetics of these phenomena. The reasons for studying these phenomena out-of-pile are:

1. The tests are conducted at constant temperatures and fission product concentrations. During irradiation, temperatures vary slightly with time and burnup increases continuously with time, which makes it difficult to define the kinetics precisely.

2. The kinetics of these phenomena do not vary a great deal from particle to particle of a given type at a given irradiation

condition. It is therefore possible to describe the performance of a large number of particles by evaluating the performance of a few particles in an out-of-pile test.

Justification of the out-of-pile program is provided by the excellent agreement between data obtained in the program and results obtained from irradiation tests (Ref. 9-18). The results of out-of-pile tests are applicable to MHFPR analyses in that they demonstrate the effects of temperature on irradiated particle performance in the absence of a neutron flux.

Irradiation Testing. The irradiation test program is designed to study fuel performance during irradiation and to evaluate failure by mechanisms that are controlled by fast neutron exposure and kernel burnup. Examples are the irradiation stability of PyC coatings and pressure vessel failure of fuel particle coatings. One goal of the test program is to demonstrate that fuel failure is less than 0.5% after exposure to peak LHTGR fast neutron exposure and kernel burnup at 1250°C. Since these failure levels are very low, demonstration of performance requires large numbers of fuel particles (approximately 1000 particles per sample). Typical irradiation capsules contain 50,000 to 100,000 coated particles. Because of the spatial distribution of fluxes within any given reactor core, this large number of fuel particles will experience a range of irradiation conditions. Capsule tests are usually designed, however, so that approximately 10,000 fuel particles experience a single set of operating conditions.

The majority of the irradiation testing is done in the General Electric Test Reactor (GETR) and in the Oak Ridge Research Reactor (ORR). Operating conditions for the tests are chosen to be representative of HTGR operating temperatures, fast neutron exposures, and kernel burnups. The capsules are instrumented to allow direct measurements of operating temperature and fast and thermal neutron exposures.

Fuel performance during capsule testing is monitored by measuring in-pile fission gas release. During irradiation, release values are measured for several short-lived gaseous species (Kr-85m, Kr-87, Kr-88, Kr-89, Xe-135, and Xe-138) (Ref. 9-19). Performance analyses are generally made in terms of Kr-85m since it is an easy nuclide to detect and release of other gaseous species (e.g., Xe and I) can be related directly to the Kr-85m data (Ref. 9-20).

Capsule designs are different in the GETR and ORR. GETR capsules are small-diameter (2.5 cm) capsules. Two attractive features are: (1) operating temperatures can be varied by as much as 600°C during irradiation to provide precise temperature control as well as the possibility of LHTGR load-following transient simulation, and (2) they can be designed to contain several individual cells that operate independently of one another, thereby allowing operating temperature variation from cell to cell. GETR capsules typically contain six individual fuel test cells. A more complete description of GETR capsule design and construction is given in Ref. 9-19.

The primary difference between GETR and ORR capsules is that ORR capsules are approximately 6.2 cm in diameter. This allows irradiation of LHTGR fuel rods and graphite moderator in a configuration representative of a segment of a LHTGR fuel element. Fuel rods were recently irradiated in ORR (capsule P13Q, Ref. 9-21) in graphite bodies containing three fuel holes and four simulated coolant holes in order to demonstrate the performance of the fuel and graphite moderator. ORR capsules can also be separated into individual cells. Tests to date have been separated into two cells. A more complete description of ORR capsules is provided in Ref. 9-17.

Fuel Performance Models Used in MHFPR Analyses

Early GA Models. Fuel performance models initially proposed for LHTGR MHFPR analysis (Ref. 9-22) evolved from limited data obtained during early testing of FSV type fuel. Schematic drawings of the models for fissile and fertile fuel are shown in Figs. 9-42 and 9-43, respectively. These figures

show the relationship between time (in an operating HTGR) and temperature assumed for the initiation and completion (100%) of fuel failure. These models were initially provided for MHFPR analyses because (1) they were known to be conservative, and (2) LHTGR fuel performance models (Ref. 9-3) were not yet complete.

The reference fissile and fertile fuel types chosen for FSV were TRISO coated $(Th/U)C_2$ and TRISO coated ThC_2, respectively. The performance of production line fuel was recently demonstrated in capsule F-30, which was the proof test for FSV fuel. Fissile and fertile fuels were irradiated to kernel burnups and fast neutron exposure beyond the maximum exposures expected in the FSV reactor. Average temperatures for the test samples ranged from 825° to 1250°C. Maximum temperatures during the course of the test ranged from 1150° to 1520°C. Maximum fuel failure fractions observed during postirradiation examination (PIE) and estimated from in-pile fission gas release data from the test capsule were less than 1% (Ref. 9-23). Comparison of these results with the performance predictions provided in Figs. 9-42 and 9-43 for 4-year-old LHTGR fuel shows that the early fuel performance models are extremely conservative. Results to be provided later in this discussion show similar excellent performance for reference LHTGR fuel. Based on this initial comparison, it is clear that the early performance models shown in Figs. 9-42 and 9-43 do not adequately describe the performance capabilities of HTGR fuels. As will be shown, recent LHTGR performance models (Ref. 9-3) provide a more accurate (but still conservative) estimate for fuel performance that justifies their use in any MHFPR analyses.

NRC Models. Fuel performance models used by NRC to predict fuel failure during a MHFPR event represent an extremely conservative interpretation of the GA models illustrated in Figs. 9-42 and 9-43. In the MHFPR analysis used to evaluate the site for Summit Power Station Units 1 and 2 (Ref. 9-24), NRC assumed that 100% failure of LHTGR fuel occurred at the beginning of the partial failure region shown in Figs. 9-42 and 9-43.*

*Discussions held during a meeting of GA, NRC, and other interested parties to discuss MHFPR analyses, Bethesda, Md., February 6, 1975.

Data provided in this report show that this is an overly conservative assumption.

LHTGR Fuel Performance Models. Models describing the performance of LHTGR fissile and fertile fuel were recently prepared (Ref. 9-3). The fuel failure mechanisms discussed were identified and characterized by the LHTGR in-pile and out-of-pile test programs. The models given in Ref. 9-3 are applicable to all LHTGR operating conditions including the hypothetical MHFPR event. Each mechanism is discussed briefly below and related to the MHFPR analysis. It is shown that only two of the potential fuel failure mechanisms would be important during a MHFPR event.

One component of predicted fuel failure is particles having a missing or defective coating layer. Because of the large number of particles in a LHTGR core, the presence of a small fraction of particles having a single missing or defective coating layer is statistically unavoidable. The effect of these particles on fuel performance during normal reactor operation is discussed in Refs. 9-3 and 9-25. The number of fuel particles having a missing or defective coating is limited by LHTGR fuel specifications to 0.3% of the TRISO UC_2 fissile fuel and 0.2% of the BISO ThO_2 fertile fuel in a reactor core. Failure of this small fraction of fuel would have a negligible impact on the fission product release predicted as fuel temperatures approach the maximum values indicated in Fig. 9-41. Models used to describe the performance of fuel having a missing or defective coating are therefore not discussed.

Kernel migration is another phenomenon that can cause fuel coating failure. This was first recognized in carbide fuel kernels (Ref. 9-26). When placed in a thermal gradient, carbon migrates through the fuel kernels from the hot to the cool side and deposits at the buffer kernel interface on the cool side of the kernel. The net result is that kernels are displaced toward the hot side of coated particles. Failure is assumed to occur by this mechanism if a migrating kernel contacts the inner PyC coating on TRISO fuel or the outer PyC coating on BISO fuel. The rates of

kernel migration for UC_2 and ThO_2 fuel kernels are characterized in Refs. 9-1 and 9-27. The driving force for kernel migration is a thermal gradient (Ref. 9-1). Since the graphite moderator and the fuel would equilibrate at the same temperature during a MHFPR event, there would be no temperature gradient across the fuel. In the absence of a thermal gradient, no kernel migration will occur; consequently, no migration-induced coating failure would occur during a MHFPR event.

Two failure mechanisms would be active during a MHFPR event. These are pressure vessel failure of TRISO fissile and BISO fertile fuel and failure of TRISO fissile fuel from reactions between the SiC layer and metallic fission products. Pressure vessel failure is a function of fast neutron exposure, kernel burnup, and temperature. As burnup increases, the pressure of gaseous fission products contained by particle coatings increases. This causes tensile stresses within the particle coatings. Due to the distribution of kernel and coating dimensions within a batch of fuel particles, there will be a wide distribution of coating stresses at any given irradiation condition (Ref. 9-28). Failure by the pressure vessel mechanism will begin when the high stress tail of the stress distribution exceeds the failure stress of the individual coatings. At the onset of a MHFPR event, the pressure vessel failure fraction would be characterized by the irradiation condition of the fuel just prior to the beginning of the event (<1% failure). The pressure vessel failure fraction would not change until temperatures (and therefore fission gas pressures) exceed those experienced by the fuel just prior to the MHFPR event. Because of the very broad stress distribution in the particle coatings, pressure vessel failure would occur gradually over a wide range of temperatures.

Failure by this mechanism is well characterized during irradiation testing. The effects of fluence, burnup, and temperature are illustrated by each irradiation test that is conducted. The irradiation tests are conducted over a 6- to 12-month period. The fuel, however, experiences peak HTGR fast neutron exposure and kernel burnup during the tests. Since (1) the pressure vessel phenomenon is dependent only on fluence, burnup,

and temperature, and (2) fuel experiences peak HTGR conditions during irradiation, pressure vessel performance data obtained from these irradiation tests provide a good demonstration of the low pressure vessel failure fractions expected during the 4-year residence of fuel in a LHTGR. Comparison of recent irradiation results with performance predicted using models presented in Ref. 9-3 shows that the LHTGR performance models provide a good description of pressure vessel failure.

The initial temperature rise during a MHFPR would occur over a short period of time relative to the average fuel age [i.e., 2 hr after irradiation, peak temperatures would be approximately 1500°C; 4 hr after initiation, peak temperatures would reach 1800°C (see Fig. 9-41)]. Failure of TRISO UC_2 fissile fuel from reactions between the SiC layer and metallic fission products would become important if temperatures were high enough and rates of reaction were sufficiently high that failure would occur in a matter of hours. Data will be presented that show that the description of TRISO UC_2 coating failure by fission product SiC reactions provided in Ref. 9-3 is conservative relative to performance observations made during out-of-pile test conditions similar to those postulated for a MHFPR event. The test data prove that failure due to SiC - fission product reactions in TRISO fuel would not occur during the first 2 hr of a MHFPR event.

Comparison of Predicted and Observed Performance of LHTGR Fuel

One goal of the LHTGR fuel test program is to provide data that will demonstrate the validity of LHTGR fuel performance models (Ref. 9-3) and justify using them to predict fuel behavior during (1) normal operation, (2) temperature excursions, (3) postulated credible accidents, and (4) the MHFPR event. Data are provided below that clearly demonstrate HTGR fuel performance capabilities at peak LHTGR fast neutron exposure and kernel burnup and temperatures in the range 1040° to 2000°C.

Irradiation Performance of Unbonded TRISO UC_2 Fuel Particles. A large number of fuel particles are tested as "unbonded" particle samples in each

irradiation capsule. The term "unbonded" refers to particle samples not irradiated in fuel rods. These samples are irradiated in trays and are recoverable for postirradiation examination and heating. This type of test allows separate examination of fissile and fertile fuel behavior.

A summary of observations on unbonded TRISO UC_2 irradiation samples is included in Table 9-22 (Ref. 9-19). Samples that either failed to meet the TRISO coating design basis (Ref. 9-28) or had one or more coatings purposely designed to evaluate LHTGR fuel particle specification limits are not included. The data were obtained from fuel capsules P13L, P13M, P13N, P13P, P13R, and P13S. Results from all unbonded particle samples in each test that satisfy the LHTGR TRISO UC_2 pressure vessel design basis are included in Table 9-22, as are results from all reference LHTGR TRISO UC_2 fuel that has been irradiated in unbonded particle tests. Results from selected samples that do not meet the TRISO particle pressure vessel design basis are included to illustrate the conservative nature of the pressure vessel design.

As many as three failure estimates are presented for each sample. The most reliable is based on PIE fission gas release measurements, which provide a direct indication of exposed fissionable material. When fission gas release values are not available, data obtained from metallographic examination of the SiC layer are used to describe fuel performance. Comparison of metallographic and fission gas release failure determinations on samples that have been examined by both techniques shows that the metallographic values overestimate failure that would result in fission gas release.

The range of irradiation exposures for the samples described in Table 9-22 exceed peak HTGR fast neutron exposure and approach peak burnup conditions in the temperature range 850° to 1600°C. The samples include 6055 coated particles; on an average, failure that would cause fission gas release was observed in 0.13% of the particles. This is clear evidence that LHTGR fissile fuel can experience fast neutron exposures and kernel burnups at temperatures as high as 1600°C with a survival rate as high as 99.8%.

Irradiation Performance of Unbonded BISO ThO_2 Fuel Particles. Capsules P13R and P13S were the first capsules that included a large number of BISO ThO_2 particles as unbonded test samples. Approximately 23,000 fertile fuel particles were irradiated in these two capsules as unbonded test samples (Ref. 9-29). The fertile fuel in these tests was irradiated at 1075°C to fast neutron exposures of 11 to 12 x 10^{21} n/cm^2 (E > 0.18 MeV)$_{HTGR}$ (peak HTGR exposure is 8 x 10^{21} n/cm^2) and kernel burnups as high as 5% FIMA, which is the average fertile particle burnup in an HTGR core (peak fertile burnup is 7.5% FIMA). Particle test variables included particle shape, coating thickness, and outer PyC properties including density, coating rate, and anisotropy.

Results of the P13R and P13S tests will be used to establish LHTGR fuel specification limits for BISO fertile fuel. Analysis of the PIE data is not yet complete; however, early results available on three samples (approximately 3000 coated particles) clearly satisfy specification requirements. Irradiation conditions and PIE fission gas release values for these samples are summarized in Table 9-23. Experimental observations have shown the fission gas release per failed particle to be 2 x 10^{-2} for Kr-85m at 1100°C (Ref. 9-30) for unbonded particles. Using this value for R/B per failed particle, the average failure observed in the three samples described in Table 9-23 is 0.05%. Because of the high fast neutron exposure experienced by these samples [$\sim$12 x 10^{21} n/cm^2 (E > 0.18 MeV)$_{HTGR}$], the LHTGR fuel performance models given in Ref. 9-3 cannot be applied directly to predict failure. Predicted failure, however, would have been 0.5% at a fast neutron exposure of 8 x 10^{21} n/cm^2.

The properties of the outer PyC layers in five other unbonded BISO ThO_2 particle samples irradiated in P13R and P13S (approximately 5000 coated particles) are slightly outside current guide lines for the specification limits. Gaseous fission product release measured during PIE of these samples was equivalent to the fission gas release resulting from failure of 0.6% of the particles. The performance of these fuel particles is mentioned here as an indication of the good performance expected even

from those fuel particles with coatings whose properties fall outside LHTGR specification limits.

Irradiation Performance of Fuel Rod Samples Containing Reference LHTGR Fissile and Fertile Fuel. In addition to the unbonded particle samples, capsules P13R and P13S contained 40 fuel rod samples irradiated in eight individual cells (Ref. 9-29). The cells were designed to operate continuously at fuel rod centerline temperatures of 1100°, 1300°, or 1500°C. Final thermal analysis of these capsules is under way, and it appears that actual operating temperatures were close to the design temperatures. One cell (P13S, cell 1) was thermal cycled periodically from 1100° to 1500°-1700°C to simulate the effect of temperature transients on LHTGR fuel performance. Fast neutron exposures ranged from 4.1 to 12.2 x 10^{21} n/cm^2 $(E > 0.18\ MeV)_{HTGR}$. Fissile fuel kernel burnups as high as 74% FIMA were experienced, while burnups in the range 2.6 to 5.6% FIMA were experienced by the fertile fuel. Capsules P13R and P13S are currently undergoing PIE. Fuel rod performance data are not complete; however, analysis of in-pile fission gas release data can be used to demonstrate the excellent performance capabilities of LHTGR fuel, as well as the conservative nature of LHTGR fuel performance models. The PIE is scheduled for completion in the near future, and the results will be described in Ref. 9-31.

Comparisons between fission gas release measured during P13R and P13S capsule operation and that predicted using LHTGR fuel performance models were recently described in detail (Ref. 9-32). The steps used to predict fission gas release were:

1. Calculate fissile (f_{fis}) and fertile (f_{fer}) fuel failure fractions using models given in Ref. 9-3.

2. Determine the fraction of fissions in fissile (F_{fis}) and fertile (F_{fer}) fuel.

3. Calculate the fraction of fissions occurring in failed fuel (F_{tot}) using

$$F_{tot} = F_{fis} f_{fis} + F_{fer} f_{fer} \quad .$$

4. Predict the fission gas release from the product of F_{tot} and fission gas release (R/B per failed particle) at the test temperature.

The fuel performance models account for effects of temperature on failure. The value for fission gas release per failed particle also varies with temperature. The temperature variation for Kr-85m (corrected version of Eq. B-1 in Ref. 9-30) is expressed as:

$$\frac{(R/B)_T}{(R/B)_0} = 0.073 + 97.39 \exp(-12{,}700/RT) \quad , \qquad (9\text{-}1)$$

where $(R/B)_T$ = fission gas release (Kr-85m) at temperature T,
$(R/B)_0$ = fission gas release (Kr-85m) at 1373°K,
R = gas constant (1.9869 cal/mole/°K,
T = temperature, °K.

Experimental observations indicate that the fission gas release per failed particle in a fuel rod is 0.005 for Kr-85m at 1100°C (Ref. 9-31). However, in order to be conservative, the Kr-85m fission gas release per failed particle is assumed to be 0.02 at 1100°C when estimating LHTGR core fission gas release values from predicted fuel failure fractions. In order to demonstrate the conservatism of the core design studies, a Kr-85m fission gas release of 0.02 per failed particle at 1100°C was assumed when predicting fission gas release values for capsule P13R and P13S fuel rod cells.

Predicted values of fission gas release were calculated for P13R and P13S fuel cells that operated continuously at design peak temperatures of

about 1100°C (volume average temperature 1040°C) and 1500°C (volume average temperature 1440°C). Volume average temperatures were used to estimate failure fractions and fission gas release. Using Eq. 9-1 and assuming a release fraction of 0.02 at 1100°C, the fission gas releases (Kr-85m) per failed particle at 1040° and 1440°C are 0.016 and 0.048, respectively. The primary failure mode under these operating conditions is pressure vessel failure. The relationships between measured and predicted fission gas release values are shown in Figs. 9-44 and 9-45. The predictions are conservative relative to the observed values for fission gas release in both cases, which suggests that the pressure vessel failure models given in Ref. 9-3 are conservative to temperatures as high as 1440°C.

Cell 1 of capsule P13S was thermal cycled at the beginning of each GETR operating cycle in order to demonstrate the effect of thermal transients on fuel performance. The nominal fuel operating temperature was 1100°C. A typical thermal cycle is shown schematically in Fig. 9-46. Temperatures in the range 1500° to 1700°C were experienced during each thermal cycle. A comparison between measured and predicted fission gas release values is shown in Fig. 9-47. The data in Fig. 9-47 show that the models are capable of predicting fuel performance at temperatures as high as 1700°C.

The maximum failure fractions predicted for the three fuel cells discussed above were about 1% at peak temperatures in the range 1440°C (cell 5, P13S) to 1700°C (cell 1, P13S). It is interesting to note (Fig. 9-41) that peak fuel temperatures do not reach 1700°C until 3.4 hr after the initiation of a MHFPR event, while average fuel temperatures do not reach 1700°C for 7.4 hr after the initiation of the event. These data suggest, therefore, that failure values should be 1% or less during the first 3.4 to 7.4 hr after MHFPR initiation.

The in-pile fission gas release values from P13R and P13S fuel rod cells can be used to estimate failure fractions for fissile fuel during the early stages of irradiation. When a fuel rod containing fissile and

fertile fuel is initially subjected to a neutron flux, all of the fissions occur in the fissile fuel. As U-233 is bred from Th-232 and the U-235 burns out of the fissile fuel, the fraction of fissions that occurs in the fertile fuel increases. In capsules P13R and P13S, the fraction of fissions occurring in the fissile fuel is greater than 50% for fast neutron exposures $<4 \times 10^{21}$ n/cm^2 $(E > 0.18 \text{ MeV})_{HTGR}$. Fissile fuel failure fractions were estimated from P13R and P13S in-pile fission gas release data assuming that all fission gas release detected for fast neutron exposures $<4 \times 10^{21}$ n/cm^2 was the result of fissile fuel failure. In order to provide a realistic estimate of failure, it was assumed in these calculations that the Kr-85m R/B per failed particle is 0.005 at 1100°C. Equation 9-1 was used to correct this fission gas release value for specific operating temperatures. The calculated failure fractions are given in Table 9-24. Failure values are given for fast neutron exposures of 1, 2, 3, and 4×10^{21} n/cm^2 for cells operating at a constant fuel rod volume average temperatures. Failure values are given after each thermal cycle for P13S, cell 1. Each cell contained approximately 5000 fissile fuel particles; the failure fractions imply failure of 1 to 3 particles per cell at most.

All of the fuel particles in P13R and P13S fuel rods meet dimensional requirements for LHTGR fissile and fertile fuel. However, coating properties (i.e., density, coating rate, and anisotropy) of the particles in only 20% of the rods satisfy LHTGR specifications. The off-specification material was included to evaluate its effect on fuel performance and fission gas release. The performance estimates described above, therefore, overestimate failure fractions for reference fissile fuel. Near the end of the irradiation, fission gas release from the fuel included to evaluate the impact of off-specification fuel swamped the fission gas release from samples containing reference fuel. This is being confirmed by PIE fission gas release measurements conducted on individual fuel rods (Ref. 9-31) and precludes use of the in-pile data to estimate fertile fuel failure.

Postirradiation fission gas release measurements have been made at 1100°C on P13R and P13S fuel rods containing fuel particles meeting preliminary LHTGR fuel product specifications (Table 9-25). The apparent fertile particle failure fractions in these samples increase from 0.2 to 1.2% as the irradiation temperature increases from 1040° to 1600°C.

Out-of-Pile Heating Observations. Data are available from out-of-pile heating studies conducted on irradiated LHTGR fuels that illustrate the capabilities of the fuel at temperatures in excess of 1600°C. Two samples of irradiated TRISO UC_2 fissile fuel were recently heated at 1800°C (20 particles per sample) in order to determine failure as a function of time. The samples met preliminary LHTGR fuel specifications with the exception that the average buffer thickness was only 85 μm (the reference LHTGR buffer thickness is 100 μm). The postirradiation heating cycle is given in Table 9-26. Performance during these tests was monitored by measuring Cs-137 and Kr-85 release. Release of Cs-137 occurred after penetration of the SiC layer by metallic fission products. Release of Kr-85m occurred after failure of the SiC and outer PyC layers. It was assumed when calculating failure from the release data that 100% Kr-85 release occurred upon failure of a coating at 1800°.

One sample had been irradiated in capsule P13P to 61% FIMA and a fast neutron exposure of 6.0×10^{21} n/cm^2 $(E > 0.18 \text{ MeV})_{HTGR}$ in the temperature range 1350° to 1630°C (Ref. 9-19). The Kr-85 releases predicted using LHTGR performance models (assuming 100% release per failed particle) and measured during heating at 1800°C are compared in Fig. 9-48 (Ref. 9-32). The models (Ref. 9-3) are clearly conservative even under these very severe conditions, which are similar to the fuel environment postulated 5 to 10 hr after initiation of a MHFPR event.

The other sample heated at 1800°C had been irradiated to about 30% FIMA in FTE-14. A comparison between measured and predicted Kr-85 release is given in Fig. 9-49 for the first 220 hr of the 1800°C test. In this case, the total Kr-85 release after 990 hr at 1800°C was negligible,

implying zero failure. The performance models are also clearly conservative in this instance.

These data provide a direct demonstration of the performance expected from irradiated TRISO UC_2 fuel during a MHFPR event. The experimental conditions duplicate the environment proposed for the postulated MHFPR event (i.e., high temperatures and high burnup in the absence of a neutron flux and thermal gradient). The data show that essentially no failure should be expected in fissile fuel having burnups less than 30% FIMA until temperatures exceed 1800°C, while failures on the order of 20% may occur in the same temperature range for higher burnup fuel during a MHFPR event.

Out-of-pile tests have also been conducted on irradiated BISO ThO_2 fuel having reference dimensions. Particles were heated from 1200° to 2000°C over the period of a week in order to determine the temperature at which failure would occur. The actual thermal history was: 20 hr at 1200°C, 4 hr to increase from 1200° to 1400°C, 20 hr at 1400°C, 4 hr to increase from 1400° to 1600°C, 20 hr at 1600°C, 4 hr to increase from 1600° to 1800°C, 20 hr at 1800°C, 4 hr to increase to 2000°C, hold at 2000°C for 2 hr, and cool to room temperature. Failure was monitored by measuring the Kr-85 release. A total of 40 particles irradiated in capsule HT-17 [burnup 1.7 to 2.2% FIMA, fast neutron exposure 2.8 to 3.7 x 10^{21} n/cm^2 $(E > 0.18 \text{ MeV})_{HFIR}$] and 40 particles irradiated in HT-18 [burnup 6.8 to 7.8% FIMA, fast neutron exposure 6.4 to 7.5 x 10^{21} n/cm^2 $(E > 0.18 \text{ MeV})_{HFIR}$] were heated. Failure (percent) values measured during the tests and predicted using fuel performance models given in Ref. 9-3 are included in Table 9-27.

The out-of-pile results obtained on low burnup fuels showed much better performance than predicted using the LHTGR fuel performance models given in Ref. 9-3 (i.e., no observed failure at 2000°C when 100% failure was predicted). The high burnup samples showed slightly higher failure values than predicted for temperatures $\leq$1800°C; however, at 2000°C less failure was observed than predicted using the models in Ref. 9-3 (60% observed, 100% predicted).

REFERENCES

9-1. "HTGR Fuels and Core Development Program Quarterly Progress Report for the Period Ending May 31, 1975," ERDA Report GA-A13444, General Atomic Company, June 30, 1975.

9-2. "HTGR Fuels and Core Development Program Quarterly Progress Report for the Period Ending August 31, 1975," ERDA Report GA-A13592, General Atomic Company, September 30, 1975.

9-3. Smith, C. L., "Fuel Particle Behavior Under Normal and Transient Conditions," USAEC Report GA-A12971 (GA-LTR-15), General Atomic Company, October 1, 1974.

9-4. Otwell, R. L., "Peach Bottom FTE-6 and -15 Temperatures," General Atomic unpublished data, October 6, 1975.

9-5. Scheffel, W. J., "Peach Bottom Core 2 and Test Element Operations To Date," Gulf General Atomic unpublished data, August 1973.

9-6. Lane, R. K., "Peach Bottom Experimental Results Showing the Effect of Partial and Full Control Rod Insertion on the Axial Flux Shape," General Atomic unpublished data, March 14, 1968.

9-7. Beavan, A. L., and R. J. Price, "Graphite Data Package for Analysis of Peach Bottom Test Elements," General Atomic unpublished data, November 26, 1974.

9-8. Lefler, W. L., "Peach Bottom Core 2 Measured Temperature Histories," General Atomic unpublished data, June 18, 1975.

9-9. Otwell, R. L., "Peach Bottom FTE-3, -4 and -14 Temperatures," General Atomic unpublished data, April 23, 1975.

9-10. Mayweather, L. I., "Post-Irradiation Examination Procedure for Peach Bottom Test Element FTE-6," General Atomic PIE Procedure 278-PB-11, May 7, 1975.

9-11. Price, R. J., and L. A. Beavan, "Final Report on Graphite Irradiation Test OG-1," USAEC Report GA-A13089, General Atomic, August 1, 1974.

9-12. Johnson, W. R., et al., "Postirradiation Examination of Capsules HT-24 and HT-25," ERDA Report GA-A13486, General Atomic, September 15, 1975.

9-13. United States Atomic Energy Commission Rules and Regulations, Title 10 - Atomic Energy; Part 100, Reactor Site Criteria, 1962.

9-14. "GASSAR-6," General Atomic Standard Safety Analysis Report, Appendix 2A, NRC Docket STN 50-535, February 5, 1975.

9-15. Dahlberg, R. C., et al., "HTGR Fuel Cycle Summary Description," General Atomic Report GA-A12801 (Rev.), January 21, 1974.

9-16. Gulden, T. D., et al., "Design and Performance of Coated Particle Fuels for the Thorium Cycle HTGR," Gulf General Atomic Report GA-A12628 (Rev.), January 24, 1974.

9-17. "Fuel Development Program Plan for the Steam Cycle HTGR," General Atomic Report GA-A13660, to be published.

9-18. "GASSAR-6," General Atomic Standard Safety Analysis Report, NRC Docket STN 50-535, February 5, 1975, Answer to Question 241.16k, to be published.

9-19. Harmon, D. P., and C. B. Scott, "Development and Irradiation Performance of LHTGR Fuel," General Atomic Report GA-A13173, to be published.

9-20. Vanslager, F. E., et al., "Fission Product Transport in HTGR Systems - A Summary," Gulf General Atomic Report GA-A10073, April 22, 1970.

9-21. Smith, C. L., "Preirradiation Report: Fuel Materials for Irradiation, P13Q," ERDA Report GA-A13265, General Atomic, June 13, 1975.

9-22. "Delmarva Power and Light, Preliminary Safety Analysis Report," Appendix C, USAEC Dockets 50-450 and 50-457.

9-23. Scott, C. B., and D. P. Harmon, "Postirradiation Examination of Capsule F-30," General Atomic Report GA-A13208, April 1, 1975.

9-24. "Safety Evaluation of the Summit Power Station Units 1 and 2," NRC Dockets 50-450 and 50-451, January 1975.

9-25. "GASSAR-6," General Atomic Standard Safety Analysis Report, NRC Docket STN 50-535, February 5, 1975, Answer to Question 241.21j-15 (Amendment 6, December 3, 1975), Answer to Questions 241.21j-20,21 (to be published).

9-26. Gulden, T. D., "Carbon Thermal Diffusion in the UC_2-Carbon System," J. Am. Ceram. Soc. 55, 14 (1972).

9-27. Stansfield, O. M., et al., "Kernel Migration in Coated Carbide Fuel Particles," Nucl. Tech. 25, 517 (1975).

9-28. Gulden, T. D., et al., "The Mechanical Design of TRISO-Coated Particle Fuels for the Large HTGR," Nucl. Tech. 16, 100 (1972).

9-29. Young, C. A., and D. P. Harmon, "Preirradiation Report: Fuel Materials for P13R and P13S Irradiation Capsules," USAEC Report GA-A13026, General Atomic, November 1974.

9-30. Haire, M. J., and D. W. McEachern, "Gaseous Radioactivity Levels in the Primary Coolant of an HTGR," General Atomic Report GA-A12946 (GA-LTR-14), October 1, 1974.

9-31. Scott, C. B., and D. P. Harmon, "Postirradiation Examination of Capsules P13R and S," to be published.

9-32. "GASSAR-6," General Atomic Standard Safety Analysis Report, NRC Docket STN 50-535, February 5, 1975, Answer to Questions 241.21j-8, 11, and 13 (Amendment 6, December 3, 1975).

TABLE 9-1
FUEL CONTAINED IN FTE-6

Body	Hole	Fissile Particle	Fertile Particle
1, 2, 3	1, 2	UO_2 TRISO	ThO_2 BISO
1, 2, 3	3, 4	$(Th,U)C_2$ [(a)] TRISO	ThC_2 BISO
1, 2, 3	5, 6	$(Th,U)C_2$ TRISO	ThC_2 TRISO
1, 2, 3	7, 8	UC_2 TRISO	ThC_2 BISO

(a) Th/U ratio = 2.75.

TABLE 9-2
FTE-6 BURNUP AND FLUENCE

	Average	Peak
FIMA fissile, %	39.07	46.49
FIMA fertile, %	1.11	1.68
FIMA total, %	11.20	13.63
Fast fluence, $x10^{21}$ n/cm^2 (E > 0.18 MeV)	2.28	3.01

TABLE 9-3
FTE-6 FUEL ROD TEMPERATURES

Fuel Rod No.	Mean Active Core Position (in.)	Irradiation Temperature (°C)		
		Average	Maximum	Minimum
Body 1				
1	1	538	645	449
2	3	562	673	466
3	5	591	710	485
4	7	629	761	506
5	9	703	862	550
6	11	783	971	598
7	13	866	1083	649
8	15	944	1188	698
9	17	996	1256	731
10	19	1037	1308	757
11	21	1071	1351	780
12	23	1100	1387	799
13	25	1100	1386	798
14	27	1080	1361	784
Body 2				
1	32	1097	1380	797
2	34	1160	1458	843
3	36	1206	1523	876
4	38	1226	1568	889
5	40	1242	1612	900
6	42	1257	1637	911
7	44	1269	1650	921
8	46	1276	1656	928
9	48	1275	1651	930
10	50	1271	1641	930
11	52	1263	1626	928
12	54	1251	1607	924
13	56	1210	1548	897
14	58	1147	1464	855
Body 3				
1	63	1131	1442	847
2	65	1158	1447	874
3	67	1166	1438	886
4	69	1146	1397	877
5	71	1128	1371	868
6	73	1110	1346	859
7	75	1092	1321	850
8	77	1073	1294	840
9	79	1055	1270	831
10	81	1045	1257	827
11	83	1049	1263	832
12	85	1070	1291	848
13	87	1072	1310	848
14	89	1061	1323	837

TABLE 9-4
FTE-6 SPINE SAMPLE TEMPERATURES

Spine Sample	Mean Active Core Position (in.)	Temperature (°C)		
		Average	Maximum	Minimum
Boronated graphite 4465-57-1	2.93	600	680	510
Diffusion 23	5.46	630	720	530
Diffusion 40	6.72	660	750	560
Diffusion 51	7.98	700	800	590
Diffusion 60	9.24	740	840	610
Diffusion 13	10.50	780	900	640
Fission product release 73P	11.76	900	1060	720
Fission product release 56P	13.02	940	1100	760
Boronated graphite 4465-57-2	15.55	1050	1230	830
Boronated graphite 4465-57-3	19.35	1120	1310	890
Diffusion 17	21.88	1170	1370	930
Diffusion 33	23.14	1190	1390	950
Diffusion 19	24.40	1180	1390	940
Diffusion 26	25.66	1170	1370	930
Fission product release 122P	33.35	1200	1410	960
Fission product release 168P	34.60	1290	1510	1020
Advanced fuel rod 3C	37.23	1310	1550	1030
Advanced fuel rod 3B	41.23	1370	1630	1060
Advanced fuel rod 3A	45.23	1390	1650	1080
Fission product release NB-4	47.86	1390	1650	1080
Fission product release 12P	49.11	1390	1650	1080
Fission product release NB-7	50.36	1380	1640	1080
Fission product release 29P	51.61	1370	1630	1070
Fission product release NB-11	52.86	1360	1610	1070
Fission product release 44P	54.11	1350	1600	1060
Fission product release NB-15	55.36	1340	1580	1050
Fission product release 148P	56.61	1260	1490	990
Thermal stability 1-M	66.51	1240	1440	1000
Thermal stability 1-N	72.27	1180	1360	960
Thermal stability 2-18	75.77	1140	1310	940
Thermal stability 2-24	77.02	1130	1290	930
Thermal stability 2-30	78.27	1120	1280	920
Thermal stability 2-6	79.52	1090	1250	900
Thermal stability 2-12	80.77	1090	1250	910
Boronated graphite 4465-57-4	83.29	1100	1260	910
Boronated graphite 4465-57-5	87.09	1130	1290	930

TABLE 9-5
THERMOCOUPLE RESISTANCE DATA

Thermocouple Type (Accuracy: ±0.2Ω)	+ to Ground Circuit (Ω)		- to Ground Circuit (Ω)		Loop (Ω)	
	Pre-Irrad.	Post-Irrad.	Pre-Irrad.	Post-Irrad.	Pre-Irrad.	Post-Irrad.
Thermocouple A W - 3% Re/W - 25% Re	NA[a]	6	NA	15	NA	20
Thermocouple B C/A	NA	35	NA	15	NA	50

[a] NA = not applicable.

TABLE 9-6
FTE-6 SLEEVE MEASUREMENTS

Sleeve identity number: 3241 Bottom connector number: 352 Sleeve number assigned to the assembly: 876	Pre-Irrad.[a] (in.)	Post-Irrad. (in.)	ΔD/D (%)
Length: accuracy	±0.03125	±0.03125	+0.043
Overall length of element (including thermocouple sheath)	144.796	143.893	-0.628
Sleeve O.D. at joint to bottom connector		3.488	+0.09
Sleeve O.D. at 24 in. above joint		3.480	-0.14
Sleeve O.D. at 48 in. above joint	3.485 ±0.005[b]	3.478	-0.20
Sleeve O.D. at 72 in. above joint		3.478	-0.20
Sleeve O.D. at 96 in. above joint		3.473	-0.34
Sleeve O.D. at cut near the upper reflector		3.486	+0.03
Sample mean		3.4805	-0.1267
Standard deviation		0.0056	
95/95 confidence limit			
Total error			
Sleeve I.D. at cut near the upper reflector		2.750	-0.07
Sleeve I.D. at cut near the bottom reflector	2.752 ±0.002[c]	2.749	-0.11
Sleeve I.D. at approximate mid-point		NA	---
Sample mean		2.7495	-0.09
Standard deviation		0.0007	0.0283
95/95 confidence limit			
Total error			

[a] The sleeves were Quality Assurance examined at the source and found to meet requirements. There is no record of actual dimensions.

[b] Sleeve O.D. per drawing 11666 is 3.485 ± 0.005 in.

[c] Sleeve I.D. per drawing 11666 is 2.752 ± 0.002 in.

TABLE 9-7
FUEL BODY DATA FOR FTE-6 BODY 1, FUEL BODY 44, LOC 2513[a]

	Pre-Irrad. x_1	Post-Irrad. x_2					$\Delta x = x_2 - x_1$	$\Delta x/x_1$ (%)
Weight of body, g								
Accuracy								
Total	4870.00	4862.25					-7.75	-0.1591
Sum of components (less fuel)	4842.21							
Length of body, in.								
Systematic error								
Standard deviation								
0°	31.108	31.079					-0.029	-0.093
90°		31.0625						
Sample mean	31.108	31.0708						
Standard deviation		0.0117					--	--
95/95 confidence limit								
Total error								
		Holes 1 and 5 x_2	Holes 2 and 6 x_2	Holes 3 and 7 x_2	Holes 4 and 8 x_2	Mean $\bar{x}_2$		
Outside diameter, in.								
Systematic error								
Standard deviation								
Location								
31		2.734	2.734	2.733	2.734	2.73375		
Top 29	2.740	2.736	2.735	2.735	2.7345	2.73513	-0.00487	-0.1777
25		2.7335	2.733	2.732	2.732	2.73263		
21		2.736	2.733	2.733	2.7345	2.73413		
17		2.7365	2.736	2.736	2.735	2.73588		
Center 15	2.740	2.736	2.737	2.735	2.736	2.736	-0.004	-0.1460
11		2.737	2.737	2.737	2.737	2.737		
7		2.738	2.737	2.737	2.737	2.73725		
Bottom 3	2.740	2.737	2.737	2.737	2.737	2.737	-0.003	-0.1095
1		2.737	2.737	2.737	2.737	2.737		
Sample mean	2.740	2.7361	2.7356	2.7352	2.7354	2.7356	-0.00396	-0.1444
Standard deviation	--	0.0014	0.0017	0.0019	0.0017	0.0017	-0.00094	-0.0341
95/95 confidence limit								
Total error								

[a] Orientation during unloading:

TABLE 9-8
FUEL BODY DATA FOR FTE-6 BODY 2, FUEL BODY 43, LOG 738[a]

	Pre-Irrad. x_1	Post-Irrad. x_2					$\Delta x = x_2 - x_1$	$\Delta x/x_1$ (%)
Weight of body, g								
Accuracy								
Total	5200.00	5210.00					+10.0	+0.1923
Sum of components (less fuel)	5186.765							
Length of body, in.								
Systematic error								
Standard deviation								
0°	31.108	30.8845					-0.2235	-0.7185
90°		30.8970						
Sample mean	31.108	30.8908						
Standard deviation		0.0088						
95/95 confidence limit								
Total error								
		Holes 1 and 5 x_2	Holes 2 and 6 x_2	Holes 3 and 7 x_2	Holes 4 and 8 x_2	Mean $\bar{x}_2$		
Outside diameter								
Systematic error								
Standard deviation								
Location								
31		2.736	2.738	2.735	2.734	2.73575		
Top 29	2.740	2.735	2.734	2.734	2.733	2.734	-0.006	-0.2190
25		2.729	2.731	2.731	2.730	2.73025		
21		2.730	2.730	2.730	2.730	2.730		
17		2.729	2.729	2.730	2.729	2.72925		
Center 15	2.740	2.730	2.730	2.729	2.731	2.730	-0.01	-0.3650
11		2.730	2.730	2.729	2.730	2.72975		
7		2.729	2.729	2.730	2.732	2.730		
Bottom 3	2.740	2.733	2.734	2.735	2.735	2.73425	-0.00575	-0.2099
1		2.736	2.735	2.735	2.734	2.735		
Sample mean	2.740	2.7317	2.7320	2.7318	2.7318	2.7318	-0.00725	-0.2646
Standard deviation	--	0.0030	0.0031	0.0026	0.0021	0.0026	-0.00238	0.0870
95/95 confidence limit								
Total error								

[a] Orientation during unloading:

TABLE 9-9
FUEL BODY DATA FOR FTE-6 BODY 3, FUEL BODY 37, LOG 738[a]

	Pre-Irrad. x_1	Post-Irrad. x_2					$\Delta x = x_2 - x_1$	$\Delta x/x_1$ (%)
Weight of body, g								
Accuracy								
Total	4907.0	4905.5					-1.50	-0.0306
Sum of components (less fuel)	4889.08							
Length of body, in.								
Systematic error								
Standard deviation								
0°	31.107	30.9435					-0.1635	-0.5256
90°		30.9375						
Sample mean	31.107	30.9405						
Standard deviation		0.0042						
95/95 confidence limit								
Total error								
		Holes 1 and 5 x_2	Holes 2 and 6 x_2	Holes 3 and 7 x_2	Holes 4 and 8 x_2	Mean $\bar{x}_2$		
Outside diameter, in.								
Systematic error								
Standard deviation								
Location								
31		2.739	2.739	2.738	2.739	2.73875		
Top 29	2.740	2.737	2.737	2.738	2.738	2.7375	-0.0025	-0.0912
25		2.735	2.734	2.734	2.735	2.7345		
21		2.729	2.730	2.733	2.731	2.73075		
17		2.732	2.731	2.730	2.730	2.73075		
Center 15	2.740	2.730	2.731	2.729	2.729	2.72975	-0.0105	-0.3832
11		2.729	2.732	2.730	2.728	2.72975		
7		2.730	2.730	2.729	2.730	2.72975		
Bottom 3	2.740	2.730	2.732	2.732	2.730	2.731	-0.009	-0.3285
1		2.734	2.733	2.732	2.734	2.73325		
Sample mean	2.740	2.7325	2.7329	2.7325	2.7324	2.7326	-0.0073	-0.2676
Standard deviation	--	0.0036	0.0030	0.0033	0.0039	0.0033	0.0043	0.1552
95/95 confidence limit								
Total error								

[a]Orientation during unloading:

TABLE 9-10
FTE-6 FUEL BODY BOW

Body	Hole	Maximum Bow[a] (mils)	Location of Maximum Bow From Bottom of Body (in.)	Orientation of Measurement
1	1	-3.0	21	
	5	+6.0	23	
	2	-26.8	21	 Holes 5, 6, 7, 8
	6	+26.6	19	Holes 1, 2, 3, 4
	3	-44.8	21	
	7	+42.0	19	
	4	-36.0	19-23	
	8	+34.4	19-21	
2	1	+21.0	21	 Holes 1, 7, 8
	5	-26.4	23	Holes 3, 4, 5
	2	-18.6	9	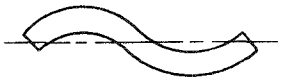 Holes 2, 6
		+3.0	25	
	6	+11.0	9	Maximum bow occurred at two locations; the bow had a sinusoidal effect.
		-12.2	23	
	3	-32.0	11	
	7	+26.0	9	
	4	-31.8	21	
	8	+27	19-21	
3	1	+12.6	9	 Holes 1, 7, 8
	5	-19.2	13	Holes 3, 4, 5
	2	+2.6	11	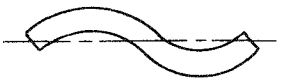 Holes 2, 6
		-8.8	21	
	6	-4.0	9	Maximum bow occurred at two locations; the bow had a sinusoidal effect.
		+4.6	23	
	3	-13.8	21	
	7	+9.8	23	
	4	-23.0	11	
	8	+15.2	13	

[a] Accuracy: ±1 mil.

TABLE 9-11
AVERAGE DIMENSIONAL CHANGES

Body	Average Temperature (°C)	Average Fast Fluence ($\times 10^{21}$ n/cm^2)	Dimensional Change (%)			
			Length		Outer Diameter	
			Measured	Calculated[a]	Measured	Calculated[a]
3	950	1.99	-0.53	-0.58	-0.27	-0.30
2	1000	2.95	-0.72	-1.2	-0.26	-0.50
1	700	1.84	-0.09	-0.15	-0.14	0.13

[a]Based on data from Ref. 9-11.

TABLE 9-12
CALCULATED RADIAL GAPS

Location of Gap Determination	Radial Gap (10^{-3} in.)	
	BOL	EOL
1. Bottom of body 1	6	6
2. Center of body 1	6	3.4[a]
3. Bottom of body 2	6	11[a]
4. Center of body 3	6	14[a]
5. Top of body 3	6	6.6

[a]Based on thickness of sleeve sections.

TABLE 9-13
FTE-6 DISTANCE d - TOP OF SPINE SAMPLE TO EDGE OF HOLE[(a)]

Body No.	Spine Stack Length, L (in.)	Pre-Irrad. d_1 (in.)	Post-Irrad. d_2 (in.)	Δd (in.)	ΔG (in.)	$\frac{-\Delta d + \Delta G}{L}$ (%)
1	28.530	2.081	2.356	0.275	-0.029	-1.065
2	28.480	2.063	2.245	0.182	-0.2235	-1.424
3	28.550	2.073	2.795	0.722	-0.1635	-3.101

(a) Accuracy: ±0.001 in.

(b) $\Delta G \equiv$ length of graphite fuel body (from Tables 9-7 through 9-9).

TABLE 9-14
SPINE SAMPLES IN FTE-6

Position	Pre-Irrad. Length (in.)	Pre-Irrad. Weight (g)	Mean Active Core Height[a]	Sample Type	Ident. Number	Composite Spine Length (in.) Pre-Irrad.	Composite Spine Length (in.) Post-Irrad.
Body 1							
Δ	0.38						
1	1.80	40.29	0.130	Graphite spacer	12		
2	3.80	77.21	2.930	Boronated graphite	4465-57-1		
3	1.26	24.53	5.460	Diffusion	23		
4	1.26	24.69	6.720	Diffusion	40		
5	1.26	24.71	7.980	Diffusion	51		
6	1.26	25.13	9.240	Diffusion	60		
7	1.26	24.48	10.500	Diffusion	13		
8	1.26	24.75	11.760	Fission product release	73p	28.530[b]	28.3230
9	1.26	25.01	13.020	Fission product release	56p		
10	3.80	78.53	15.550	Boronated graphite	4465-57-2	$\frac{\Delta L}{L}$ = -0.7255%	
11	3.80	78.99	19.350	Boronated graphite	4465-57-3		
12	1.26	24.72	21.880	Diffusion	17		
13	1.26	24.55	23.140	Diffusion	33		
14	1.26	24.52	24.400	Diffusion	19		
15	1.26	24.63	25.660	Diffusion	26		
16	1.47	33.58	27.025	Graphite spacer	13		
d[c]	2.081						
Σ	30.991[b]						
Body 2							
Δ	0.38						
1	2.50	57.38	31.471	Graphite spacer	14		
2	1.24	24.94	33.346	Fission product release	122p		
3	1.25	25.00	34.596	Fission product release	168p		
4	4.01	93.58	37.226	Advanced fuel rods	3c		
5	4.00	91.08	41.231	Advanced fuel rods	3b		
6	4.00	92.57	45.231	Advanced fuel rods	3a		
7	1.25	101.58	47.856	Fission product release	Nb-4		
8	1.25	24.55	49.106	Fission product release	12p	28.480[b]	28.3852
9	1.25	101.44	50.356	Fission product release	Nb-7		
10	1.25	25.06	51.606	Fission product release	29p	$\frac{\Delta L}{L}$ = -0.3329%	
11	1.25	101.58	52.856	Fission product release	Nb-11		
12	1.25	24.67	54.106	Fission product release	44p		
13	1.25	101.67	55.356	Fission product release	Nb-15		
14	1.25	24.60	56.606	Fission product release	148p		
15	1.47	33.67	57.966	Graphite spacer	15		
d[c]	2.063						
Σ	30.923[b]						

TABLE 9-14 (Continued)

Position	Pre-Irrad. Length (in.)	Pre-Irrad. Weight (g)	Mean Active Core Height[a]	Sample Type	Ident. Number	Composite Spine Length (in.) Pre-Irrad.	Composite Spine Length (in.) Post-Irrad.
Body 3							
Δ	0.38						
1	2.50	57.25	62.394	Graphite spacer	16		
22	5.75	137.49	66.519	Thermal stability - 1	M		
3	5.75	137.41	72.269	Thermal stability - 1	N		
4	1.25	26.03	75.769	Thermal stability - 2	18		
5	1.25	23.83	77.019	Thermal stability - 2	24		
6	1.25	23.90	78.269	Thermal stability - 2	30	28.550[b]	28.4100
7	1.25	24.63	79.519	Thermal stability - 2	6		
8	1.25	24.79	80.769	Thermal stability - 2	12	$\frac{\Delta L}{L}$ = 0.4904%	
9	3.80	79.88	83.294	Boronated graphite	4465-57-4		
10	3.80	78.55	87.094	Boronated graphite	4465-57-5		
11	0.70	15.98	89.344	Graphite spacer	17		
d[b]	2.073						
Σ	31.003[a]						

[a] Active core height starts at 26.00 in. from Ref. 0 in Drawing 11510, used as base. Experimental fuel height is specified as 26.15 in. from Ref. 0 (Drawings 11497 and 11510). Body 1 bottom line is 1.15 in. under active core height.

[b] Discrepancy in body lengths from that of Table 9-7 due to reference values given for spine samples in Drawings 11510, 11511, and 11512.

[c] Plenum d from Table 9-13.

TABLE 9-15
FTE-6 FUEL STACK LENGTH

Hole No.	Stack length (in.) Pre-Irrad.	Stack length (in.) Post-Irrad.	ΔL (in.)	ΔL/L (%)	Plenum P[a] (in.) Pre-Irrad.	Plenum P[a] (in.) Post-Irrad.	ΔP (in.)	$\frac{-\Delta P + \Delta G}{L}$[b] (%)
Systematic error								
Standard deviation								
1	27.3225	26.6373	-0.6852	-2.5078	2.571	2.896	+0.325	-1.2956
2	27.326	26.5703	-0.7557	-2.7655	2.592	2.945	+0.353	-1.3979
3	27.2905	26.8483	-0.4422	-1.6203	2.595	2.662	+0.067	-0.3518
4	27.281	26.8453	-0.4357	-1.5971	2.603	2.751	+0.148	-0.6488
5	27.254	26.8283	-0.4257	-1.5620	2.637	2.782	+0.145	-0.6384
6	27.259	26.8443	-0.4147	-1.5213	2.628	2.865	+0.237	-0.9758
7	27.294	26.8043	-0.4897	-1.7942	2.600	2.722	+0.122	-0.5532
8	27.252	26.7443	-0.5077	-1.8630	2.634	2.830	+0.196	-0.8256
Sample mean	27.2849	26.7653	-0.5196	-1.9043	2.6075	2.8066	+0.1991	-0.8359
Standard deviation	0.0291	0.1068	0.1140	0.4719	0.0233	0.0948	0.0999	0.3655
95/95 confidence limit								
Total error								
Systematic error								
Standard deviation								
1	27.326	26.4683	-0.8577	-3.1388	2.553	2.960	+0.407	-2.3073
2	27.325	26.4763	-0.8487	-3.1059	2.563	3.003	+0.440	-2.4282
3	27.282	26.7943	-0.4877	-1.7876	2.602	2.883	+0.281	-1.8492
4	27.292	26.7023	-0.5897	-2.1607	2.593	2.862	+0.269	-1.8046
5	27.258	26.7213	-0.5367	-1.9690	2.621	2.813	+0.192	-1.5243
6	27.262	26.7193	-0.5427	-1.9907	2.619	2.855	+0.236	-1.6855
7	27.242	26.6743	-0.5677	-2.0839	2.630	2.930	+0.300	-1.9217
8	27.287	26.6653	-0.6217	-2.2784	2.582	2.911	+0.329	-2.0248
Sample mean	27.2843	26.6527	-0.6316	-2.3144	2.5954	2.9021	+0.3068	-1.9432
Standard deviation	0.0303	0.1180	0.1423	0.5190	0.0280	0.0616	0.0833	0.3035
95/95 confidence limit								
Total error								

TABLE 9-15 (Continued)

Hole No.	Stack Length (in.) Pre-Irrad.	Stack Length (in.) Post-Irrad.	ΔL (in.)	ΔL/L (%)	Plenum P[a] (in.) Pre-Irrad.	Plenum P[a] (in.) Post-Irrad.	ΔP (in.)	$\frac{-\Delta P + \Delta G^{(b)}}{L}$ (%)
Systematic error								
Standard deviation								
1	27.353	26.4483	-0.9047	-3.3075	2.550	3.1342	+0.5842	-2.7335
2	27.338	26.4283	-0.9097	-3.3276	2.563	3.1796	+0.6166	-2.8535
3	27.293	26.7083	-0.5847	-2.1423	2.601	2.911	+0.310	-1.7349
4	27.294	26.6933	-0.6007	-2.2009	2.605	2.925	+0.320	-1.7714
5	27.249	26.6963	-0.5527	-2.0283	2.644	2.954	+0.310	-1.7377
6	27.252	26.7053	-0.5467	-2.0061	2.646	2.930	+0.284	-1.6421
7	27.280	26.6743	-0.6057	-2.2203	2.616	2.961	+0.345	-1.8640
8	27.227	26.7253	-0.5017	-1.8427	2.652	2.940	+0.288	-1.6583
Sample mean	27.2858	26.6349	-0.6508	-2.3845	2.6096	2.9919	+0.3822	-1.9994
Standard deviation	0.0437	0.1223	0.1617	0.5885	0.0381	0.1038	0.1362	0.4959
95/95 confidence limit								
Total error								

[a] Plenum P = distance from top of fuel rod to edge of hole.

[b] ΔG = length change in graphite fuel body (see Tables 9-7 through 9-9).

TABLE 9-16
FTE-6 FUEL ROD REMOVAL SUMMARY

Body	Hole	Force (lb)		Visual Examination
		Initial	Sustaining	
1	1	5	0	Several rods had cracked end caps and surface cracks.
	2	30	0	Several rods had cracked end caps and surface cracks.
	3	25	10	About half of the rods had cracked end caps.
	4	15	10	Three rods had cracked end caps.
	5	10	<10	Two rods had cracked end caps.
	6	10	<10	Five rods had cracked end caps and surface cracks.
	7	12	<12	Good general condition.
	8	10	<10	Several rods had cracked end caps and surface cracks.
2	1	25	25	Majority of rods had cracked end caps and surface cracks.
	2	30	5	Majority of rods had cracked end caps and surface cracks.
	3	25	0	Several rods at top end of body had surface cracks.
	4	20	0	Several rods at top end of body had surface cracks.
	5	25	15	Several rods had cracked end caps and surface cracks.
	6	10	5	Several rods had cracked end caps.
	7	20	10	Several rods were broken in half and had cracked end caps.
	8	30	10	Several rods had cracked end caps.
3	1	15	5	Several rods had cracked end caps and exhibited bowing.
	2	25	15	Several rods had cracked end caps and exhibited bowing at lower end of body.
	3	40	30	Majority of rods had cracked end caps.
	4	50	30	Rods at lower end of body had cracked end caps.
	5	35	20	Rods at lower end of body had cracked end caps.
	6	0	0	Rods at lower end of body had cracked end caps.
	7	25	10	Rods at lower end of body had cracked end caps.
	8	10	5	Rods at lower end were cracked in half.

TABLE 9-17
FTE-6 FUEL ROD BOW

Rod	Mean Active Core Height (in.)	Bow (mils)
2-1-10	49.68	21.0
2-1-11	51.63	17.9
2-1-12	53.58	0.9
2-2-5	39.93	15.2
2-2-10	49.68	16.6
2-2-13	55.53	16.4
3-1-1	63.29	21.8
3-1-2	65.24	18.3
3-1-3	67.19	17.7
3-1-4	69.14	22.6
3-1-5	71.09	23.2
3-1-6	73.04	20.7
3-1-7	74.99	17.4
3-1-12	84.74	21.4
3-1-13	86.69	19.6
3-2-3	67.19	15.9
3-2-7	74.99	11.2
3-2-13	86.69	17.8
3-8-9	78.89	6.8

TABLE 9-18
FTE-6 AVERAGE FUEL ROD DIMENSIONAL CHANGES

Body	Hole	Fuel Type	Temp. Range (°C)	Fast Fluence Range ($\times 10^{21}$ n/cm^2)	Shrinkage (%)					
					Length	Length[(a)]	Diameter	Diameter[(a)]	Average	Average[(a)]
1	1 2	UO_2 TRISO/ ThO_2 BISO	538–1100	0.78–2.89	2.15 2.34	2.25	1.76 1.79	1.78	1.95 2.06	2.01
	3 4	$(Th,U)C_2$ TRISO/ ThC_2 BISO			1.46 1.48	1.47	0.97 0.94	0.96	1.22 1.21	1.22
	5 6	$(Th,U)C_2$ TRISO/ ThC_2 TRISO			1.48 1.36	1.42	0.92 0.83	0.88	1.20 1.10	1.15
	7 8	UC_2 TRISO/ ThC_2 BISO			1.66 1.63	1.65	1.24 1.29	1.27	1.45 1.46	1.46
2	1 2	UO_2 TRISO/ ThO_2/BISO	1100–1276	2.89–3.01	2.79 2.74	2.77	2.42 2.36	2.39	2.60 2.55	2.58
	3 4	$(Th,U)C_2$ TRISO/ ThC_2 BISO			2.02 2.02	2.02	1.56 1.55	1.56	1.79 1.78	1.79
	5 6	$(Th,U)C_2$ TRISO/ ThC_2 TRISO			1.81 1.85	1.83	1.43 1.37	1.40	1.62 1.61	1.62
	7 8	UC_2 TRISO/ ThC_2 BISO			2.16 2.15	2.16	1.89 1.96	1.93	2.03 2.06	2.05
3	1 2	UO_2 TRISO/ ThO_2 BISO	1045–1166	1.22–2.77	3.03 2.84	2.94	2.63 2.67	2.65	2.83 2.76	2.80
	3 4	$(Th,U)C_2$ TRISO/ ThC_2 BISO			2.05 2.06	2.06	1.52 1.52	1.52	1.78 1.79	1.79
	5 6	$(Th,U)C_2$ TRISO/ ThC_2 TRISO			1.96 1.91	1.94	1.39 1.48	1.44	1.67 1.70	1.69
	7 8	UC_2 TRISO/ ThC_2 BISO			2.14 2.07	2.11	1.77 1.69	1.73	1.95 1.88	1.92

(a) Dimensional change for fuel rod type.

TABLE 9-19
COMPARISON OF RADIAL STRAIN

Body	TREVER[a] Calculated TRISO/BISO	Measured UO_2 TRISO/ ThO_2 BISO	Measured $(Th,U)C_2$ TRISO/ ThC_2 BISO	Measured UC_2 TRISO/ ThC_2 BISO	Measured[b] $(Th,U)C_2$ TRISO/ ThC_2 TRISO
1	-2.25	-1.78	-0.96	-1.27	-0.88
2	-1.75	-2.39	-1.56	-1.93	-1.40
3	-2.25	-2.65	-1.52	-1.73	-1.44
Total Element	-2.08	-2.27	-1.35	-1.64	-1.24

[a] Based on data from Ref. 9-4.

[b] TREVER calculations for TRISO/TRISO fuel rods are not yet available.

TABLE 9-20
TEST MATRIX - PROTOTYPE LHTGR FUEL ROD THERMAL AND MECHANICAL PROPERTY STUDY

Rod Type	Rods Required	Shim[a]		Fuel Load[b] (Th/U)	Matrix Type[c]	Curing Media (Crucible)	Curing Temp. (°C)	Curing Rate (°C/min)
		Type	Vol %					
A-1	8	--	0	20:1	M1	TS-1240	1600	10
A-2	8	--	0	20:1	M1	H-451	1800	10
A-3	12	--	0	20:1	M1	H-451	1600	10
A-4	8	--	0	20:1	M2	H-451	1800	22
A-5	8	--	0	20:1	M2	H-451	1800	10
A-6	8	--	0	20:1[d]	M1	H-451	1600	10
B-1	8	H-451	11	20:1	M1	H-451	1600	10
B-2	8	H-451	11	20:1	M1	H-451	1800	10
B-3	8	H-451	11	40:1	M1	H-451	1600	10
B-4	8	TS-1240	11	20:1	M1	TS-1240	1600	10
B-5	8	X-4029	11	20:1	M1	H-451	1600	10
C-1	8	H-451	23	20:1	M1	H-451	1800	10
C-2	8	H-451	23	20:1	M2	H-451	1800	22
C-3	12	H-451	23	20:1	M1	H-451	1600	10
C-4	8	H-451	23	20:1	M2	H-451	1800	10
D-1	8	H-451	36	10:1	M1	H-451	1600	10
D-2	12	H-451	36	20:1	M1	H-451	1600	10
D-3	8	TS-1240	36	20:1	M1	TS-1240	1600	10
D-4	8	H-451	36	20:1	M1	H-451	1600	10

[a] See Ref. 9-12 for description of shim particle types.

[b] TRISO UC_2 (weak acid resin)/BISO ThO_2 unless otherwise specified.

[c] M1 = 38 wt % Lonza KS15-HTR graphite filler, 47 wt % Ashland A-240 petroleum pitch, 15 wt % additives. M2 = 38 wt % Lonza KS15-HTR graphite filler, 47 wt % Ashland low sulfur A240 petroleum pitch, 15 wt % additives.

[d] TRISO UC_2 (VSM)/BISO ThO_2.

TABLE 9-21
NOMINAL PROPERTIES OF REFERENCE LHTGR
FISSILE AND FERTILE FUEL PARTICLES

Property	Fissile	Fertile
Kernel		
Type	UC_2	ThO_2
Enrichment (U-235)	93%	--
Diameter (μm)	200	500
Standard deviation (μm)	20	50
Density (g/cc)	11.1	9.5
Buffer		
Thickness (μm)	100	85
Standard deviation (μm)	15.0	12.8
Density (g/cc)	1.10	1.10
IPyC		
Thickness (μm)	25	--
Standard deviation (μm)	3.8	--
Density (g/cc)	1.90	--
SiC		
Thickness (μm)	25	--
Standard deviation (μm)	3.8	--
Density (g/cc)	3.20	--
OPyC		
Thickness (μm)	35	75
Standard deviation (μm)	5.3	11.3
Density (g/cc)	1.80	1.85

Sample Description					
			Gas Release[i]		
Batch No.	Capsule	Position	Avera Temperat (°C	Failure[j] (%)	Comments
4413-5E	P13L	C1T3	1660	(k)	Meets TRISO UC_2 design basis
4413-5E	P13L	C3T3	1405	(k)	Meets TRISO UC_2 design basis
4413-5E	P13L	C5T3	855	(k)	Meets TRISO UC_2 design basis
4403-143	P13L	C2T3	1425	(k)	Meets TRISO UC_2 design basis
4413-21	P13L	C2T6	1460	(k)	Meets TRISO UC_2 design basis
4000-304	P13M	C4T1	1300	0.80	Meets TRISO UC_2 design basis
4000-304	P13M	C4T7	1300	(k,l)	Meets TRISO UC_2 design basis
4000-325	P13M	C4T5	1300	0.42	Meets TRISO UC_2 design basis
4161-00-023-3	P13P	1-1	1455	0.36	Does not meet LHTGR TRISO UC_2 design basis
4161-01-034-2	P13P	1-2	1420	0.18	Meets TRISO UC_2 design basis
4161-032-2	P13P	1-4	1350	0.18	Does not meet LHTGR TRISO UC_2 design basis
4161-01-032-1	P13P	3-4	1605	0.23	Does not meet LHTGR TRISO UC_2 design basis
4161-034-1	P13P	3-2	1208	0.23	Does not meet LHTGR TRISO UC_2 design basis
4161-023-2	P13P	3-1	1085	0.30	Does not meet LHTGR TRISO UC_2 design basis
6151-00-035	P13R	3-4, 5	1075[l]	0.02	Reference LHTGR TRISO UC_2 fissile fuel
6151-08-015	P13S	3-7, 8, 9	1075[l]	0.07	Reference LHTGR TRISO UC_2 fissile fuel
6151-00-035	P13S	4-10, 11, 12	1075[l]	0.02	Reference LHTGR TRISO UC_2 fissile fuel

[a] Time average fuel irradiation temperature.

[b] Maximum fuel temperature during irradiation.

[c] Number of fissions occurring inside the SiC la

[d] Number of particles examined.

[e] Determined during macroscopic examination.

[f] Determined during microscopic examination.

[g] Includes particles having SiC layers that are SiC layer caused by pressure vessel failure.

[h] Coatings having cracked SiC and PyC layers.

[i] Postirradiation fission gas release (Kr-85m R

[j] Assumes 2×10^{-2} R/B per failed particle for

[k] Not determined.

[l] High FGR value is inconsistent with metallogr

[m] Design operating temperature

TABLE 9-23
SUMMARY OF UNBONDED PARTICLE BISO ThO_2 IRRADIATION OBSERVATIONS

Sample Description			Irradiation Conditions			Results		
Batch Number	Capsule	Position	Average Temperature[a] (°C)	Fast Neutron Exposure (10^{21} n/cm^2, $E \geq 0.18$ MeV$_{HTGR}$)	Burnup (% FIMA)	Sample Size[b]	(R/B, Kr-85m @ 1100°C)	Failure[c] (%)
6542-09-010	P13R	3-11, 12	1075	11.9	4.8	998	2.4×10^{-5}	0.12
6542-18-015	P13R	4-3, 4	1075	11.5	4.4	953	2.2×10^{-6}	0
6542-23-025	P13S	3-7, 8	1075	11.8	4.2	992	2.8×10^{-6}	0

[a] Design operating temperature.

[b] Number of particles per sample.

[c] Assumes a R/B per failed particle of 2×10^{-2} for Kr-85m at 1100°C.

TABLE 9-24

TRISO UC_2 FAILURE FRACTIONS ESTIMATED FROM IN-PILE FISSION GAS RELEASE MEASUREMENTS MADE ON P13R AND P13S FUEL ROD CELLS FOR FAST NEUTRON EXPOSURES $\leq 4 \times 10^{21}$ N/CM^2 ($E \geq 0.18$ MeV)$_{HTGR}$

Capsule/Cell	Irradiation Conditions			Fission Gas Release Kr-85m R/B	Estimated Fissile Fuel Failure Fraction
	Fast Neutron Exposure (10^{21} n/cm^2, $E \geq 0.18$ MeV$_{HTGR}$)	Fissile Kernel Burnup (% FIMA)	Temperature[a] (°C)		
P13R/Cell 1	1	21	1040	2(-7)	5(-5)
	2	38	1040	2(-7)	5(-5)
	3	48	1040	8(-7)	2(-4)
	4	57	1040	1.5(-6)	4(-4)
P13R/Cell 2	1	19	1040	2(-7)	5(-5)
	2	35	1040	4(-7)	1(-4)
	3	46	1040	7(-7)	2(-4)
	4	53	1040	1.5(-6)	4(-4)
P13R/Cell 5	1	16	1240	8(-7)	1(-4)
	2	29	1240	3(-6)	4(-4)
	3	39	1240	3(-6)	4(-4)
	4	47	1240	4(-6)	5(-4)
P13S/Cell 1	0.3	8	1540[b]	1(-7)[c]	2(-5)
	0.7	15	1700[b]	1(-7)[c]	2(-5)
	1.1	22	1700[b]	1(-7)[c]	2(-5)
	1.4	27	1600[b]	1(-7)[c]	2(-5)
	1.8	33	1550[b]	1(-7)[c]	2(-5)
	2.1	37	1650[b]	2(-7)[c]	5(-5)
	2.7	44	1610[b]	1(-6)[c]	2(-4)
	3.0	47	1610[b]	1(-6)[c]	2(-4)
	3.4	51	1450[b]	1(-6)[c]	2(-4)
	3.8	53	1695[b]	1(-6)[c]	2(-4)
P13S/Cell 2	1	18	1040	2(-7)	5(-5)
	2	31	1040	2(-7)	5(-5)
	3	42	1040	8(-7)	2(-4)
	4	56	1040	3(-6)	7(-4)
P13S/Cell 5	1	16	1440	3(-6)	2(-4)
	2	28	1440	4(-6)	3(-4)
	3	38	1440	4(-6)	3(-4)
	4	46	1440	4(-6)	3(-4)

[a] Design, volume average temperature unless otherwise indicated.

[b] Peak temperature attained during thermal cycles from a volume average temperature of 1040°C.

[c] Measured at 1040°C after cycling to the indicated temperature.

TABLE 9-25

BISO ThO_2 FAILURE ESTIMATED FROM PIE FISSION GAS RELEASE VALUES MEASURED ON FUEL RODS CONTAINING LHTGR REFERENCE FISSILE AND FERTILE FUEL PARTICLES, P13R AND P13S

Sample Identification			Irradiation Conditions				PIE Results		
Fertile Particle Batch No.	Capsule	Fuel Rod No.	Temperature[a] (°C)	Fast Neutron Exposure (10^{21} n/cm^2 E $\geq$ 0.18 MeV)	Fertile Kernel Burnup (% FIMA)	Fertile Particles per Rod	Micro Metallographic Examination	R/B from Failed Fuel Kr-85m at 1100°C	Failure[b] (%)
6542-02-020	P13R	2B	1040	12.2	5.6	1300	(d)	1.3×10^{-5}	0.3
6542-02-020	P13R	5B	1240	9.1	2.8	1600	(d)	3.7×10^{-5}	0.8
6542-02-020	P13R	6B	1040	4.1	0.7	1400	(d)	1.4×10^{-5}	0.6
6542-02-020	P13S	1B	1500-1700[c]	7.8	3.4	1400	(d)	5.7×10^{-5}	1.2
6542-02-020	P13S	2D	1040	12.2	4.6	1200	(d)	9.0×10^{-6}	0.2
6542-02-020	P13S	5B	1440	8.8	2.6	1600	(d)	2.8×10^{-5}	0.6

[a] Design, volume average temperature.

[b] Calculated assuming a Kr-85m R/B per failed particle of 0.005 at 1100°C and that only ThO_2 fuel has failed in these rods.

[c] Peak temperatures achieved during thermal cycles.

[d] Not completed.

TABLE 9-26
POSTIRRADIATION HEATING THERMAL CYCLE USED TO STUDY THE EFFECTS OF TIME AT 1800°C ON Kr-85 RELEASE FROM IRRADIATED TRISO UC_2 FUEL PARTICLES

Total Elapsed Time (hr)	Event
0	Start heating at 1800°C
1	Cycle from 1800°C to room temperature to 1800°C
148	Cycle from 1800°C to room temperature to 1800°C
148 to 990	Continuous heating at 1800°C

TABLE 9-27
MEASURED AND PREDICTED FAILURE FRACTIONS FOR IRRADIATED BISO ThO_2 PARTICLES IN OUT-OF-PILE HEATING TESTS TO 2000°C

Irradiation Conditions		Failure Values[a] (%)			
Fast Neutron Exposure (10^{21} n/cm^2) [$(E \geq 0.18\ MeV)_{HFIR}$]	Kernel Burnup (% FIMA)	1400°C	1600°C	1800°C	2000°C
2.8 - 3.7	1.7 - 2.2[b]	0 (0.1)	0 (0.1)	0 (0.1)	0 (100)
6.4 - 7.5	6.8 - 7.8[c]	2.5 (0.5)	30 (10)	58 (40)	60 (100)

[a] Values not in parentheses are experimental; those in parentheses are predicted. Predicted values are based on kernel burnup.

[b] Burnup value used for failure predictions was 2%.

[c] Burnup value used for failure predictions was 7.3%.

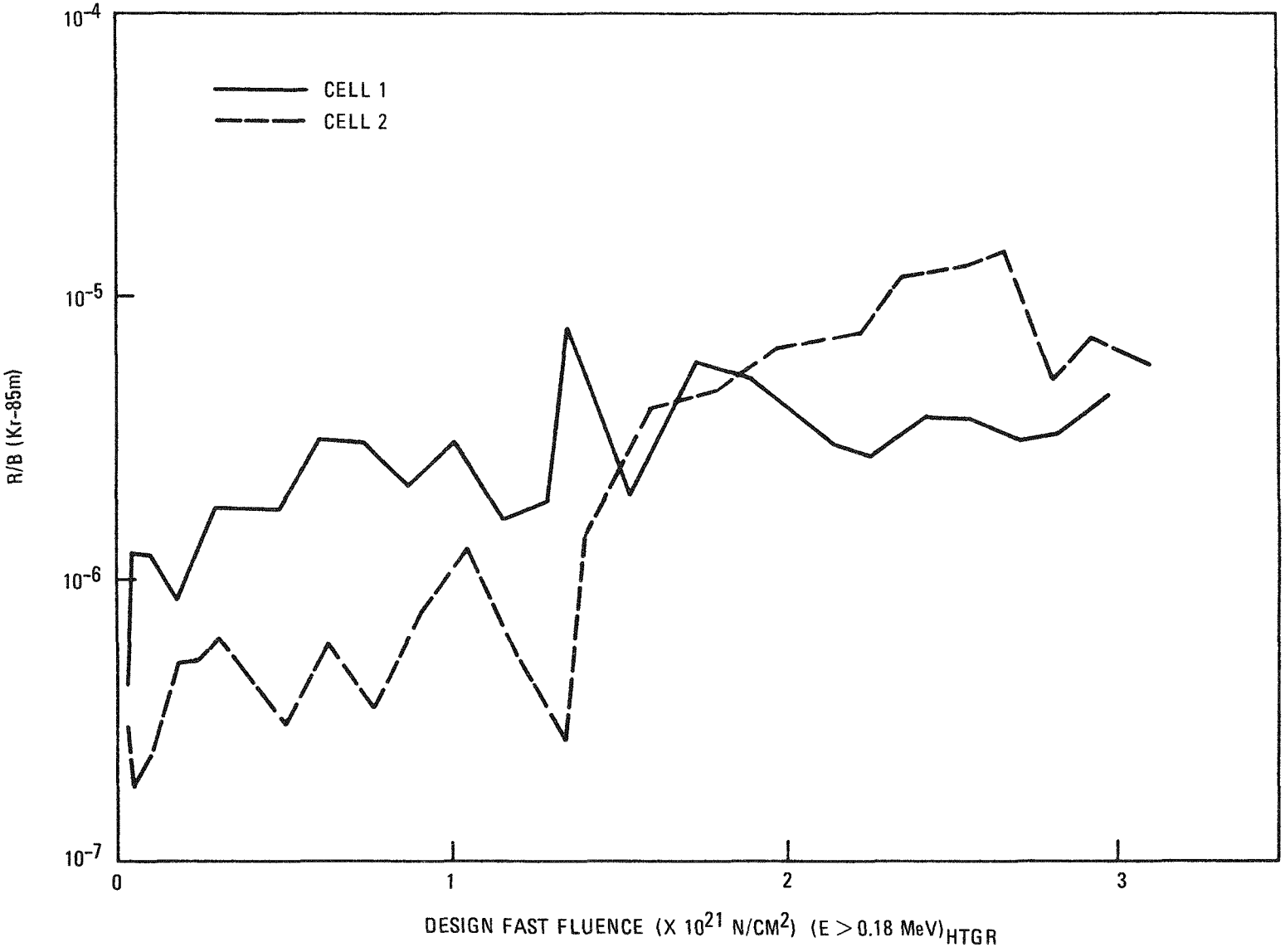

Fig. 9-1. Capsule P13T R/B versus fast fluence to November 7, 1975

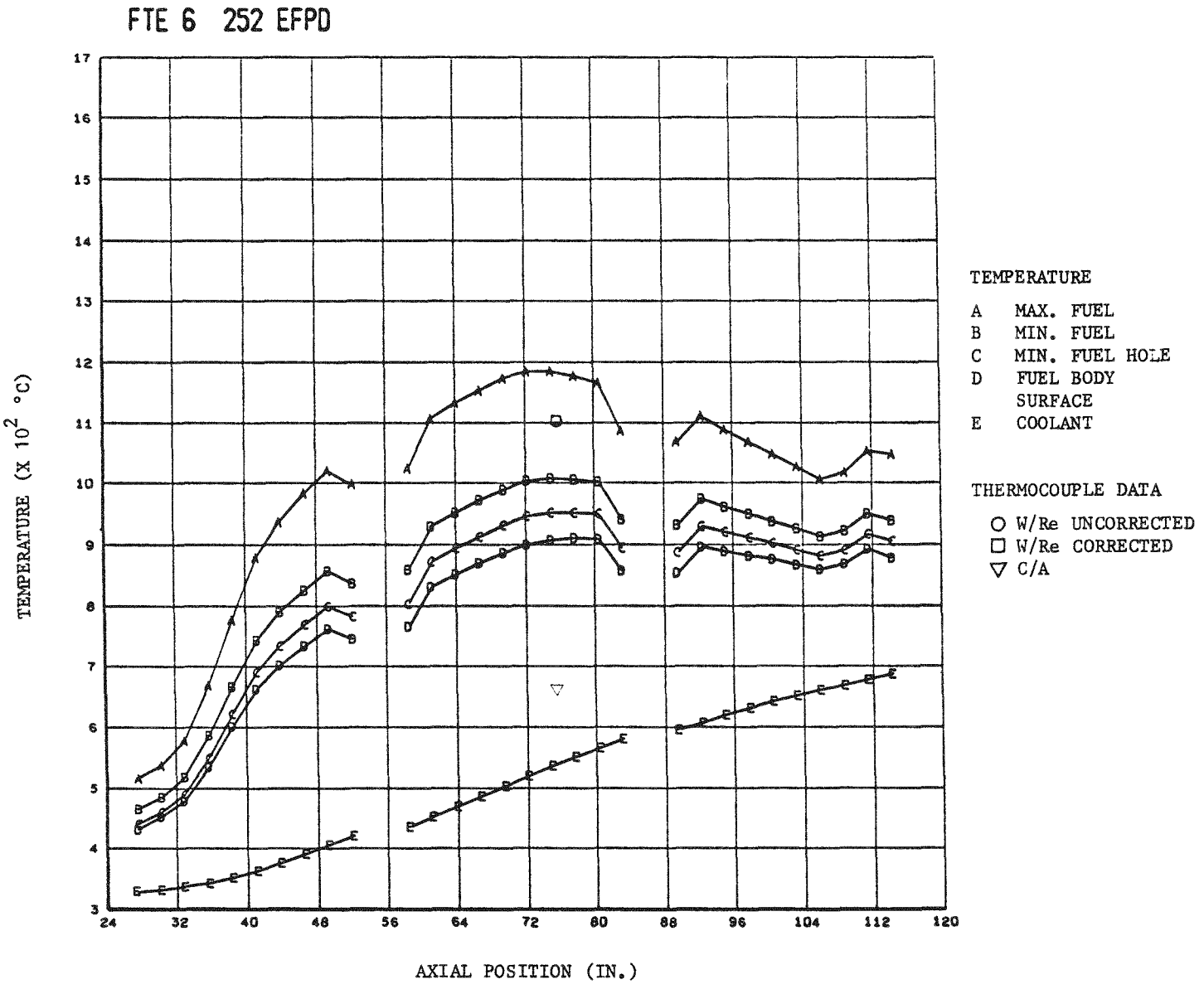

Fig. 9-2. FTE-6 temperature distributions: (a) 252 EFPD

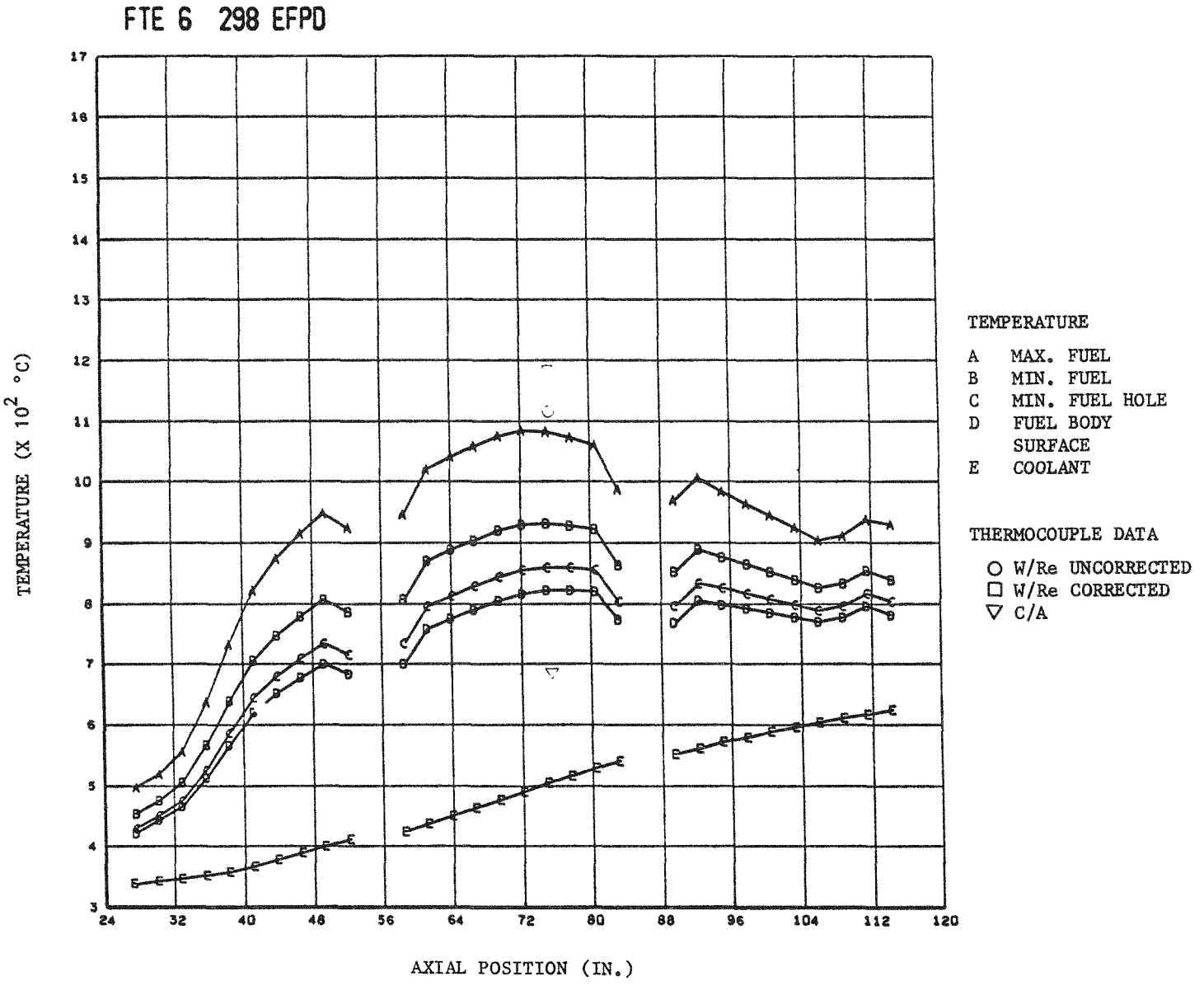

Fig. 9-2. FTE-6 temperature distributions: (b) 298 EFPD

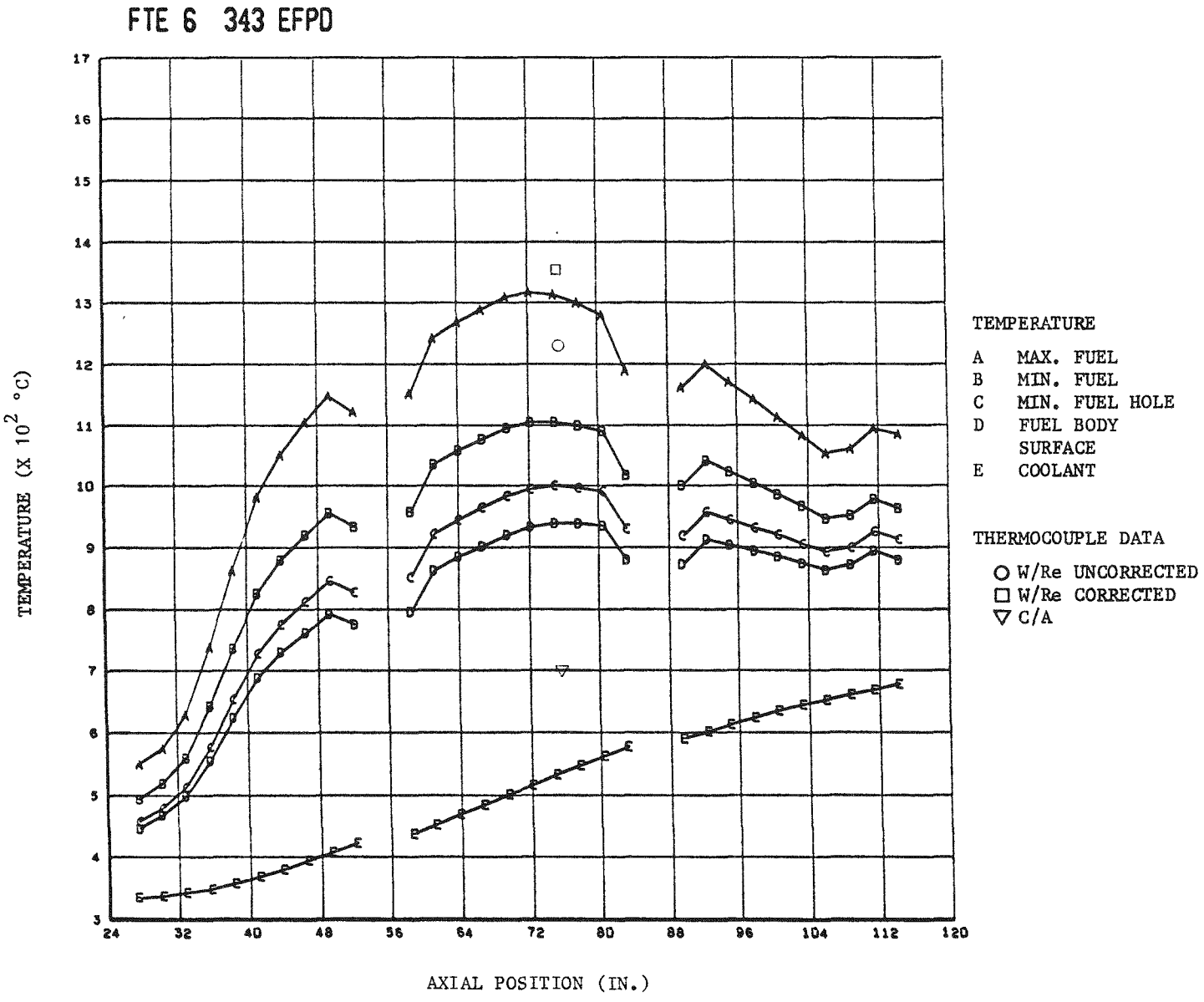

Fig. 9-2. FTE-6 temperature distributions: (c) 343 EFPD

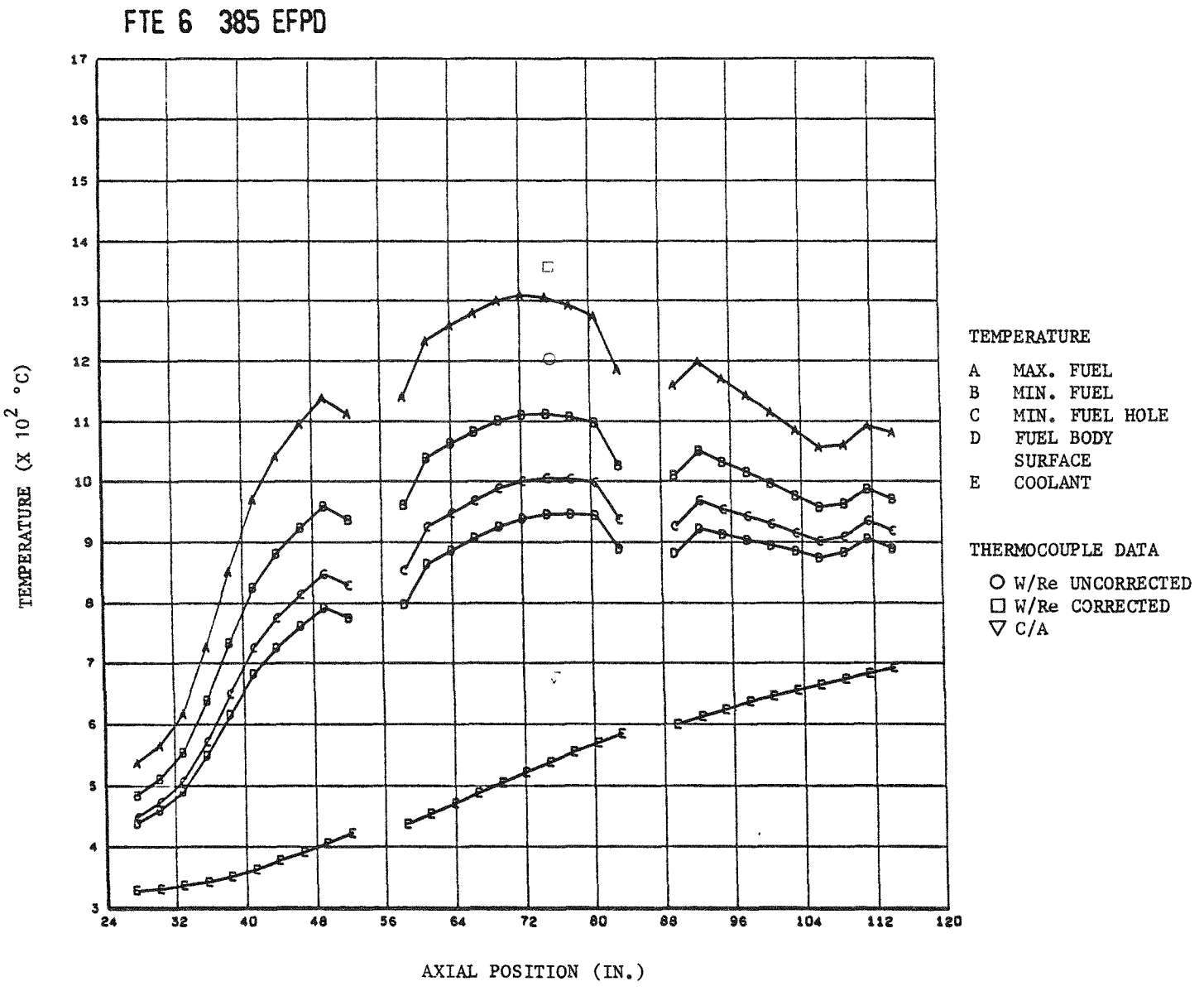

Fig. 9-2. FTE-6 temperature distributions: (d) 385 EFPD

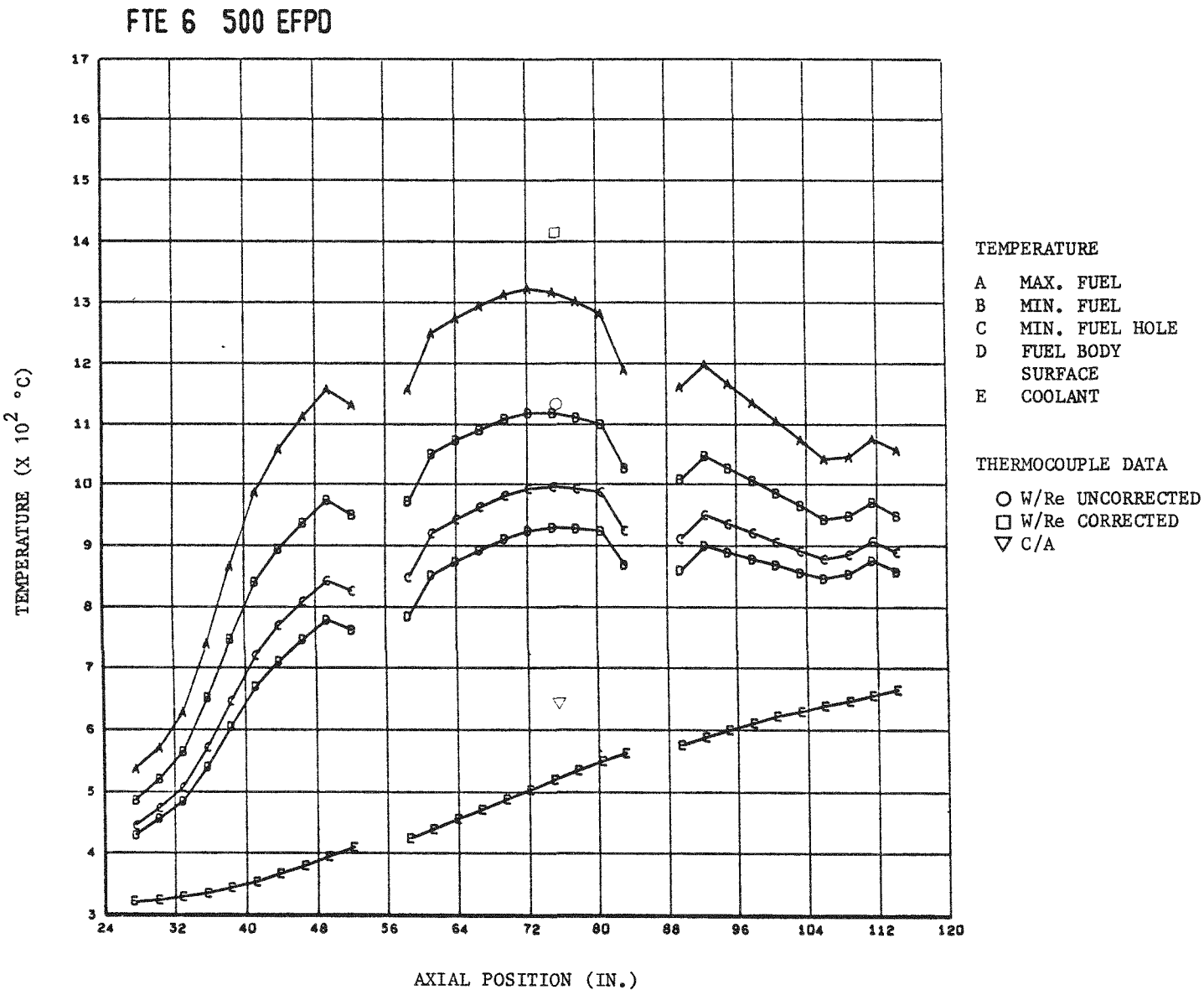

Fig. 9-2. FTE-6 temperature distributions: (e) 500 EFPD

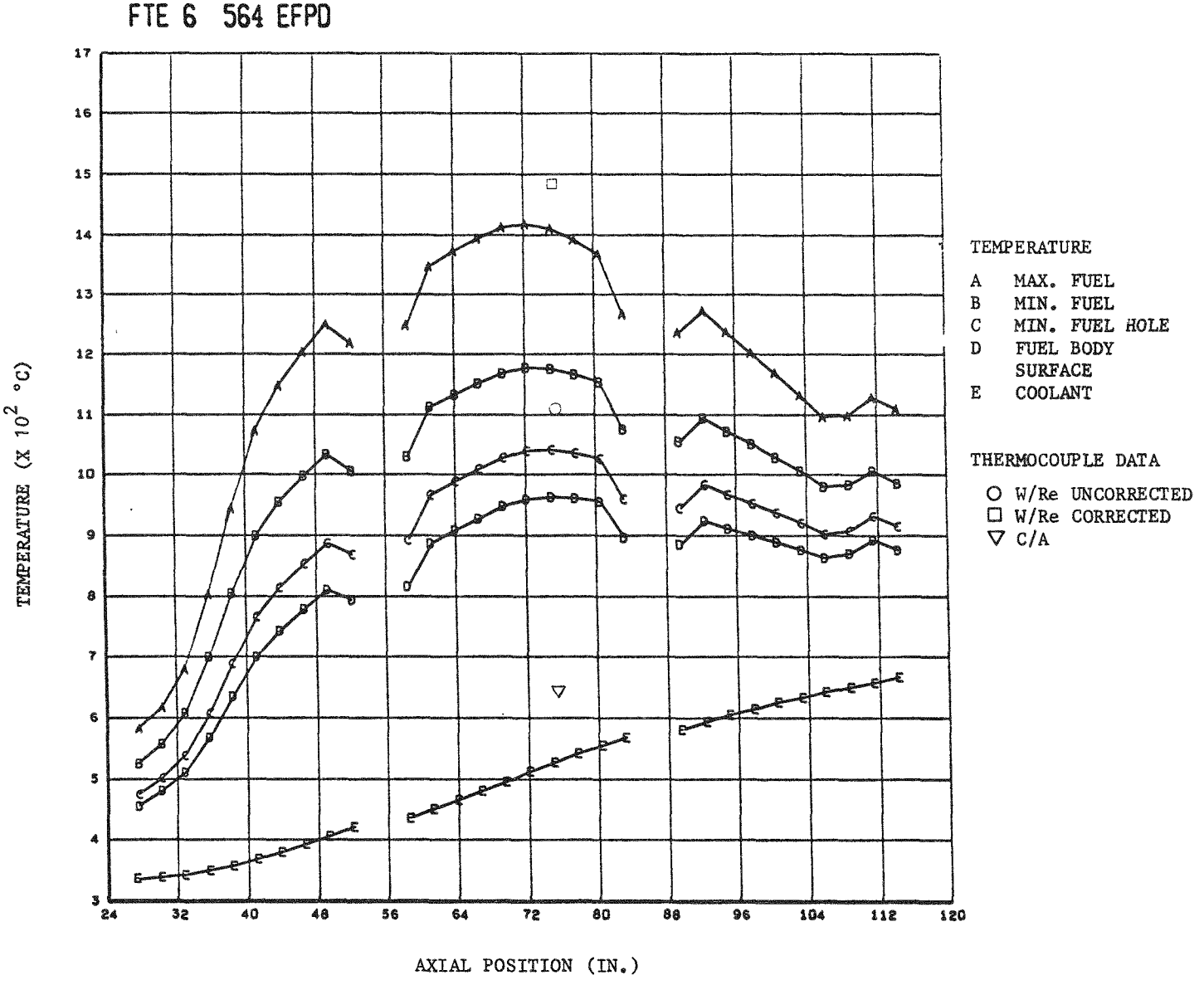

Fig. 9-2. FTE-6 temperature distributions: (f) 564 EFPD

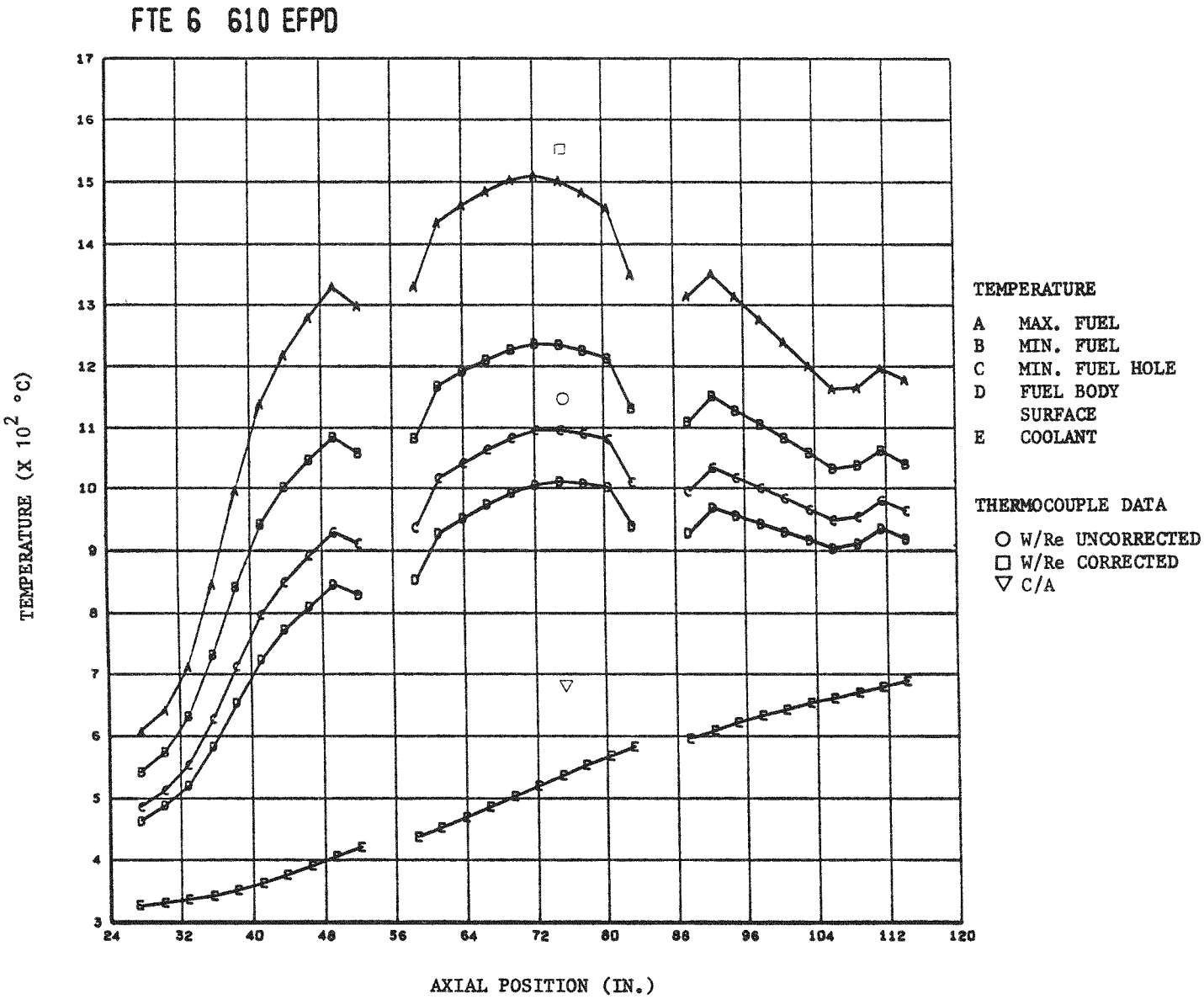

Fig. 9-2. FTE-6 temperature distributions: (g) 610 EFPD

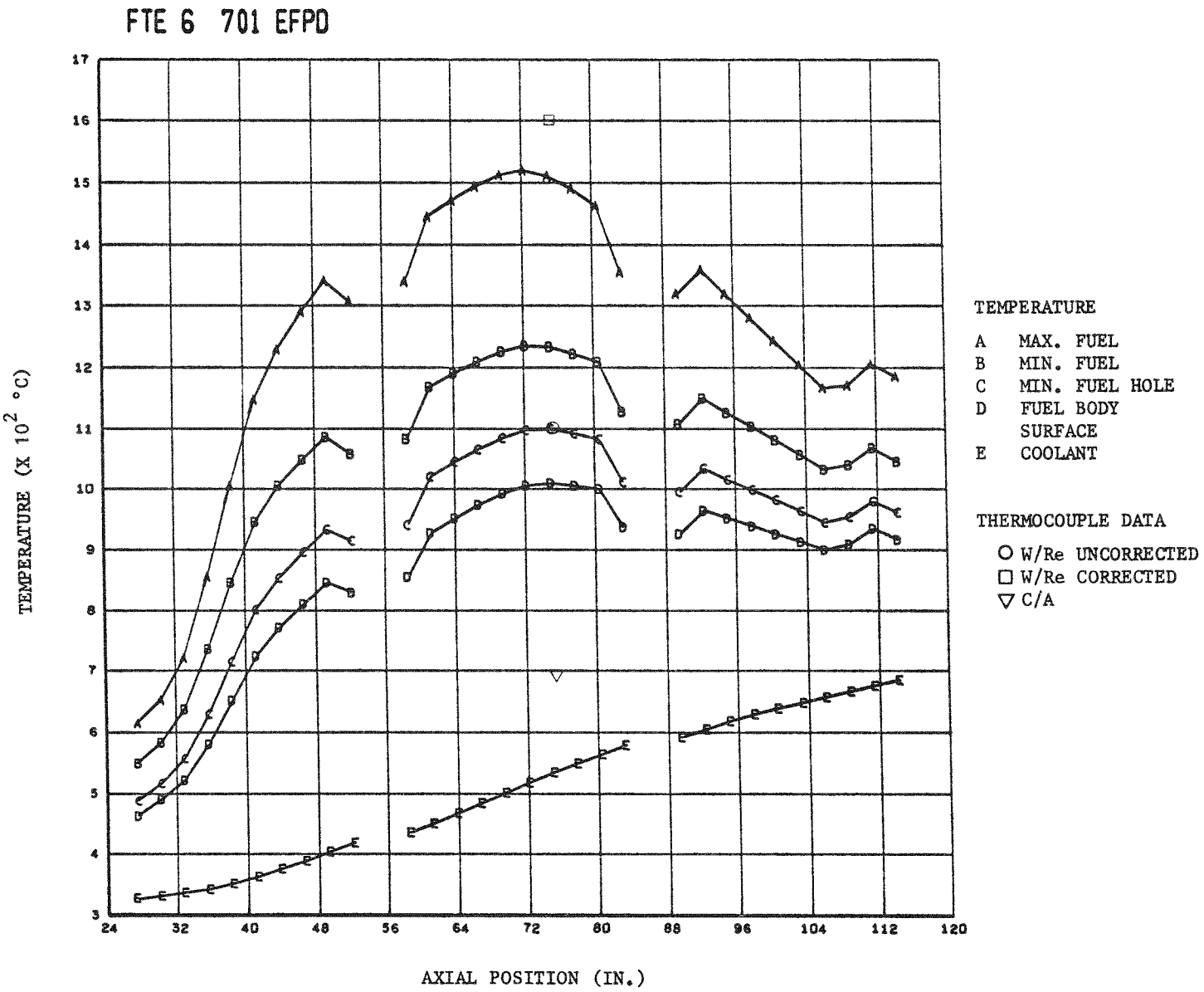

Fig. 9-2. FTE-6 temperature distributions: (h) 701 EFPD

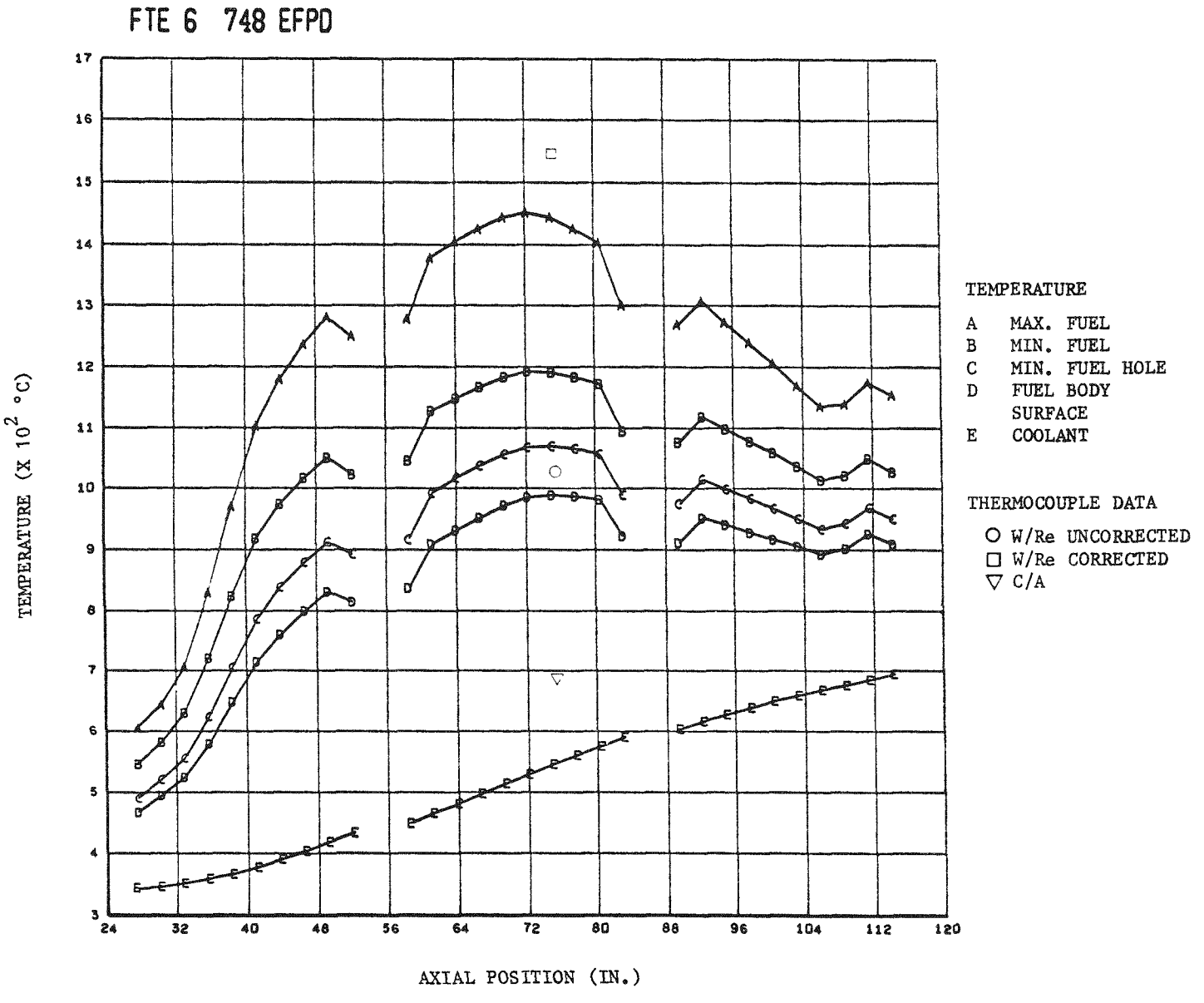

Fig. 9-2. FTE-6 temperature distributions: (i) 748 EFPD

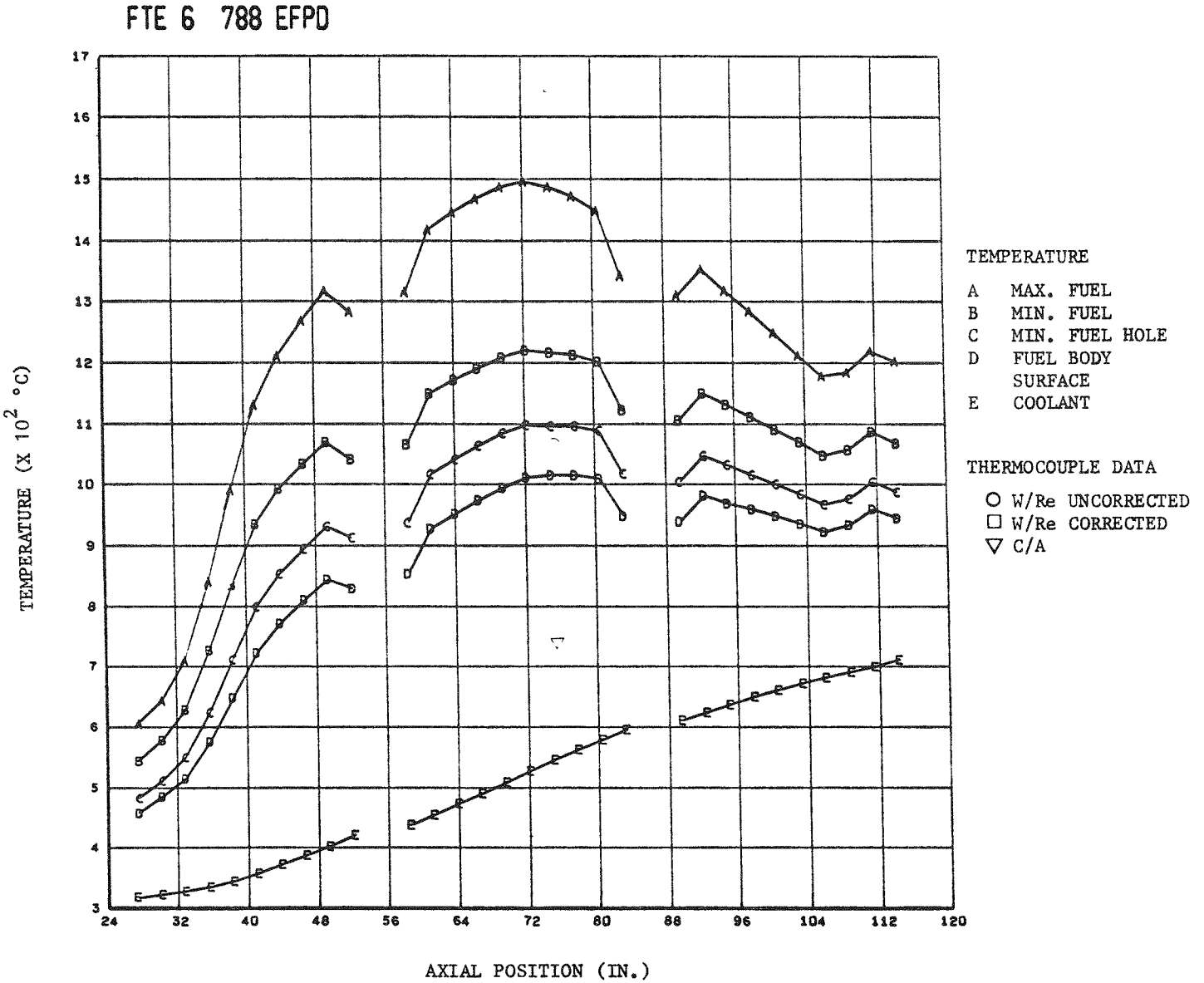

Fig. 9-2. FTE-6 temperature distributions: (j) 788 EFPD

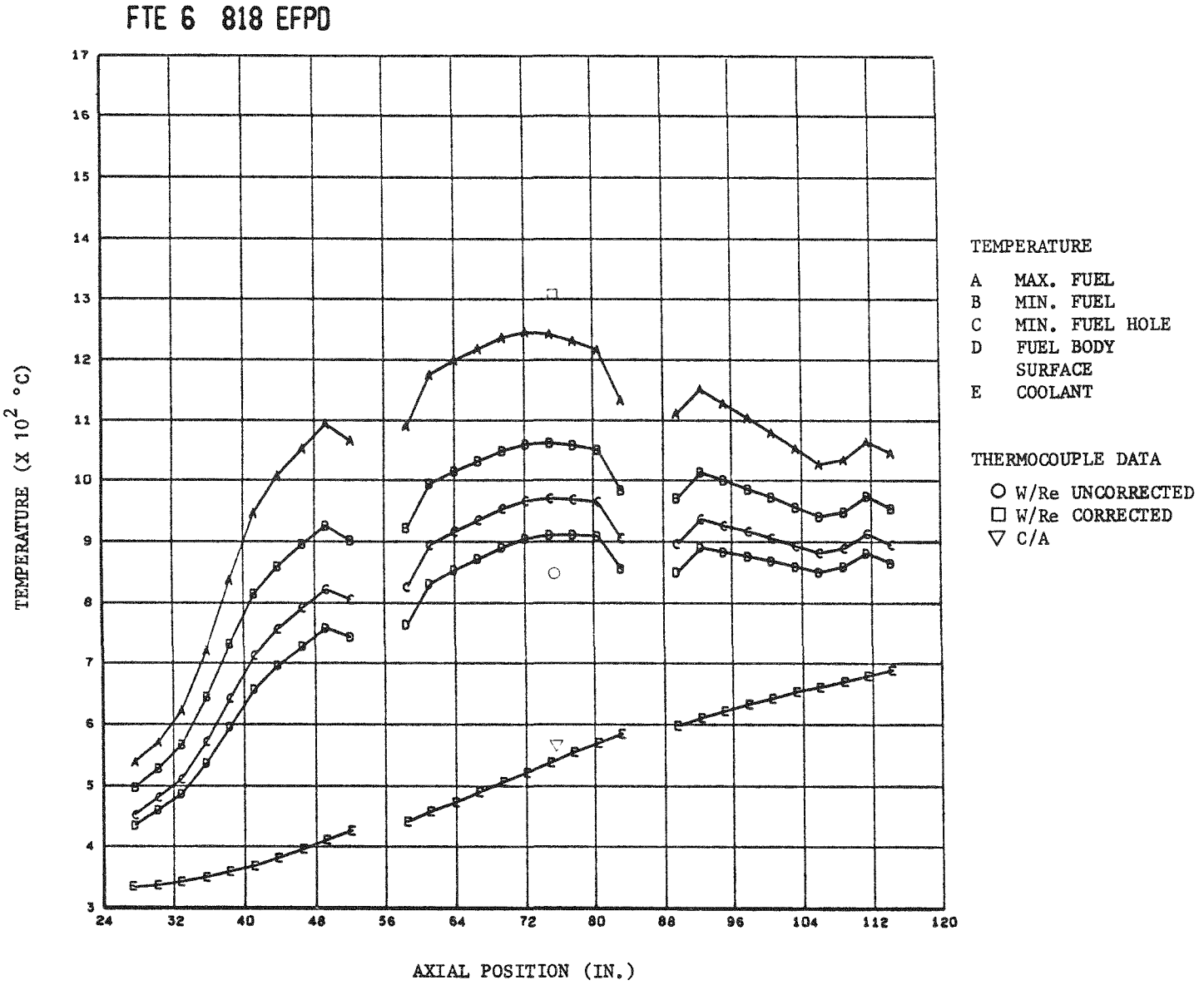

Fig. 9-2. FTE-6 temperature distributions: (k) 818 EFPD

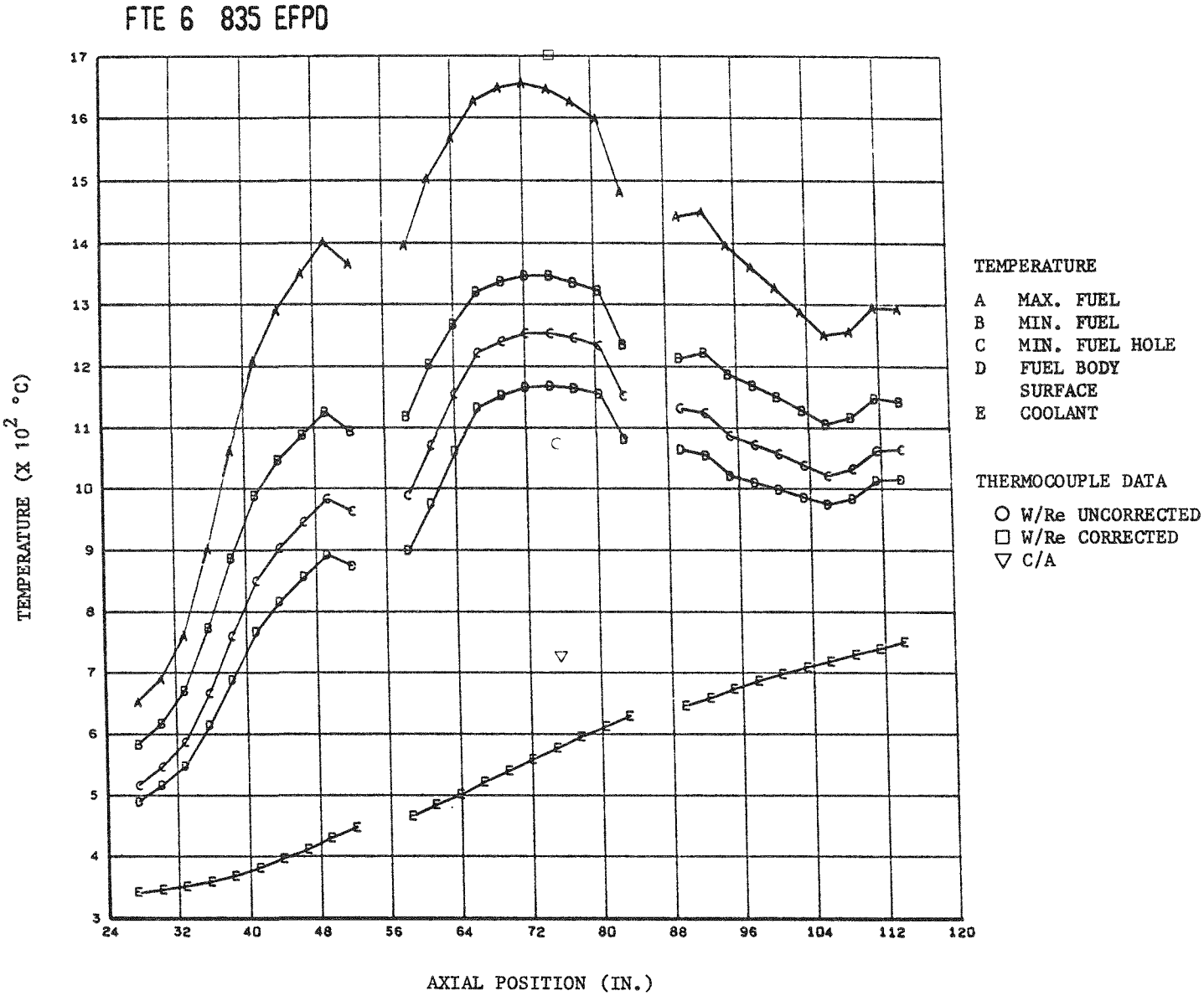

Fig. 9-2. FTE-6 temperature distributions: (1) 835 EFPD

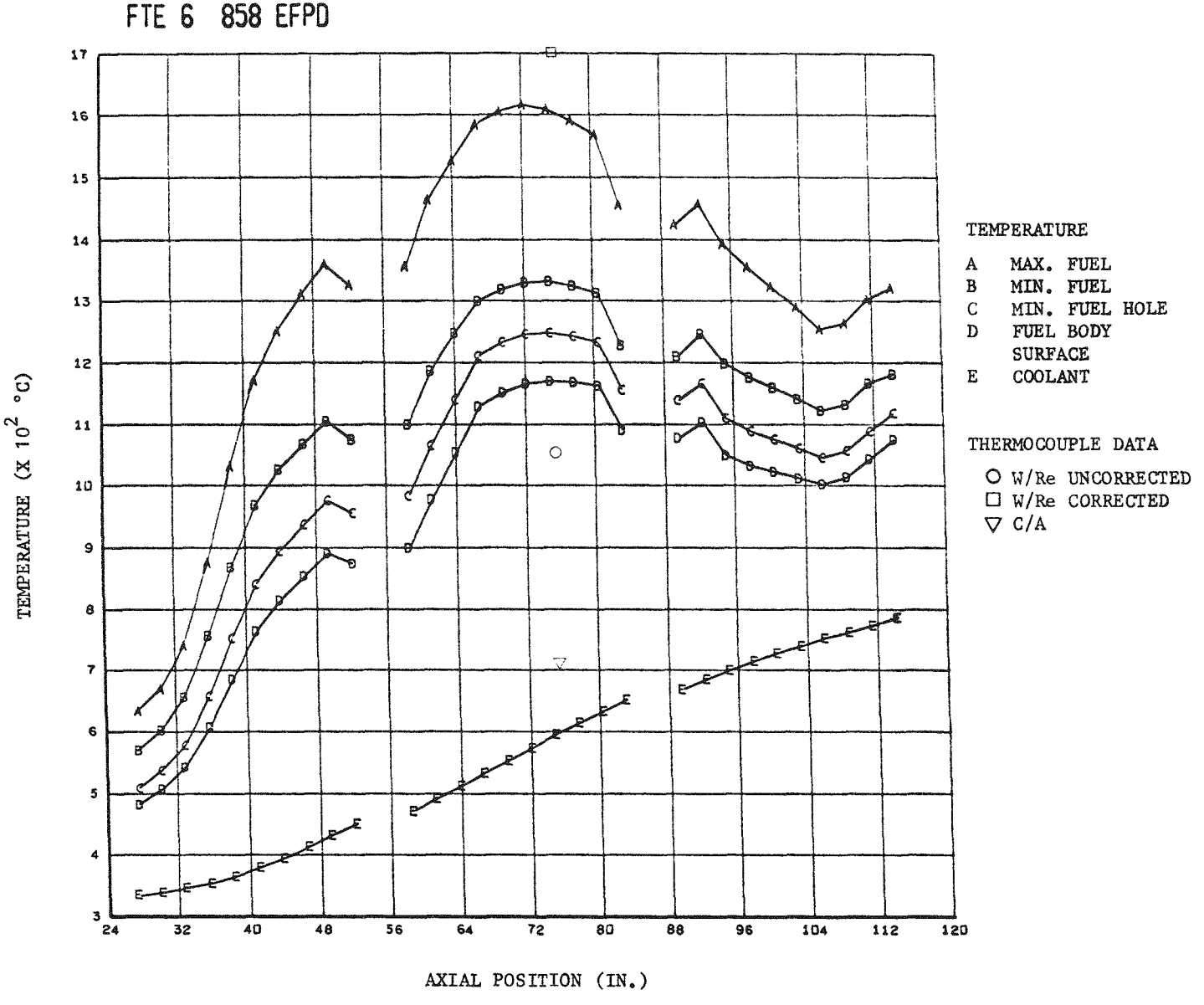

Fig. 9-2. FTE-6 temperature distributions: (m) 858 EFPD

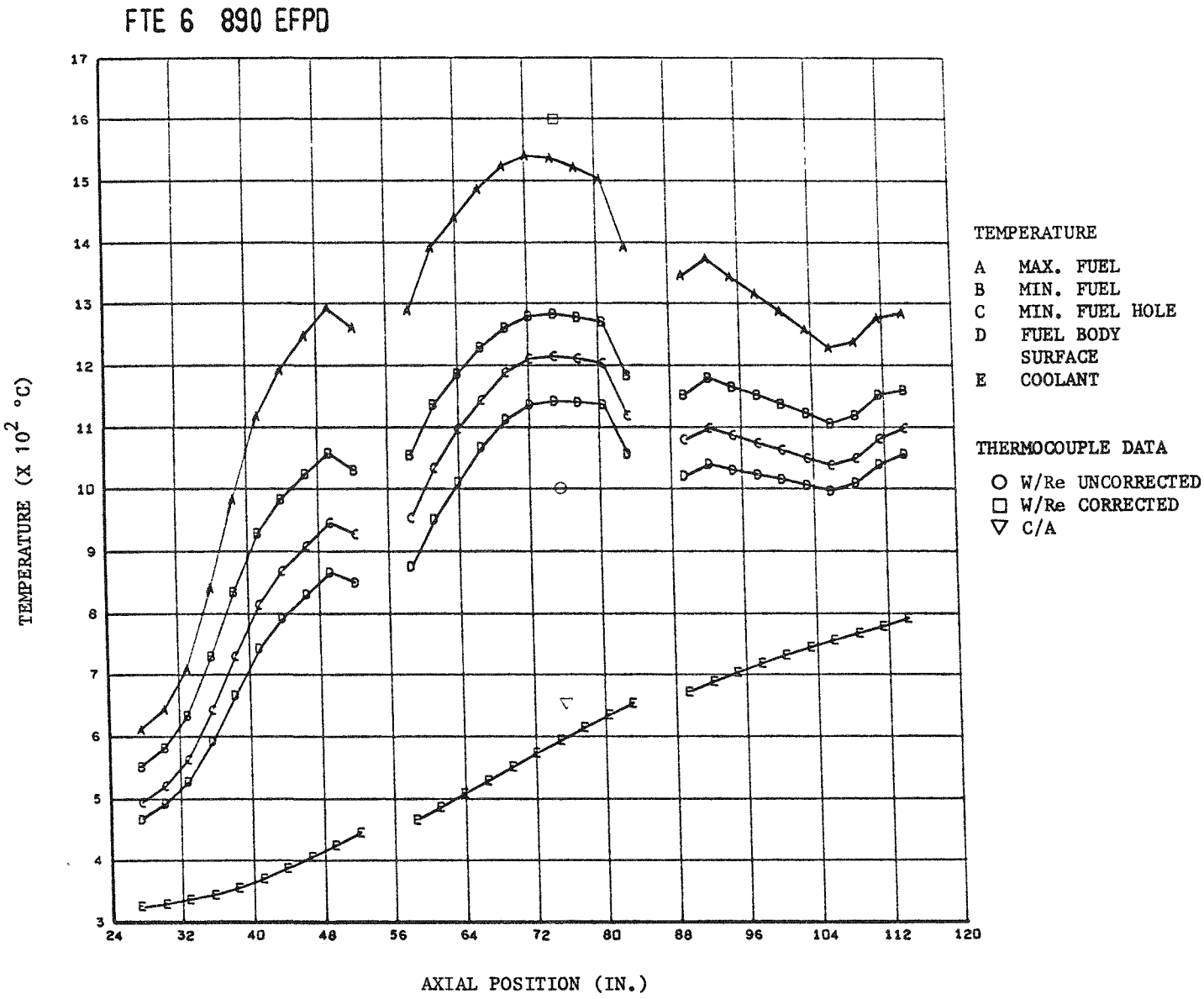

Fig. 9-2. FTE-6 temperature distributions: (n) 890 EFPD

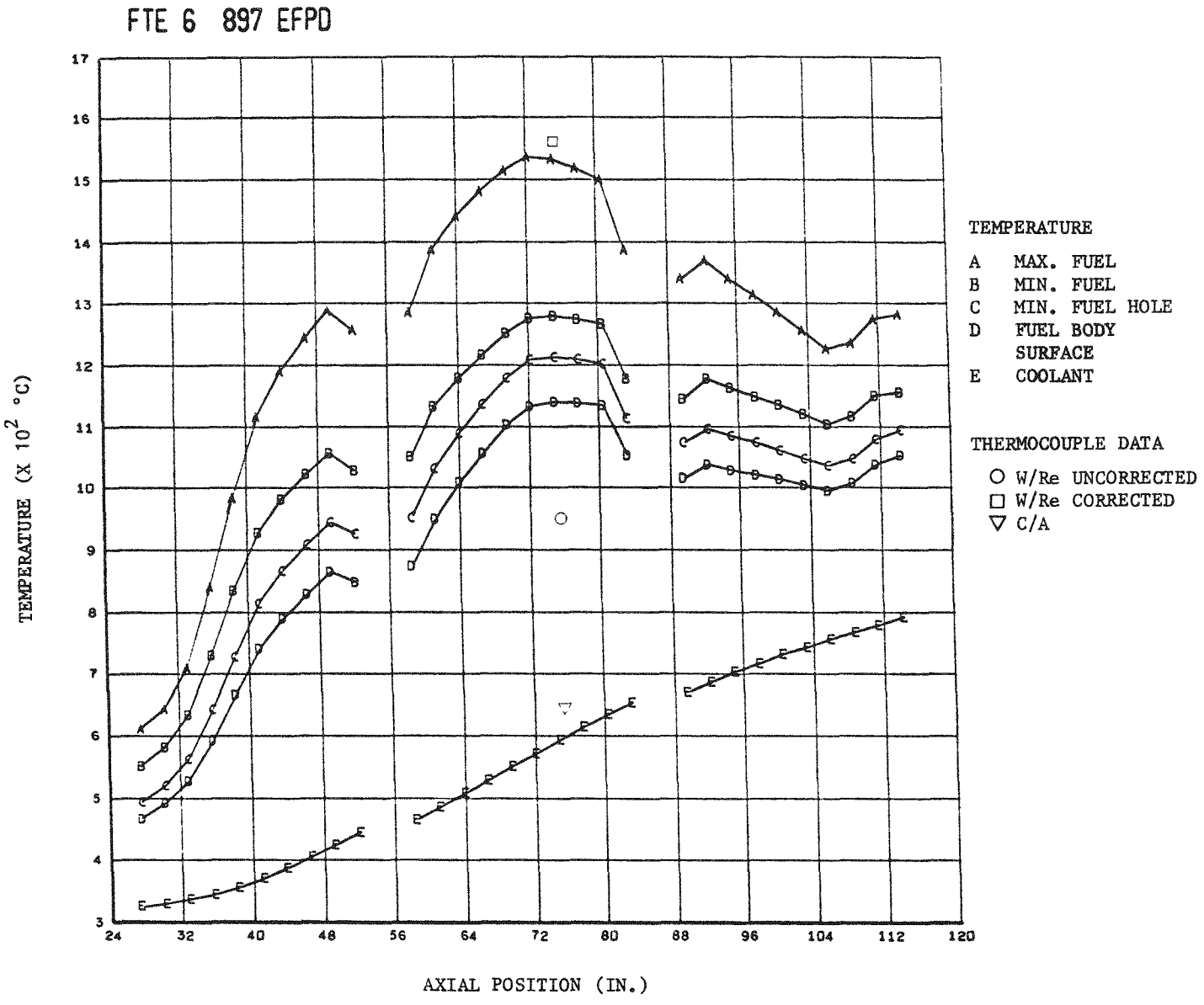

Fig. 9-2. FTE-6 temperature distributions: (o) 897 EFPD

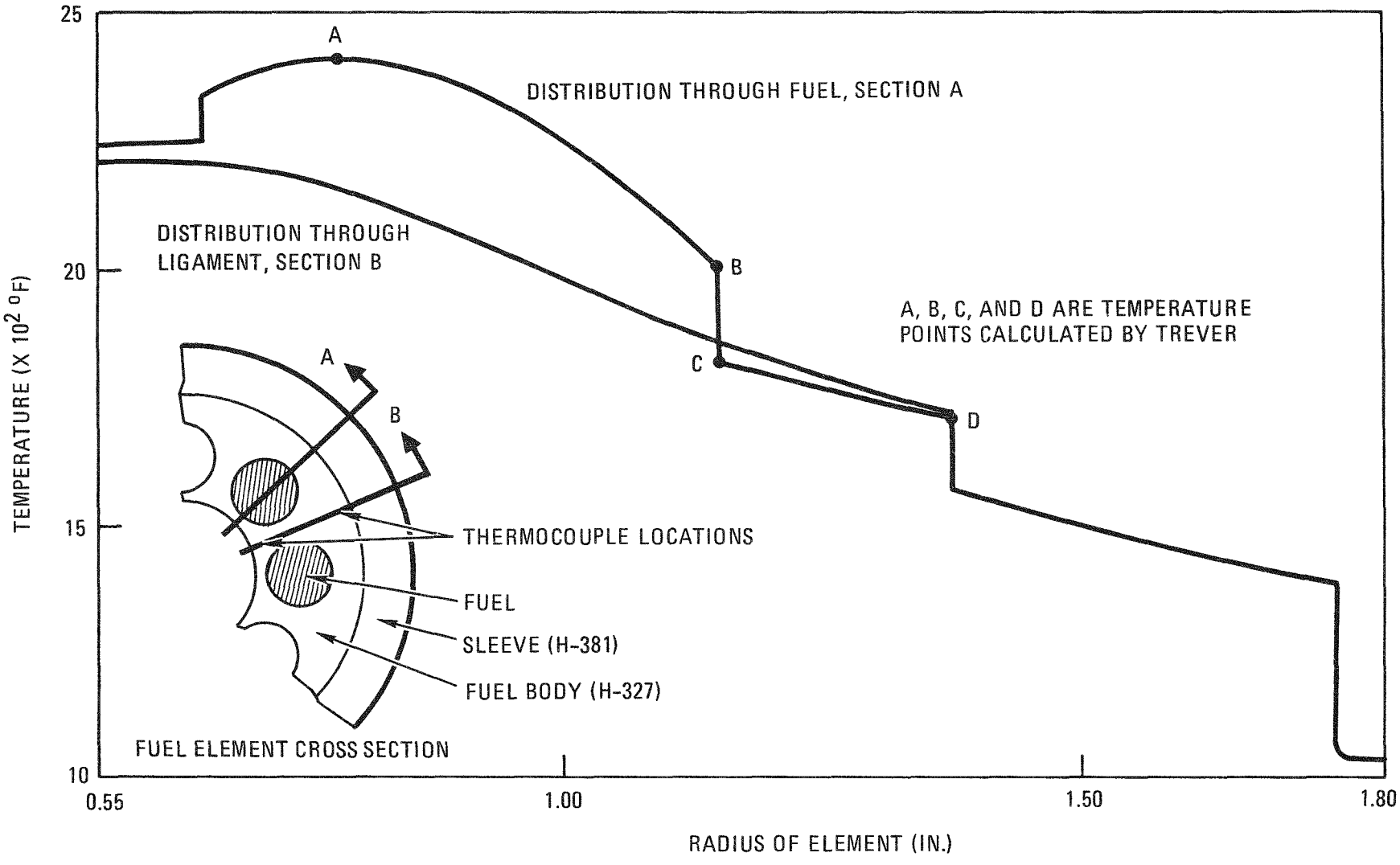

Fig. 9-3. Radial temperature distribution in a typical fuel test element

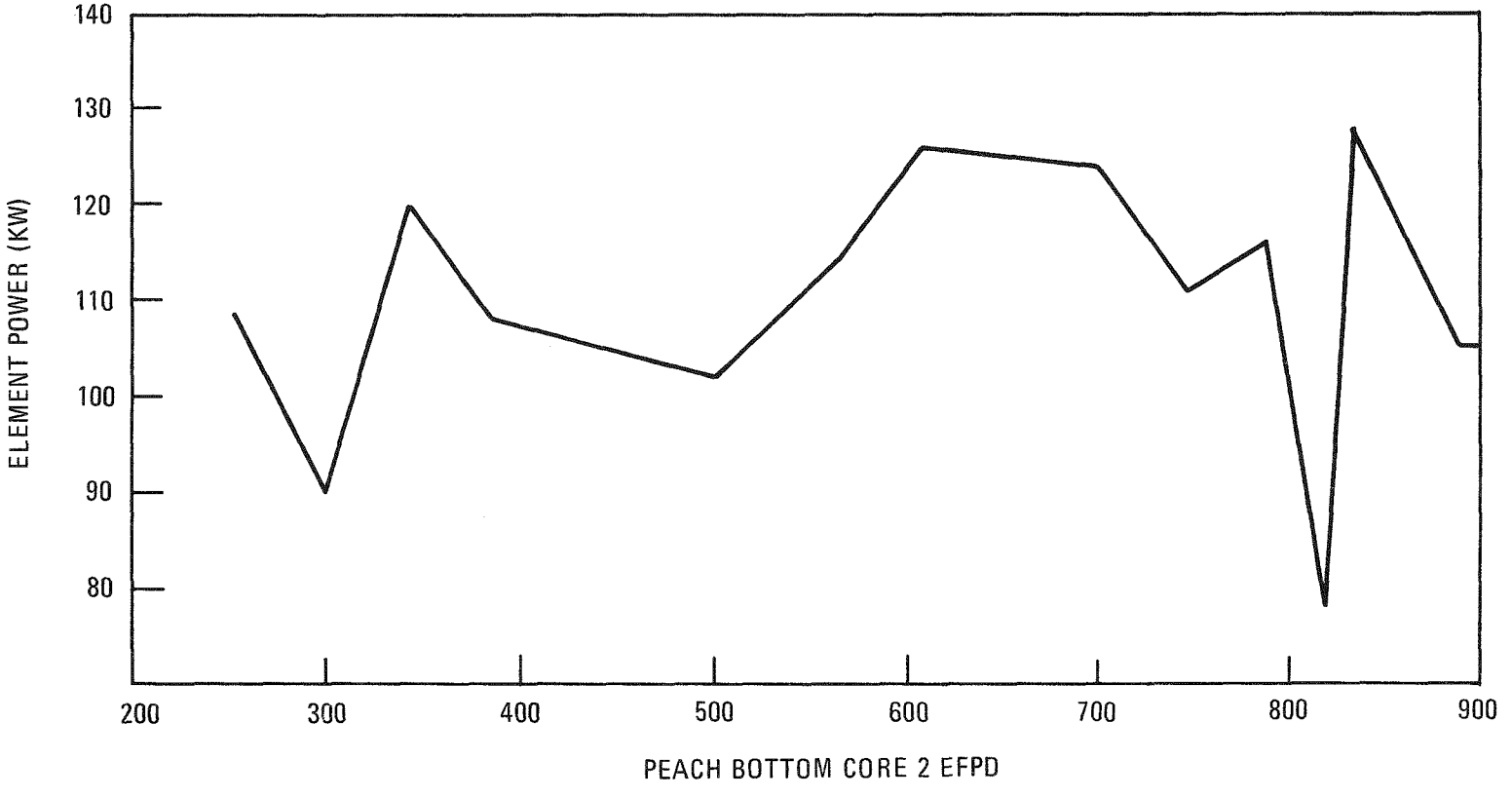

Fig. 9-4. FTE-6 power history

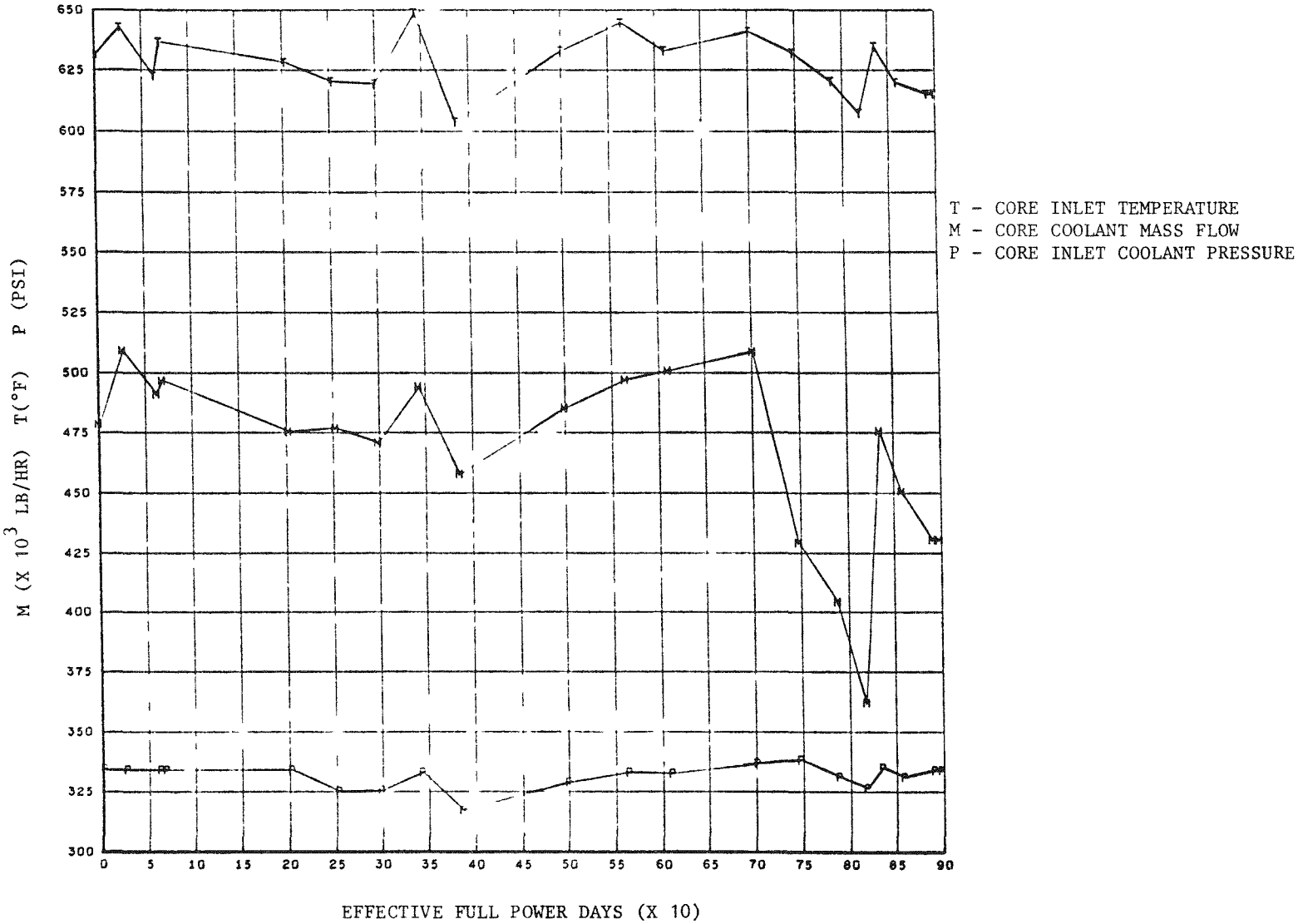

Fig. 9-5. Peach Bottom Core 2 operating parameters

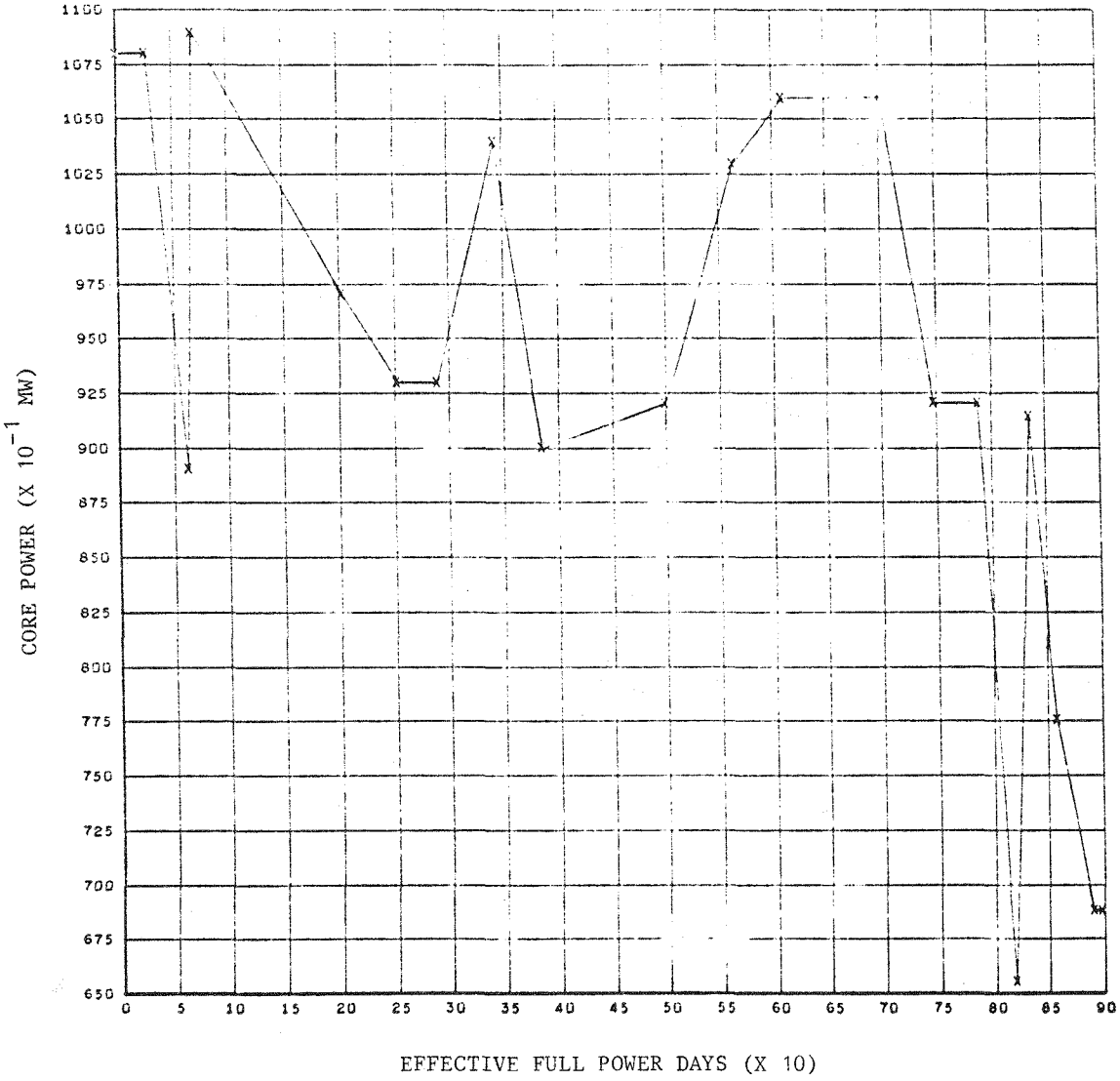

Fig. 9-6. Peach Bottom Core 2 power

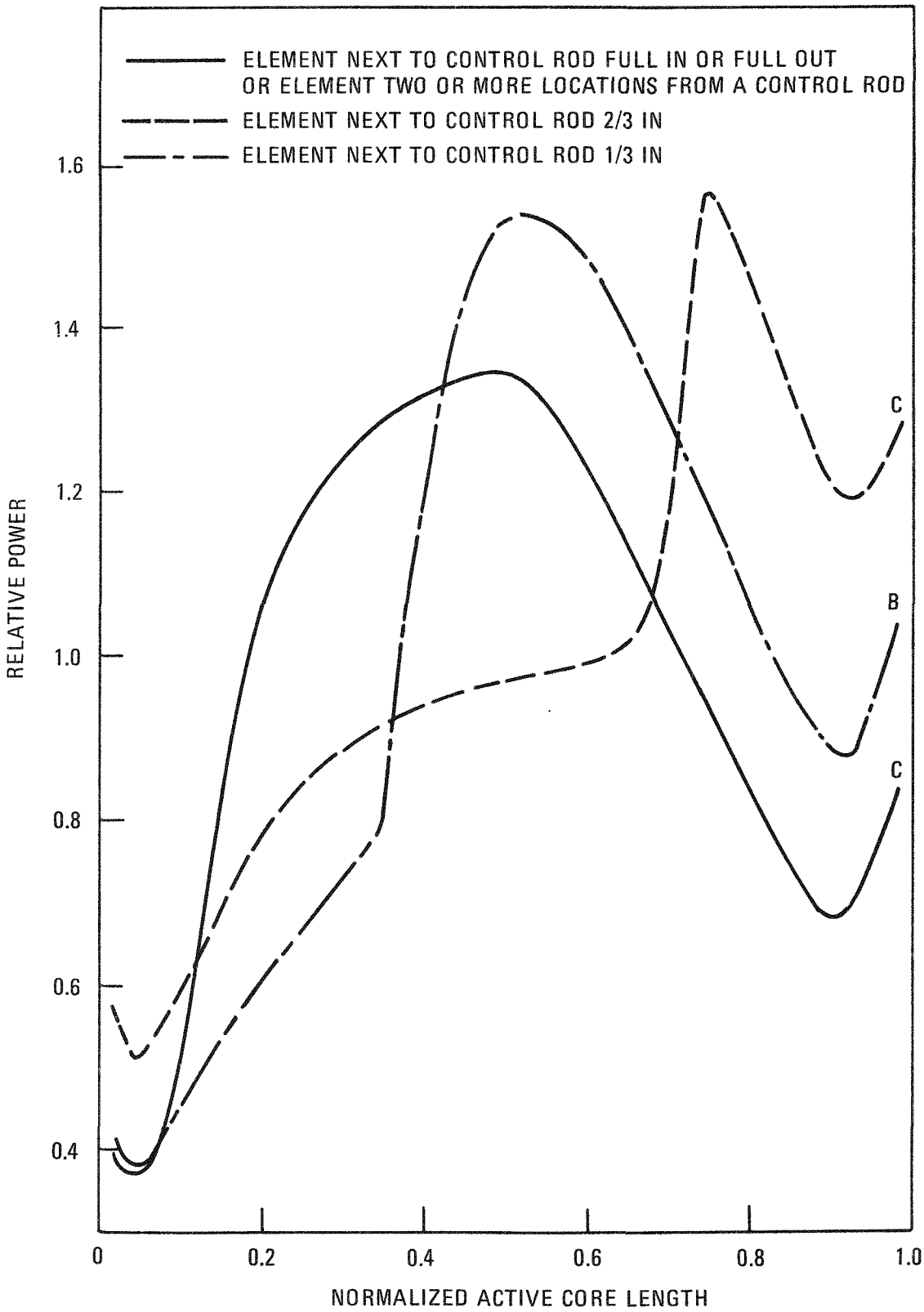

Fig. 9-7. Peach Bottom axial power distribution

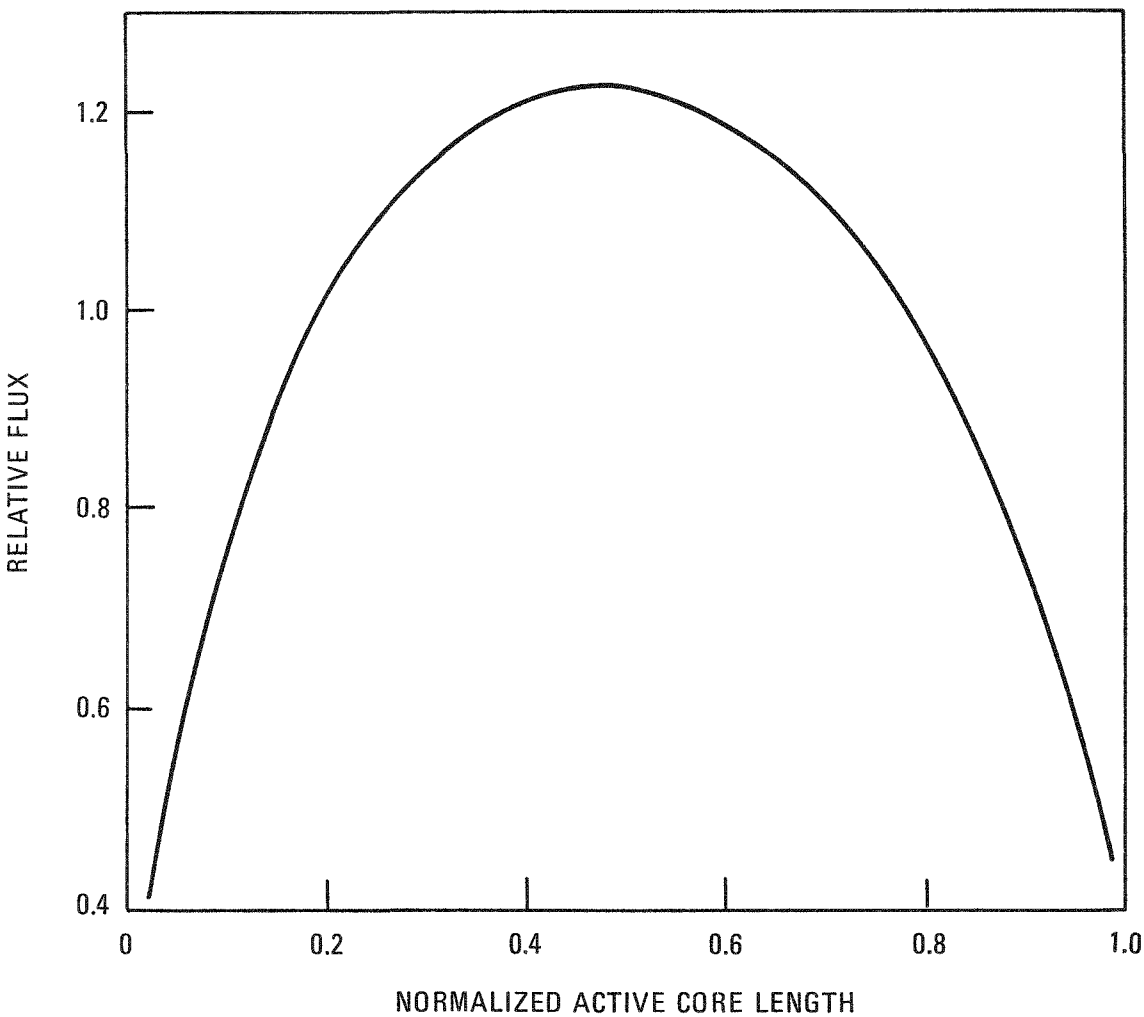

Fig. 9-8. Peach Bottom fast flux axial distribution, MOL (600 EFPD), FEVER results

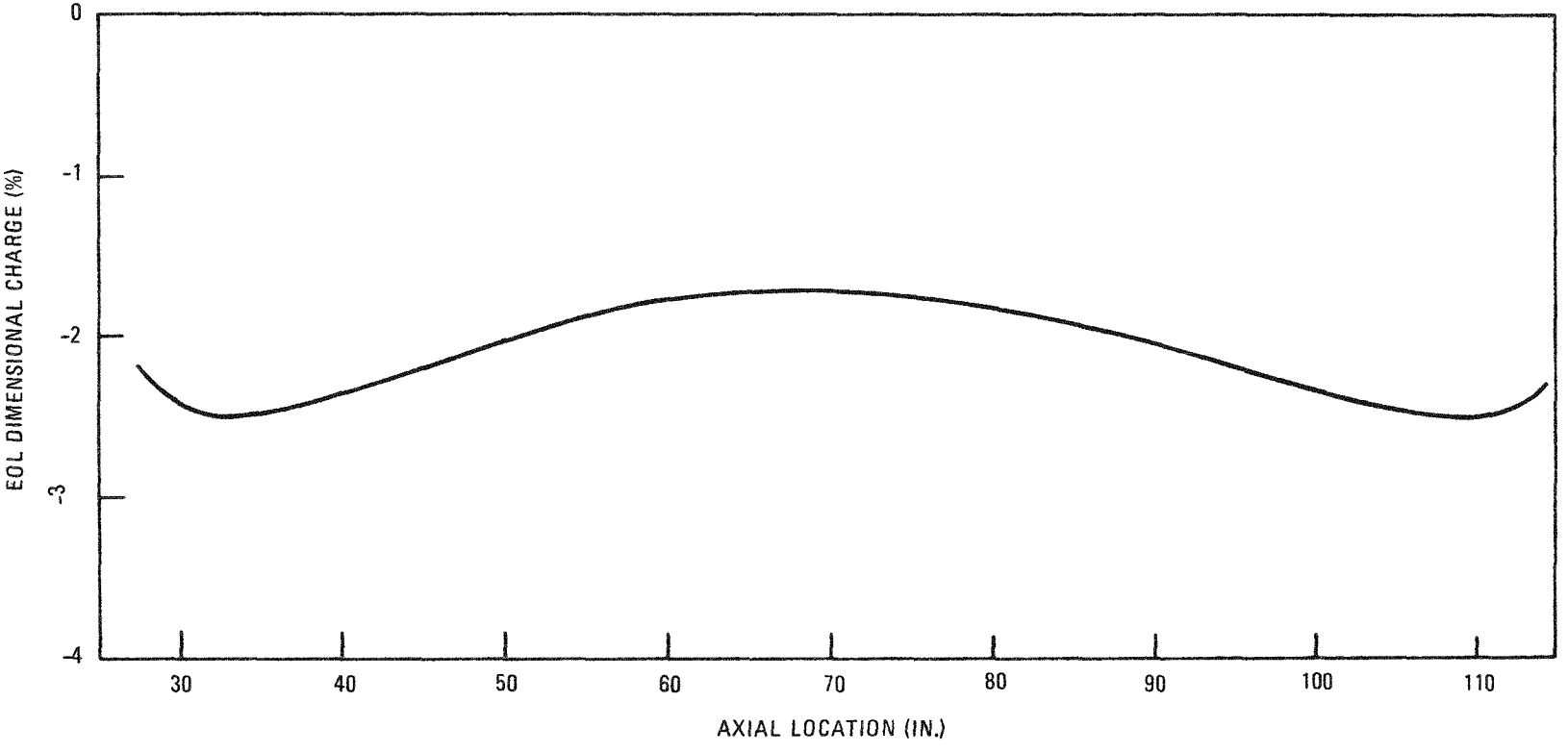

Fig. 9-9. FTE-6 fuel and EOL radial irradiation strain, TREVER calculation, TRISO/BISO fuel rod type

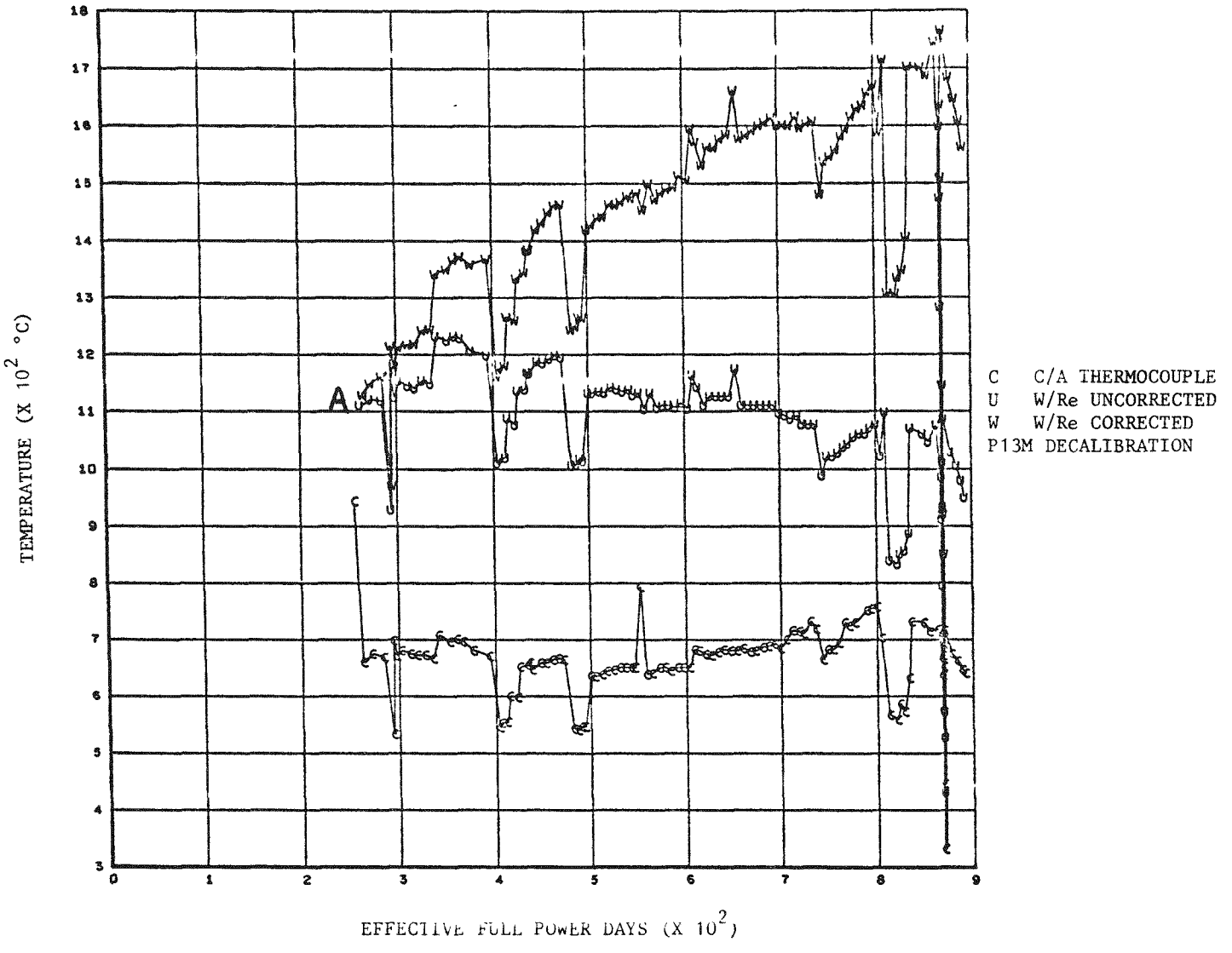

Fig. 9-10. FTE-6 thermocouple data

Fig. 9-11. FTE-6 identification

Fig. 12. FTE-6 composite photograph of total element

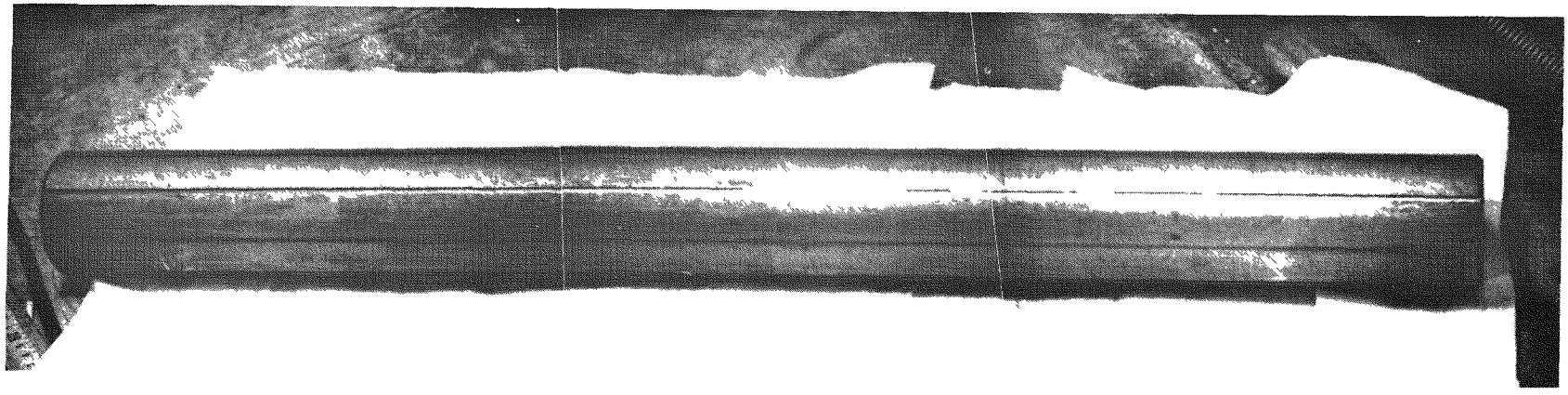

Fig. 9-13. FTE-6 bottom fuel body (1)

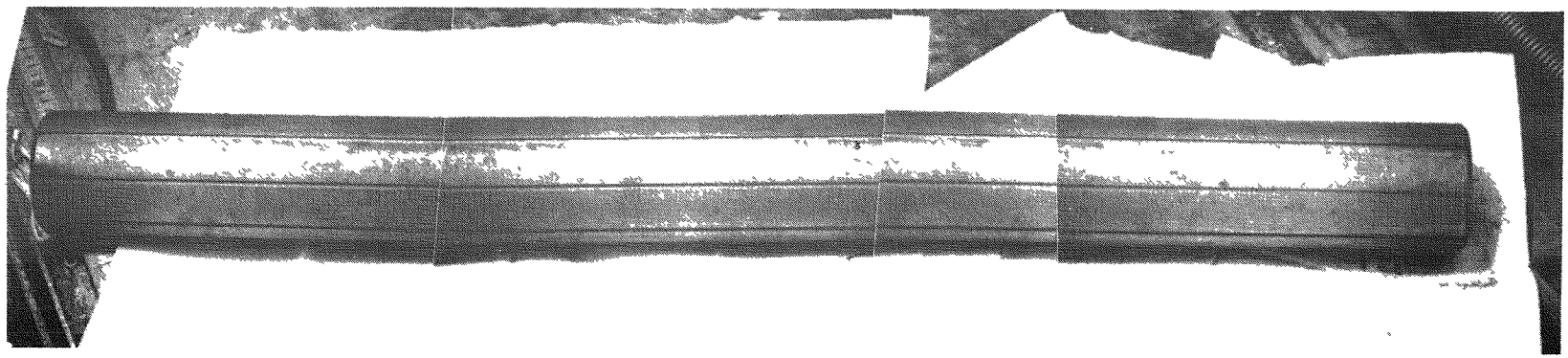

Fig. 9-14. FTE-6 center fuel body (2)

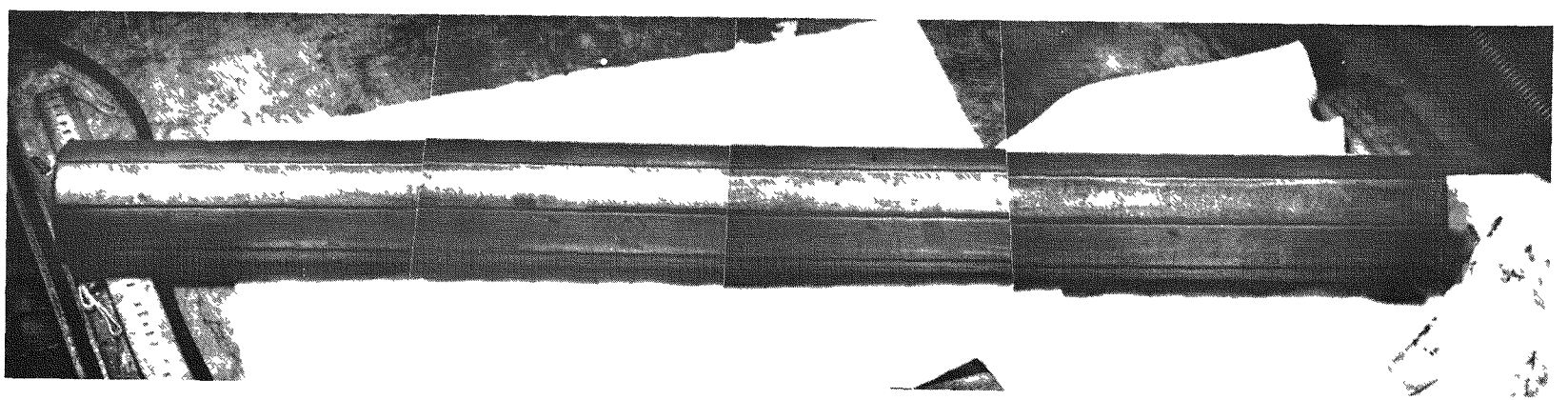

Fig. 9-15. FTE-6 top fuel body (3)

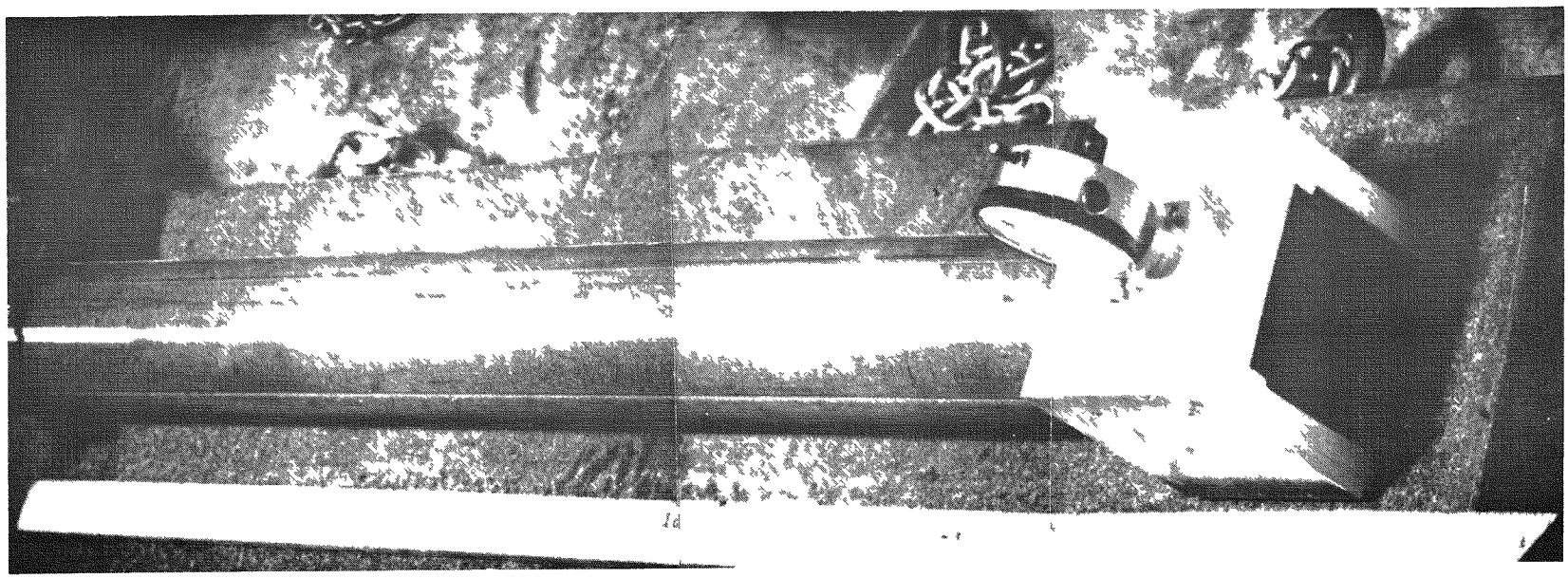

Fig. 9-16. FTE-6 fuel body bow setup

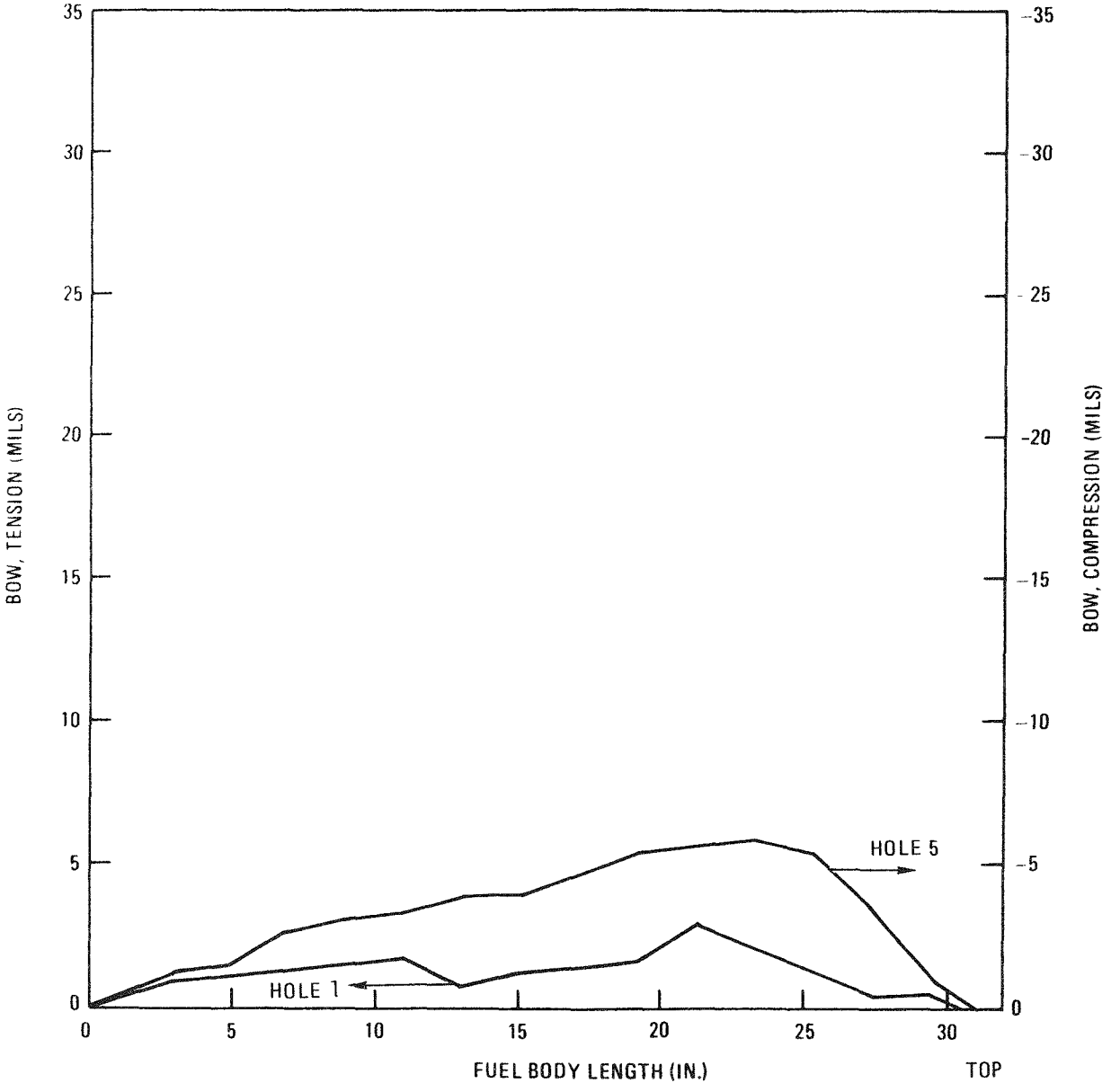

Fig. 9-17. FTE-6 fuel body bow: (a) body 1, holes 1 and 5

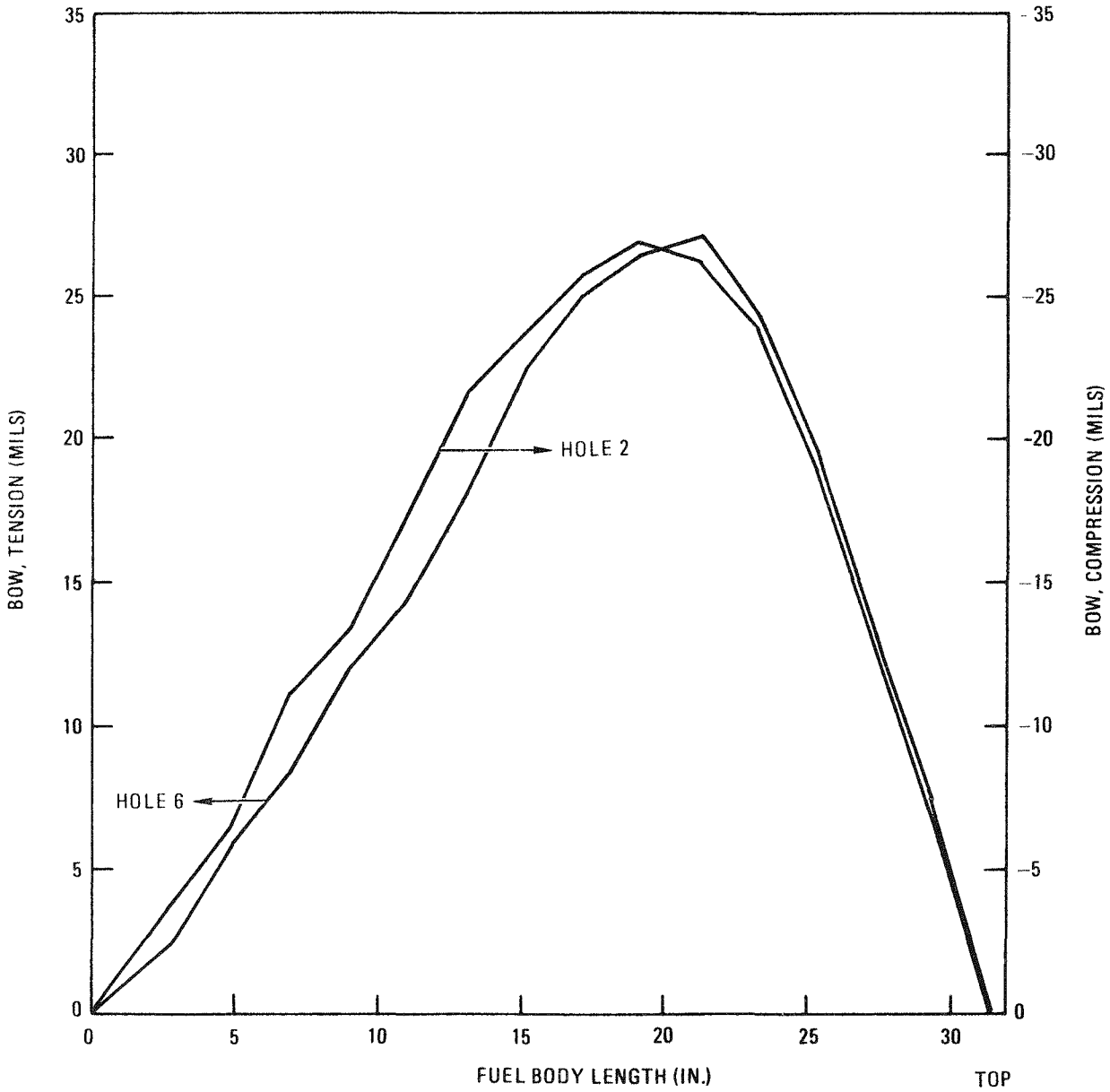

Fig. 9-17. FTE-6 fuel body bow: (b) body 1, holes 2 and 6

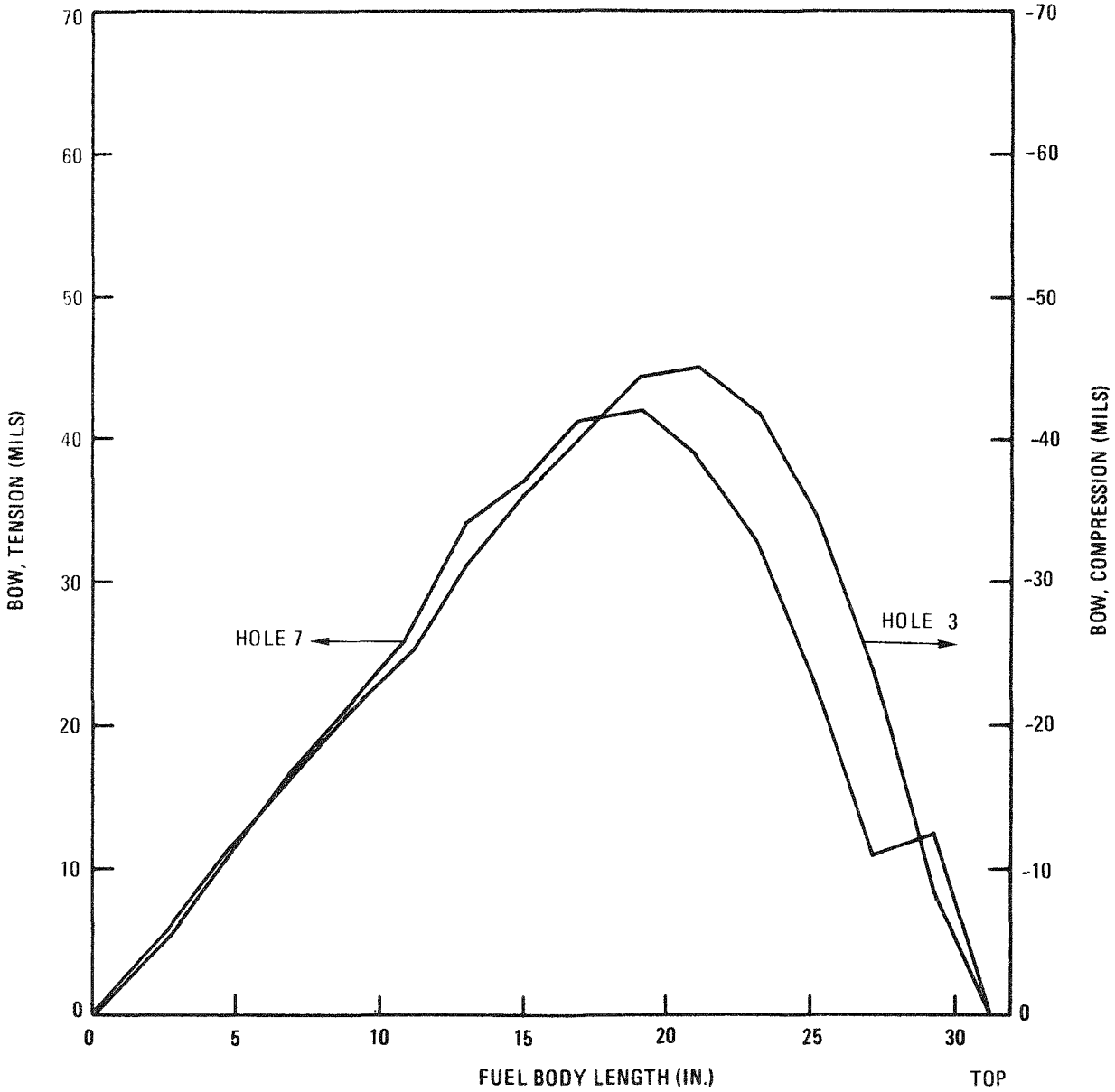

Fig. 9-17. FTE-6 fuel body bow: (c) body 1, holes 3 and 7

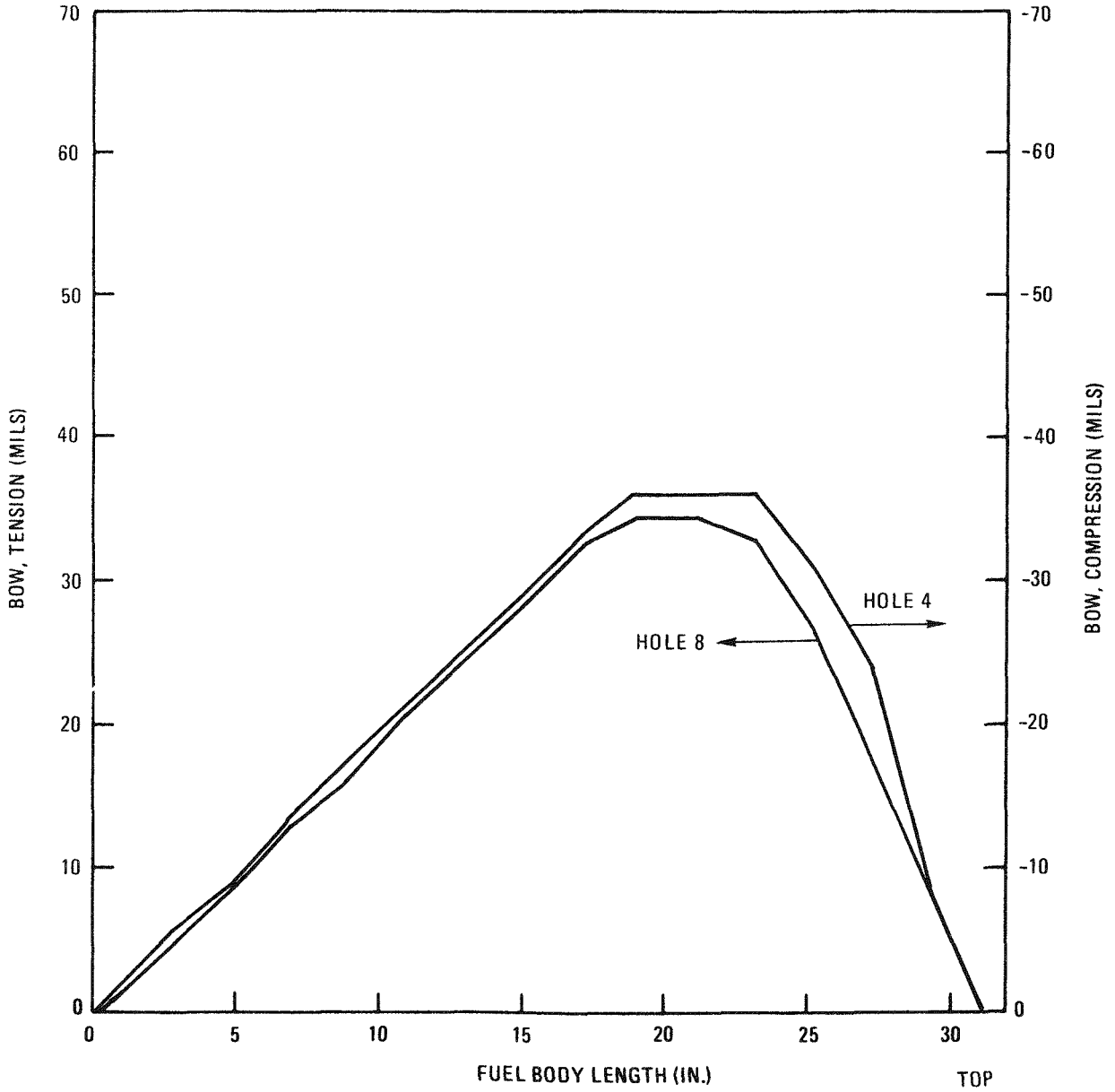

Fig. 9-17. FTE-6 fuel body bow: (d) body 1, holes 4 and 8

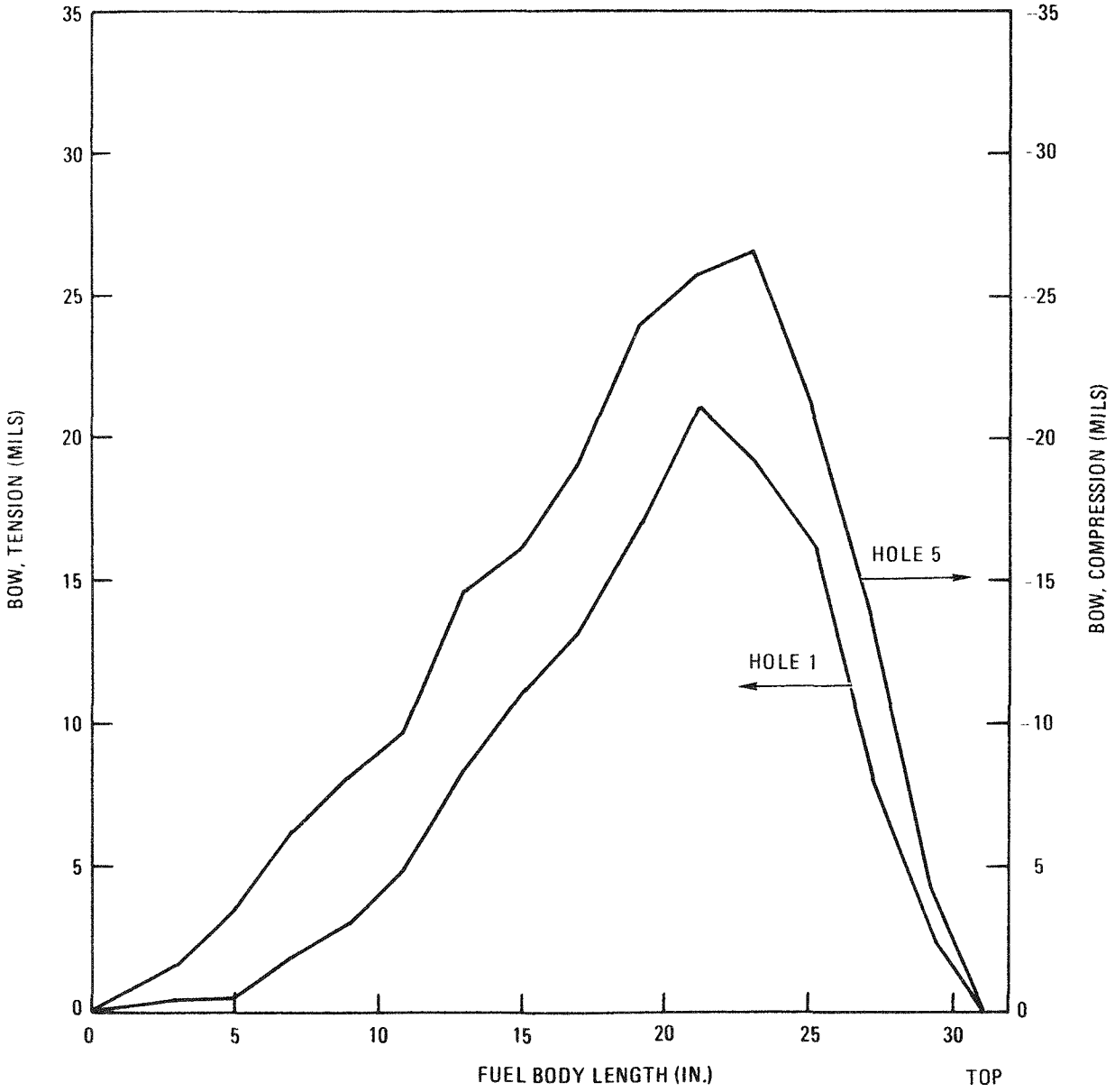

Fig. 9-17. FTE-6 fuel body bow: (e) body 2, holes 1 and 5

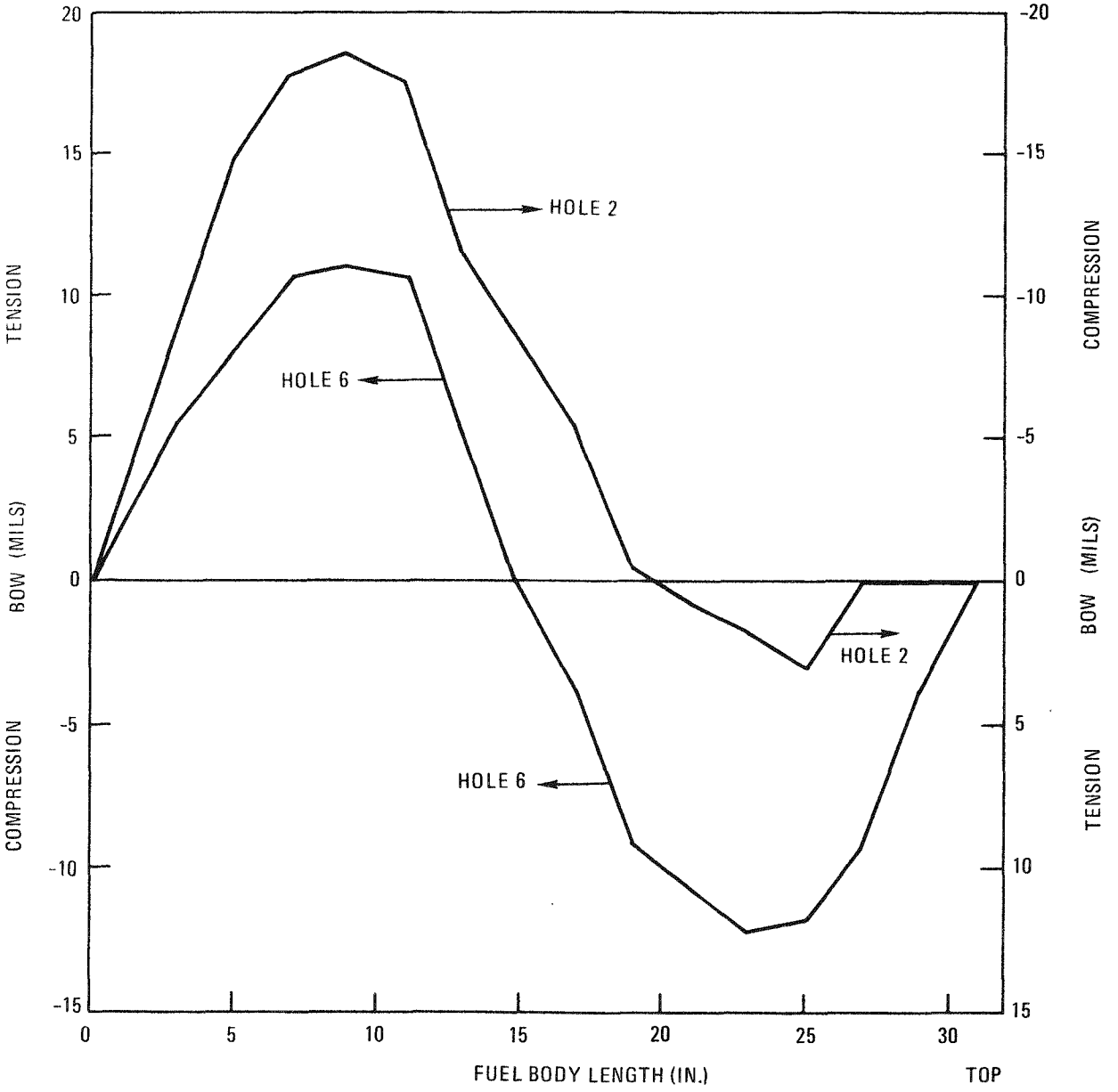

Fig. 9-17. FTE-6 fuel body bow: (f) body 2, holes 2 and 6

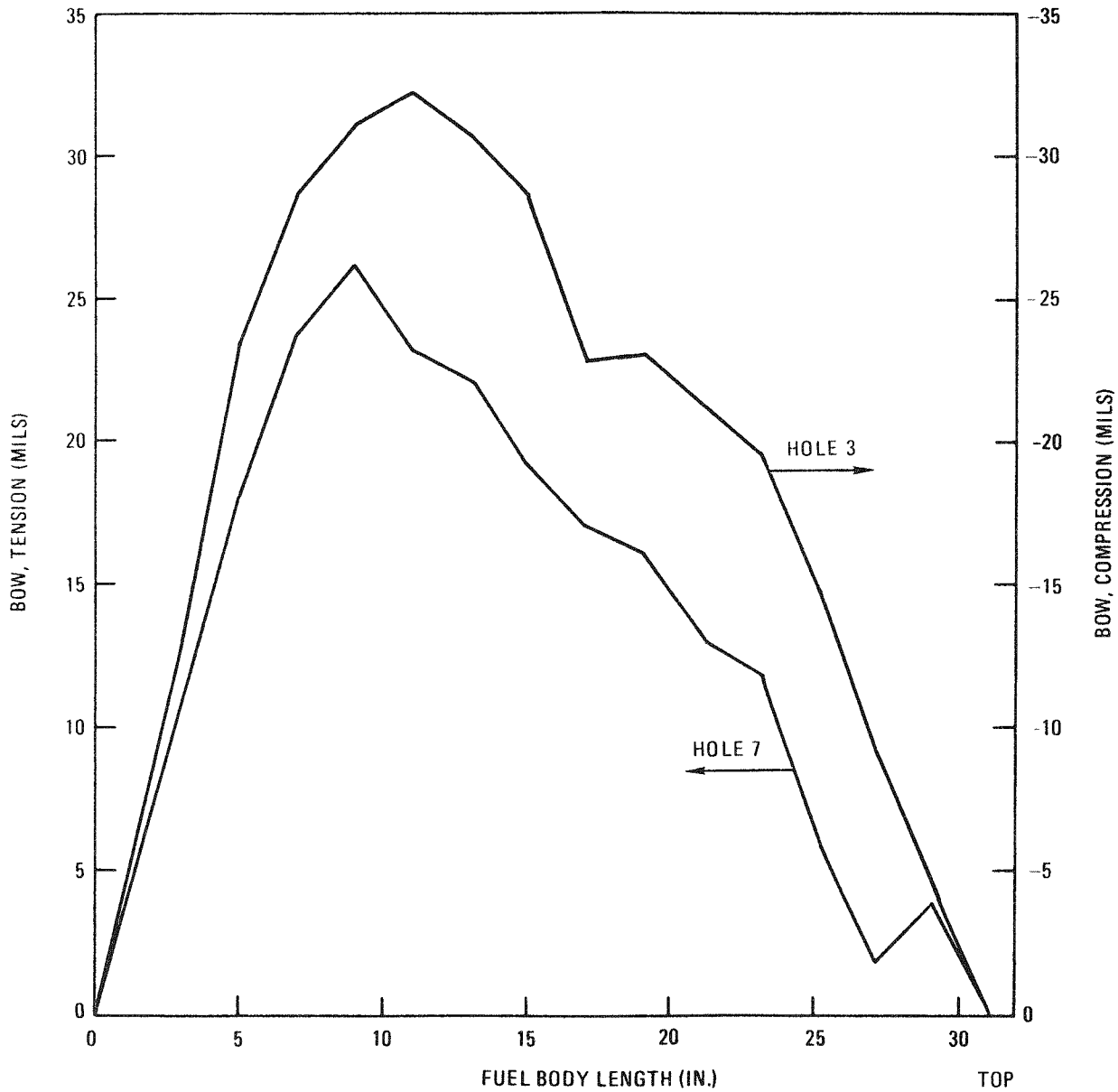

Fig. 9-17. FTE-6 fuel body bow: (g) body 2, holes 3 and 7

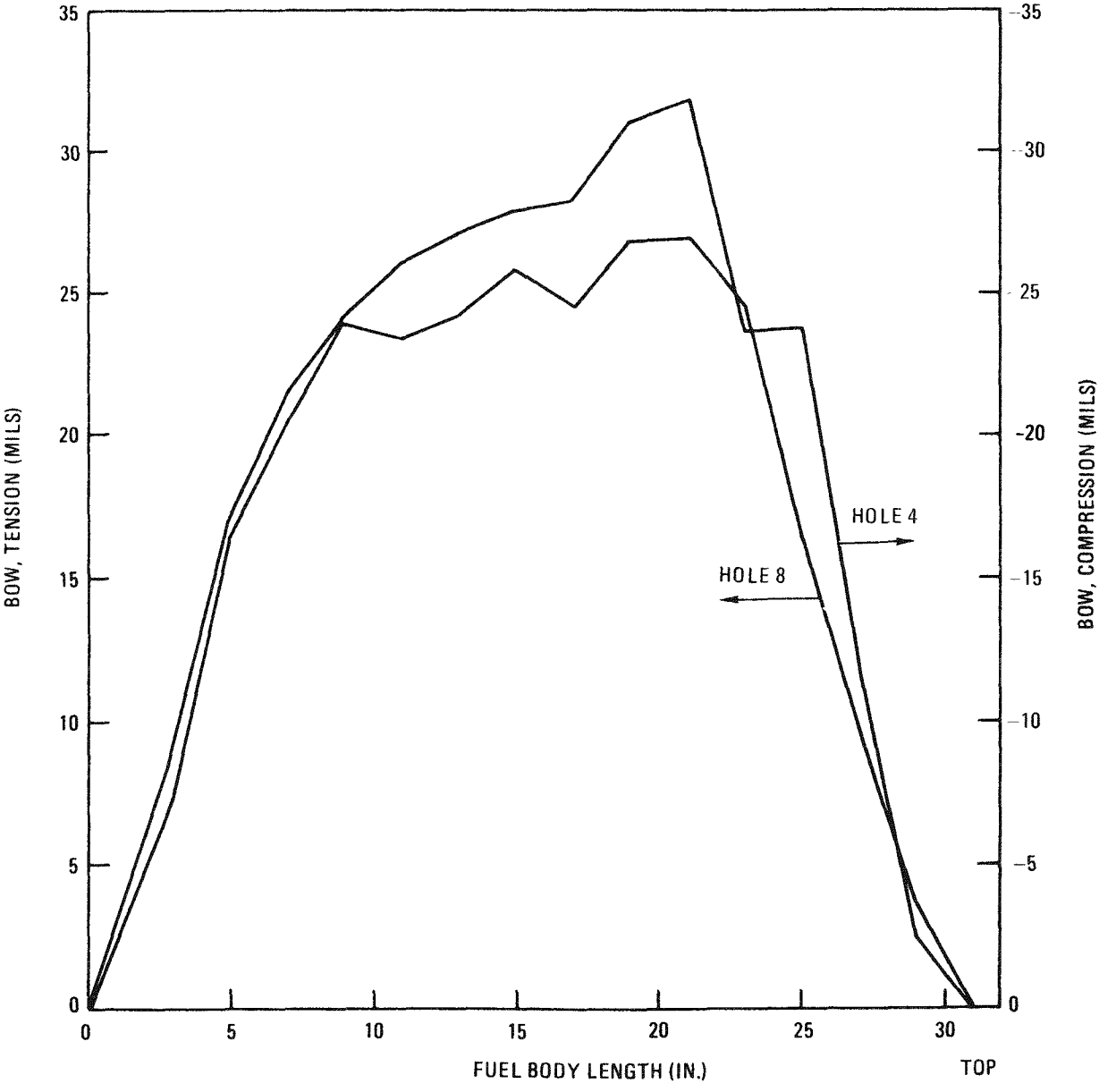

Fig. 9-17. FTE-6 fuel body bow: (h) body 2, holes 4 and 8

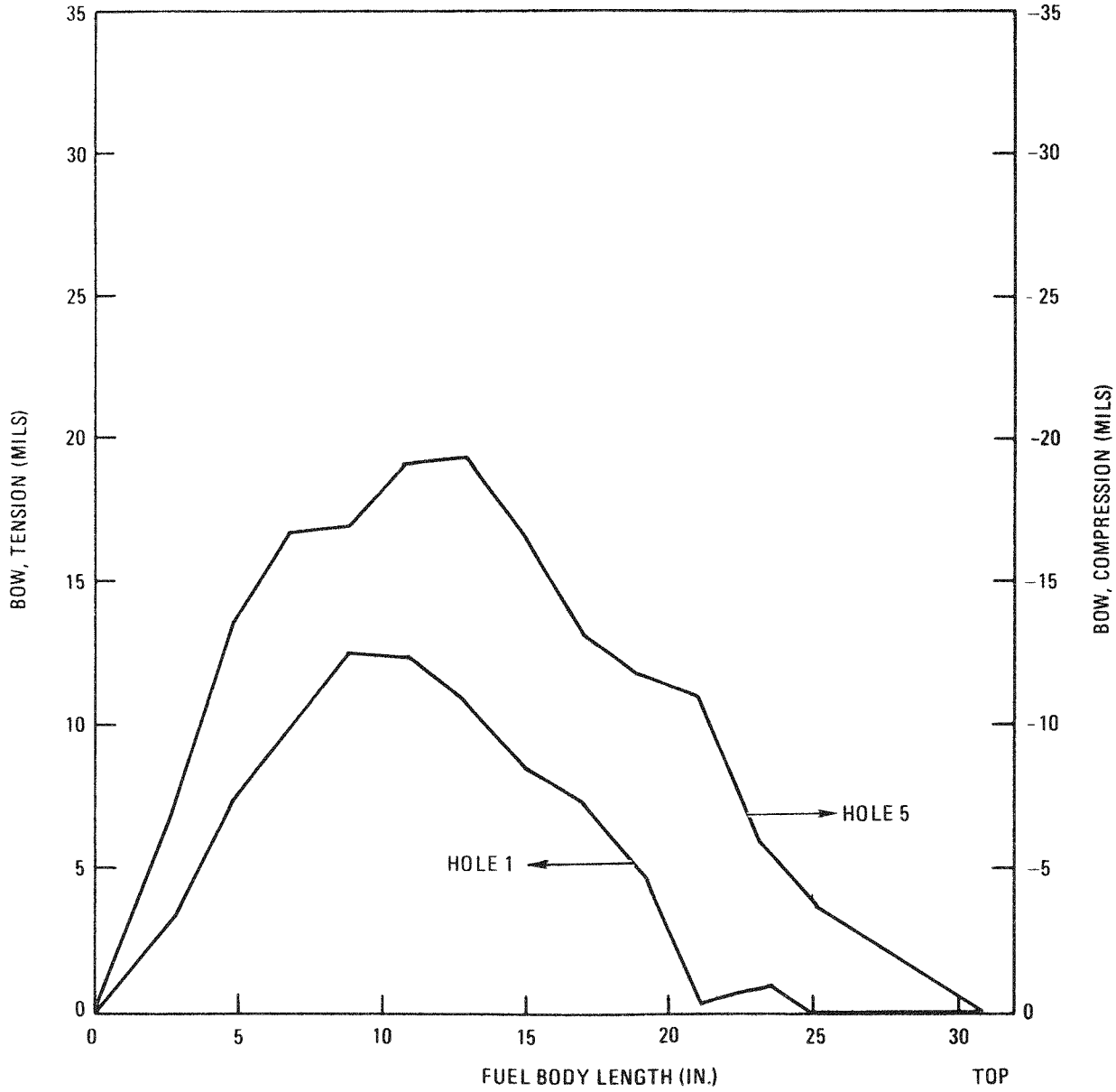

Fig. 9-17. FTE-6 fuel body bow: (i) body 3, holes 1 and 5

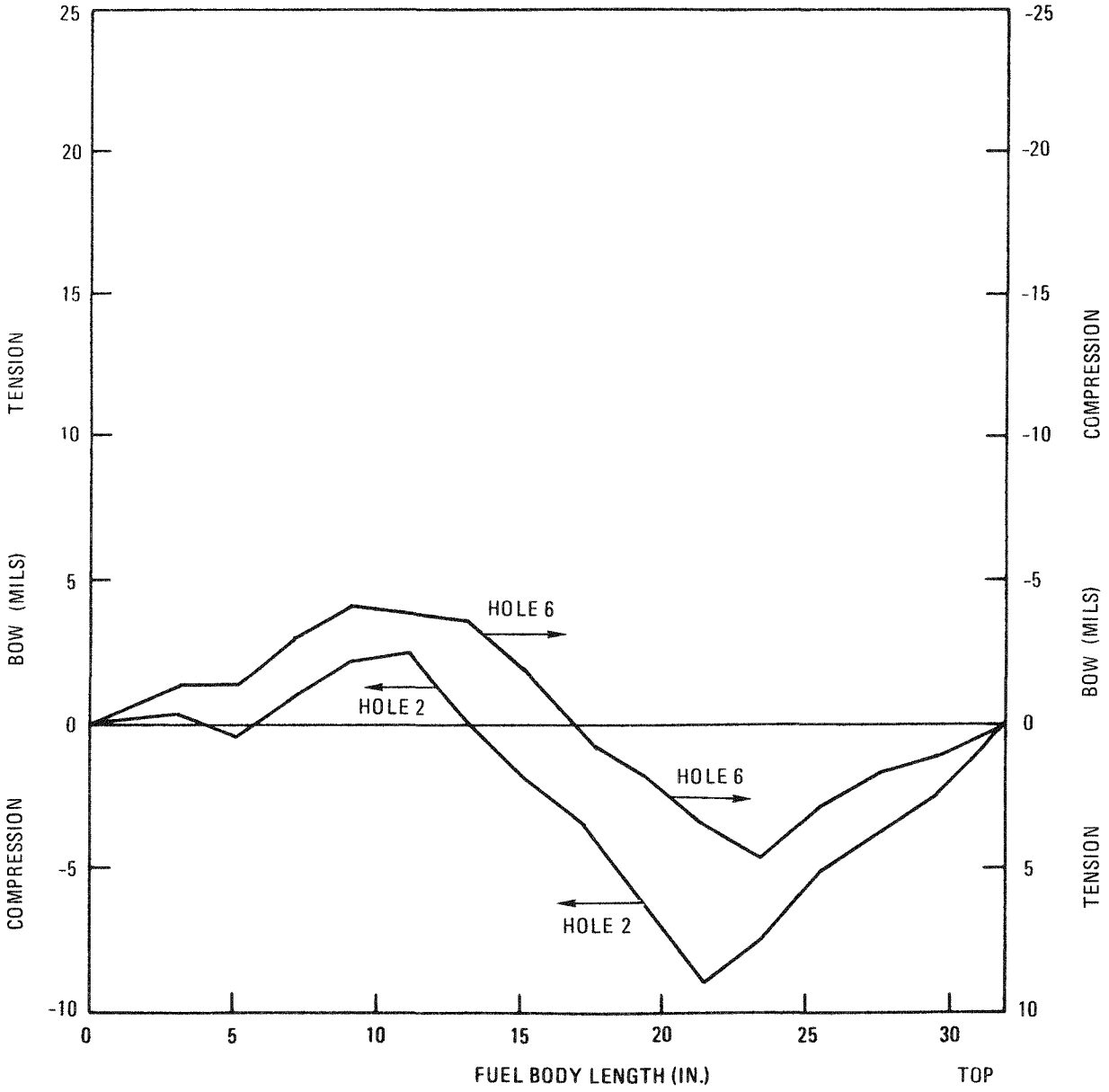

Fig. 9-17. FTE-6 fuel body bow: (j) body 3, holes 2 and 6

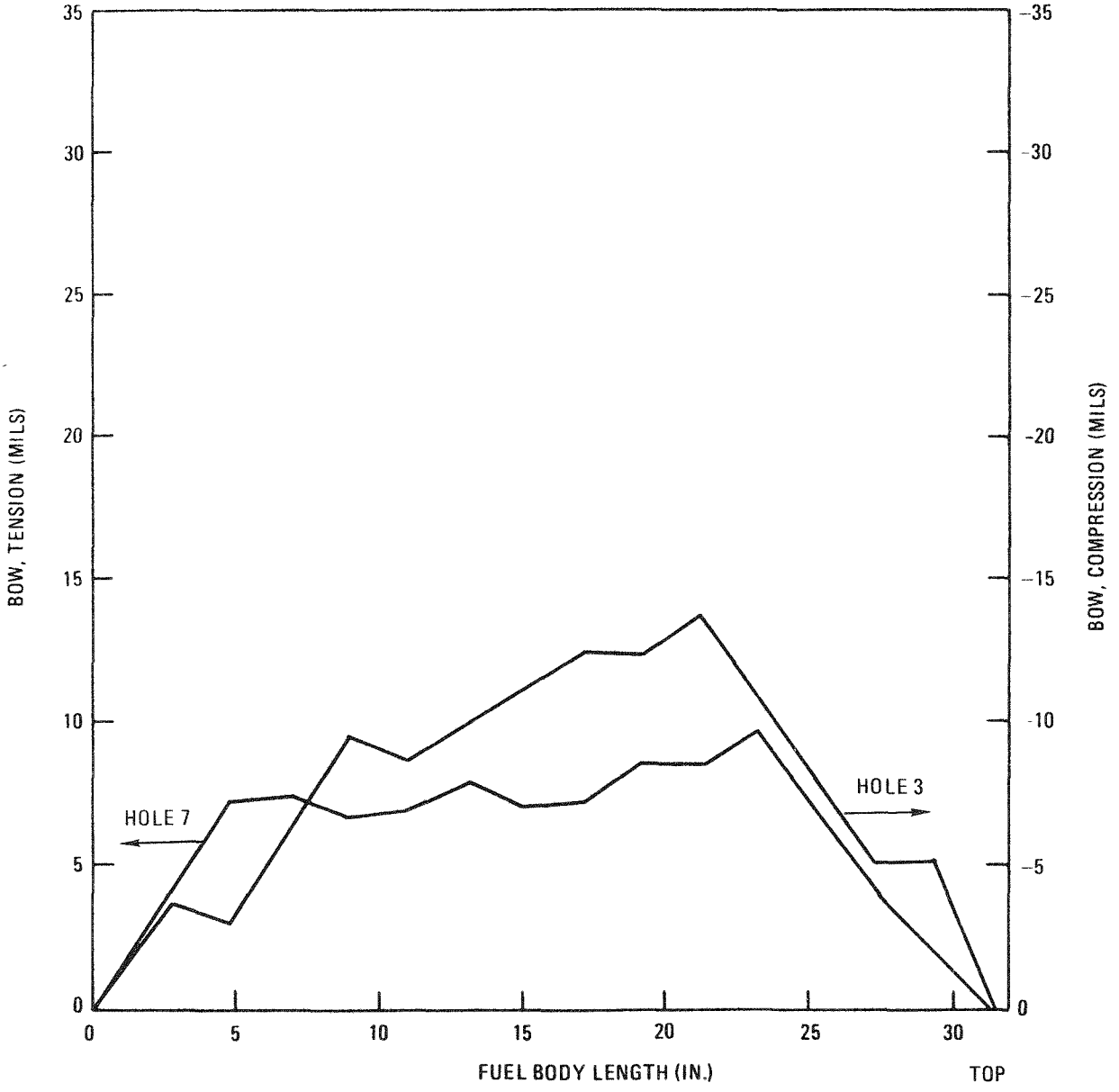

Fig. 9-17. FTE-6 fuel body bow: (k) body 3, holes 3 and 7

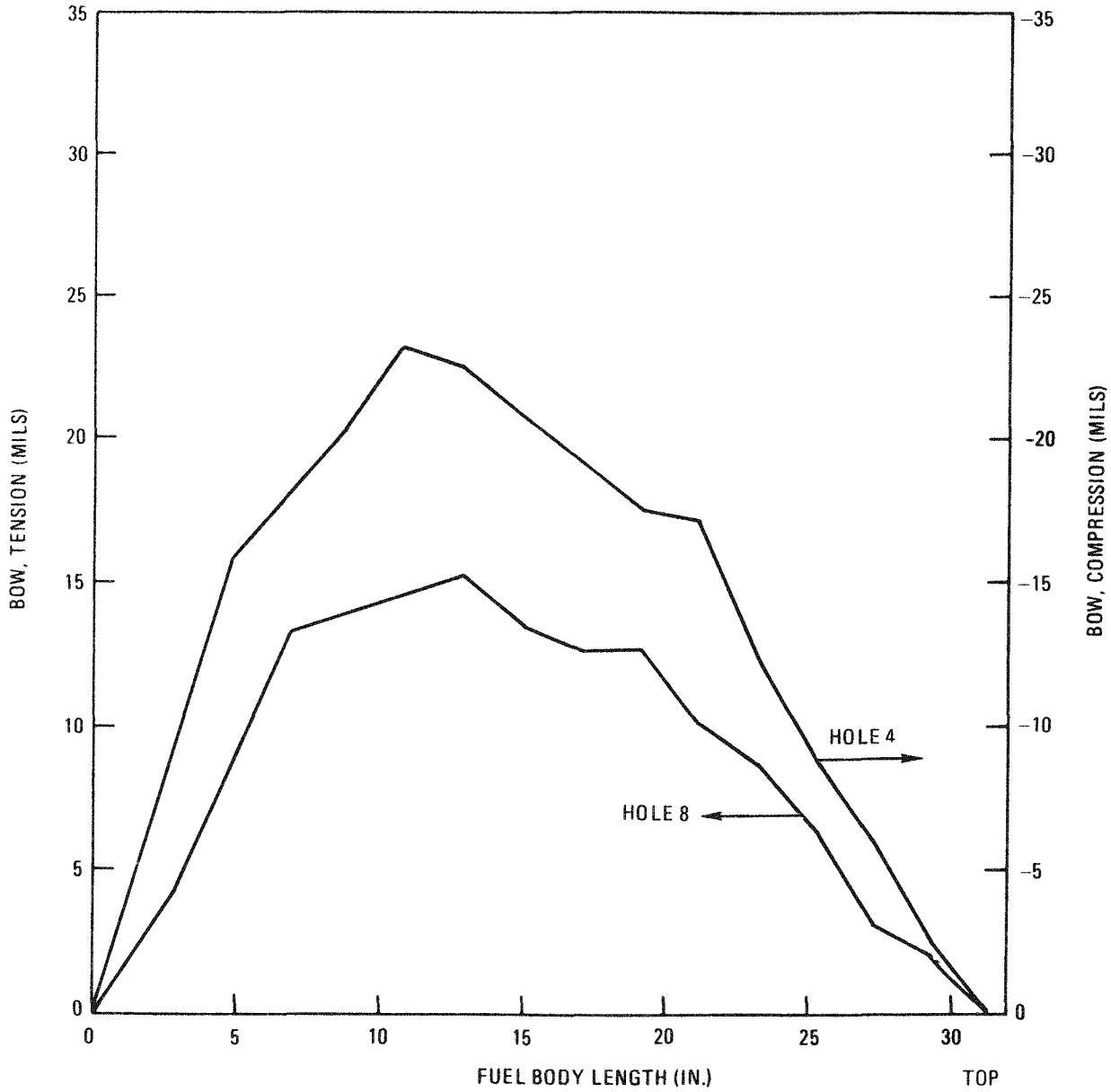

Fig. 9-17. FTE-6 fuel body bow: (1) body 3, holes 4 and 8

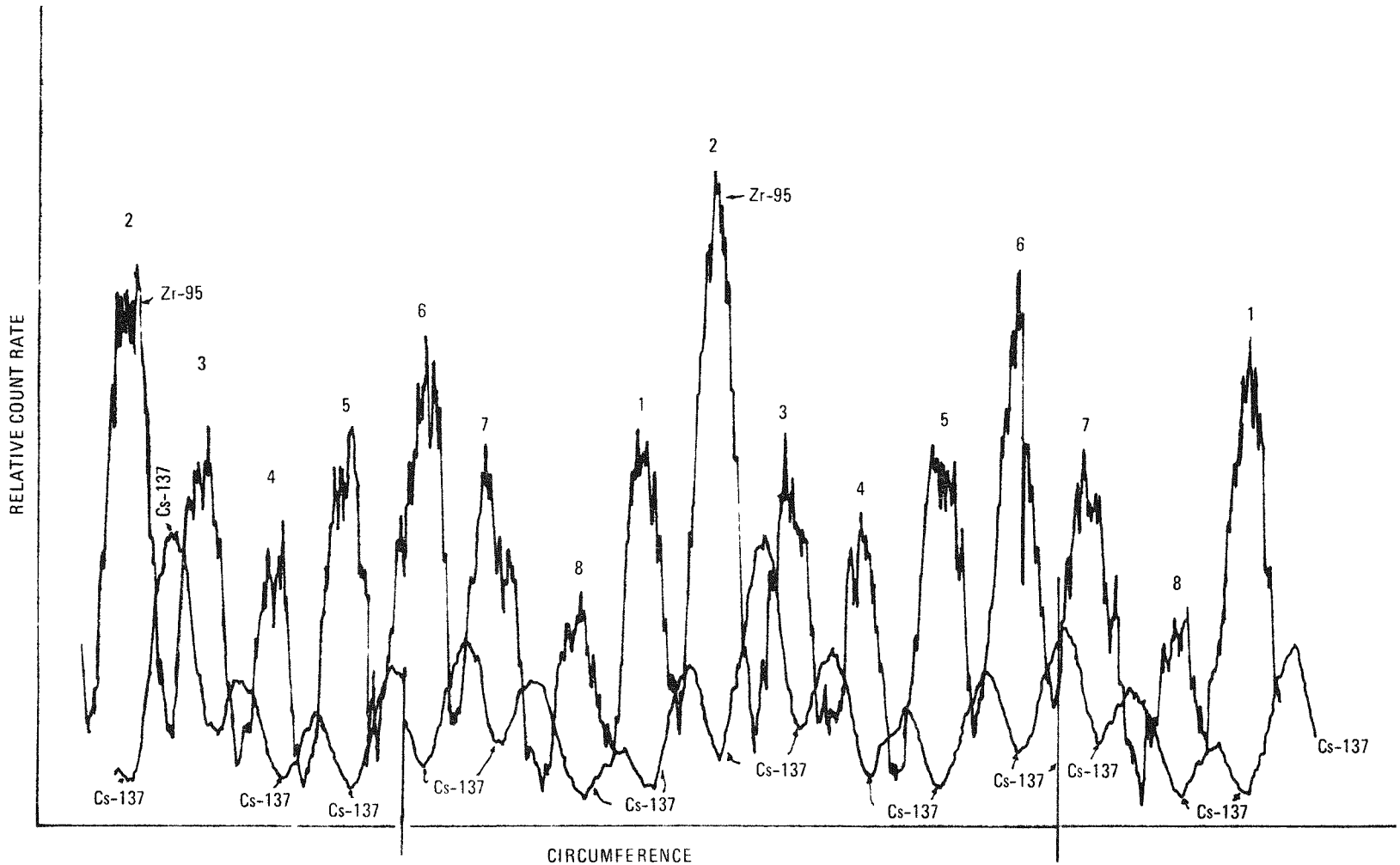

Fig. 9-18. FTE-6 stack power variations, body 2

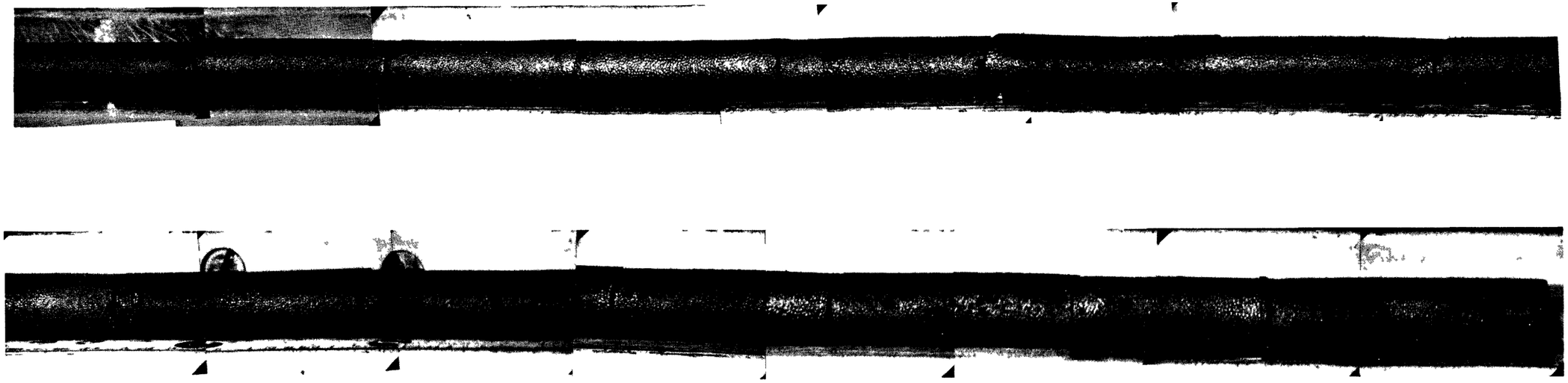

Fig. 19. FTE-6 composite photograph of stack 1, body 1 (bottom body)

Fig. 20. FTE-6 composite photograph of stack 2, body 1 (bottom body)

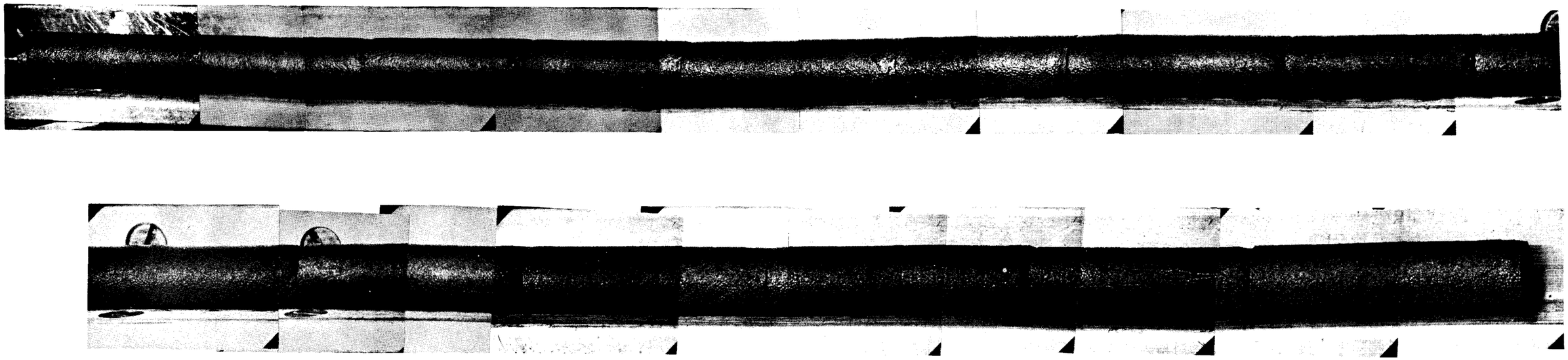

Fig. 21. FTE-6 composite photograph of stack 6, body 1 (bottom body)

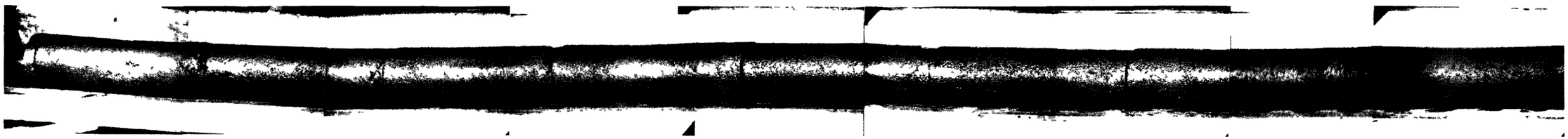

Fig. 22. FTE-6 composite photograph of stack 8, body 1 (bottom body)

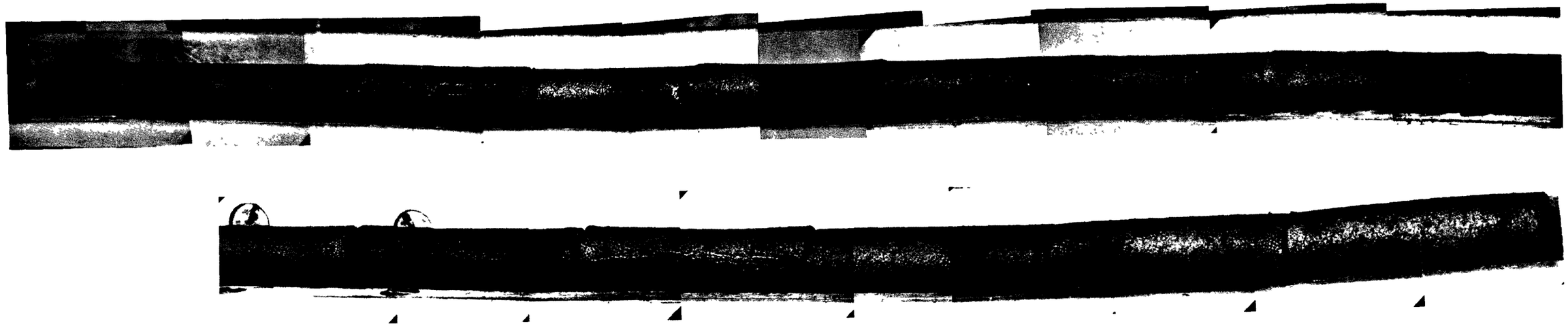

Fig. 23. FTE-6 composite photograph of stack 1, body 2 (center body)

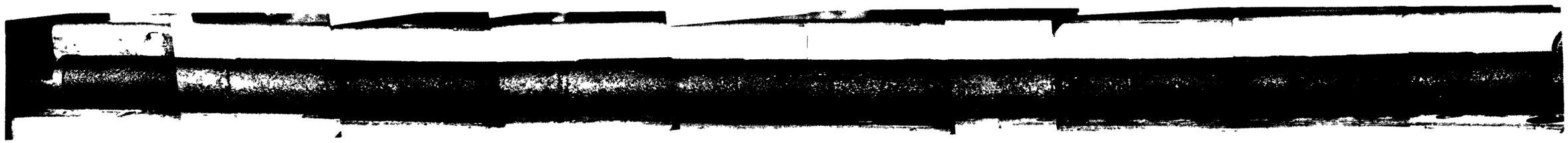

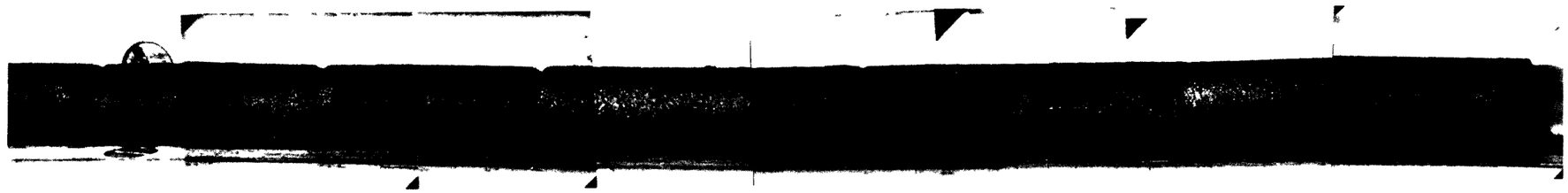

Fig. 24. FTE-6 composite photograph of stack 3, body 2 (conter body)

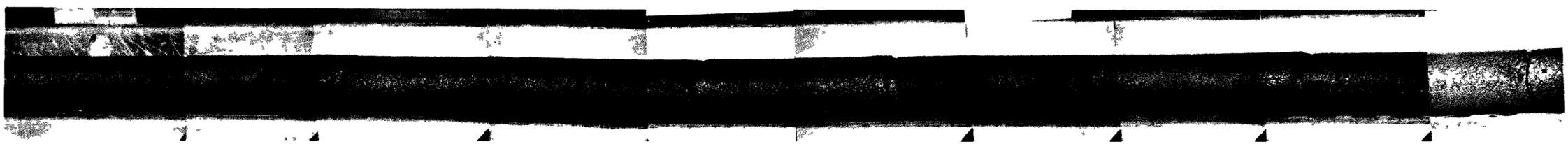

Fig. 25. FTE-6 composite photograph of stack 5, body 2 (center body)

Fig. 26. FTE-6 composite photograph of stack 7, body 2 (center body)

Fig. 27. FTE-6 composite photograph of stack 2, body 3 (top body)

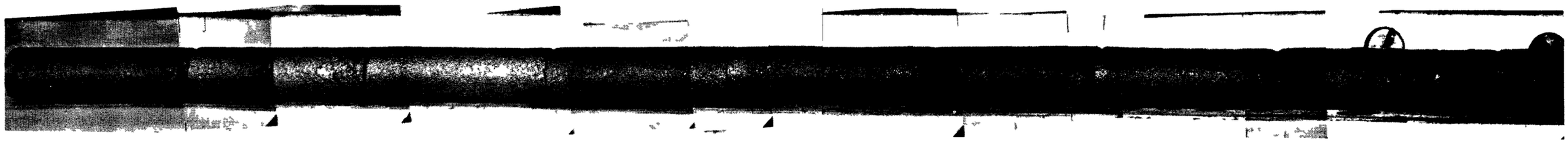

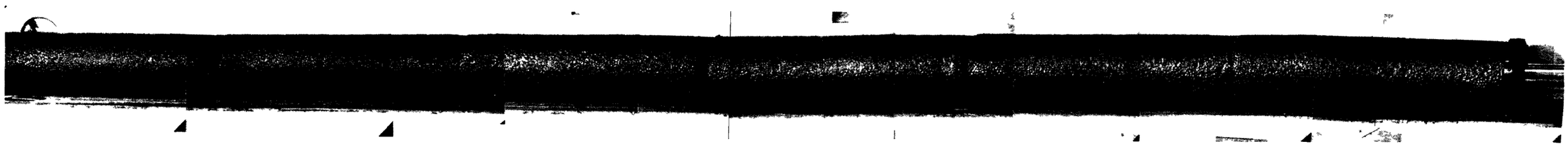

Fig. 28. FTE-6 composite photograph of stack 4, body 3 (top body)

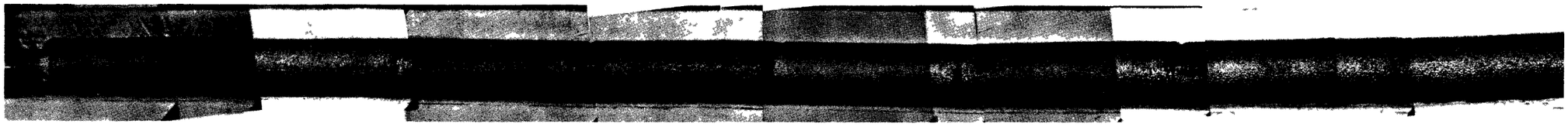

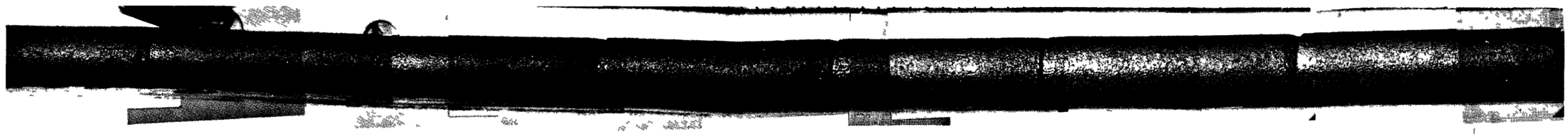

Fig. 29. FTE-6 composite photograph of stack 6, body 3 (top body)

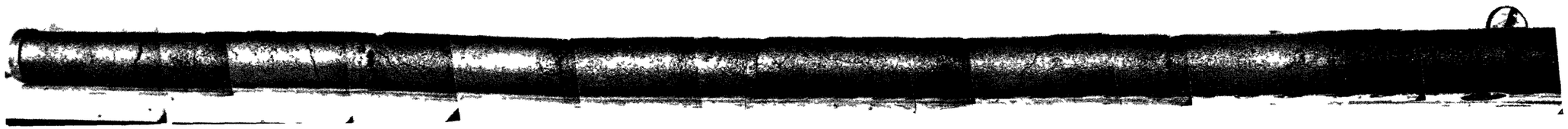

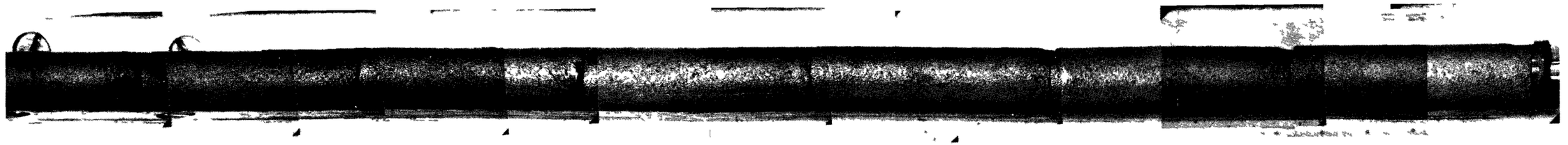

Fig. 30. FTE-6 composite photograph of stack 8, body 3 (top body)

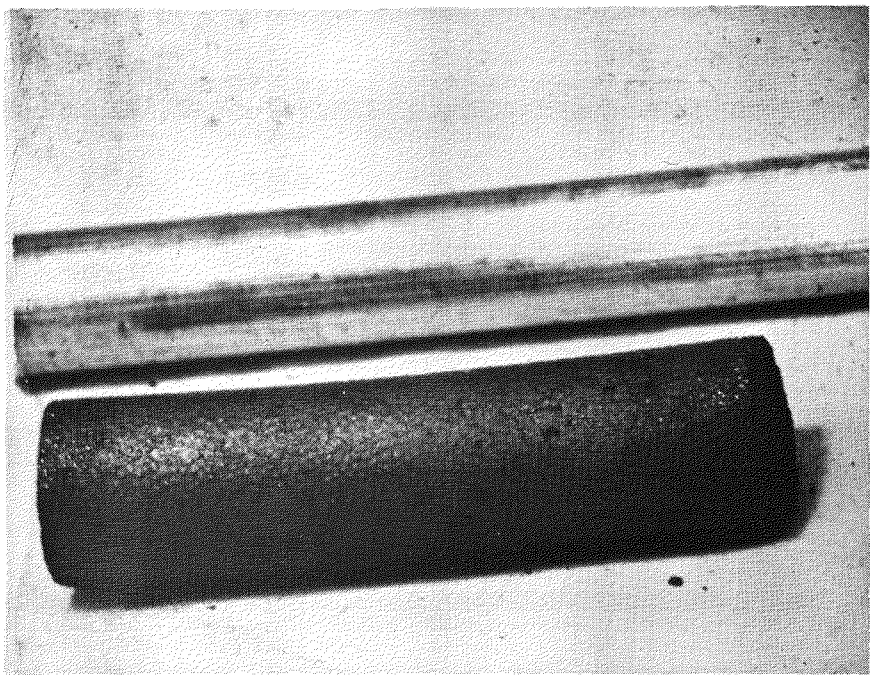

Fig. 9-31. FTE-6 typical bowed rod (2-2-1) - center body

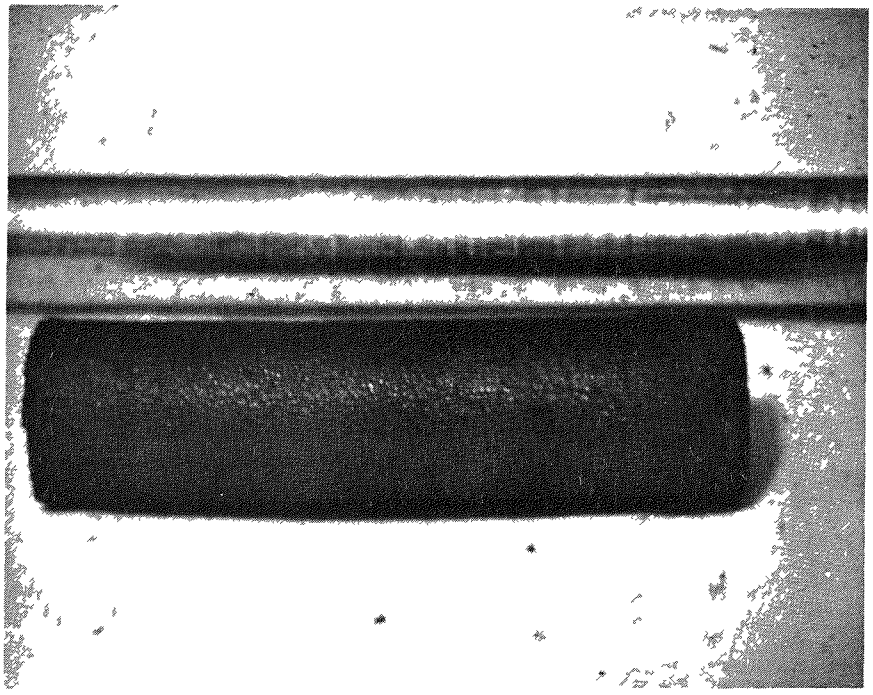

Fig. 9-32. FTE-6 typical bowed rod (3-1-12) - top body

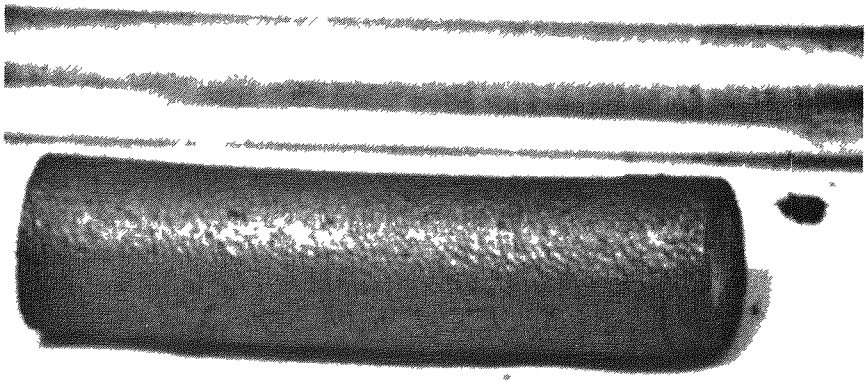

Fig. 9-33. FTE-6 typical bowed rod (3-1-3) - top body

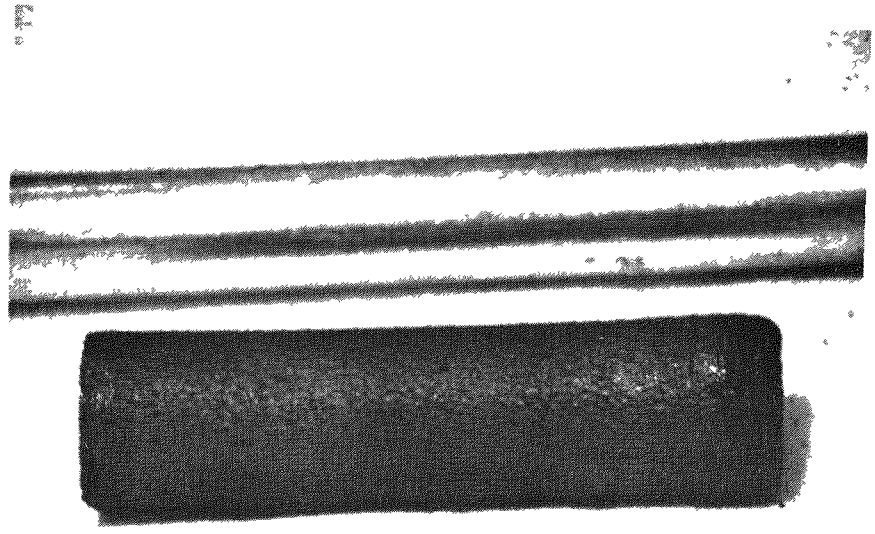

Fig. 9-34. FTE-6 typical bowed rod (3-2-3) - top body

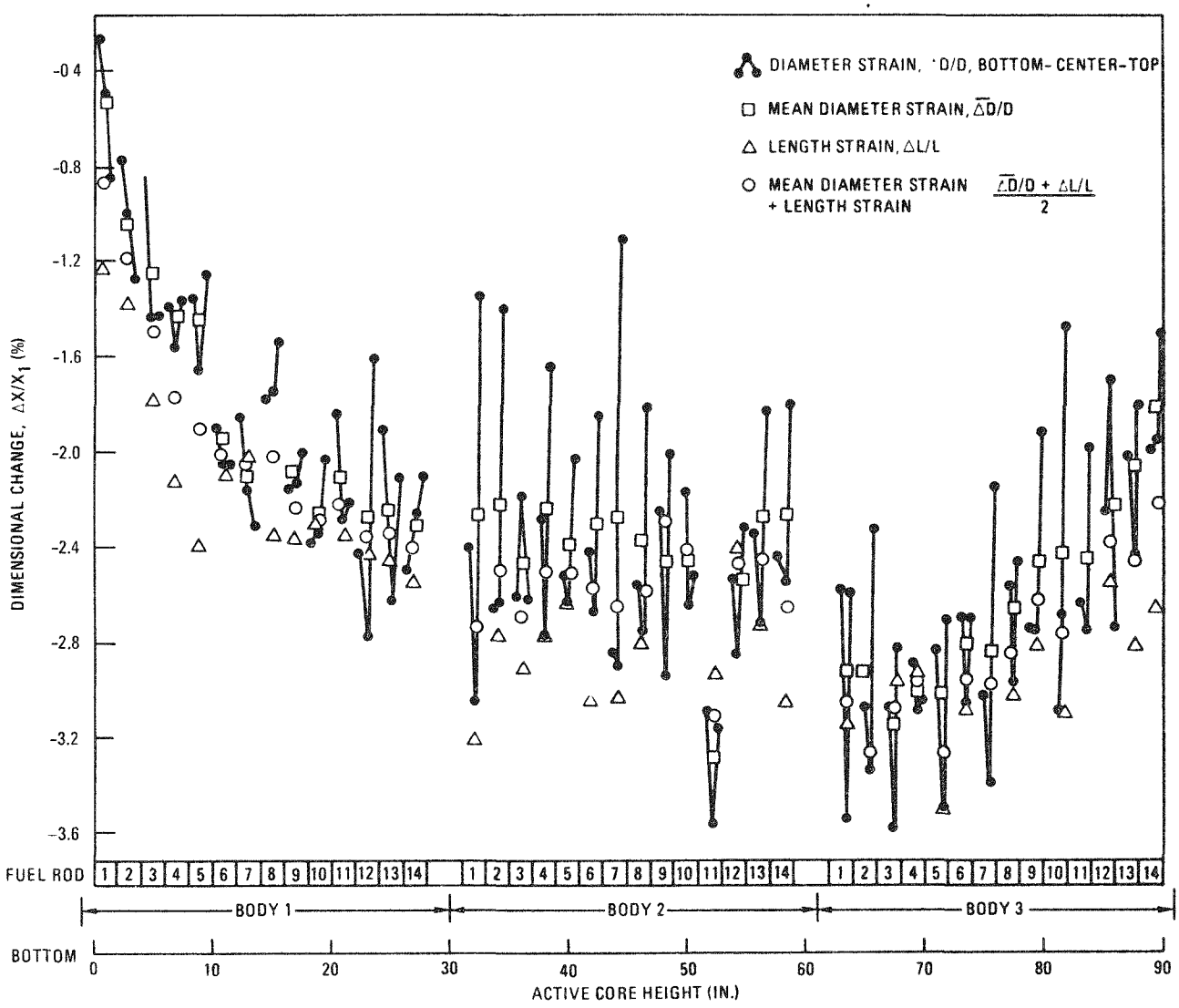

Fig. 9-35. Fuel rod strain: (a) hole 1, UO_2 TRISO/ThO_2 BISO

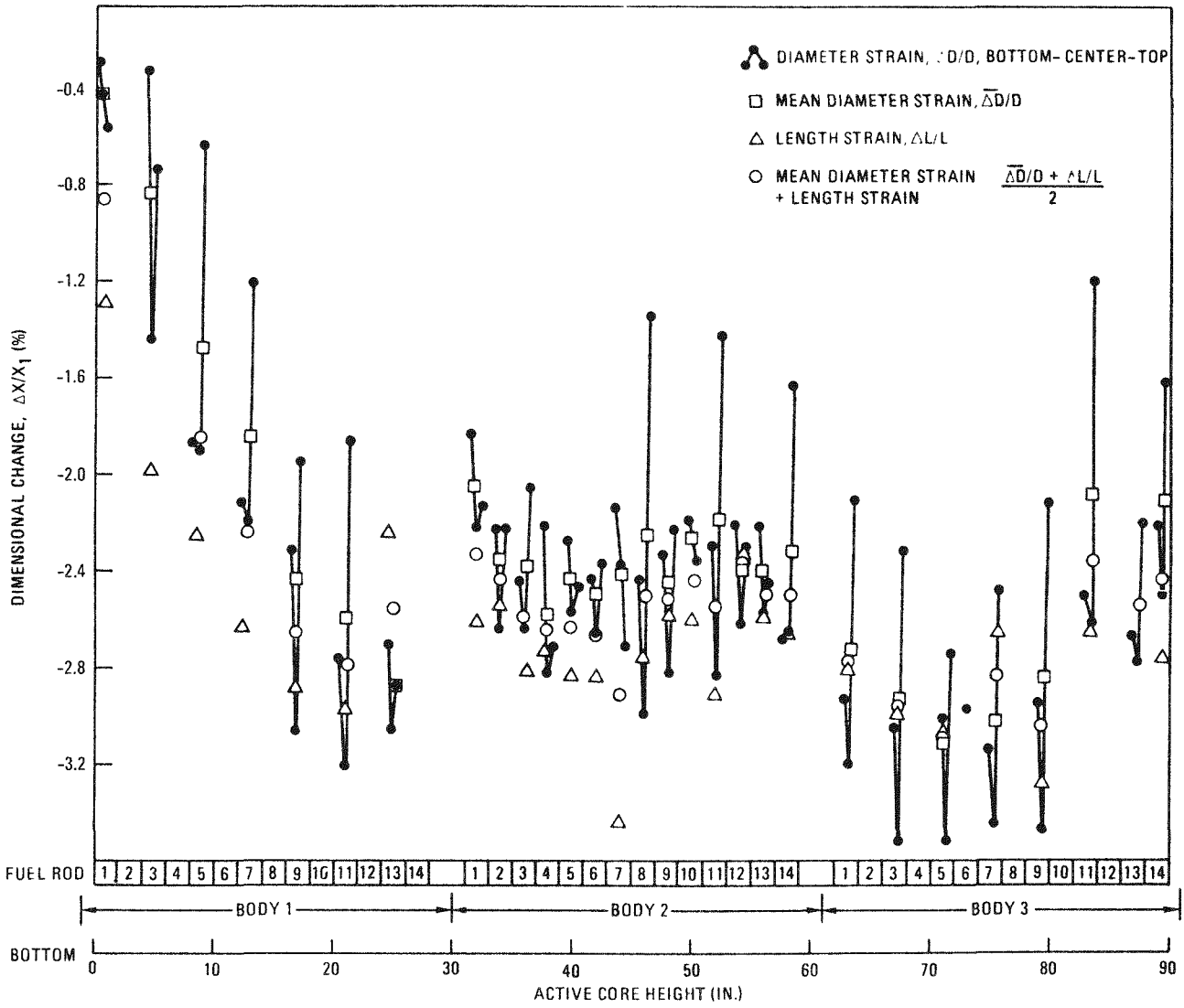

Fig. 9-35. Fuel rod strain: (b) hole 2, UO_2 TRISO/ThO_2 BISO

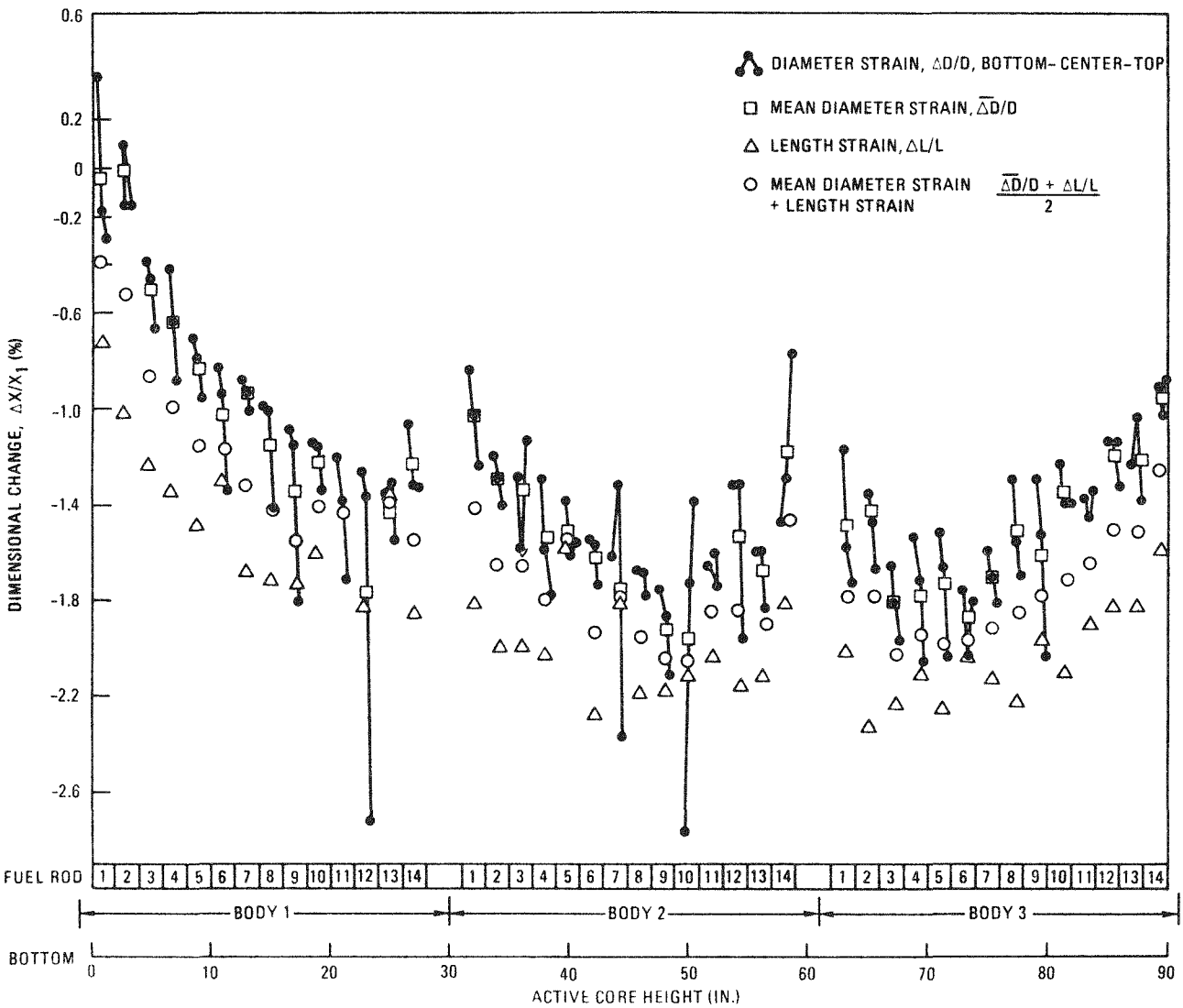

Fig. 9-35. Fuel rod strain: (c) hole 3, $(Th,U)C_2$ TRISO/ThC_2 BISO

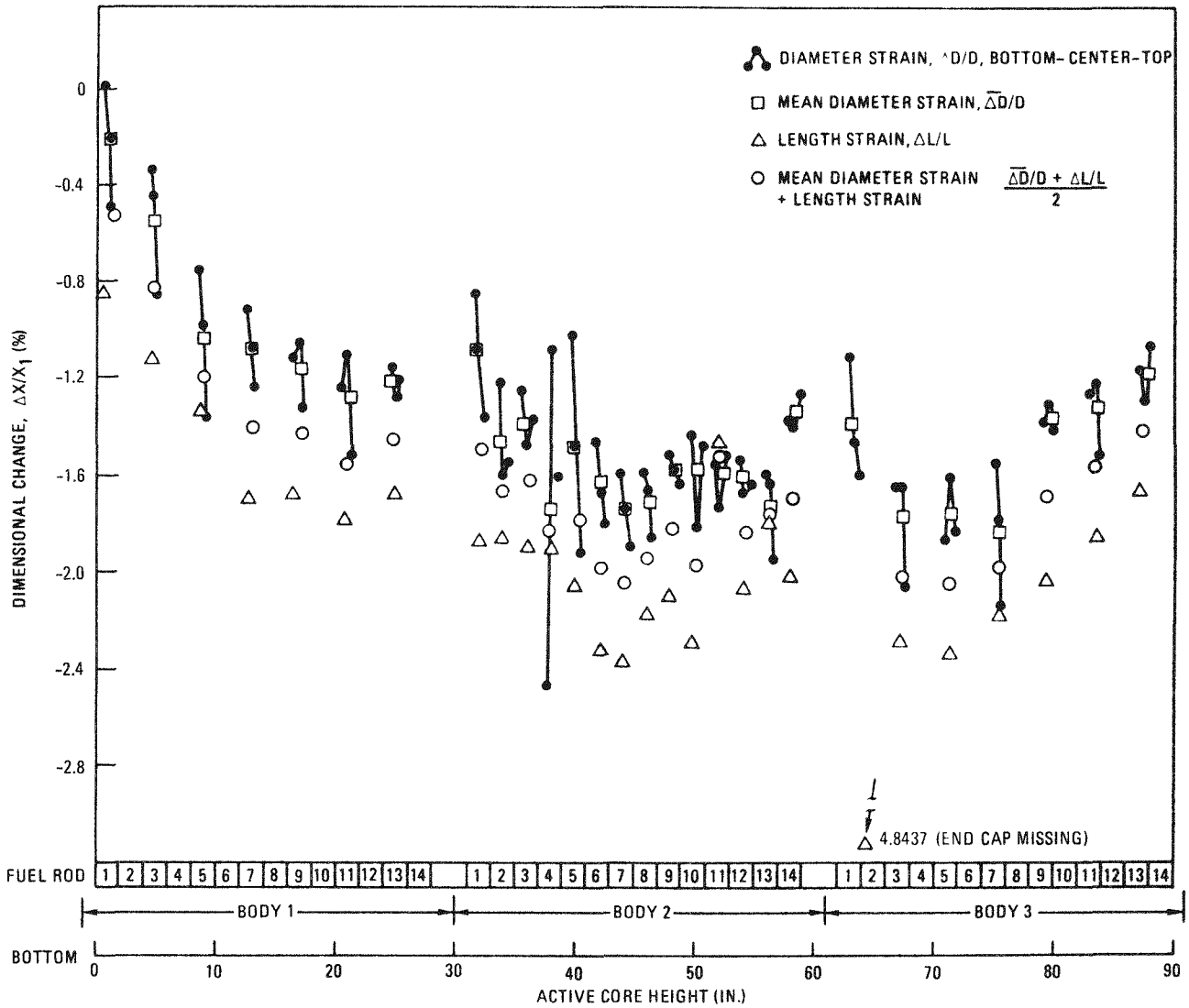

Fig. 9-35. Fuel rod strain: (d) hole 4, $(Th,U)C_2$ TRISO/ThC_2 BISO

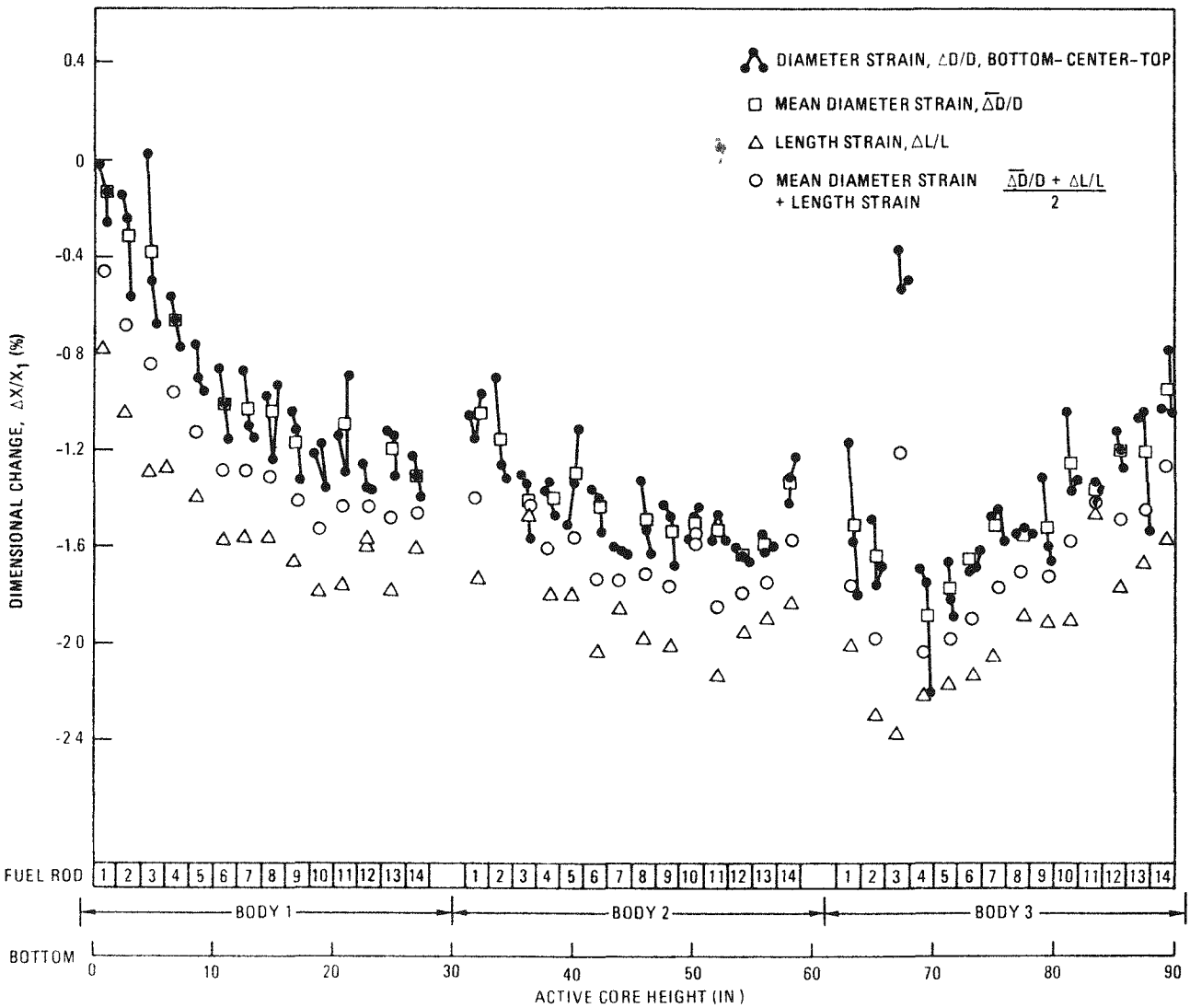

Fig. 9-35. Fuel rod strain: (e) hole 5, $(Th,U)C_2$ TRISO/ThC_2 TRISO

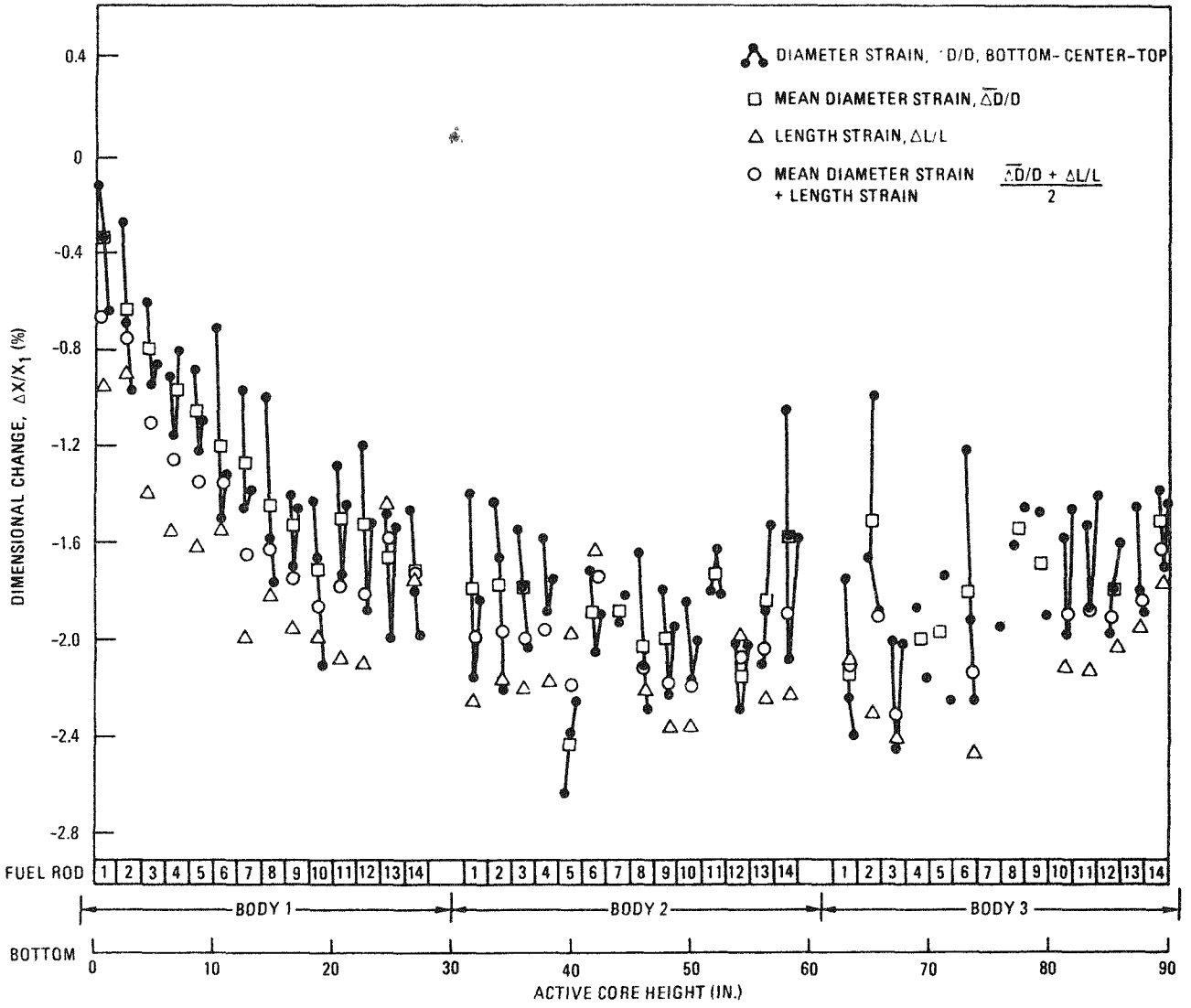

Fig. 9-35. Fuel rod strain: (f) hole 6, $(Th,U)C_2$ TRISO/ThC_2 TRISO

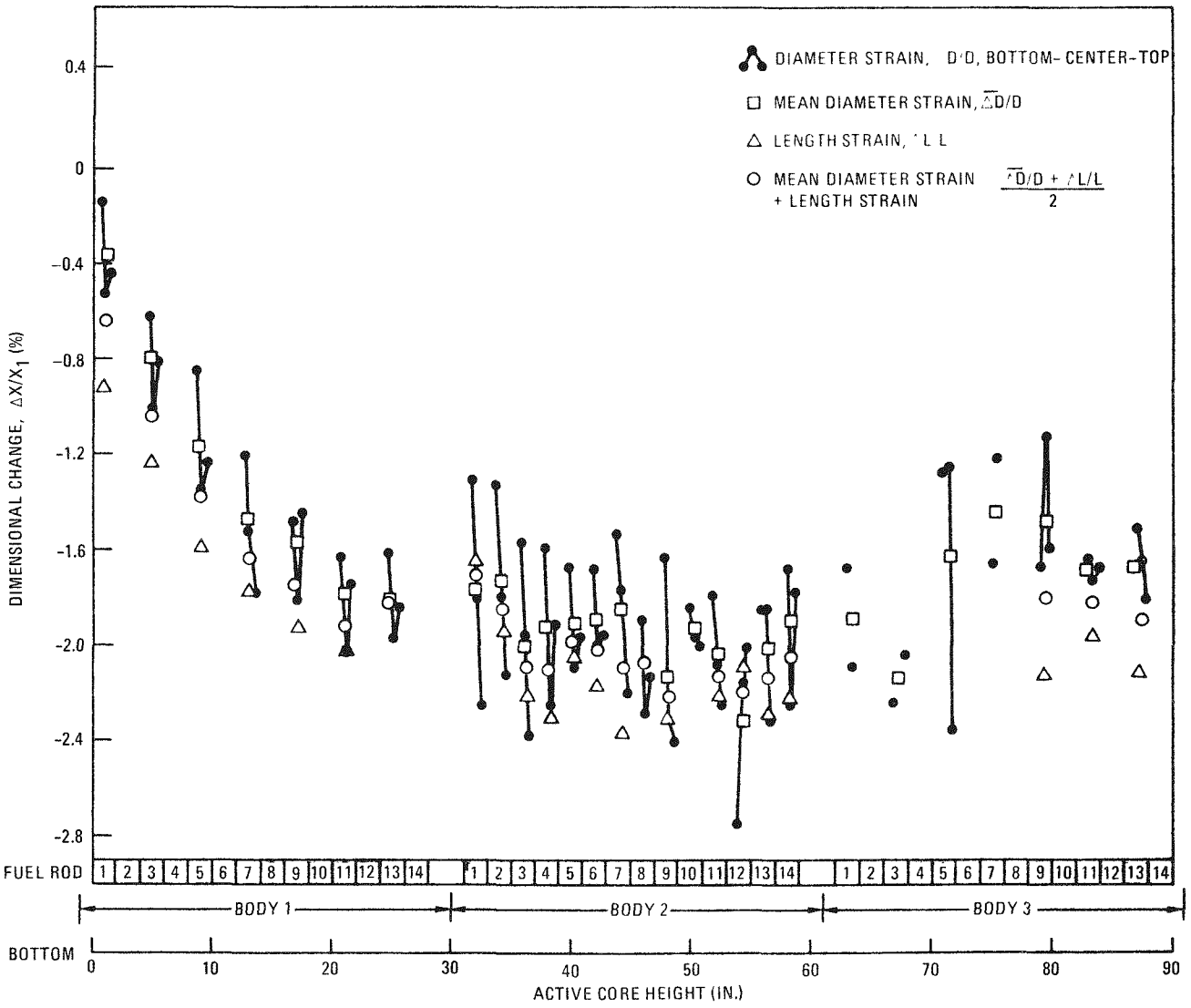

Fig. 9-35. Fuel rod strain: (g) hole 7, UC_2 TRISO/ThC_2 BISO

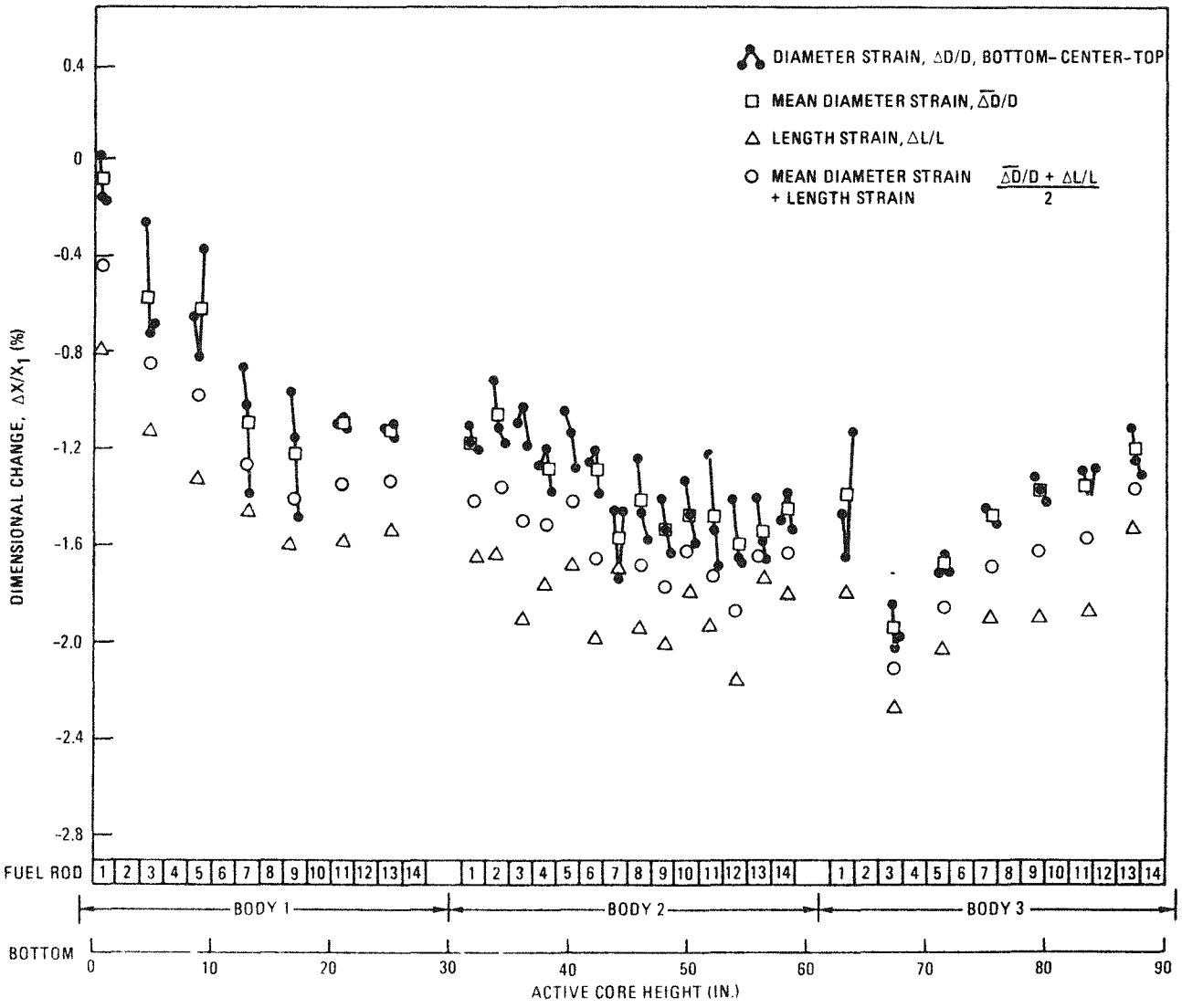

Fig. 9-35. Fuel rod strain: (h) hole 8, UC_2 TRISO/ThC_2 BISO

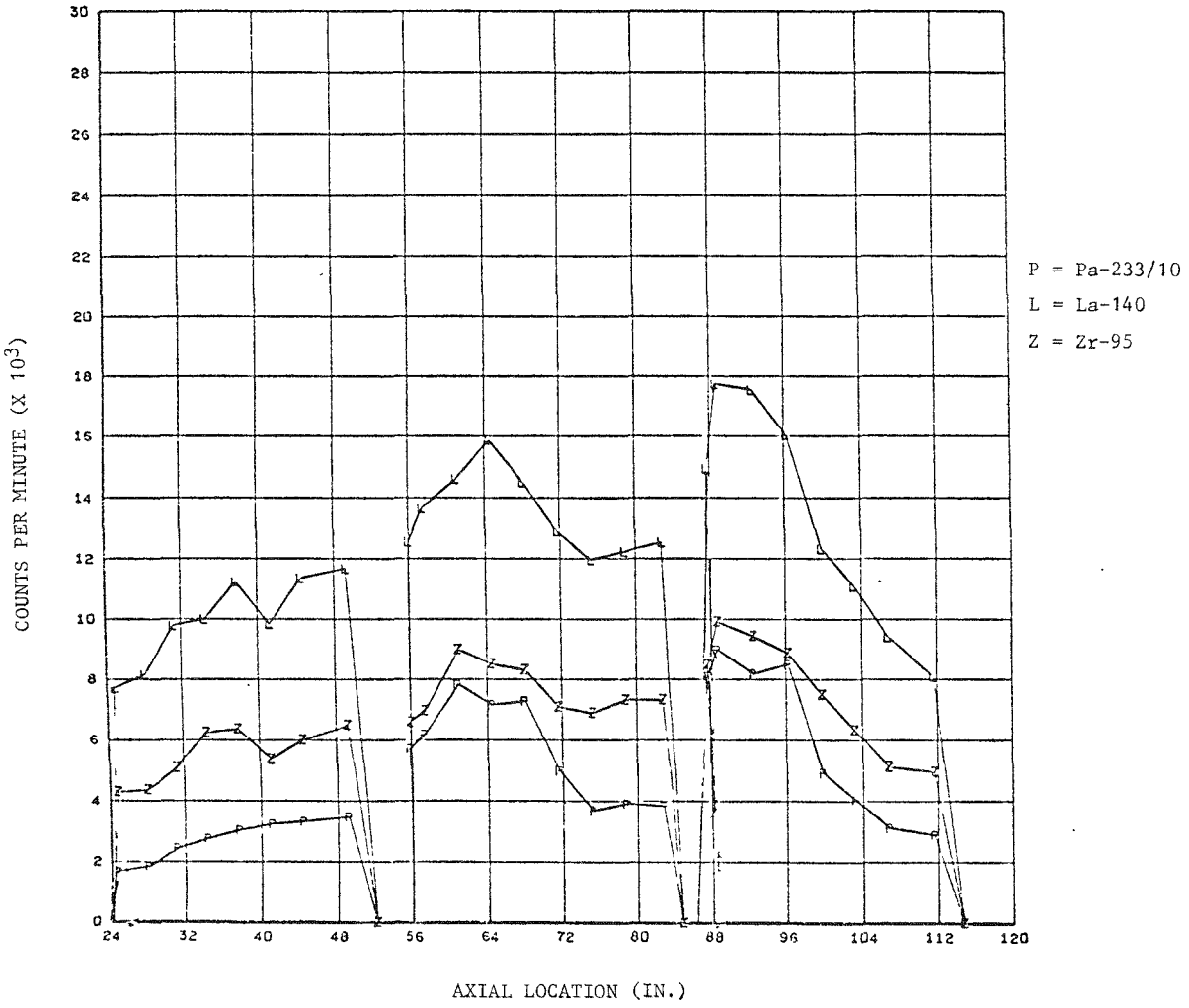

Fig. 9-36. Peach Bottom Core 2 gamma scan: (a) Pa-233, La-140, and Zr-95

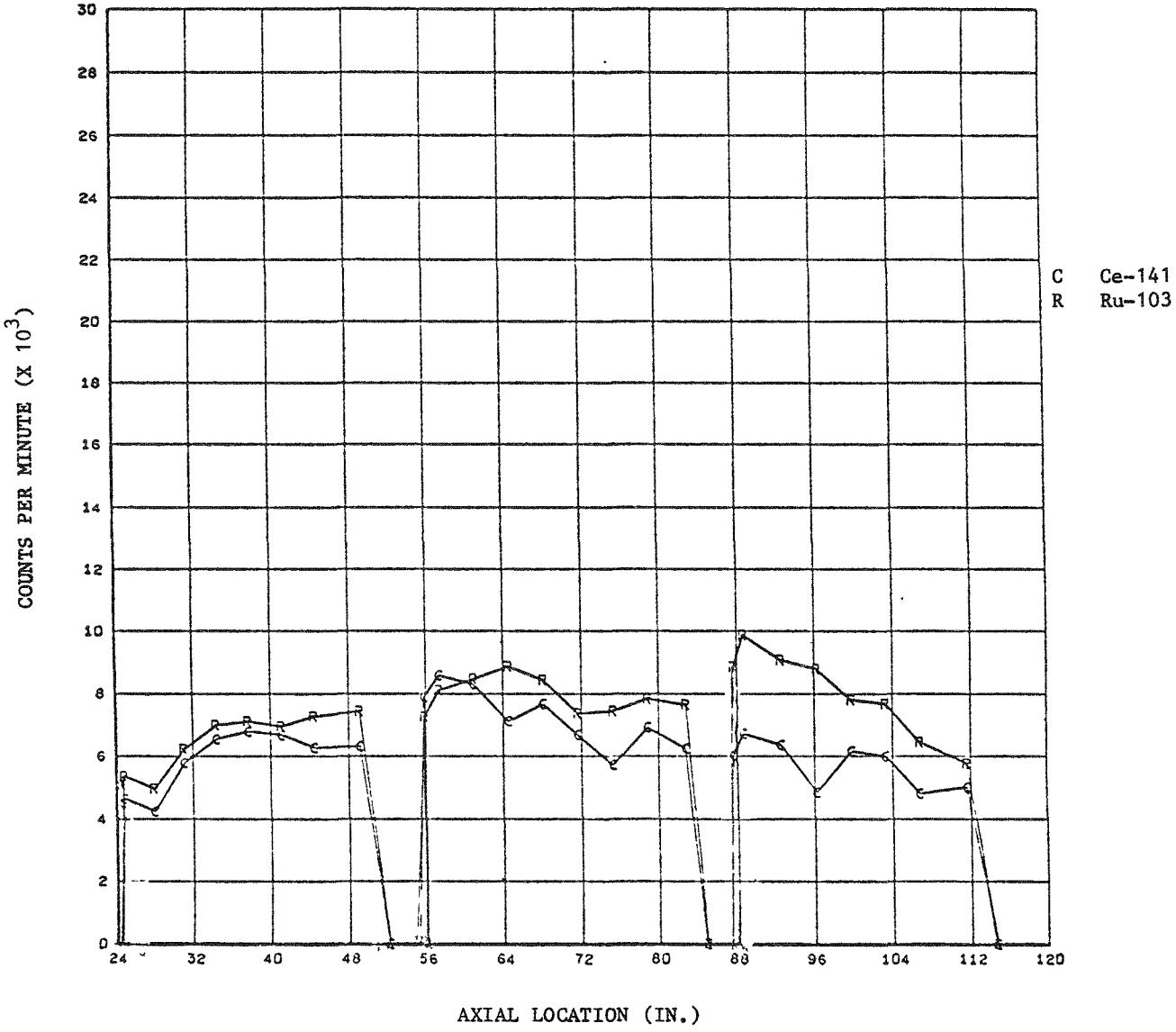

Fig. 9-36. Peach Bottom Core 2 gamma scan: (b) Ce-141 and Ru-103

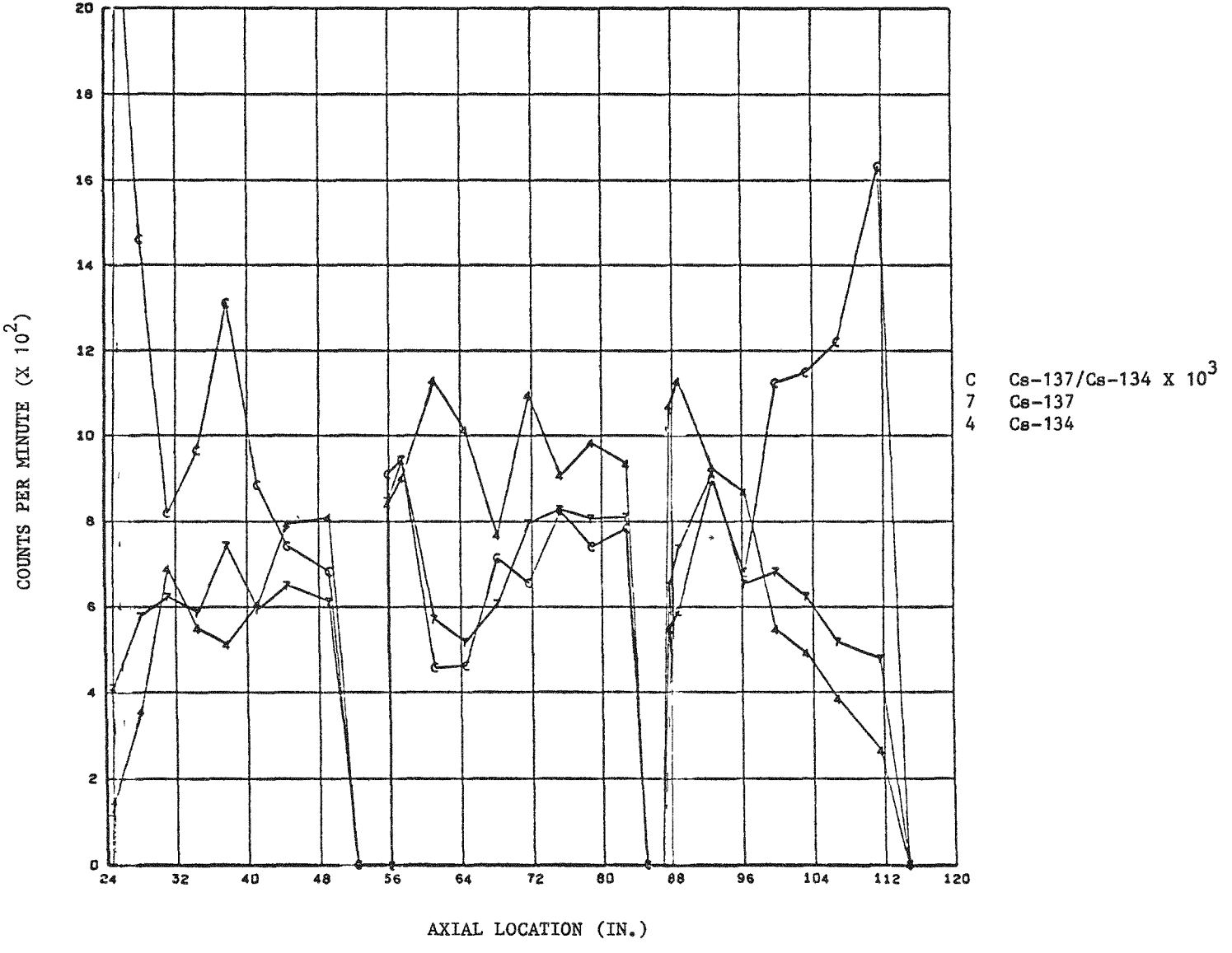

Fig. 9-36. Peach Bottom Core 2 gamma scan: (c) Cs-137/Cs-134, Cs-137, and Cs-134

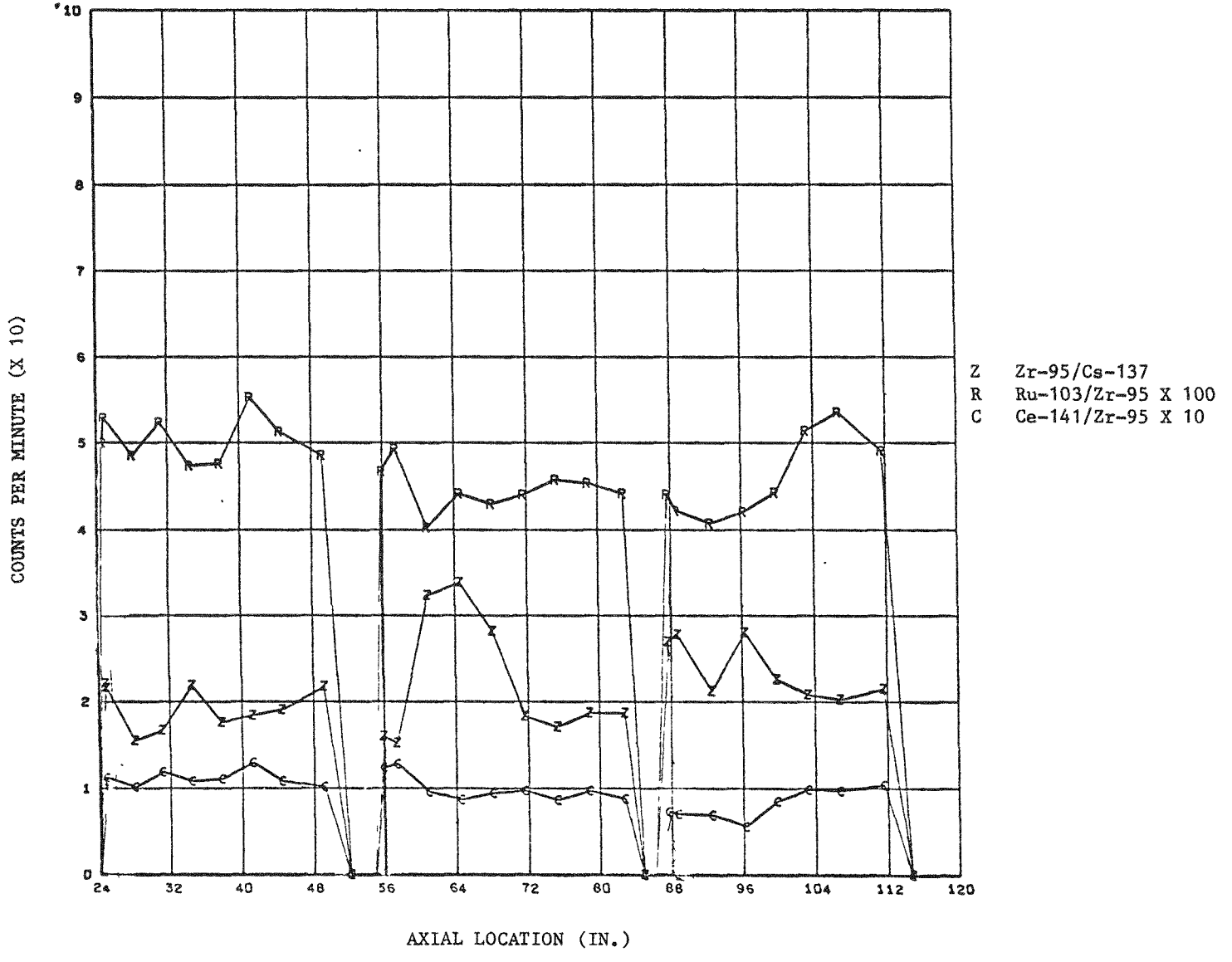

Fig. 9-36. Peach Bottom Core 2 gamma scan: (d) Zr-95/Cs-137, Ru-103/Zr-95, and Ce-141/Zr-95

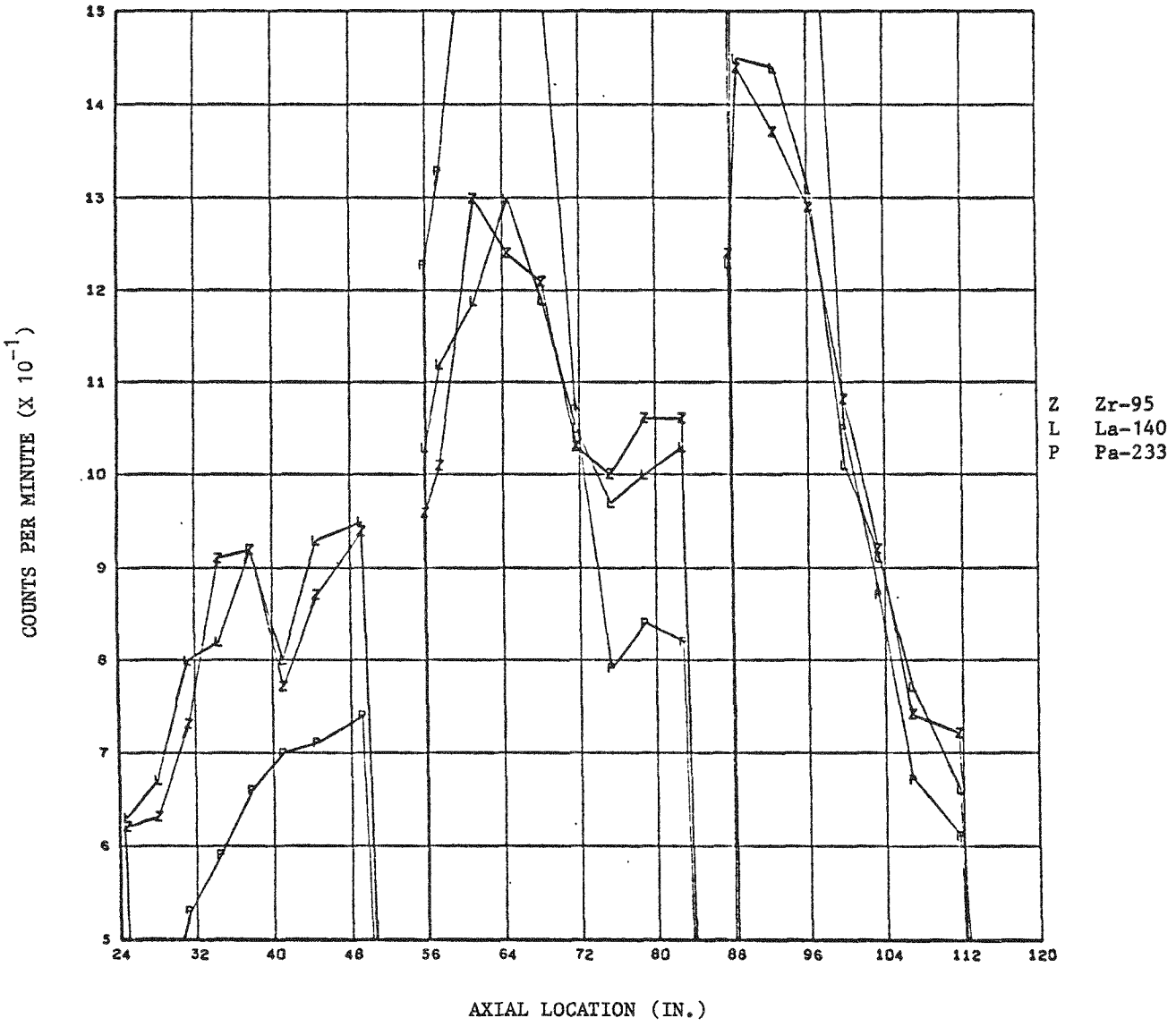

Fig. 9-36. Peach Bottom Core 2 gamma scan: (e) Zr-95, La-140, and Pa-233

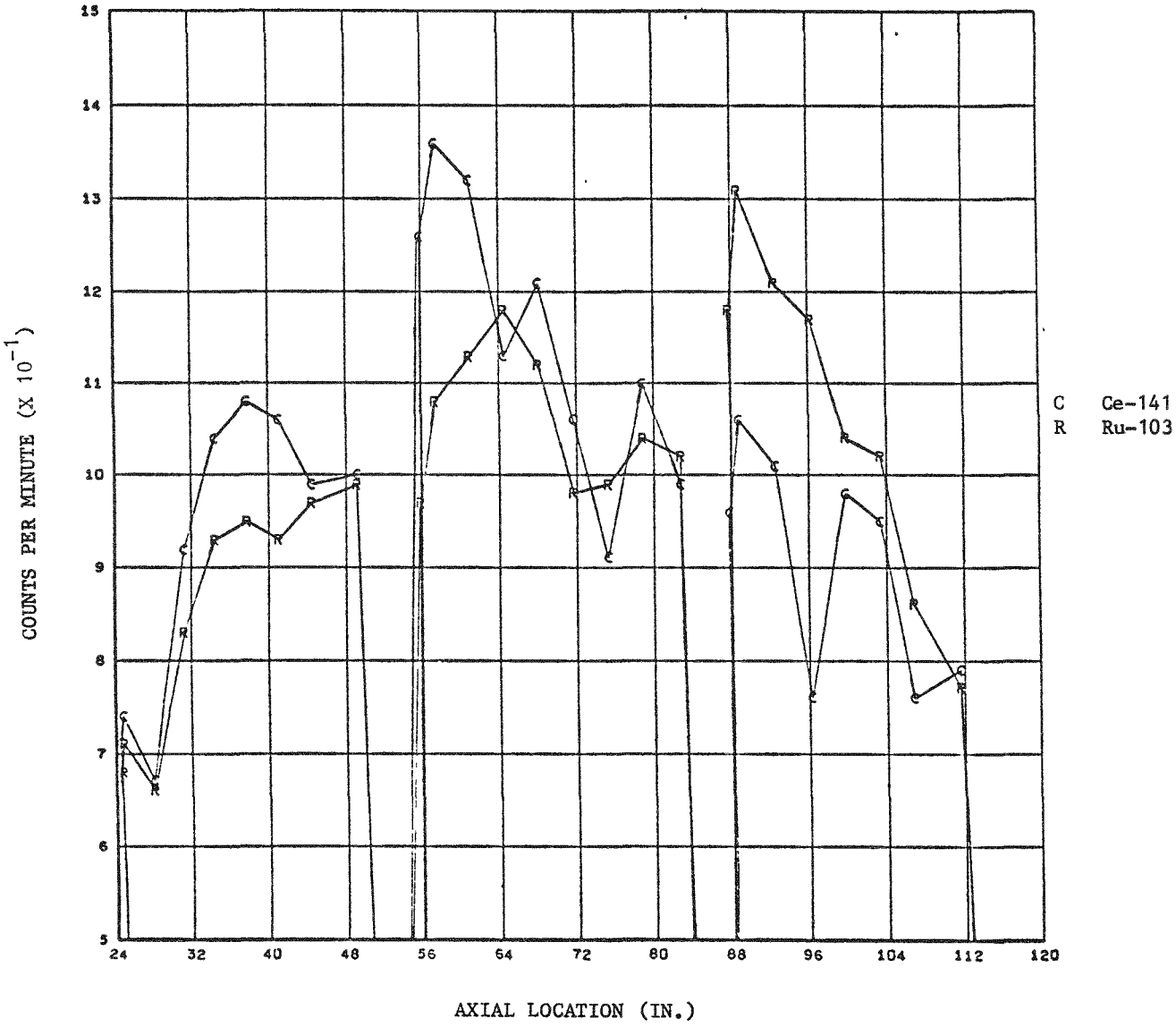

Fig. 9-36. Peach Bottom Core 2 gamma scan: (f) Ce-141 and Ru-103

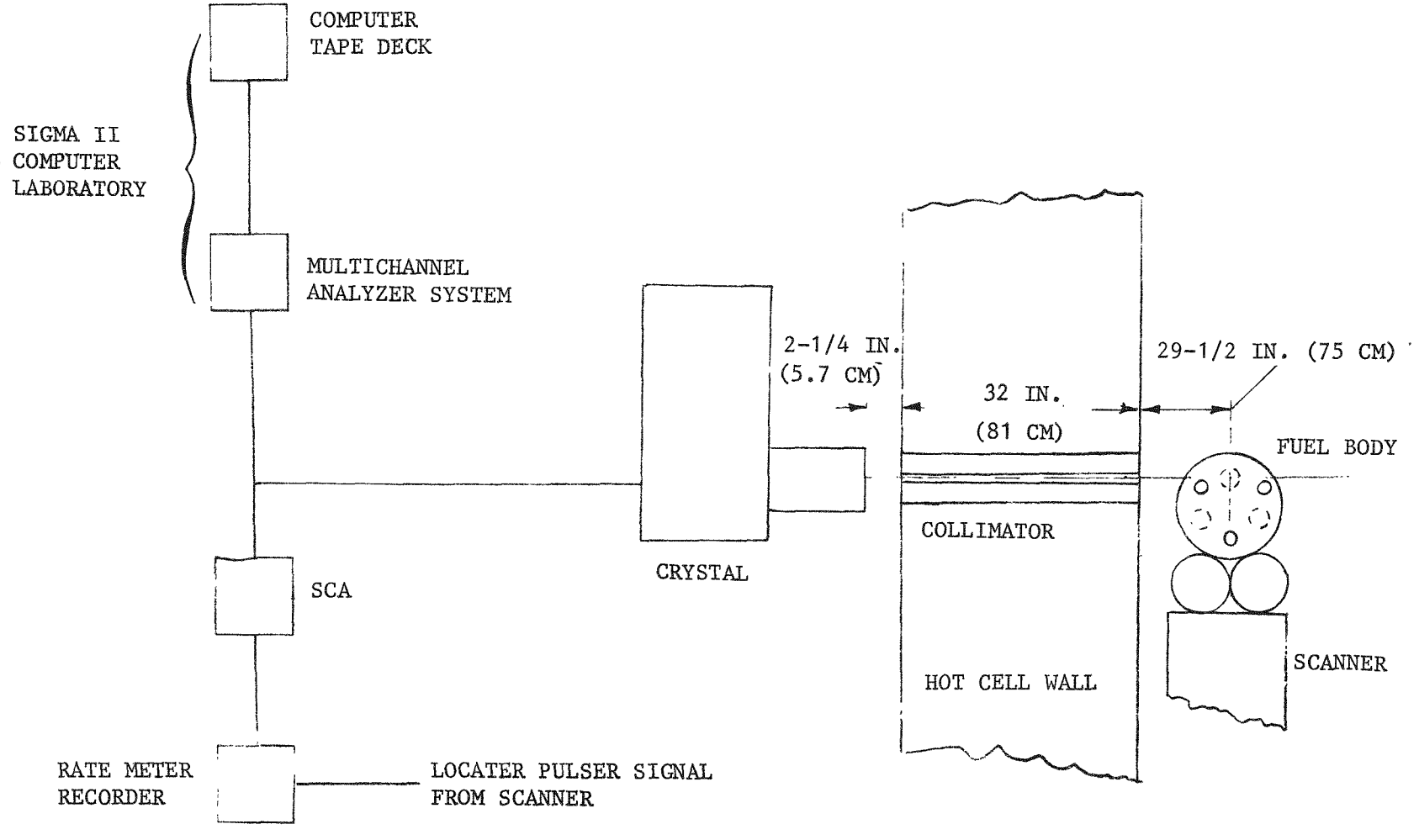

Fig. 9-37. Schematic of gamma scanning apparatus

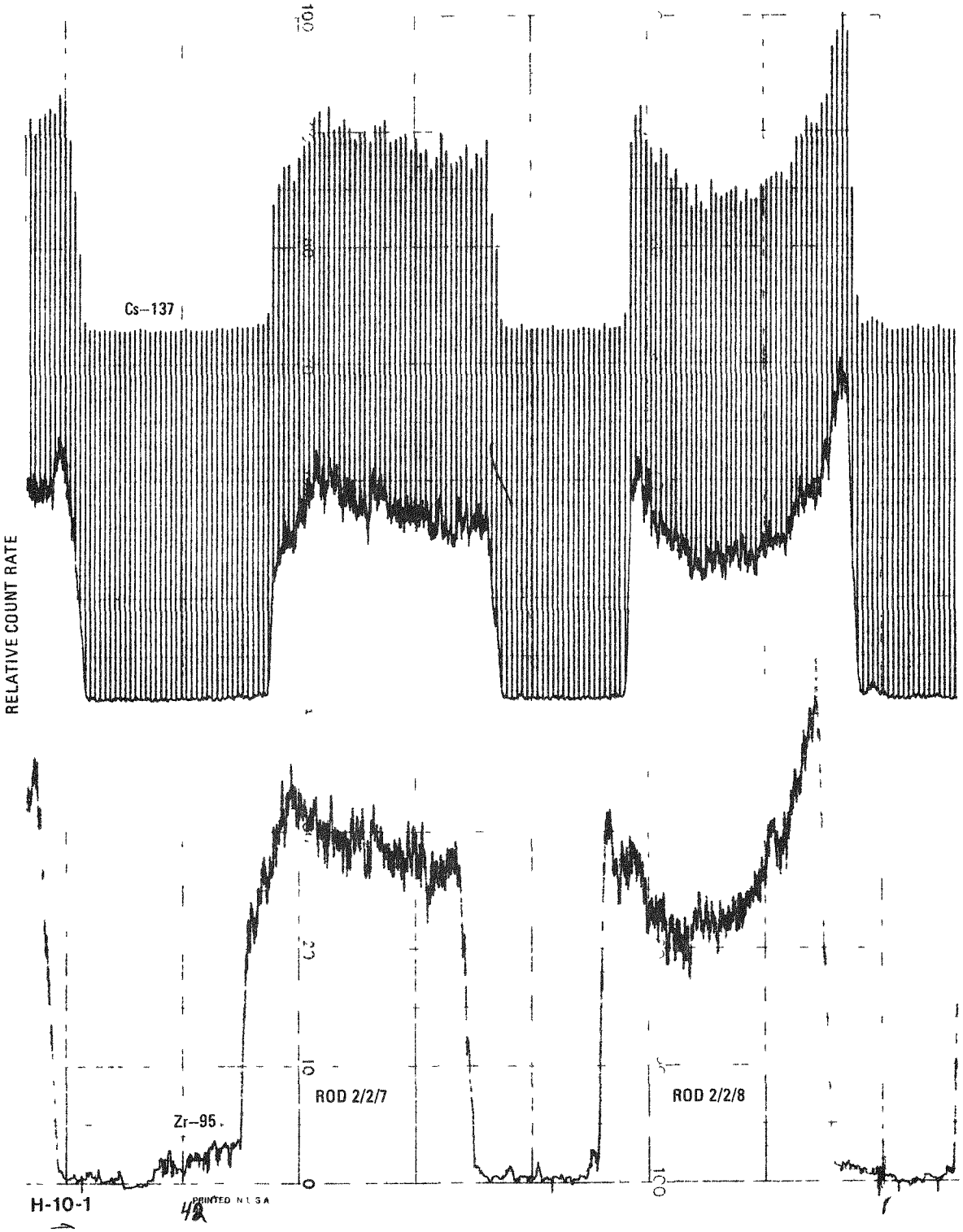

Fig. 9-38. FTE-6 body 2, hole 2 fuel inhomogeneity

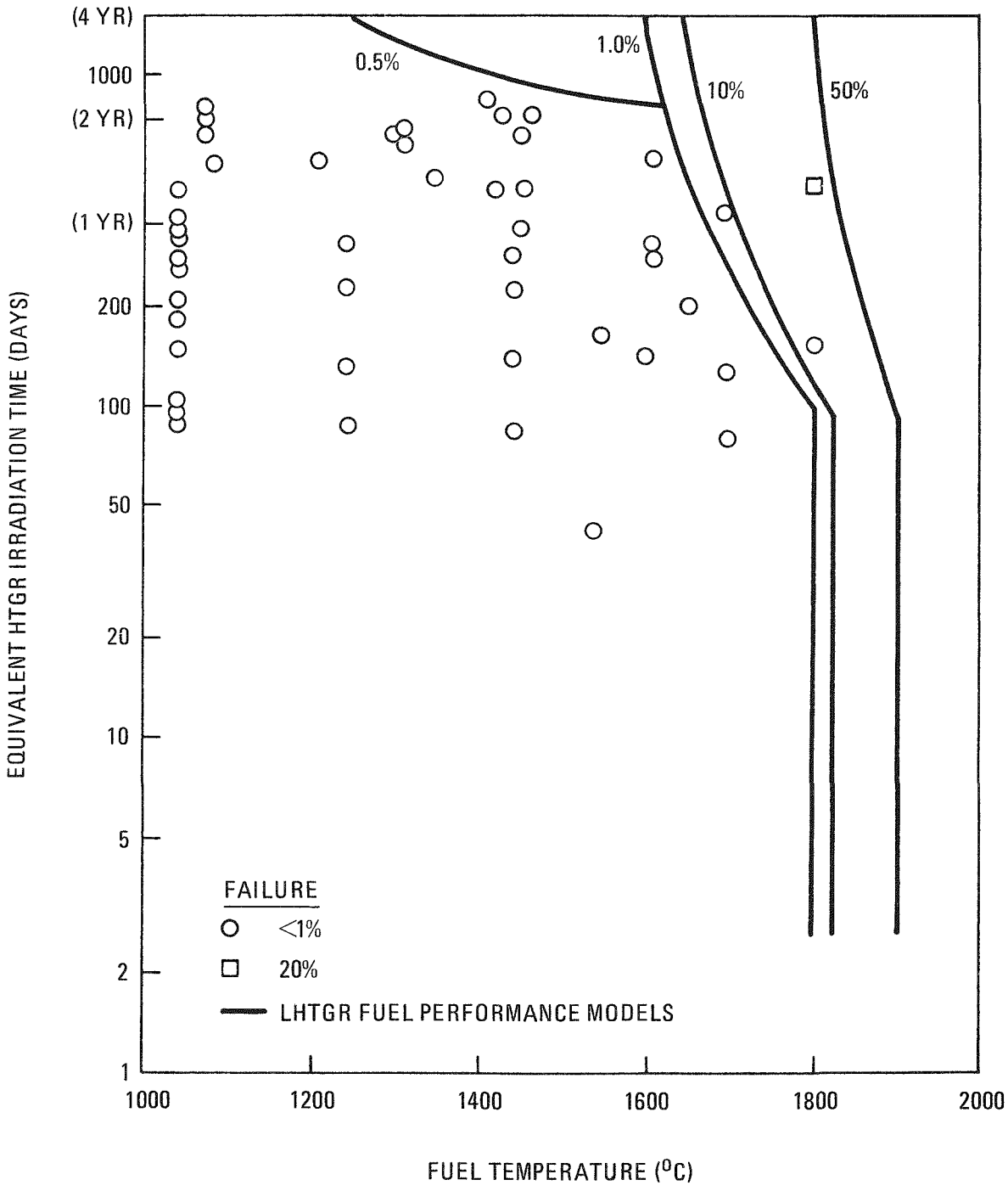

Fig. 9-39. Comparison of LHTGR TRISO UC_2 fuel performance observations and LHTGR fuel performance model predictions

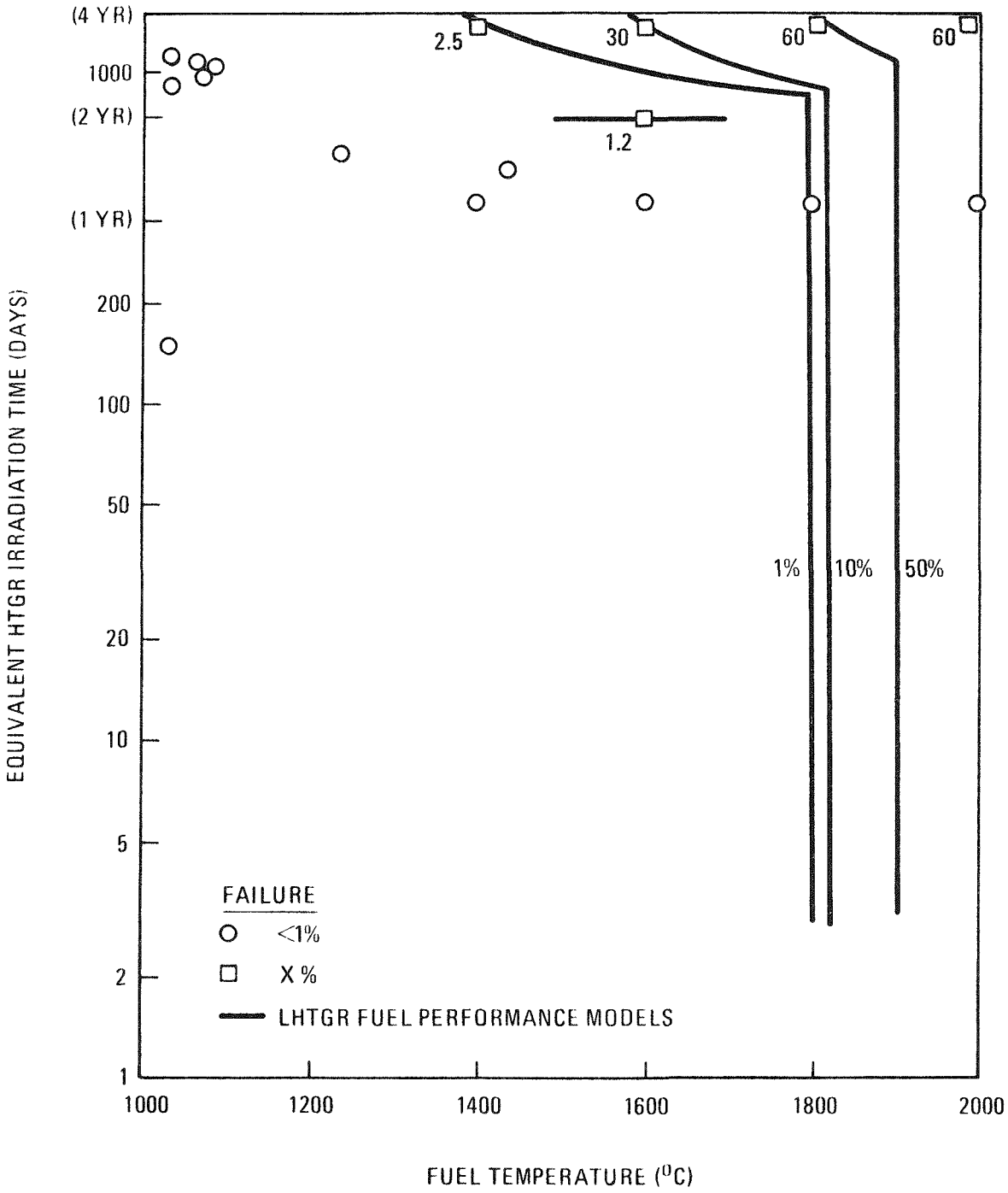

Fig. 9-40. Comparison of LHTGR BISO ThO_2 fuel performance observations and LHTGR fuel performance model predictions

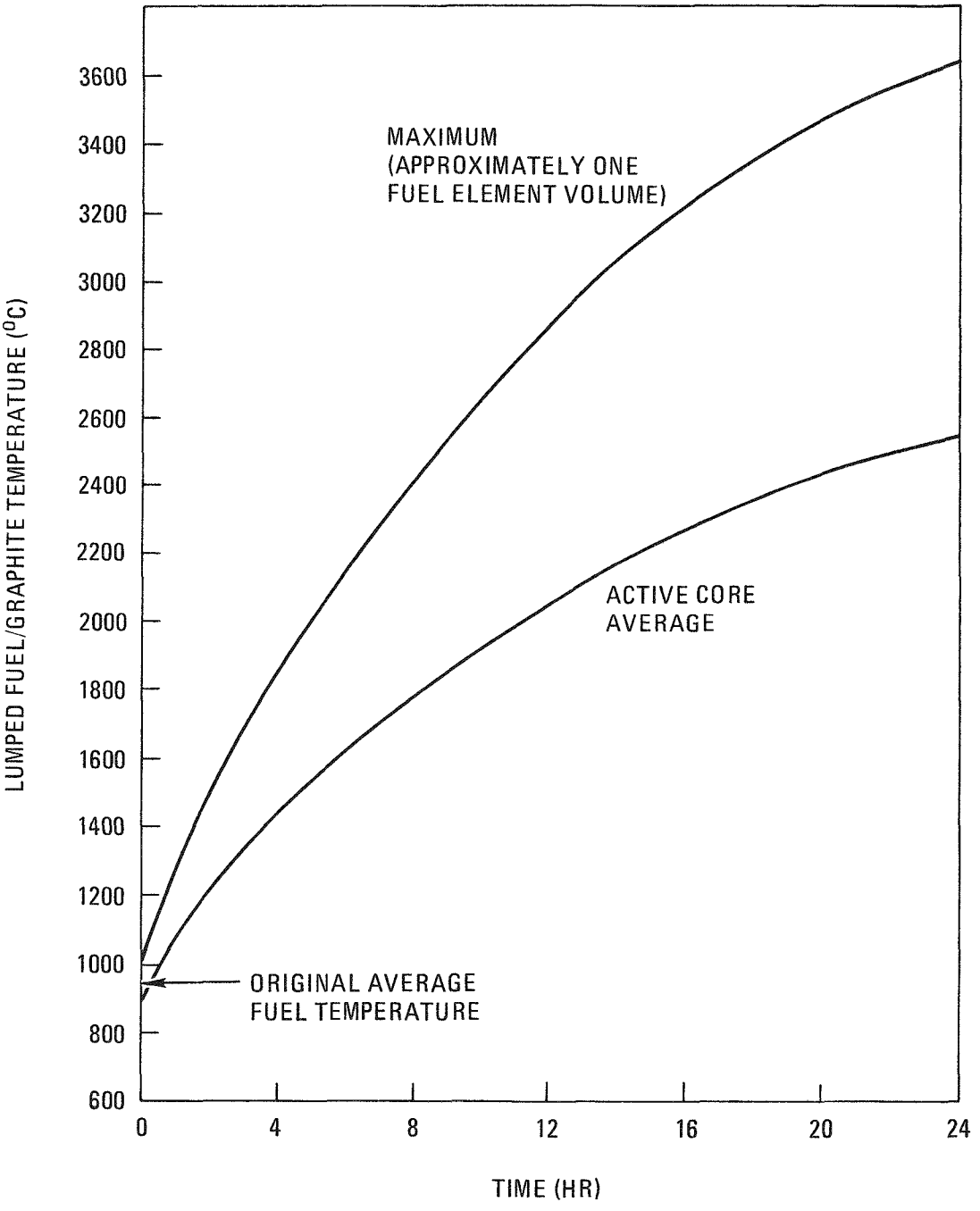

Fig. 9-41. Variation in fuel temperature with time during the hypothetical MHFPR event

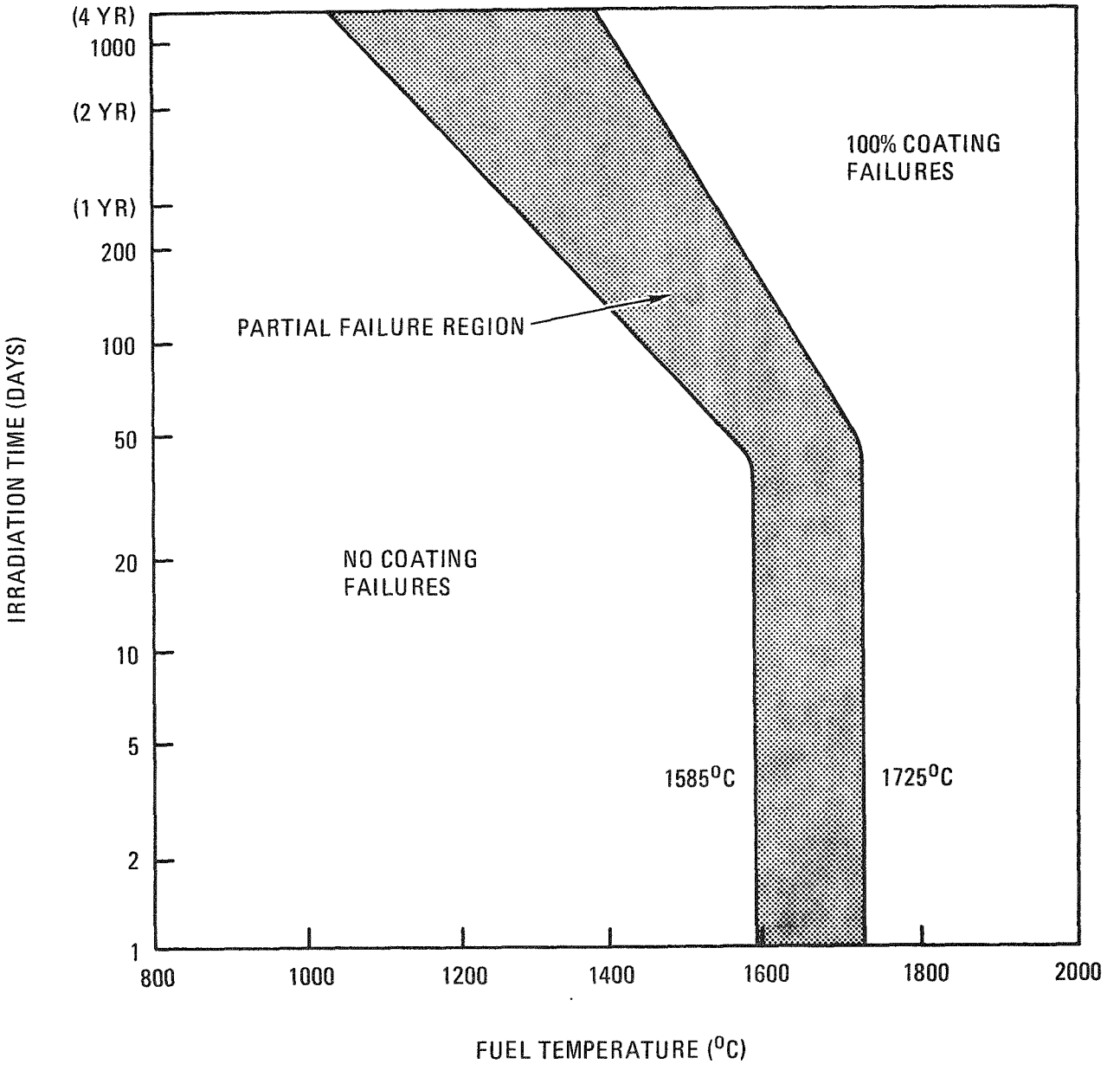

Fig. 9-42. Schematic of the model used by GA to describe TRISO UC_2 failure during a MHFPR event in Summit Power Station Units 1 and 2

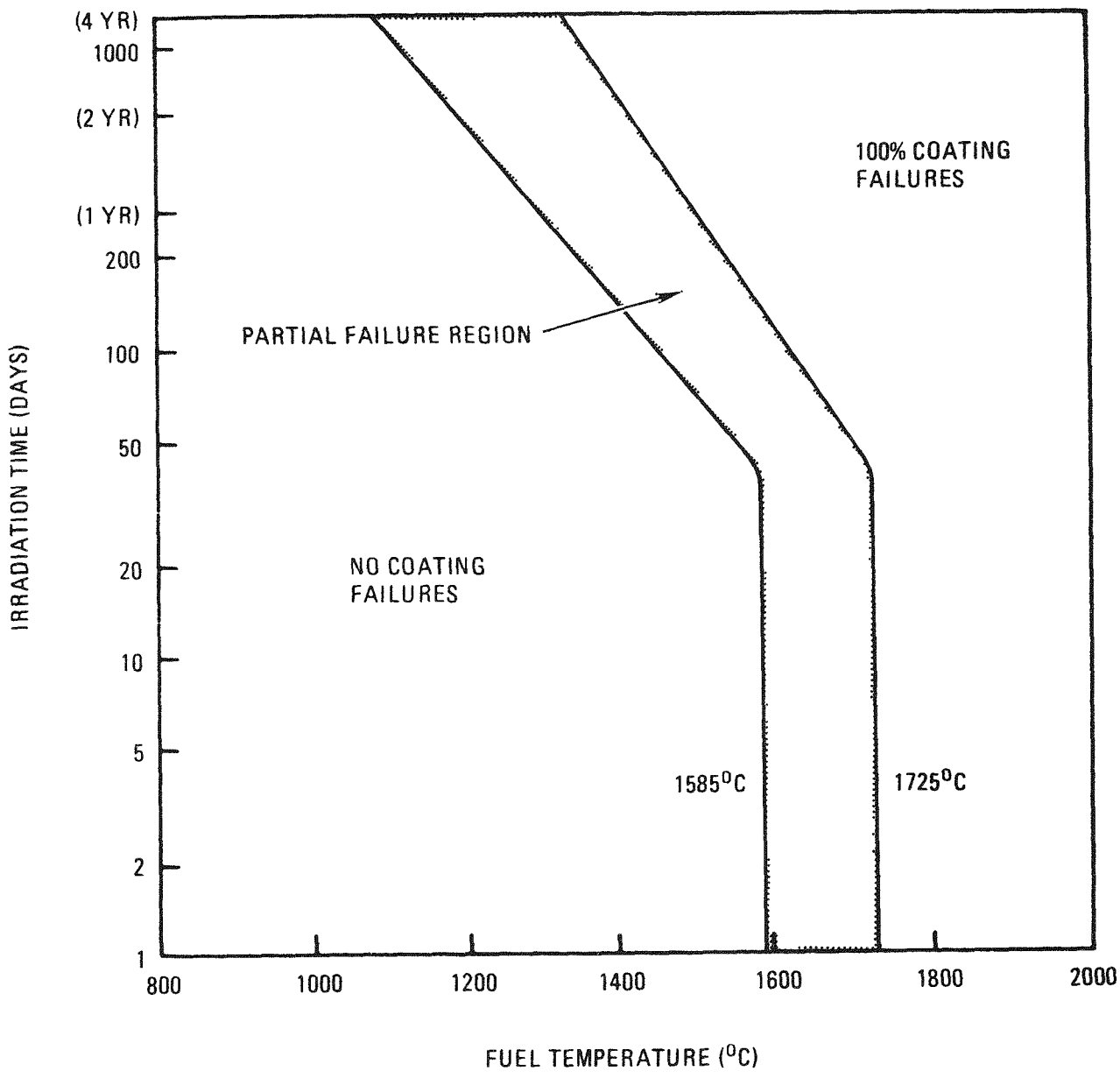

Fig. 9-43. Schematic of the model used by GA to describe BISO ThO_2 failure during a MHFPR event in Summit Power Station Units 1 and 2

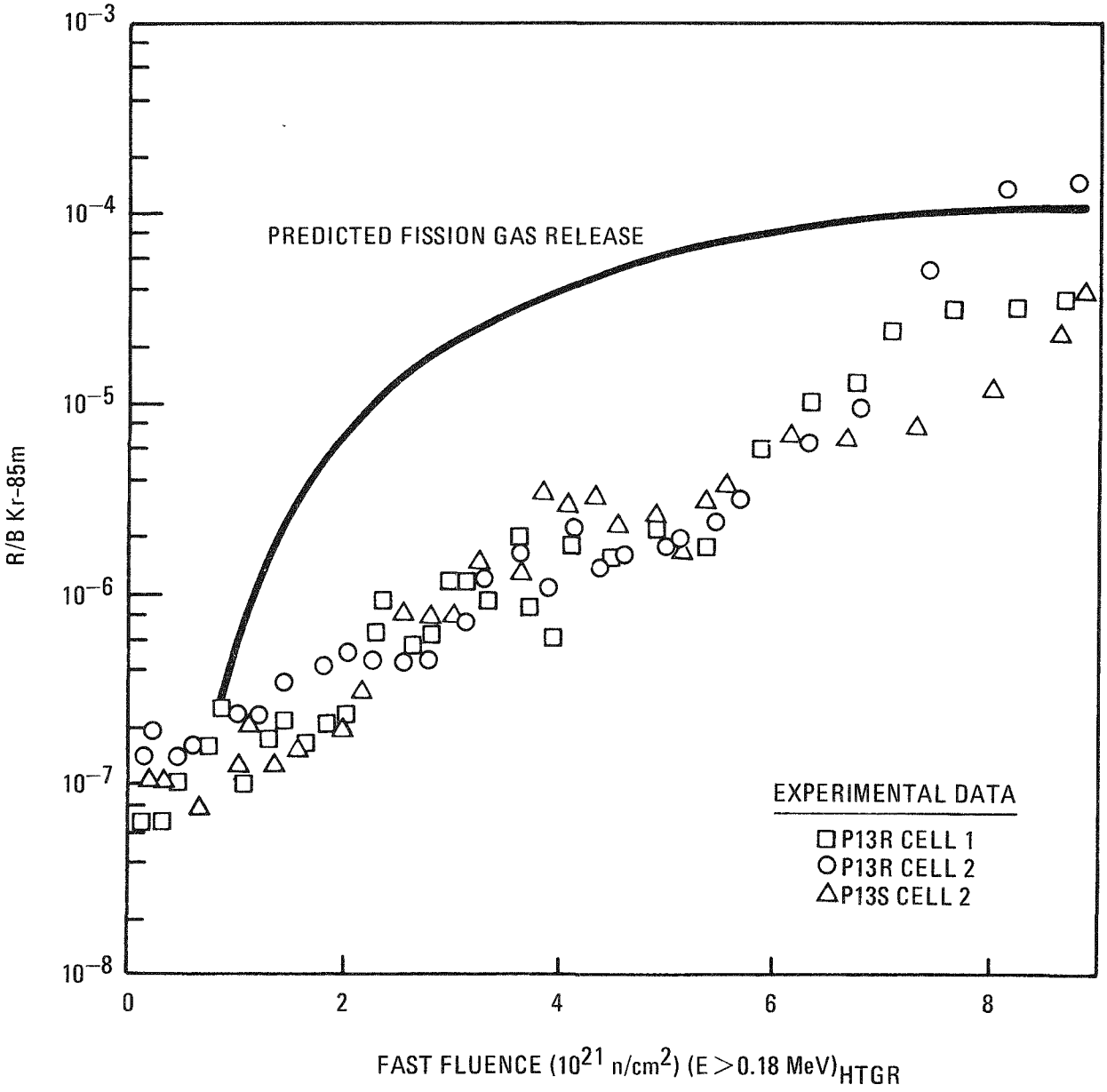

Fig. 9-44. Comparison between measured and predicted values of fission gas release (Kr-85m) for P13R and P13S fuel cells operating continuously at peak fuel rod temperatures of 1100°C (volume average temperature 1040°C)

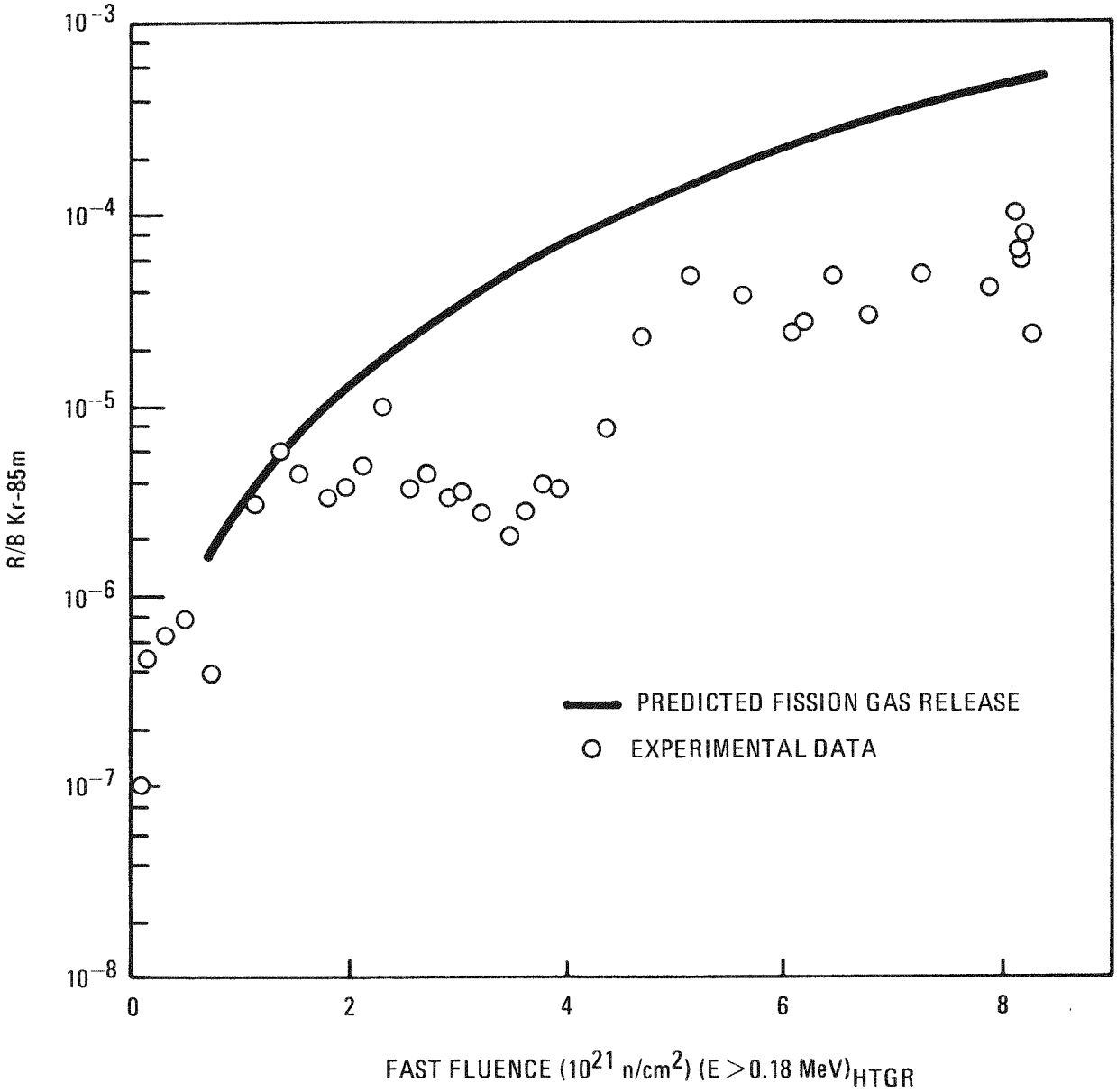

Fig. 9-45. Comparison between measured and predicted values of fission gas release (Kr-85m) for Cell 5 of P13S which operated continuously at a peak fuel rod temperature of 1500°C (volume average temperature 1440°C)

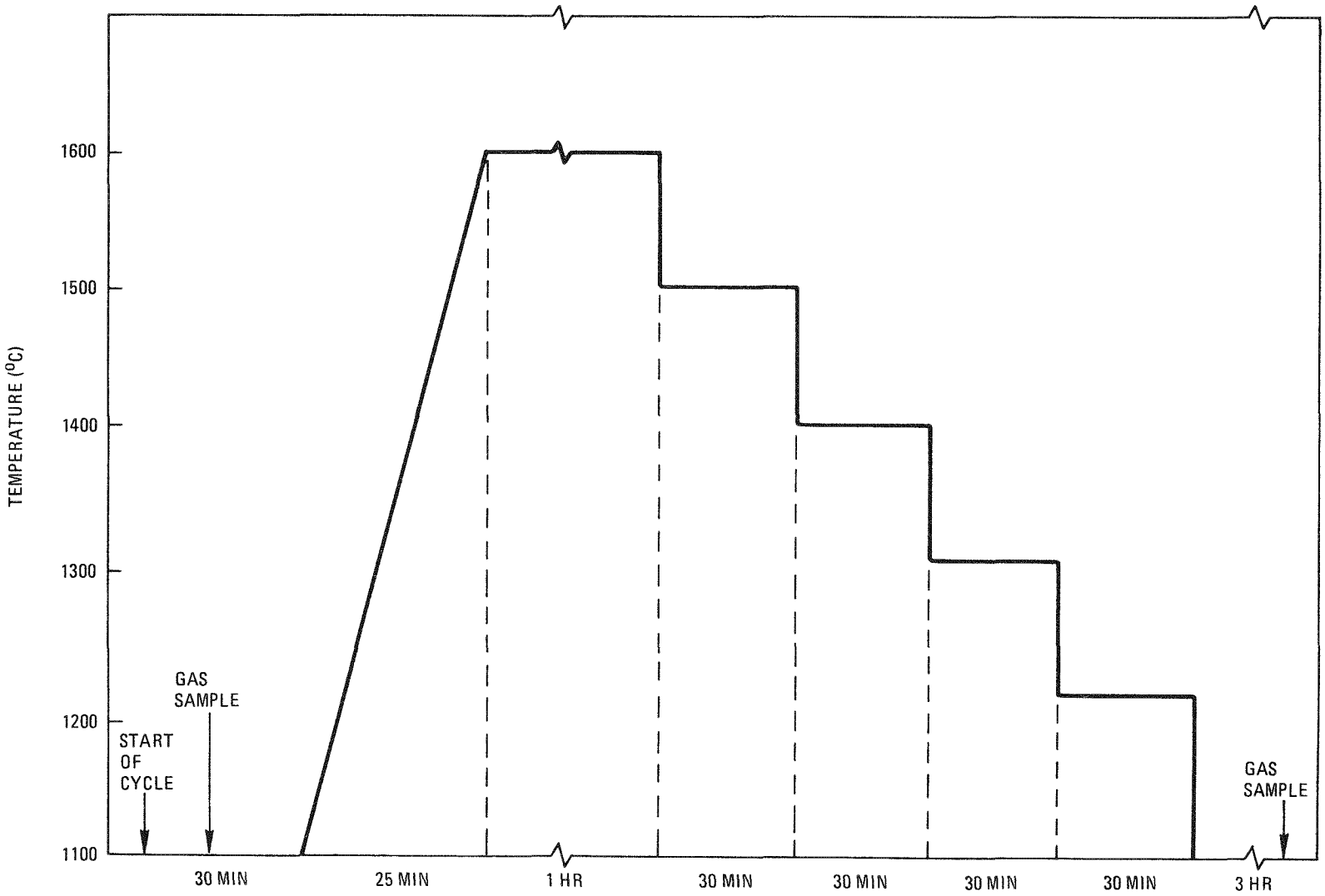

Fig. 9-46. Typical simulation of a load-following transient experienced by P13S Cell 1

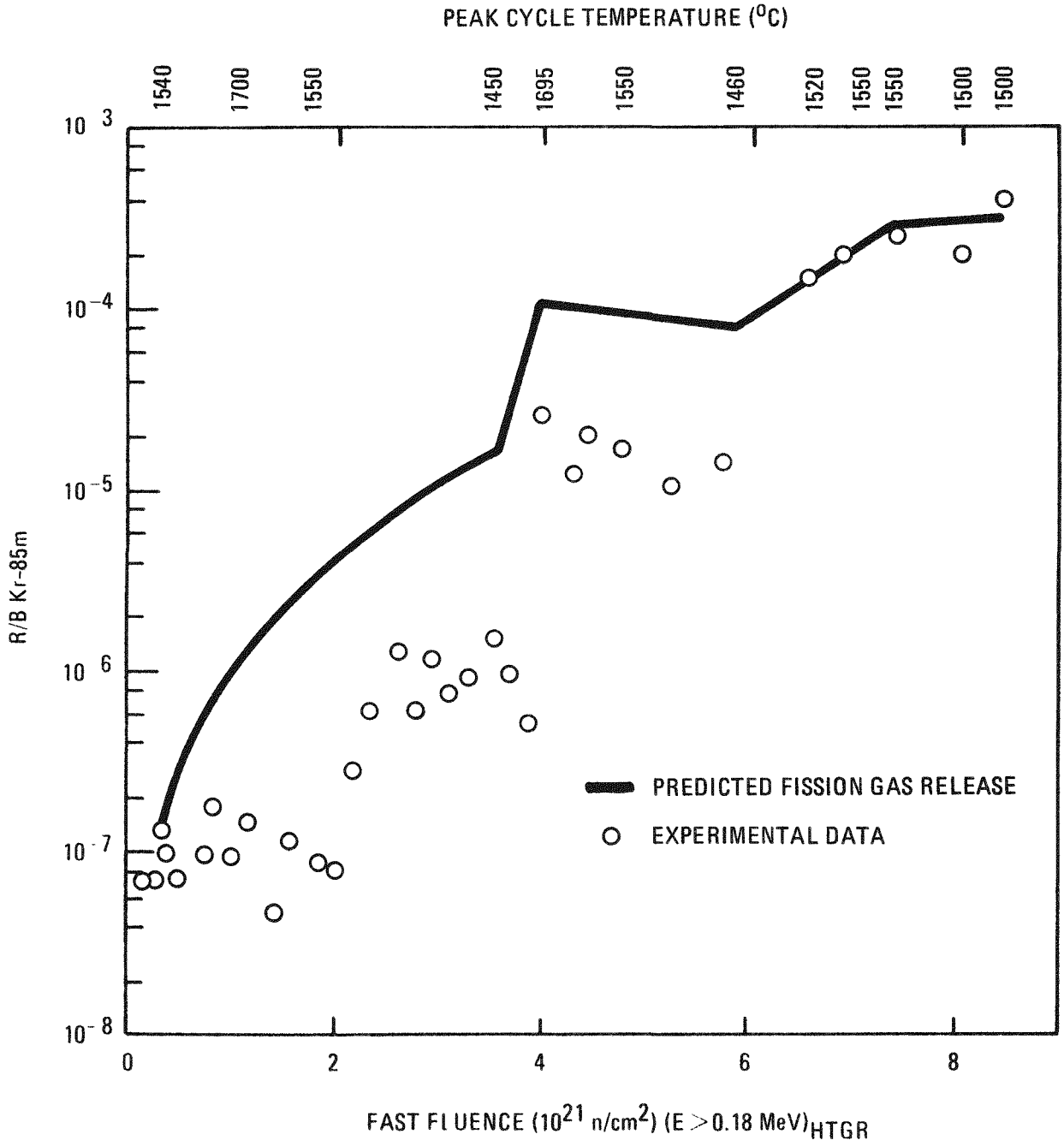

Fig. 9-47. Comparison of fission gas release measured during irradiation of the P13S thermal cycling cell (No. 1) and predicted using fuel performance models given in Ref. 9-3

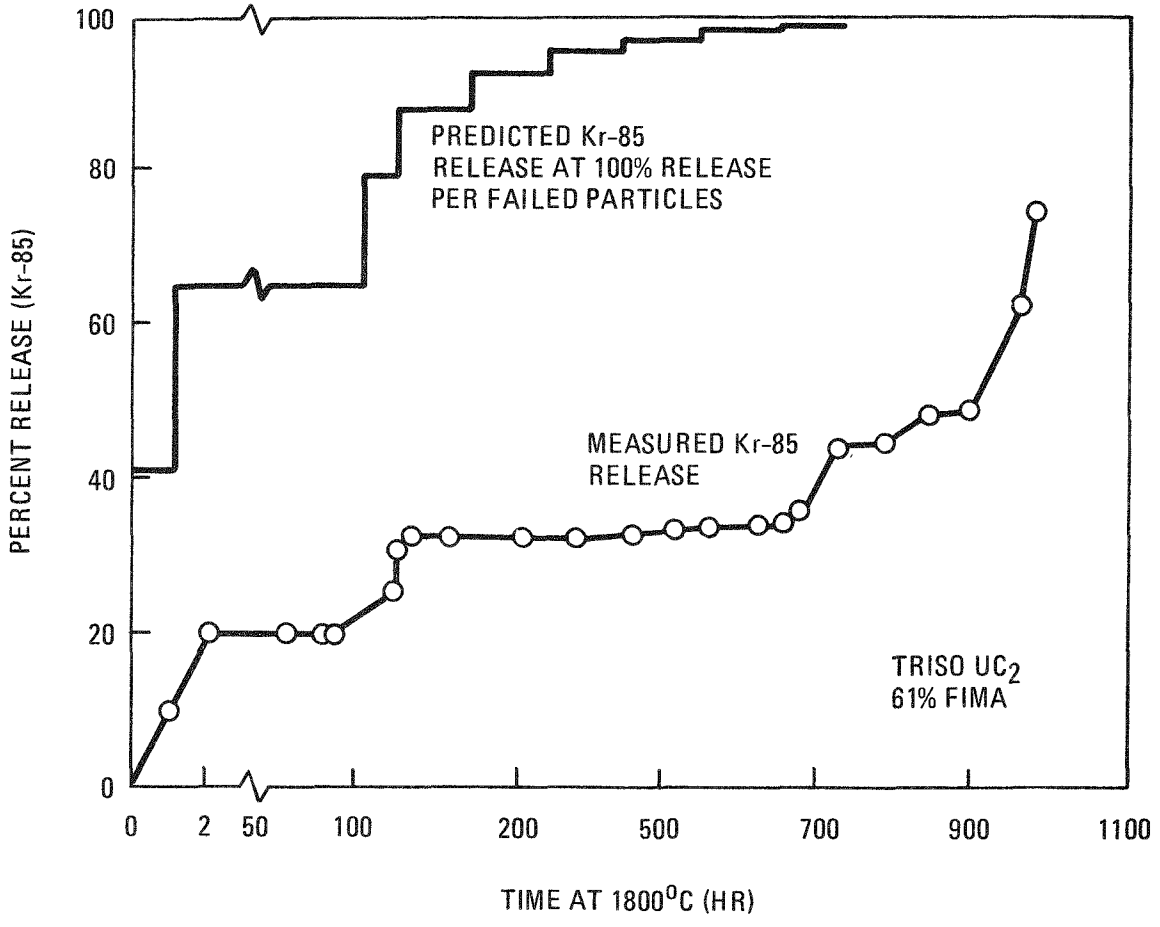

Fig. 9-48. Comparison of fission product release measured during post-irradiation heating of irradiated TRISO UC_2 fuel at 1800°C and predicted using models given in Ref. 9-3

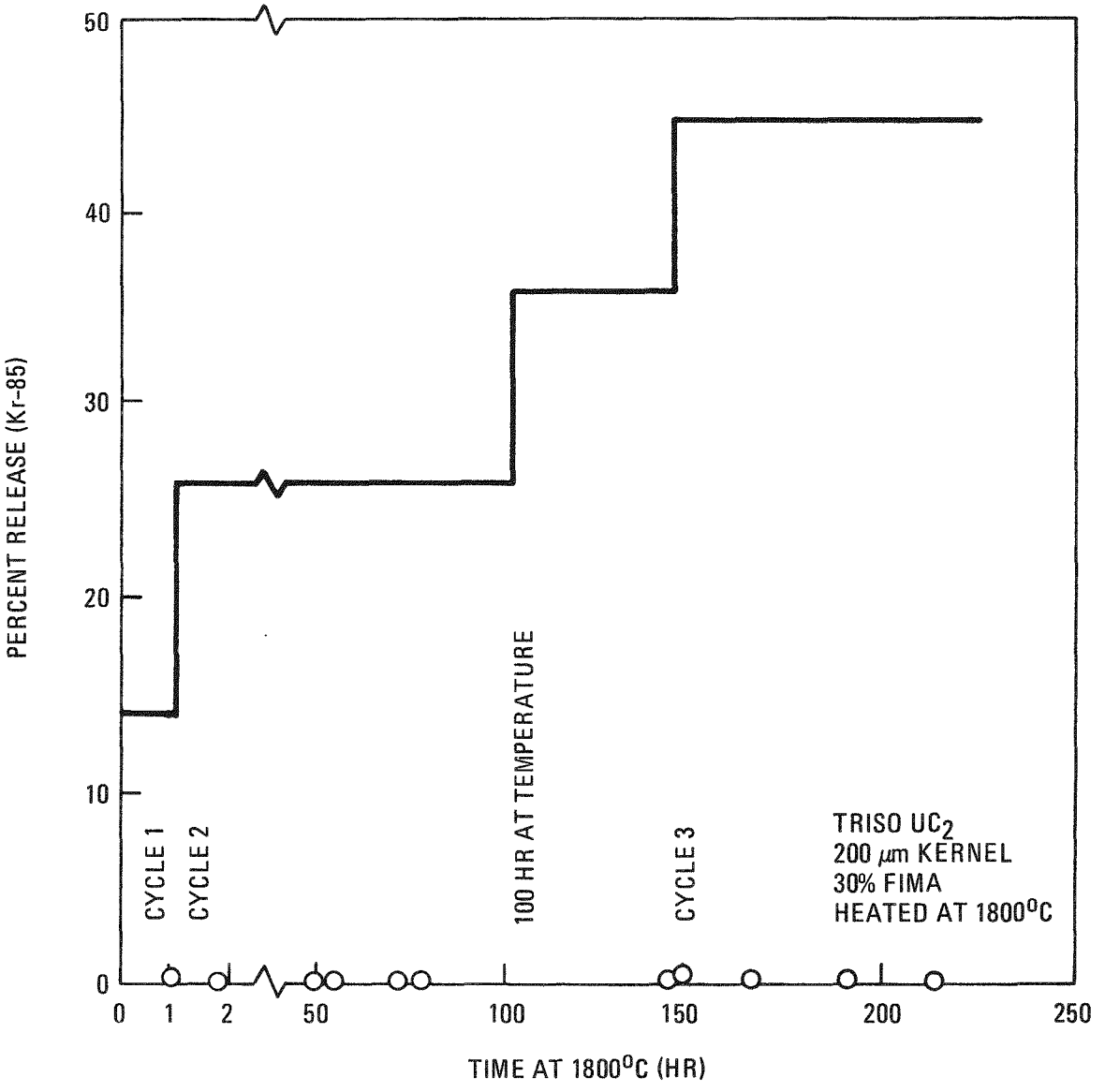

Fig. 9-49. Comparison of fission product release measured during post-irradiation heating of irradiated TRISO UC_2 fuel at 1800°C and predicted using models given in Ref. 9-3

11. GRAPHITE DEVELOPMENT
189a No. SU004

TASK 100: FABRICATION AND OPERATION OF IRRADIATION CAPSULES IN THE ORR

This task consists of the fabrication and operation of the irradiation capsules used to determine the irradiation behavior of the graphites.

Capsule OG-3 is under irradiation in the C-3 position of the ORR. Irradiation began on June 17, 1975 and the capsule will be discharged December 8, 1975. All crucibles are operating close to their design temperatures. Design work on capsule OG-4 has been completed and drawings have been issued.

TASK 200: GRAPHITE SPECIMEN PREPARATION AND PROPERTY MEASUREMENTS FOR CAPSULE IRRADIATIONS

Specimens of Great Lake Carbon Company (GLCC) grade H-451 (lots 266, 426, and 440), Union Carbide Corporation (UCC) grade TS-1240, and AirCo Speer (AS) grade SO-818 are under irradiation in a series of capsules to determine changes in dimensions and properties.

Capsule OG-2, which contained H-451 and TS-1240 specimens, completed irradiation during FY-75 and a final topical report (Ref. 11-1) has been issued covering the results.

Capsule OG-3, which contains specimens from OG-2 along with new specimens of H-451, TS-1240, and SO-818, is currently under irradiation in the ORR (see Task 100).

Capsule OG-4 is in the planning stage. Specimen selection and calculations of irradiation conditions are under way.

TASK 300: CHARACTERIZATION OF CANDIDATE GRAPHITES FOR PROPERTIES AND PURITY

In-depth characterization of GLCC's grade H-451, UCC's grade TS-1240, and AS's grade SO-818 is continuing.

The characterization work on H-451 (lot 426) and TS-1240 (lot 1) has been completed and a final topical report is in preparation. Thermal conductivity data for H-451 (lot 426) are given in Table 11-1.*

In-depth characterization of lot 440 of grade H-451 and lots 1 and 2 of grade SO-818 is continuing. Additional purity, density, and tensile property data for grade SO-181 (lot 1) are presented in Tables 11-2 and 11-3.

TASK 400: STATISTICAL STUDY OF GRAPHITE STRENGTH

Work under this subtask is continuing; there are no current results to report.

TASK 500: FATIGUE BEHAVIOR OF GRAPHITE

A series of room-temperature fatigue tests on unirradiated H-451 graphite (axial orientation) has been completed. The specimens were 0.5-in.-diameter by 1.0-in.-long cylinders from the quarter-length edge location of log 5651-90. A 6-in.-thick slab was cut from the log 9 in. from one end. Specimens were taken from the same quadrant, between 1 in. and 4 in. from the edge. The coring plan is shown in Fig. 11-1.* A group of specimens for tests at a given stress level was spaced roughly uniformly over the material section. The tests were uniaxial 1:1 tension-compression (zero mean stress) tests conducted in a specially constructed test cage in which two coaxial rams move in linear ball bearings. The cage is mounted on a Fatigue Dynamics crank and lever fatigue machine with a BLH load cell installed in the load train. The stress pattern is sinusoidal. The frequency was 400 cycles/min. The specimens were cemented to ground cylindrical metal end pieces with epoxy cement, using V-block jigs to ensure alignment.

*Tables and figures appear at the end of the text.

The first series of 28 tests were straight-pull tensile tests conducted in the fatigue cage to provide base line data. The results are given in Table 11-4. Subsequently six groups of 7 to 8 specimens were tested with peak stresses approximately equal to the mean tensile stress minus 0, 1, 2, 3, 4, and 5 standard deviations. Specimens were tested to failure or to 100,000 cycles, whichever occurred first. Results are tabulated in Table 11-5. The core number in the table corresponds to Fig. 11-1.

The data are plotted as peak stress versus log (cycles to failure) in Fig. 11-2. Specimens that survived 100,000 cycles or more without failure are shown as open circles. The lines corresponding to 10%, 50%, and 90% failure probability were constructed graphically. The endurance limit for 50% survival to 100,000 cycles was 1600 psi. The mean single-cycle tensile strength, including the fatigue specimens that fractured during the first loading cycle, was 2692 psi; thus, the 100,000 cycle endurance limit for 50% survival corresponds to 59% of the mean single-cycle tensile strength.

TASK 600: STRUCTURAL INTEGRITY OF GRAPHITE BLOCKS

A Program Plan for the structural verification subtask is in preparation. It includes detailed analyses to predict residual stresses in irradiated graphite elements and experiments to measure these stresses for comparison with the predictions. Experiments to establish the stress limits for unirradiated and irradiated graphite elements are also included.

TASK 700: PROGRAM PLAN

Executive summaries of a Program Plan "Graphite Development Program for Steam Cycle HTGR" are under review by ERDA-RRD.

REFERENCE

11-1. Price, J. R., and L. A. Beavan, "Final Report on Graphite Irradiation Test OG-2," ERDA Report GA-A13556, General Atomic Company, to be published.

TABLE 11-1
THERMAL CONDUCTIVITY OF H-451 GRAPHITE, GLCC[a] LOT 426
Log 6484-34 (GLCC log 198), density = 1.73 g/cm^3 and
log 6484-41 (GLCC log 184), density = 1.72 g/cm^3

GDB[b] Specimen Number	Orientation[c]	Location in Log[d]	Thermal Conductivity (cal/cm-sec-°C)				
			22°C	200°C	400°C	600°C	800°C
6484-34-3A-L51A	Parallel	Midlength	0.271	0.227	0.186	0.164	0.138
-L51B	↓	center	0.327	0.268	0.211	0.162	0.147
-L55A		↓	0.315	0.292	0.241	0.190	0.165
-L55B			0.317	0.266	0.228	0.192	0.163
-3B-L62A			0.281	0.271	0.224	0.182	0.158
-L62B			0.382	0.442	0.231	0.180	0.163
-L66A			0.384	0.275	0.224	0.187	0.167
-L66B	↓	↓	0.323	0.265	0.225	0.174	0.142
Mean			0.325	0.288	0.221	0.179	0.155
Std. dev.			0.041	0.065	0.017	0.011	0.011
6484-34-3A-L78A	Perpendicular	Midlength	0.312	0.270	0.201	0.173	0.149
-L78B	↓	center	0.310	0.273	0.200	0.144	0.141
-L81A		↓	0.341	0.303	0.222	0.189	0.156
-L81B			0.324	0.266	0.197	0.175	0.136
-3B-L90A			0.258	0.284	0.235	0.179	0.163
-L90B			0.308	0.259	0.199	0.170	0.142
-L93A			0.312	0.282	0.205	0.180	0.144
-L93B	↓	↓	0.296	0.266	0.226	0.192	0.168
Mean			0.308	0.275	0.211	0.175	0.150
Std. dev.			0.024	0.014	0.015	0.015	0.011
6484-41-3A-L003A	Parallel	Midlength	0.325	0.280	0.219	0.179	0.151
-L003B	↓	center	0.341	0.272	0.215	0.157	0.150
-L004A		↓	0.430	0.296	0.203	0.175	0.148
-L004B			0.381	0.366	0.219	0.190	0.148
-3B-L003A			0.339	0.301	0.224	0.188	0.167
-L003B			0.328	0.306	0.232	0.198	0.158
-L004A	↓	↓	0.312	0.268	0.228	0.189	0.157
Mean			0.351	0.298	0.220	0.183	0.154
Std. dev.			0.041	0.033	0.009	0.013	0.007
6484-41-3A-L016A	Perpendicular	Midlength	0.308	0.272	0.205	0.189	0.150
-L016B	↓	center	0.293	0.245	0.204	0.159	0.139
-L022A		↓	0.340	0.286	0.221	0.178	0.138
-L022B			0.309	0.272	0.215	0.174	0.162
-3B-L016A			0.382	0.274	0.216	0.188	0.163
-L016B			0.361	0.281	0.219	0.179	0.151
-L022A	↓	↓	0.336	0.244	0.197	0.168	0.145
Mean			0.333	0.268	0.211	0.176	0.150
Std. dev.			0.032	0.017	0.009	0.011	0.010

[a] GLCC = Great Lakes Carbon Company.

[b] GDB = Graphite Development Branch, General Atomic Company.

[c] Parallel = parallel to extrusion direction, perpendicular = perpendicular (radial) to extrusion direction.

[d] Position in parent extrusion (∿18 in. in diameter by ∿34 in. long).

TABLE 11-2
IMPURITY CONTENT (IN PPM) OF SO-818 GRAPHITE, LOT 1

[GDB Log No./AS Log No.][a] GDB Sample No.	Location in Log[b]	Ash	B	Fe	V	Ti	S
[6484-20/AS 16]							
6484-20-3A-L016	MLC	<10	<0.5	<1.0	<0.5	<1.0	8.1
-3B-L016	MLC	30	<0.5	<1.0	<0.5	<1.0	10.8
-3A-L036	MLE	<10	<0.5	<1.0	<0.5	<1.0	13.0
-3B-L036	MLE	40	<0.5	<1.0	<0.5	<1.0	4.4
-1A-L016	EC	30	<0.5	<1.0	<0.5	<1.0	6.4
-1B-L016	EC	<10	<0.5	<1.0	<0.5	<1.0	9.0
-1A-L036	EE	40	<0.5	<1.0	<0.5	<1.0	11.2
-1B-L036	EE	<10	<0.5	<1.0	<0.5	<1.0	<1.0
Mean	Whole log	<22.5	<0.5	<1.0	<0.5	<1.0	<8.0

[a] GDB = Graphite Development Branch, General Atomic Company; AS = AirCo Speer Division of Air Reduction Company.

[b] MLC = midlength center, EC = end center, MLE = midlength edge, and EE = end edge.

TABLE 11-3
TENSILE PROPERTIES OF SO-818 GRAPHITE, AS[a] LOT 1
Log 6484-20 (AS 16), density = 1.76 g/cm^3, 0.505-in.-diameter x 3.00-in.-long samples

GDB[b] Specimen No.	Position and Orientation[c]	Density (g/cm^3)	Elastic Modulus on Second Loading[d] (10^6 psi)	Permanent Set After First Loading (%)	Fracture Strain (%)	Ultimate Strength (psi)
6484-20-3A-L002B	MLC(||)	1.737	1.00	0.024	0.212	1492
-L005B		1.722	0.99	0.247	0.247	1605
-L006B		1.721	0.93	0.034	0.190	1256
-L008B		1.734	0.98	0.029	0.234	1533
-3B-L002B		1.767	1.10	0.016	0.254	1965
-L005B		1.741	1.04	0.020	0.245	1745
-L006B		1.742	1.02	0.029	0.220	1520
-L008B		1.752	1.06	0.020	0.244	1740
-3A-L002A						1686
-L005A						1496
-L006A						1632
-L008A						1796
-L003A						1626
-L009A						1691
-3B-L002A						2003
-L005A						1821
-L006A						1910
-L008A						1756
-L003A						2035
-L009A						1496
Mean		1.740	1.01	0.025	0.231	1690
Std. dev.		0.015	0.052	0.006	0.022	199
6484-20-3A-L011	MLC(⊥)	1.731	0.92	0.025	0.232	1516
-L013		1.730	0.84	0.040	0.222	1272
-L018		1.719	(e)	(e)	(e)	890
-L020		1.719	0.86	0.028	0.207	1256
-3B-L011		1.734	0.91	0.025	0.246	1521
-L013		1.731	0.91	0.025	0.244	1521
-L018		1.741	0.90	0.027	0.216	1356
-L020		1.738	0.88	0.030	0.199	1246
-3A-L012						1446
-L014						1651
-L015						1641
-L017						1531
-L019						1286
-L021						1246
-3B-L012						1627
-L014						1496
-L015						843
-L017						1351
-L019						1346
-L021						1297
Mean		1.730	0.90	0.029	0.224	1367
Std. dev.		0.008	0.035	0.005	0.018	218

TABLE 11-3 (Continued)

GDB[b] Specimen No.	Position and Orientation[c]	Density (g/cm^3)	Elastic Modulus on Second Loading[d] (10^6 psi)	Permanent Set After First Loading (%)	Fracture Strain (%)	Ultimate Strength (psi)
6484-20-3A-L031B	MLE(||)	1.740	1.06	0.021	(f)	(f)
-L034B		1.711	0.99	0.018	0.259	1716
-L035B		1.750	1.06	0.025	0.241	1686
-L038B		1.752	1.10	0.023	0.244	1771
-3B-L031B		1.810	1.22	0.014	0.249	2097
-L034B		1.761	1.08	0.030	0.240	1723
-L035B		1.750	1.12	0.020	0.239	1839
-L038B		1.770	1.13	0.022	0.259	1898
-3A-L031A						2074
-L034A						1706
-L035A						1986
-L038A						1910
-L039A						2148
-L039B						1857
-3B-L031A						2373
-L034A						2099
-L035A						1888
-L038A						1943
-L039A						2587
-L039B						2397
Mean		1.755	1.09	0.022	0.247	1984
Std. dev.		0.028	0.066	0.005	0.009	254
6484-20-3A-L041	MLE(⊥)	1.740	0.91	0.026	0.249	1558
-L043		1.740	0.94	0.029	0.235	1488
-L048		1.713	0.89	0.030	0.219	1373
-L050		1.720	0.90	0.030	0.229	1448
-3B-L041		1.792	1.02	0.014	0.244	1719
-L043		1.793	1.02	0.020	0.226	1637
-L048		1.795	0.96	0.036	0.221	1422
-L050		1.793	1.01	0.028	0.222	1533
-3A-L042						1538
-L044						1613
-L045						125
-L047						1354
-L049						1434
-L051						1498
-3B-L042						1737
-L044						1826
-L045						1746
-L047						1377
-L049						1567
-L051						1622
Mean		1.761	0.96	0.027	0.231	1481
Std. dev.		0.036	0.056	0.007	0.011	346

TABLE 11-3 (Continued)

GDB[b] Specimen No.	Position and Orientation[c]	Density (g/cm^3)	Elastic Modulus on Second Loading[d] (10^6 psi)	Permanent Set After First Loading (%)	Fracture Strain (%)	Ultimate Strength (psi)
6484-20-1A-L002B	EC(||)	1.779	1.20	0.010	0.274	2221
-L005B		1.771	1.23	0.013	0.240	2005
-L006B		1.770	1.20	0.014	0.252	2045
-L008B		1.767	1.15	0.019	0.260	2046
-1B-L002B		1.770	1.25	0.017	0.259	2056
-L005B		1.781	1.18	0.015	0.260	2000
-L006B		1.777	1.18	0.016	0.261	2045
-L008B		1.782	1.18	0.013	0.254	2080
-1A-L002A						1998
-L005A						1884
-L006A						1964
-L008A						1879
-L003A						1837
-L009A						1748
-1B-L002A						1798
-L005A						(f)
-L006A						1829
-L008A						2100
-L003A						1908
-L009A						2023
Mean		1.775	1.20	0.015	0.257	1972
Std. dev.		0.006	0.030	0.003	0.010	120
6484-20-1A-L011	EC(⊥)	1.753	1.00	0.021	0.262	1749
-L013		1.766	1.03	0.020	0.272	1874
-L018		1.753	1.01	0.022	0.237	1548
-L020		1.786	1.02	0.020	0.255	1773
-1B-L011		1.751	0.98	0.024	0.246	1613
-L013		1.779	1.06	0.019	0.282	1978
-L018		1.751	0.95	0.025	0.203	1374
-L020		1.783	1.02	0.020	0.265	1798
-1A-L012						1752
-L014						2017
-L015						2033
-L017						1572
-L019						1687
-L021						1822
-1B-L012						1921
-L014						1946
-L015						(f)
-L017						1488
-L019						1697
-L021						1752
Mean		1.765	1.01	0.021	0.253	1757
Std. dev.		0.015	0.034	0.002	0.024	183

TABLE 11-3 (Continued)

GDB[b] Specimen No.	Position and Orientation[c]	Density (g/cm^3)	Elastic Modulus on Second Loading[d] (10^6 psi)	Permanent Set After First Loading (%)	Fracture Strain (%)	Ultimate Strength (psi)
6484-20-1A-L031B	EE(∥)	1.811	1.17	0.014	0.224	1796
-L034B		1.811	1.11	0.022	0.220	1696
-L035B		1.826	1.22	0.011	0.280	2246
-L038B		1.806	1.14	0.022	0.237	1835
-1B-L031B		1.818	1.27	0.010	0.283	2486
-L034B		1.805	1.22	0.014	0.291	2330
-L035B		1.822	1.30	0.011	0.303	2591
-L038B		1.811	1.25	0.012	0.275	2345
-1A-L031A						2091
-L034A						2100
-L035A						2490
-L038A						2165
-L039A						2697
-L039B						2391
-1B-L031A						2324
-L034A						2475
-L035A						2590
-L038A						2375
-L039A						2291
-L039B						2396
Mean		1.814	1.21	0.014	0.264	2285
Std. dev.		0.075	0.066	0.005	0.032	270
6484-20-1A-L041	EE(⊥)	1.760	1.02	0.028	0.214	1483
-L043		1.763	0.97	0.025	0.225	1518
-L048		1.754	0.97	0.024	0.272	1759
-L050		1.786	1.06	0.015	0.256	1909
-1B-L041		1.784	0.98	0.019	0.237	1719
-L043		1.813	1.03	0.017	0.263	1899
-L048		1.793	1.02	0.018	0.224	1599
-L050		1.806	1.06	0.017	0.235	1719
-1A-L042						1613
-L044						1713
-L045						1818
-L047						1747
-L049						1588
-L051						1991
-1B-L042						1968
-L044						2037
-L045						1558
-L047						1983
-L049						1648
-L051						1807
Mean		1.782	1.01	0.020	0.241	1754
Std. dev.		0.022	0.038	0.005	0.021	169

[a] AS = AirCo Speer Division of Air Reduction Company.

[b] GDB = Graphite Development Branch, General Atomic Company.

[c] Position in parent extrusion (∿18-in. diameter by ∿34 in. long): MLC = midlength center, MLE = midlength edge, EC = end center, EE = end edge, ∥ = parallel to extrusion, and ⊥ = perpendicular (radial) to extrusion.

[d] Specimens were loaded to 1000 psi, unloaded to zero stress, and reloaded to failure while recording the stress-strain curve. Elastic modulus = chord modulus between 100 and 1000 psi on second loading.

[e] Specimen broke during first load cycle.

[f] Bond failure.

TABLE 11-4
TENSILE STRENGTH OF AXIAL H-451 GRAPHITE SPECIMENS TESTED IN FATIGUE FIXTURE

Core No.	Sample No.	Diameter (in.)	Load at Fracture (lb)	Tensile Strength (psi)
3	A	0.50011	597	3042
4	A	0.50011	576	2935
5	A	0.49976	531	2705
8	A	0.49991	507	2581
9	A	0.49914	547	2803
10	A	0.49995	439	2241
12	A	0.50013	561	2855
13	A	0.50005	470	2394
15	A	0.50005	518	2644
17	A	0.49992	579	2949
26	A	0.50018	446	2270
27	A	0.50009	535	2515
28	A	0.50018	567	2882
30	A	0.50033	458	2322
31	A	0.49997	615	3134
34	A	0.49998	555	2825
35	A	0.50022	512	2612
36	A	0.50003	482	2458
38	A	0.50017	506	2579
39	A	0.50005	531	2702
6	A	0.50023	500	2546
11	A	0.50017	579	2946
12	A	0.50013	627	3196
14	A	0.50005	519	2644
16	A	0.49984	597	3045
25	A	0.50014	627	3196
29	A	0.49795	531	2725
30	A	0.50033	579	2943
32	A	0.49997	561	2858
37	A	0.50017	494	2514
				2747 Mean
				262 Std. dev.

TABLE 11-5
UNIAXIAL FATIGUE TESTS ON AXIAL H-451 GRAPHITE
(1:1 TENSION:COMPRESSION)

Core No.	Sample No.	Diameter (in.)	Stress Range (psi)		No. of Cycles to Failure
			Max.	Min.	
3	B	0.50424	2476	-2415	10
5	B	0.49949	2217	-2155	24
6	B	0.50009	2273	-2155	3
7	B	0.49939	2458	-2581	115
8	B	0.49991	2155	-2276	162
9	B	0.49989	2212	-2155	<1 [(a)]
10	B	0.49943	2394	-2644	34
11	B	0.50006	2458	-2458	5,200
12	B	0.50017	2459	-2459	45
13	B	0.50008	2546	-2394	40
14	B	0.50010	2322	-1721	<1 [(a)]
15	B	0.50010	2550	-2394	16
16	B	0.50008	2515	-2322	832
17	B	0.50037	2212	-2212	87
18	B	0.50018	2155	-2155	3
19	B	0.49871	2212	-2212	36
20	B	0.50022	2155	-2155	2
21	B	0.50010	2155	-2270	162
22	B	0.50036	1905	-1905	7,000
23	B	0.50010	1939	-1939	7,768
25	B	0.49991	1999	-1939	351
26	B	0.50002	1999	-1939	577
27	B	0.50002	1939	-1999	6
28	B	0.49986	1999	-1939	137
29	B	0.49910	1939	-1939	56
30	B	0.49961	1999	-1939	115
31	B	0.50005	1939	-1999	59
32	B	0.49996	1997	-1997	117

TABLE 11-5 (Continued)

Core No.	Sample No.	Diameter (in.)	Stress Range (psi)		No. of Cycles to Failure
			Max.	Min.	
34	B	0.49991	1633	-1633	39,300
35	B	0.49984	1752	-1752	100,000[b]
36	B	0.49984	1752	-1752	121,200[b]
37	B	0.50005	1752	-1752	200
38	B	0.50005	1692	-1722	115,100[b]
39	B	0.50000	1722	-1781	7,600
41	B	0.49962	1722	-1781	465
42	B	0.50415	1663	-1841	17,900
43	B	0.49998	2761	-2761	5
44	B	0.49994	2761	-2791	3
45	B	0.49994	2405	-2672	<1[a]
46	B	0.49990	2405	-2732	<1[a]
47	B	0.50021	2494	-2613	<1[a]
48	B	0.50051	2613	-2672	<1[a]
18	A	0.50029	2672	-2672	<1[a]
19	A	0.49965	2672	-2672	<1[a]
20	A	0.50019	1722	-1722	3,851
21	A	0.50020	1663	-1781	12,400
3	C	0.50033	1445	-1445	13,100
10	D	0.49954	1445	-1445	121,200[b]
16	E	0.49992	1445	-1445	4,500
22	C	0.50000	1484	-1445	103,000[b]
32	D	0.49978	1484	-1484	119,000[b]

[a] First cycle failure.

[b] No failure.

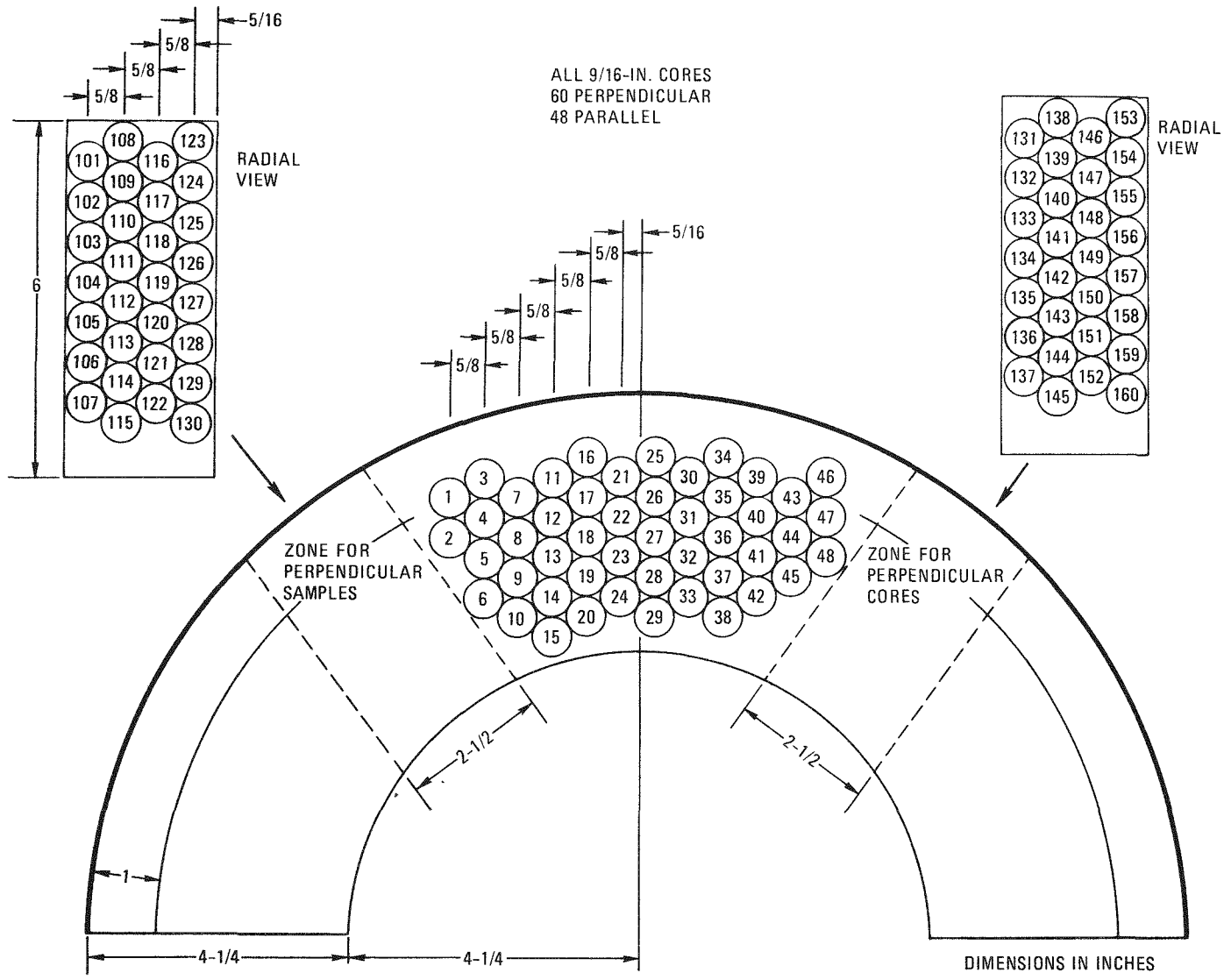

Fig. 11-1. Coring pattern for H-451 graphite fatigue specimens

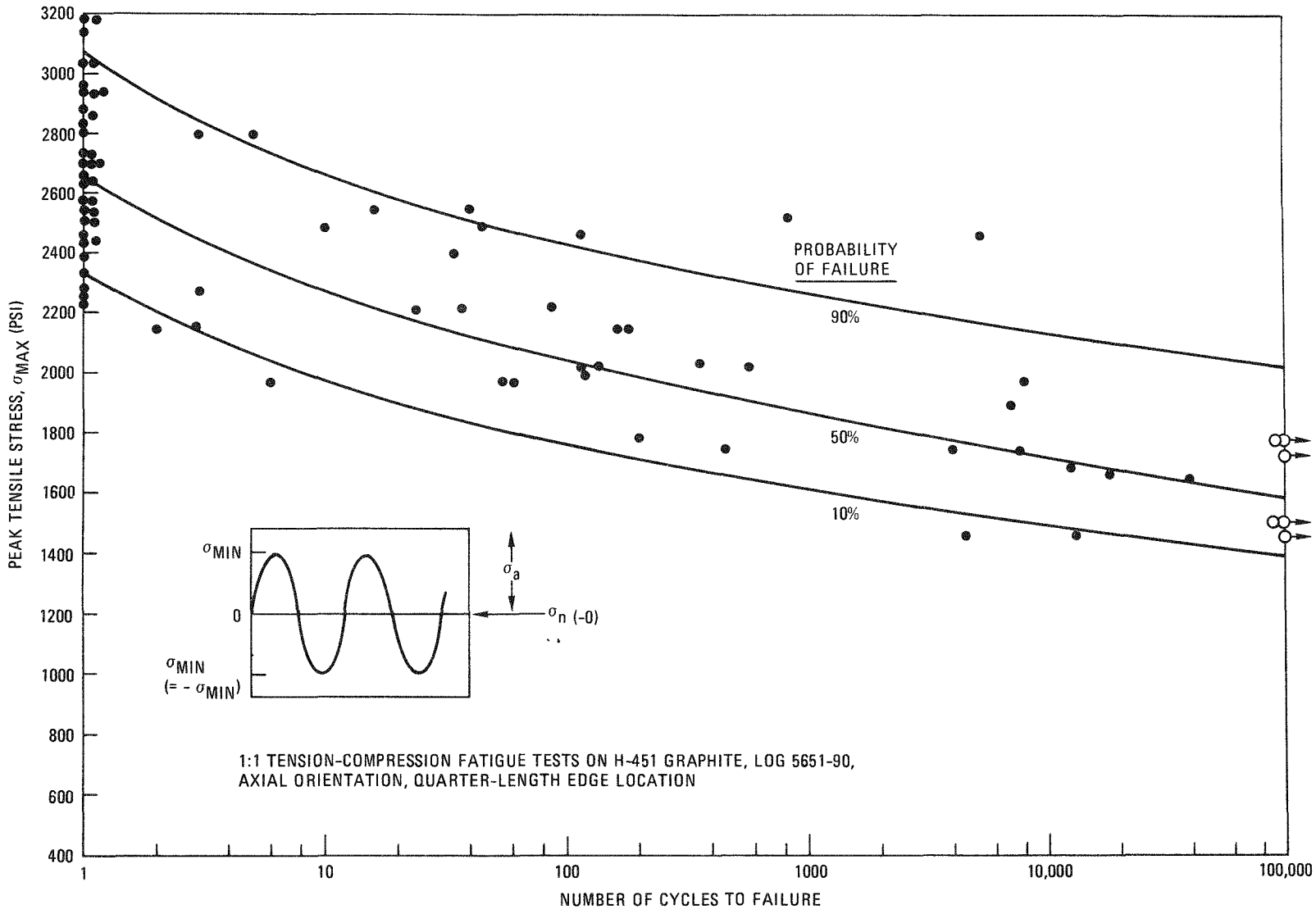

Fig. 11-2. Fatigue test data on axial H-451 graphite; cycles to failure versus peak tensile stress for uniaxial tests, 1:1 tension-compression

APPENDIX

PROJECT REPORTS PUBLISHED DURING THE QUARTER

Johnson, W.R., et al., "Postirradiation Examination of Capsules HT-24 and HT-25," ERDA Report GA-A13486, General Atomic, September 15, 1975.

Price, R. J., "Mechanical Properties of Graphite for High-Temperature Gas-Cooled Reactors: A Review," ERDA Report GA-A13524, General Atomic, September 22, 1975.

Brogli, R.H., et al., "The High Conversion HTGR for Resource Conservation," ERDA Report GA-A13606, General Atomic, October 1, 1975.